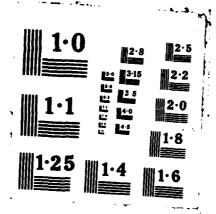
UPPER-THERHOSPHERIC OBSERVATIONS AND NEUTRAL-GAS DYNAMICS AT HIGH LATITUD. (U) AIR FORCE INST OF TECH MRIGHT-PATTERSON AFB OH C R TSCHAN 1987 AFIT/CI/NR-87-135D F/G 4/1 AD-A188 058 1/4 UNCLASSIFIED > **0**







UPPER-THERMOSPHERIC OBSERVATIONS AND NEUTRAL-GAS DYNAMICS AT HIGH LATITUDES DURING SOLAR MAXIMUM

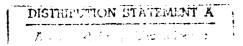
by

Christopher Raymond Tschan

A dissertation submitted in partial fulfillment of the requirements for the degree of Doctor of Philosophy (Atmospheric Science) in The University of Michigan 1987

Doctoral Committee:

Associate Research Scientist Timothy L. Killeen, Co-Chairman Professor Paul B. Hays, Co-Chairman Professor V. C. Liu Professor Andrew F. Nagy Research Scientist Gonzalo J. Hernandez



UNCLASSIFIED .
SECURITY CLASSIFICATION OF THIS PAGE (When Date Enters

		والمراجع والم والمراجع والمراجع والمراجع والمراجع والمراجع والمراجع والمراج
REPORT DOCUMENTATION	PAGE	READ INSTRUCTIONS BEFORE COMPLETING FORM
1. REPORT NUMBER	2. GOVT ACCESSION NO.	3. RECIPIENT'S CATALOG NUMBER
AFIT/CI/NR 87-135D	ADA 1880:	58'
4. TITLE (and Subtitie)		5. TYPE OF REPORT & PERIOD COVERED
Upper-Thermospheric Observations and Neutral-Gas Dynamics at High Latitudes During Solar Maximum		######################################
		6. PERFORMING ORG. REPORT NUMBER
7. AUTHOR(s)		8. CONTRACT OR GRANT NUMBER(s)
Christopher Raymond Tschan		
9. PERFORMING ORGANIZATION NAME AND ADDRESS AFIT STUDENT AT:		10. PROGRAM ELEMENT, PROJECT, TASK AREA & WORK UNIT NUMBERS
University of Michigan		
11. CONTROLLING OFFICE NAME AND ADDRESS AFIT/NR		12. REPORT DATE
WPAFB OH 45433-6583		13. NUMBER OF PAGES
14. MONITORING AGENCY NAME & ADDRESS(II different	t from Controlling Office)	296 15. SECURITY CLASS. (of this report)
		UNCLASSIFIED
		15a. DECLASSIFICATION/DOWNGRADING SCHEDULE
16. DISTRIBUTION STATEMENT (of this Report)		L
ADDROVED FOR BURLING DELEACE, DIGE	. T	
APPROVED FOR PUBLIC RELEASE; DISTR	KIBUTION UNLIMITE	ΣD [
,		
17. DISTRIBUTION STATEMENT (of the abstract entered I	n Block 20, if different fro	m Report)
		j
		1
18. SUPPLEMENTARY NOTES		Oran Walan
APPROVED FOR PUBLIC RELEASE: IAW	AFR 190-1	LYNN E. WOLAVER A 177
		Dean for Research and
		Professional Development
_		AFIT/NR
19. KEY WORDS (Continue on reverse side if necessary and	I identify by block number)	
		· ;
		i
20. ABSTRACT (Continue on reverse side if necessary and	identify by block number)	
ATTACHED		1
		I
		ì

Kinnaksingsingalisissi beresembersingan periodasia periodasia perioda perioda perioda perioda perioda perioda

To My Parents

Automion For
NTIS CRASI DTIC TAS Undeceded Just resecut
By Distribution /
Acknowled Discussion
Dist A Ship (8) or special
A-1



ACKNOWLEDGMENTS

This work might not exist if it were not for Dr. Tim Killeen whose intellectual inspiration pointed me in the right direction. Of course, there were a few others who made sure I remained moving in that direction. The main players were: Drs. Gerry McCormac and Gonzalo Hernandez. I'd also like to thank a few others. Thanks to Profs. Paul Hays and Andrew Nagy, as well as Drs. Tom Cravens, Alan Burns, and Dave Gell at the U of M Space Physics Research Lab. Thanks also to Prof. V. C. Liu of the Aerospace Engineering Dept. There were of course, fellow students who provided a sounding board for many of the ideas in this thesis. Those who suffered the most were: Jeff Thayer, Bruno Nardi, and Jean-Jacques Ponthieu. In general, the SPRL provided the right atmosphere for success. In addition, the computations at NCAR could never have carried out without the patient help of Drs. Barbara Emery, Ray Roble, and Cicely Ridley as well as Ben Foster and Ken Hansen. All I can say once again is thanks.

I also wish to thank the other Dynamics Explorer principal investigators who provided data to supplement that of the Fabry-Perot interferometer. These people are:

Drs. Rod Heelis, George Carignan, Walt Heogy, and Larry Wharton.

The opportunity to pursue this degree would not have been possible if it were not for the United States Air Force, which selected and funded me. Any undertaking like this one entails some risk of failure. However, the Air Force, like my parents, never doubted that I had what it takes to complete this program successfully. It was because of that trust that I was able to call up the discipline needed to stay on track and finish in the required time period. I intend to repay their confidence with distinguished service in the very near future.

Finally, I'd like to thank my wife for her patience. After all, she put up with my complaints day after day and somehow managed to raise our two sons too. There is no tougher job than that.

TABLE OF CONTENTS

DEDICATION
ACKNOWLEDGEMENTS
LIST OF FIGURES
LIST OF TABLES
LIST OF APPENDICES xvii
CHAPTER
I. INTRODUCTION
 1.1 Thesis Objective 1.2 Overview of the Thermosphere 1.3 Outline of Thermospheric Data and Models 1.4 Statement of Thesis Results
II. REVIEW OF BASIC THERMOSPHERIC PROPERTIES
 2.1 Overview 2.2 Neutral-Gas Forces Influencing Thermospheric Circulation 2.3 The Mean State of the Thermosphere 2.3.1 Thermospheric Neutral Composition 2.3.2 The Mean State of the Ionosphere and its Relation to the
Thermosphere 2.3.3 The Mean Thermal Structure of the Thermosphere 2.3.3.1 Thermospheric Heating Due to Absorption of Solar-EUV Radiation 2.3.3.2 Joule Heating of the Thermosphere 2.3.3.3 Thermospheric Heating Due to Particle Precipitation 2.3.3.4 Other Thermospheric Heat Sources 2.3.3.5 Cooling Mechanisms in the Thermosphere 2.3.4 Global-Thermospheric Neutral Winds
2.4 Perturbations From the Mean Thermospheric State 2.4.1 Variations in Solar-EUV Heating 2.4.2 Variations in the Coupling Between the IMF and Magnetosphere
2.5 Summary

III.	REVIEW OF THE INFLUENCE OF THE SOLAR WIND, MAGNETOSPHERE, AND IONOSPHERE ON THE THERMOSPHERE . 47
	3.1 Overview of Solar-Wind/Magnetospheric/Ionospheric Interactions 3.2 Solar-Wind/Magnetosphere Interaction 3.3 IMF Effects Seen at Ionospheric Altitudes
	3.4 The Influence of High-Latitude Electric Fields and Ion Densities on the Thermosphere
	3.5 Summary
IV.	REVIEW OF THEORETICAL MODELING OF THE THERMOSPHERE . 79
	4.1 Overview
	4.2 Transport Equations for a Weakly-Ionized Multi-Constituent Collision-Dominated Gas
	4.3 Review of the Contribution from Individual Terms
	4.4 One-Dimensional Numerical Models of the Thermosphere
	4.5 Two-Dimensional Numerical Models of the Thermosphere
	4.6 Three-Dimensional Numerical Models of the Thermosphere
	4.7 Results of and Improvements to the NCAR-TGCM 4.8 Summary
v.	DIURNALLY-REPRODUCIBLE NCAR-TGCM NEUTRAL-GAS FORCE ANALYSIS
	5.1 The Solar-Maximum December-Solstice Diurnally-Reproducible NCAR-TGCM Calculations
	5.2 Diurnally-Reproducible Neutral Winds and Ion Drifts
	5.3 Individual Force Analysis
	5.3.1 The Ion-Drag Force
	5.3.2 The Pressure-Gradient Force
	5.3.3 The Coriolis Force
	5.3.4 The Horizontal-Momentum-Advection Force
	5.3.5 The Viscous-Drag Force
	5.4 Balance of Neutral-Gas Forces
	5.4.1 Diurnal Variations of the Maximum Forces in Each Hemisphere
	5.4.2 Force Balance Over the Invariant Poles 5.5 NCAR-TGCM Neutral Winds and Forces Along a Simulated Satellite
	Track
	5.6 Observations of "Seasonal" and Diurnal Neutral-Wind Variations
	5.6.1 Universal-Time Variations of the Orientation of the Polar-Cap Neutral Winds
	5.6.2 Dominance of the Duskside Neutral-Circulation Cell
	5.6.3 Diurnal Variation of the Maximum Polar-Cap Neutral Winds
	5.6.4 Size Comparison Between Ion-Convection and Neutral-Wind- Circulation System
	5.6.5 Phase Difference Between Ion-Convection and Neutral-Wind- Circulation Systems
	5.7 Summary

۷1.	DYNAMICS EXPLORER-2 DATA ANALISIS	00
	6.1 Overview of the DE-2 Dataset	
	6.2 The DE-2 Spacecraft Instrumentation	
	6.2.1 The DE-FPI Instrument	
	6.2.2 The DE-WATS Instrument	
	6.2.3 The DE-WAYS Instrument	
	6.2.4 The DE-IDM Instrument	
	6.2.5 The DE-NACS Instrument	
	6.2.6 The DE-LANG Instrument	
	6.3 Individual-Orbit Dual-Hemisphere DE-2 Datasets for Different IMF	
	Configurations	
	6.3.1 General Observations	
	6.3.2 The Four-Characteristic Neutral-Wind Signatures	
	6.3.3 DE-2 Ion-Drift Data	
	6.3.4 Neutral-Gas Momentum Forces Derived From DE-2 Data	
	6.3.5 The Ion-Neutral Momentum-Coupling Time Constants	
	6.3.6 Supporting DE-2 Data	
	6.4 Observations of Similarities and Differences in the High-Latitude	
	Neutral-Wind Systems of Opposite Hemispheres	
	6.4.1 Width of the Polar-Cap Antisunward Neutral Flow	
	6.4.2 The Influence of IMF-Controlled Ion Convection on Averaged	
	High-Latitude Neutral Winds	
	6.4.3 Universal-Time Variations in the Averaged High-Latitude	
	Antisunward Neutral Winds	
	6.4.4 "Seasonal" Differences in the High-Latitude Neutral Winds	
	6.5 Summary	
VII.	TIME-DEPENDENT NCAR-TGCM NEUTRAL-WIND SIMULATIONS . 2	02
• • • •		-
	7.1 Time-Dependent Thermospheric Neutral-Wind Simulation	
	Background	
	7.2 Description of the Time-Dependent Simulation Period	
	7.3 The Time-Dependent TGCM Simulations	
	7.3.1 Overview of the Ion-Convection Prescriptions	
	7.3.2 The Analytical High-Latitude Parameterization	
	7.3.3 The Experimental High-Latitude Ion-Convection	
	Parameterization Parameterization	
	7.4 Comparison of TGCM Neutral-Wind Simulations with DE-2	
	Neutral Winds	
	7.5 Summary	
VIII.	PROSPECTS FOR NUMERICAL THERMOSPHERIC FORECASTS . 2	
V 111.	PROSPECTS FOR NUMERICAL THERMOSPHERIC FORECASTS.	:52
	9.1 Describle Methods of Ferresesting the High Letitude Ion Commention	
	8.1 Possible Methods of Forecasting the High-Latitude Ion-Convection	
	Parameters	
	8.2 Attempts to Forecast the IMF	
	8.3 Forecasting Model-Ion-Convection Parameters	
	8.4 Areas Requiring Additional Effort Before An Effective	
	Thermospheric-Forecast Capability Can Be Established	
	·	

IX.	RESULTS AND CONCLUSIONS
	9.1 Summary of Research
	9.2 Synopsis of Major Results
	9.2.1 Major Morphological Results
	9.2.2 Neutral-Gas Momentum-Forcing Mechanisms
	9.2.3 NCAR-TGCM Neutral-Wind-Verification Test
	9.2.4 High-Latitude Ion-Convection Modeling
	9.2.5 Numerical Thermospheric Forecasting
	9.2.6 Future Work
ADDE	NDICES
APPL	NDICES
REFE	RENCES

T1.		
М'1	øυ	٣O
-	مدخة	_

	LIST OF FIGURES
Figu	re
1.1	A vertical profile of temperature for comparison of the thermosphere to other regions of the Earth's atmosphere
2.1	Calculated global-mean profiles of neutral-gas densities for major constituents at thermospheric altitudes during both solar maximum and solar minimum.
2.2	Same as figure 2.1 except showing global-mean profiles of the most important and reactive minor species
2.3	Same as figure 2.1 except showing global-mean ion densities
2.4	Schematic of high-latitude ion-temperature and density features
2.5	Same as figure 2.1 except showing global-mean profiles of electron, ion, and which neutral temperatures
2.6	Diagram of ionization thresholds for thermospheric constituents and altitude at solar flux in different UV intervals is attenuated by a factor of e ⁻¹
2.7	Schematic diagram of the major solar-UV radiation energy flow channels in the thermosphere
2.8	Schematic of the main routes taken by solar-wind energy which is transferred first to the magnetosphere and then to the thermosphere
2.9	Schematic diagram of energy flow in the thermosphere due to high-latitude processes
2.10	Global temperature distribution in the thermosphere due to solar-EUV/UV processes at equinox during moderate solar activity
2.11	Theoretical high-latitude neutral winds at 300 km under the influence of solar-EUV/UV heating only, no high-latitude heating processes considered.
2.12	Plots of averaged neutral wind data, from a ground-based location in Alaska, showing sunward neutral winds on the duskside of the polar cap
2.13	DE-2 satellite measurements of vector ion drifts and neutral winds along the track of the satellite at high latitudes
2.14	Cross-sectional view of the solar interior and atmosphere
2.15	Approximate height in the solar atmosphere from which various solar emissions originate
	ix

2.16	Time variation of selected solar-UV emissions during solar-cycle 21 and the $F_{10.7}$ index	4
2.17	Depiction of regions of diffuse and discrete aurora	4
3.1	Sector structure of the sun	5
3.2	Illustration of the anticorrelation between the IMF \boldsymbol{x} and \boldsymbol{y} components	5
3.3	Schematic of major regions of the Earth's magnetosphere	5
3.4	Illustration of the equatorial plane of the Earth's magnetosphere as viewed by the closed-magnetosphere model	5
3.5	Noon-midnight plane of the Earth's magnetosphere depicting magnetic merging of the IMF with the field lines of the Earth	5
3.6	Illustration of the positive direction for each component in both the GSE and GSM orthogonal-coordinate systems.	6
3.7	Direct comparision of field-line configurations in the noon-midnight plane between the closed magnetosphere for strictly IMF B_z -northward conditions with no magnetic merging and the open magnetosphere for strictly IMF B_z -southward conditions	66
3.8	Illustration of polar-cap equipotential contours which map down along field lines from the magnetosphere under $B_{\rm z} < 0$ and $B_{\rm y} = 0$ conditions	63
3.9	Same as figure 3.8 but for $B_z > 0$ and $B_y = 0$ conditions	61
3.10	The history of a single field line during the magnetic-merging (reconnection) process for $B_z < 0$ conditions	63
3.11	The variation in magnetic-merging-line position in each hemisphere corresponding to changes in the B_y and B_z components of the IMF	63
3.12	Location and shape of the geomagnetic cusp or cleft footprint at thermospheric altitudes.	65
3.13	A magnetotail cross-section of asymmetric addition of magnetic flux to the magnetospheric tail lobes for $B_z < 0$ and $B_y > 0$ conditions	65
3.14	The IMF and geomagnetic-field topology for various B_y orientations under $B_z < 0$ conditions	67
3.15	The dayside ion-convection pattern in the northern hemisphere for various B_y conditions and $B_z < 0$	68
3.16	The weighting of ion convection toward the dawnside in both hemispheres resulting from the day-to-night conductivity gradient	71

3.17	The history of a single magnetic-field line for $B_z > 0$ conditions
3.18	Ionospheric-convection patterns for $B_z > 0$ conditions corresponding to variations in the B_y component
3.19	Illustration of the cross-cap potential measured by a satellite and the corresponding ion-convection pattern
4.1	Theoretical zonally-averaged meridional-circulation patterns 93
4.2	Comparison between meridional circulation calculated during solstice for (a) solar-cycle minimum and (b) solar-cycle maximum
4.3	Horizontal neutral winds for June solstice at 300 km produced by the Straus et al. three-dimensional spectral model
4.4	Schematic of the analytic auroral-oval ion-density enhancement 96
4.5	Diagram showing some of the 13 variables which must by specified in the Heelis et al. ion-convection model and the ways they are measured 102
4.6	NCAR-TGCM global wind pattern due only to solar-EUV/UV heating for solar-maximum conditions at equinox
4.7	High-latitude neutral winds in both hemispheres due only to solar-EUV/UV under heating solar-maximum conditions during December solstice 107
4.8	NCAR-TGCM high-latitude symmetric ion-convection cells and corresponding neutral winds in both hemispheres
5.1	NCAR-TGCM diurnally-reproducible neutral winds in both hemispheres and at selected universal times for solar-maximum December solstice 117
5.2	Same as figure 5.1, except ion drifts are plotted
5.3	The ion-drag force shown for the same conditions as given in figure 5.1 120
5.4	Same as figure 5.3, except the pressure-gradient force is plotted
5.5	Northern and southern-hemisphere neutral-wind and pressure-gradient fields superposed on the neutral-temperature fields
5.6	Same as figure 5.3, except the Coriolis force is plotted
5.7	Same as figure 5.3, except the inertial or horizontal-momentum-advection force is plotted
5.8	Same as figure 5.3, except the viscous-drag force is plotted
5.9	The maximum forces on neutral-gas parcels in the northern hemisphere and southern hemisphere as a function of local solar time of the invariant pole

5.10	The diurnal variation of the individual zonal neutral-gas momentum-forcing components for both hemispheres	138
5.11	Same as figure 5.10, except for the meridional components	139
5.12	Same as figure 5.10, except for the total individual forces	140
5.13	Comparison of TGCM forces in high latitudes of opposite hemispheres at Z=1 pressure level in the 0600/1800 local-time plane at 10 UT	142
5.14	Same as figure 5.13, except at 22 UT	143
5.15	Angular variation in universal time of the antisunward ion drifts and neutral winds from the noon-midnight local-time plane for the diurnally-reproducible NCAR-TGCM run	146
5.16	The diurnal variation of the neutral-wind field divergence $(10^{-5}~{\rm s}^{-1})$, in the nightside portions of the dawn and dusk cells for both hemispheres	149
5.17	NCAR-TGCM neutral-parcel trajectories, for both the northern and southern hemispheres, with the starting point at the invariant-pole location and plotted in invariant-geomagnetic coordinates	151
5.18	The ratio of the divergence of the nightside portions of the dawn-to-dusk neutral-circulation cells, calculated using the data in figure 5.16 and presented as a function of universal time	149
5.19	The values of the maximum antisunward neutral winds in both hemispheres plotted as a function of universal time and local-solar time of the invariant-pole longitude	153
5.20	Illustration of the relative sizes and positions of the neutral-wind and ion-convection patterns for the northern hemisphere at 00 UT	156
5.21	3 F	158
5.22	The phase lag or lead of the ion-convection pattern with respect to the neutral- wind circulation for both hemispheres as a function of universal time and local solar time of the invariant-pole longitude	160
6.1	Schematic of the DE-2 spacecraft showing the placement and orientation of the various instruments	164
6.2	Diagram of the local-time-plane coverage (shaded) of the DE-2 orbits which provided coverage of both hemispheres on the same orbit	169
6.3	Diagram of the orbital path of the ISEE-3 satellite during 1982 and early 1983	170
6.4	Schematic of the high-latitude ion-convection-pattern sampling done by a polar-orbiting satellite.	176

6.5	Data from six DE-2 instruments in both hemispheres, representative of $B_z < 0$, $B_y > 0$ conditions	80
6.6	Same as figure 6.5, except representative of $B_z < 0$, $B_y < 0$ conditions	.81
6.7	Same as figure 6.5, except for $B_z > 0$ conditions	82
6.8	Same as figure 6.5, except for $B_z >> 0$ conditions	.84
6.9	Diagram of neutral winds from DE-2 orbit 7236 in both hemispheres with a single line of invariant-geomagnetic latitude superimposed	.92
6.10	High-resolution averaged DE-2 neutral winds in both hemispheres at the conjugate-sampling universal times and sorted according to IMF conditions	.94
6.11	Universal-time variation of averaged DE-2 high-latitude antisunward neutral-wind direction with respect to the noon-midnight local-time plane and categorized by the sign of the IMF B _y -component	.98
7.1	High-resolution IMF components in GSM coordinates and total field magnitude measured by ISEE-3 for the simulation period of November 24 - 26, 1982 2	204
7.2	Hourly-averaged values of the IMF components for the November 24 - 26, 1982 period	210
7.3	Diagram of the variation of the geomagnetic activity, as shown by the K_p index, for the November 24 - 26, 1982 period with an "X" used to indicate the time of the relevant DE-2 data	211
7.4	Diagram showing measured and calculated cross-cap potentials for the November 24 - 26, 1982 period	12
7.5	The variation of solar-wind velocity and plasma density determined by the ISEE-3 satellite for the November 24 - 26, 1982 period	214
7.6	The hemispheric-power index, H _p , determined from the ion and electron precipitation flux measurments on the NOAA-6 and 7 satellites for the November 24 - 26, 1982 period	215
7.7	The electrostatic-potential distribution for both the northern and southern hemispheres of DE-2 orbit 7221	216
7.8	An example of the location of the ion-convection cells when they are centered on the invariant-pole location and the location when they are centered on the position given by DE-2 measured ion drifts	221
7.9	An example of the equipotential pattern from the Heelis et al. model, superposed on an orbit of measured DE-2 ion drifts	229
7.10	A comparison of the DE-2 measured ion drifts with the model ion drifts using the analytic high-latitude ion-convection parameterization and model ion	

	drifts using the experimental method of high-latitude ion-convection parameterization
7.11	Comparison between the measured DE-2 neutral winds in the 0600/1800 local-time plane and the analytical run of the NCAR-TGCM and the experimental run of the NCAR-TGCM for northern hemisphere orbits 7211, 7212, and 7213
7.12	Same as figure 7.11 but for the northern and southern hemispheres of orbit 7214
7.13	Same as figure 7.11 but for the northern and southern hemispheres of orbit 7217
7.14	Same as figure 7.11 but for the northern and southern hemispheres of orbit 7219
7.15	Same as figure 7.11 but for the northern and southern hemispheres of orbit 7221
7.16	Same as figure 7.11 but for the northern and southern hemispheres of orbit 7223
7.17	Same as figure 7.11 but for the northern and southern hemispheres of orbit 7230
7.18	Same as figure 7.11 but for the northern and southern hemispheres of orbit 7232
7.19	Same as figure 7.11 but for the northern and southern hemispheres of orbit 7236
7.20	Same as figure 7.11 but for the northern and southern hemispheres of orbit 7238
7.21	Same as figure 7.11 but for the northern and southern hemispheres of orbit 7241
7.22	Same as figure 7.11 but for the northern hemisphere of orbit 7244 249
8.1	The power spectrum of the component of the IMF normal to the solar-equatorial plane, observed by Mariner-4
8.2	A three-panel plot of the time response of the average value of the IMF B_z -component to various changes in the IMF B_z -component over a two-hour period
8.3	A three-dimensional plot of the time response of the absolute value of the IMF B_z -component to various changes in the IMF B_z -component over a two-hour period
8.4	Flowchart of the methodology for thermospheric forecasting

|--|

	LIST OF TABLES	
	LIST OF TABLES	
Tab	<u>le</u>	
2.1	Global-mean solar energy absorbed in the thermosphere in units of 10^{11} watts	24
2.2	Comparison of the solar-EUV wavelength intervals or lines necessary to	
	maintain 50% of the thermospheric neutral temperature for different parts of the solar cycle	39
2.3	Compilation of short-term and estimated long-term variation of solar-	
	EUV/UV radiation at different wavelengths, based on available rocket and satellite data	42
3.1	Percentage of the averaged dawn and dusk potential drops in the northern	
3.1	hemisphere, using DE-2 satellite measurements	70
4.1	The relative importance of individual upper thermospheric momentum forces	
	computed at different universal times in the southern hemisphere, for near-summer-solstice conditions	87
4.2	Description of the 13 adjustable parameters in the Heelis et al. ion-convection	
	model	103
5.1	Compilation of diurnally-reproducible NCAR-TGCM velocity and force plots	
	designed for easy comparison between hemispheres and also between figures	15
5.2	Locations of the offset invariant-geomagnetic poles and universal times at	
	which each invariant pole experiences local noon and midnight 1	134
6.1	Mean ion-neutral momentum-transfer time constants in both hemispheres by IMF category	188
		100
6.2	Maximum antisunward zonal component of the neutral winds, categorized by IMF conditions, hemisphere, and universal times when conjugate region	
	sampling is possible	195
7.1	The radii of the ion-convection patterns used in the NCAR-TGCM to test the experimental technique of using DE-2 ion drifts to provide model input	223
		220
7.2	The locations of the center of the ion-convection pattern observed using DE-2 ion-drift data for the November 24-26, 1982 period	224
7.3	The measured and final cross-cap potentials used as input to the TGCM and	
	based on the DE-2 ion-drift measurements	228
	×v	

7.4	The final values of the angles of the zero-potential lines, with respect to the noon-midnight local-time plane, used as input to the experimental run of the TGCM.		
	the room	200	
7.5	A compilation of the magnitude of the average difference vectors resulting from a comparison between the DE-2 measured neutral winds and both runs of the NCAR-TGCM	237	
7.6	Results of the qualitative comparison between DE-2 observed and TGCM-simulated neutral winds.	243	

LIST OF APPENDICES

<u>Appendix</u>

A.	Exothermic ion-neutral, neutral-neutral, and quenching reactions used in the NCAR-TGCM	2′	74
В.	DE-2 satellite orbits with high-latitude neutral-wind coverage in both	9'	70

ABSTRACT

The primary objective of this work was to understand the neutral-gas dynamics in the high-latitude regions of the Earth's upper thermosphere. To achieve this? an understanding of the morphology of the neutral winds and the forces which drive or modify them was required. To this end, a unique 70-orbit December-solstice dataset was established, which included satellite neutral winds and other supporting data from Dynamics Explorer 2 (DE-2), with coverage of both polar caps during the same orbit. Analysis of this data led to the characterization of four basic high-latitude neutral-wind signature categories for each hemisphere under various interplanetary-magnetic-field (IMF) configurations. Furthermore, sunward neutral winds on the duskside of the polar cap, resulting from the mapping of the twin-cell ion convection onto the neutral gas through ion-neutral collisions, were well established in all cases. However, the dawnside sunward neutral winds were not as well established. The existence of a small region of dawnside neutral winds was noted in the winter northern hemisphere, but was usually absent in the summer southern hemisphere. Analysis of the individual neutral-gas forces for solar-maximum December-solstice from the NCAR thermospheric general circulation model (TGCM), led to the realization that the polar-cap pressure-gradient force in the winter northern hemisphere had a different orientation than in the summer southern hemisphere, resulting in the observed dawnside neutral-wind signatures. The variations in the orientation of the polar-cap pressure-gradient forces in opposite hemispheres were ascribed to temperature gradients, resulting from a superposition of solar-EUV, Joule and cusp heating, as well as density variations.

The unique DE-2 dataset was then applied to two different time-dependent tests of the NCAR-TGCM, with the intention of evaluating the eventual use of the TGCM for thermospheric forecasting. The first test was a quantitative evaluation of the accuracy of TGCM-simulated neutral winds, which were compared against DE-2 measured neutral winds. The results of this test were that the NCAR-TGCM provides good first-order simulated neutral winds. However, the TGCM time-dependent neutral winds were, on average, in error by 10 - 40% of the measured neutral-wind velocity. This was primarily attributed to the inability to accurately model the ion-drag neutral-gas momentum source. The second test was intended to assess our ability to use DE-2 measured ion-drift data to provide a more realistic time-dependent prescription of model ion-convection parameters in both hemispheres for the TGCM. Results show that use of ion-drift data, under selected geophysical conditions, can improve the ability of the TGCM to simulate thermospheric neutral winds.

Finally, a possible technique for providing a time-dependent prescription of the high-latitude ion-convection parameters in both hemispheres, for use in a short-range numerical thermospheric forecast of 12 to 24 hours, was noted. This technique involves associating a past series of observed ion-convection parameters corresponding to particular change in the orientation of the IMF, with a similar epoch currently being observed. This technique shows promise, but more data, of the type provided by DE-2, is needed before a full-scale evaluation can take place.

Author: Christopher Raymond Tschan, Captain, USAF

Title: Upper-Thermospheric Observations and Neutral-Gas Dynamics at High Latitudes

During Solar Maximum

Date: 1987

Number of pages: 296

Degree: Ph.D

Institution: University of Michigan

CHAPTER I

INTRODUCTION

1.1 Thesis Objective

This thesis discusses a series of experimental and theoretical studies designed to observe, understand, and simulate the neutral-gas circulation in the high-latitude regions of Earth's upper thermosphere, under solar-maximum December-solstice conditions, in a more comprehensive manner than ever previously attempted. The primary objective is to identify and separate the neutral-wind-circulation features which are seasonally influenced from those which are controlled by the configuration of the interplanetary-magnetic-field (IMF) or universal-time variations in the positions of the ion-convection pattern.

1.2 Overview of the Thermosphere

The thermosphere is that part of Earth's atmosphere dominated by a high-temperature, relatively-tenuous neutral gas, beginning at approximately 90 km and extending to about 500 km (figure 1.1). The region of interest for this work is the upper thermosphere which may be thought of as lying between the altitudes of 300 - 500 km. This is the region of the upper atmosphere through which many satellite orbits pass. Therefore, numerous in-situ satellite measurements of the properties related to both neutral and ionic constituents have been made in the upper thermosphere.

The thermosphere is more complex than one might initially imagine, due in part to the diversity and variability of its energy and momentum sources and sinks. Starting

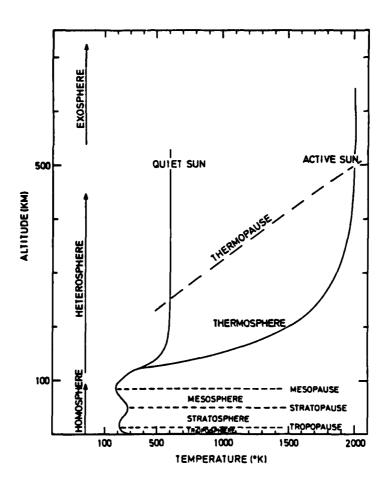


Figure 1.1 - A vertical profile of temperature from the surface to 700 km allowing direct comparison of the thermospheric temperature profile to that of other regions of the earth's atmosphere (Banks and Kockarts, 1973).

with the sources, there are two main categories. They are solar-extreme-ultraviolet (EUV) / ultraviolet (UV) radiation and the solar wind. The solar-EUV/UV radiation is deposited on the sunlit side of the thermosphere while the solar wind deposits its energy at high latitudes through auroral processes (Roble, 1986). Although less than 1% of the sun's radiative energy is in the UV spectrum with wavelengths < 200 nm (Lean, 1987), this radiation is the largest global-energy source for the thermosphere. However, the shorter EUV wavelengths are quite variable on time scales of both solar cycles and monthly rotations (Lean, 1987), further complicating our knowledge of thermospheric heating. The high-latitude energy sources of Joule heating and energetic particle precipitation originate in the solar wind, are also quite variable, and can even exceed the globally-averaged solar-EUV/UV source at times of large geomagnetic disturbances (Roble, 1986). Other thermospheric energy sources are the dissipation of thermal tides and upwardly-propagating gravity waves (Rishbeth and Garriott, 1969; Roble, 1986).

There are a number of thermospheric energy sinks. Energy can be lost from the thermosphere by the following processes: horizontal and vertical heat transport, loss of heat by visible and infrared emissions, and chemical transport (Rishbeth and Garriott, 1969; Roble et al., 1987b). Downward molecular heat conduction to the much cooler mesosphere is the major heat sink for the thermosphere (Chamberlain, 1973). Horizontal thermal advection, due to global-scale neutral-wind systems, functions as a heat-redistribution mechanism. Chemical transport is a significant heat sink for the thermosphere, principally via the loss of the 5.1 eV of dissociation energy stored in the atomic oxygen products of the photodissociation of O₂. Atomic oxygen, produced by photodissociation in the upper atmosphere, cannot recombine locally in a two-body reaction and diffuses down to altitudes of 90 - 100 km where three-body recombination can take place. At the time of recombination, the 5.1 eV of O₂ dissociation energy is released, far below the location where the original dissociation occurred. Radiation out of the thermosphere, in the visible and infrared wavelength intervals, is another energy

sink. These losses include: radiative cooling by the $5.3~\mu m$ non-local thermodynamic equilibrium (NLTE) emission of NO, the $63~\mu m$ emission from the fine structure of atomic oxygen, and the NLTE emission of CO_2 at $15~\mu m$ in the lower thermosphere (Roble et al., 1987b). Cooling due to NO is significant, especially at solar maximum (Roble and Emery, 1983), and is now understood sufficiently well to be incorporated into large-scale numerical models. Eddy transport can function as a heat sink at or below the turbopause and is not considered further in this work. The variability of the energy sources and sinks, mentioned above, leads to complex global-thermospheric wind systems since large episodic perturbations from the mean state are common.

The ionosphere primarily results from the absorption of solar-EUV radiation and energetic particles moving down into the thermosphere from the magnetosphere along magnetic-field lines. At peak levels of ionization, the ion density approaches only 0.1% of the total neutral density. From the point of view of a plasma physicist, the thermosphere/ionosphere is considered a weakly-ionized plasma. However, even this relatively low ion density can have an important influence on the neutral-gas dynamics, particularly at high latitudes where the ionosphere is tightly coupled to the magnetosphere above. The motions of the ionosphere, as a result of this coupling, have a significant effect on the motions of the neutral gas in the high-latitude thermosphere, due to frequent ion-neutral collisions.

1.3 Outline of Thermospheric Data and Models

Much has been learned about the basic properties of the thermosphere and ionosphere through investigations employing satellite, rocket, and ground-based measurements over many years. The current state of this knowledge is summarized in chapter II. The experimental results analyzed in this thesis were obtained by the NASA Dynamics Explorer-2 (DE-2) spacecraft, which was the first to measure nearly-simultaneous vector ion drifts and vector neutral winds, along the track of the satellite.

To expand our knowledge of global-scale thermospheric dynamics, data was collected from a total of six of the DE-2 satellite instruments, which are briefly described in chapter VI. In addition to the DE-2 ion drifts and neutral winds, the following supporting parameters were also collected: neutral composition, ion/electron number density, and temperatures for electrons, ions, and neutrals. As a result, a new and unique database was formed, which included data from all available DE-2 orbits which covered both polar regions. This database made analysis of thermospheric parameters at high latitudes, in both hemispheres, possible for the first time. A summary of observations from this dataset, including calculation of the time-dependent ion-drag force in both hemispheres, is provided in Chapter VI.

Since ion drifts and neutral winds along the track of the satellite were provided by DE-2, ion-neutral momentum and energy coupling could now be placed on a quantitative basis and this has been one of the major motivations for this work. In particular, the dependence of the ion-neutral coupling on the following geophysical phenomena can be studied:

- (a) universal-time variations in the position of the ion-convection pattern.
- (b) seasonal differences over conjugate regions in both hemispheres.
- (c) the response to changes in the IMF.

(d) the time response to geomagnetic substorms.

In addition, there have been no previous experimental studies of the similarities, or lack thereof, in the thermospheric neutral-wind patterns occurring in conjugate regions of opposite hemispheres. This thesis presents an experimental and theoretical study of conjugacy in thermospheric dynamics.

The word "conjugacy", as used here and for the rest of this work, is intended to have the same meaning as defined by Mizera and Evans (1986). Mizera and Evans specified conjugacy to mean linkage between phenomena in opposite hemispheres rather

than the usual sense of phenomena in the northern and southern hemispheres occurring along the same magnetic-field line.

Important tools for theoretical studies of the thermosphere are the global numerical models. One of the most highly-developed three-dimensional time-dependent (3DTD) thermospheric models available today is the National Center for Atmospheric Research thermospheric general circulation model (NCAR-TGCM). The NCAR-TGCM is based on a general circulation model of dynamic meteorology, which solved the primitive equations, using finite-differencing techniques to study tropospheric meteorology. It was subsequently modified for study of the thermosphere by allowing for fast vertical diffusion of heat and momentum as well as incorporating thermospheric physics and chemistry (Dickinson et al., 1981). The model has 24 constant-pressure surfaces in the vertical from approximately 97 to 500 km. The latitude and longitude grid-point spacings are five degrees, in the geographic coordinate system, and the time steps used are typically 150 seconds. The current status of the NCAR-TGCM, including development of the equations used in the model, as well as results from earlier models, are provided in chapter IV.

A limitation on the use of the NCAR-TGCM for previous investigations of thermospheric dynamics has been that model performance has never been directly compared with long-term global-thermospheric neutral-wind data since a database of neutral winds, such as the one presented in chapter VI, has never before been available. A fundamental goal of this work is to conduct a study of the distribution of the ion-drag and other forces influencing the neutral-gas dynamics spatially, temporally, under various geophysical conditions, and in both hemispheres, using both observational and theoretical modeling techniques. Without such a study, the dynamics of the thermosphere can not be fully understood nor can numerical models, such as the NCAR-TGCM, be satisfactorily validated to provide confidence in their realism and performance.

Specifically, the high-latitude forcing functions used as inputs to global-scale numerical models are in a rudimentary state. According to Hays et al. (1984), parameterizations or empirical models of these forcing functions must be improved before significant point-by-point comparisons between thermospheric models and data can be conducted. Any attempt to validate or improve a TGCM must include the following:

- (a) weigh the relative importance of the various momentum-forcing terms.
- (b) improve the prescribed boundary conditions and make them as realistic as possible.
- (c) tighten previous constraints on the model and test it more rigorously against observational data in both hemispheres.

A better understanding of the time-dependent ionospheric-convection electric field and its effect on thermospheric dynamics is one objective of this research (see chapter VII). Since ion drag is the primary momentum source at high latitudes, the morphology of ion convection in both hemispheres must be understood. This is critical because an incorrect specification of the convection-electric field is unlikely to result in a correct numerical simulation of neutral winds. However, this can only be done on a global scale with sufficient ion-drift data. This data is now available from the NASA DE-2 satellite for solar-cycle 21 maximum. Once the time dependency of ion convection is understood, attempts can be made to realistically parameterize the ion-convection pattern. These parameterizations must then be tested through 3DTD numerical simulation of the neutral winds, which can then be compared to measured neutral winds, now also available from DE-2.

Utilizing output of the diurnally-reproducible (i.e., steady-state forcings) NCAR-TGCM, it was found that in addition to ion drag, the pressure-gradient force played a dominant role in modifying the high-latitude neutral winds in the polar-cap of both hemispheres (chapter V). Modeling efforts revealed the differences in the polar-cap

pressure-gradient distribution between the winter northern hemisphere and the summer southern hemisphere. The orientation of the pressure-gradient force was then shown to be responsible for the sunward neutral-wind flow observed on the dawnside of the polar cap. This provides a theoretical explanation for a high-latitude thermospheric phenomena observed for more than a decade, the causes of which had never been fully understood.

The dual-hemisphere database (chapter VI) also contained data for a particularly interesting two-day period during which a variety of unique IMF configurations and geophysical phenomena occurred. Since the November 24 - 26, 1982 period was so interesting, it was selected for the most ambitious time-dependent simulation ever attempted by the NCAR-TGCM. A new parameterization for more realistically describing the ion-convection pattern input to the model was tested. This scheme used the existing Heelis et al. (1982) ion-convection model, but fit it to the DE-2 ion-drift data in such a way as to compensate for some of the shortcomings of the model. The neutral winds on subsequent orbits were then used as a verification tool in much the same sense as weather forecasts in the troposphere are verified, using measured data which occurred at the time the forecast was valid. These results are also described in Chapter VI.

In chapter VIII, an effort was made to see if the results in chapters V through VII could be used to forecast thermospheric high-latitude neutral winds. Several approaches for forecasting the ion-convection parameters based on observed changes in the IMF were evaluated. One technique was good enough to warrant consideration for possible future application.

In summary, the first database of DE-2 thermospheric neutral winds, ion drifts, and supporting data having coverage of both hemispheres on the same orbit, was presented and analyzed. This database has made it possible to place, on a quantitative basis, processes involving ion neutral momentum coupling for a number of different geophysical conditions during solar maximum. In addition, the DE-2 ion-drift data was used to realistically parameterize the ion-convection model for use in the 3DTD NCAR-

TGCM. This led to a study of TGCM performance for the November 24 - 26, 1982 period using the DE-2 measured neutral winds to compare directly with the TGCM-simulated neutral winds. The relative importance of different momentum-forcing terms was also established quantitatively using both the measured data and TGCM-calculated forces. In the auroral regions, ion drag had the largest influence. However, the pressure-gradient force was dominant inside the polar cap and played an important role in steering the high-latitude neutral-wind circulation as well as explaining many observed features in the measured neutral winds. This data analysis and modeling effort resulted in generalizations of the global-scale neutral-wind circulation not previously possible.

1.4 Statement of Thesis Results

A new comprehensive database describing the dynamics of the high-latitude thermosphere in northern and southern hemispheres has been collated using results from six instruments on DE-2 for the solar-maximum December-solstice period of November 1982 through January 1983. The results have been used to investigate the basic morphology, forcing mechanisms and differences between the thermospheric neutral winds of both hemispheres, at altitudes of 300 - 500 km. The NCAR-TGCM has also been exercised for a steady-state (diurnally-reproducible) solar-maximum December-solstice case, in order to theoretically understand the measured thermospheric circulation. In addition, the measured ion-drift and neutral-wind data have been used to find ways to improve the realism of model parameters, as well as to test the time-dependent simulation capabilities of the model, with the intention of building towards an ultimate thermospheric forecast capability. The individual terms in the momentum and thermodynamic equations solved by the model, neutral-parcel trajectories, and momentum-forcing histories have been used in this analysis. The major results have been categorized into the following five subsections and are briefly stated below.

a) Morphological results for both hemispheres

- Four basic neutral-wind signature categories exist, which were based on IMF orientation.
- The antisunward polar-cap neutral flow was wider in the northern hemisphere than in the southern hemisphere, when the satellite orbital plane was oriented along certain geographic longitudes, due to more significant non-dipolar terms in the northern hemisphere magnetic-field topology.
- The divergent dawnside neutral circulation was influenced by differences in the orientation of the pressure-gradient force between the summer southern hemisphere and the winter northern hemisphere.

b) Neutral-gas forcing mechanisms

- Inside the polar cap of both hemispheres, the pressure-gradient force, not the iondrag force, was dominant.
- The horizontal extent of the high-latitude neutral circulation system, measured in the inertial-reference frame, exceeded that of ion convection on the dawnside of the polar cap due to the dusk-to-dawn-directed component of the pressuregradient force.
- Ion-neutral momentum-coupling time constants were at least twice as large in the winter northern hemisphere as in the summer southern hemisphere.

c) NCAR-TGCM time-dependent neutral-wind simulation test

- The first database of neutral winds was used to test the ability of the TGCM to simulate measured satellite neutral winds. Although the TGCM correctly simulated the first-order IMF $B_z < 0$ conditions, the magnitude of the simulated neutral winds were, on average, in error by 10 - 40%.

d) High-latitude ion-convection modeling

- In general, the analytical technique for determining TGCM ion-convection constraints, used in the first time-dependent neutral-wind simulation test,

worked best, especially in the winter hemisphere where the measured ion convection was highly-variable and irregular.

- DE-2 ion-drift data provided the ion-convection specification for the second TGCM test in which the goal was to introduce more realism into model constraints. Techniques which use measured ion-drift data, for input into the TGCM, were best suited for use in the summer hemisphere, but performed well in both hemispheres during the onset of a geomagnetic storm.
- e) Use of the TGCM as a short-range thermospheric-forecasting tool
 - The methodology for a basic thermospheric-forecasting capability was established. This technique was based on the use of time-dependent high-latitude ion-convection prescriptions corresponding to observed changes in the IMF. However, many time-dependent series of ion-convection parameters need to be derived and documented before an accurate test of this technique can take place.

CHAPTER II

REVIEW OF BASIC THERMOSPHERIC PROPERTIES

2.1 Overview

The objective of this work is to understand the driving forces behind the high-latitude neutral winds in both hemispheres. To do this one must know which forces influence the neutral gas and how these forces arise. To this end, the forces which accelerate the neutral gas above a point on the rotating Earth are described. Then, the mean state of the thermosphere is reviewed. The neutral winds resulting from the mean thermospheric state generally follow the day-to-night pressure gradient at low and midlatitudes while displaying the signature of ion convection at high latitudes. While the mean state is easiest to conceptualize, perturbations from the mean state are actually observed. For this reason, the causes of perturbations from the mean state are also covered.

2.2 Neutral-Gas Forces Influencing Thermospheric Circulation

Viewing the basic horizontal momentum equation for a neutral thermospheric gas in a rotating reference frame, equation 2.1, the local time-rate-of-change of the neutral-wind velocity is balanced by five "force" terms, although each of the terms shown have units of acceleration (m/s²). The most important force term at high latitudes is often ion drag, equation 2.2, which is directly-dependent on ion density as shown in equation 2.3. The simplified horizontal hydrodynamical momentum equation for a neutral thermospheric gas is:

$$\partial \mathbf{V}/\partial t = \mathbf{F}_{\text{ion drag}} + \mathbf{F}_{\text{pressure gradient}} + \mathbf{F}_{\text{Coriolis}} + \mathbf{F}_{\text{viscous drag}} + \mathbf{F}_{\text{inertial}}$$
 (2.1)

$$\mathbf{F}_{\text{ion drag}} = \mathbf{v}_{\text{ni}} \left(\mathbf{V}_{i} - \mathbf{V}_{n} \right) \tag{2.2}$$

where
$$v_{ni} = n_i v_{in} / n_n$$
 (2.3)

$$\mathbf{F}_{\text{pressure gradient}} = -\nabla P / \rho$$
 (2.4)

where
$$\nabla P = k \nabla (nT)$$
 (2.5)

$$\mathbf{F}_{\text{Coriolis}} = -2 \left(\Omega \times \mathbf{V} \right) \tag{2.6}$$

$$\mathbf{F}_{\text{viscous drag}} = \mu \left(\frac{\partial^2 \mathbf{V}}{\partial^2 \mathbf{h}} \right) / \rho$$
 (2.7)

$$\mathbf{F}_{\text{inertial}} = - (\mathbf{V} \cdot \nabla) \mathbf{V} \tag{2.8}$$

22.2.0| **1**72.22.24.24| **172**2.23.24| **1**722.22.22.24| 1832.24.24|

where n is the number density of ions or neutrals, depending on the subscript; V refers to the velocity of the ions or neutrals, again depending on the subscript; ν_{ni} and ν_{in} refer to the ion-neutral and neutral-ion collision frequencies respectively, Ω refers to the angular rotation rate of the Earth (i.e., 7.29×10^{-5} rad/s); ρ is the mass density; and μ is the coefficient of viscosity (Chamberlain, 1973). The variables in equation 2.3 are altitude and time dependent, and are quite variable at high latitudes. Therefore, knowledge of the vertical ion-density profile and the behavior of the ionosphere is necessary.

As mentioned in section 2.1, the motion of the F-region ions have important consequences on momentum transfer from the ions to the neutrals, via the ion-drag

force, in regions of high-speed convecting ions. Furthermore, the pressure-gradient force, which results from temperature gradients as well as density variations, influences the neutral winds on both global and local scales. These are the major forces acting on the neutral gas. However, secondary forces also influence the neutral winds.

The Coriolis force is an apparent secondary force, which arises due to our choice of a reference frame associated with grid points on a rotating globe. The Coriolis force acts to deflect parcels to the right in the northern hemisphere and to the left in the southern hemisphere. The viscous-drag force is also a secondary force. Its purpose is to smooth vertical shears in the neutral winds. Since the coefficient of viscosity is essentially altitude independent, but the mass density of the neutral gas is decreasing exponentially with height, the kinematic viscosity (μ/ρ) increases exponentially with altitude. Therefore, the neutral thermosphere moves more and more like a slab as altitude increases. Finally, the inertial or non-linear horizontal velocity (or more commonly momentum) advection term is presented. If the inertial term is combined on the left-hand-side of equation 2.1 with the local time-rate-of-change of velocity term, the result would be the total or substantial derivative. Note that the gravity force term is not presented here because in this simple horizontal depiction of the neutral-gas transport equation, it is assumed that component of the gravity force in the horizontal plane is negligible.

2.3 The Mean State of the Thermosphere

2.3.1 Thermospheric Neutral Composition

In section 2.2, it was mentioned that the ion-drag and the pressure-gradient forces have, in general, the most significant influence on the thermospheric neutral winds. From equations 2.3 and 2.5, it can be seen that changes in the neutral-gas density effect both of these forces. For this reason, it is important to understand the neutral thermospheric composition. Roble et al. (1987) provided the latest calculations on the

global-mean state of the thermosphere using a self-consistent model. These onedimensional (1D) model results are presented here, instead of in chapter IV, because of the insight they provide into basic thermospheric processes.

In the upper thermosphere O and N_2 are the dominant gases. Global-mean vertical profiles of the major constituents of the thermosphere are shown from the recent 1D model calculations in figure 2.1. The most abundant minor gas is O_2 , which represents less than one percent of the total concentration at 300 km during both solar minimum and solar maximum. It can also be seen that the composition of the major upper-thermospheric constituents varies little from solar maximum to solar minimum. However, some of the other minor thermospheric gases, which include NO, $N(^4S)$, and $N(^2D)$, vary considerably with solar cycle (Roble et al., 1987b). The altitude variation of these minor constituents for both solar maximum and solar minimum is displayed in figure 2.2.

The density of thermospheric gases falls off exponentially with height. However, since vertical molecular diffusion dominates over turbulent mixing, above approximately 110 km, each individual constituent seeks its own equilibrium neutral scale height:

$$H_n = k T_n / m_n g \tag{2.9}$$

where k is Boltzmann's constant, g is gravity, m is mass, T is temperature, and the subscript n refers to the individual neutral constituent. As a consequence, the mean molecular mass decreases from about 30 atomic mass units (amu) at the base of the thermosphere to less than 16 amu at 500 km as the lighter neutral constituents become dominant (Banks and Kockarts, 1973).

In the thermosphere, both major and minor constituents are subject to frequent collisions. As a result, the thermospheric velocity-distribution functions of all the

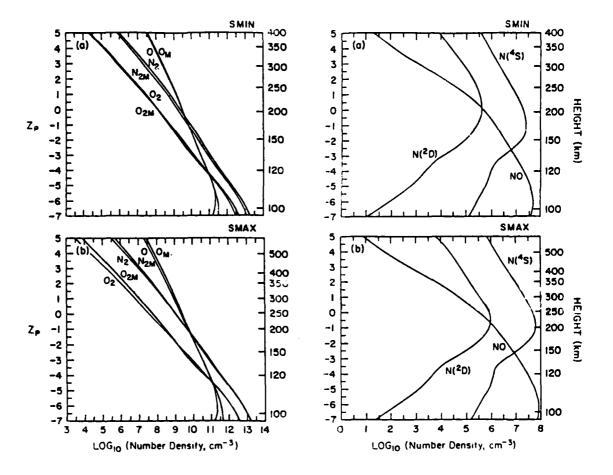


Figure 2.1 - Calculated global-mean profiles of neutral-gas densities for major constituents at thermospheric altitudes during both solar maximum and solar minimum (after Roble et al.. Profiles marked with the 1987b). subscript "m" refer to data from the empirically-based mass spectrometer and incoherent scatter radar (MSIS) model (Hedin, 1983). The scale on the left side of the graphs refers to constantpressure levels used in several National Center for Atmospheric Research (NCAR) thermospheric models. Note that the Z = +4 pressure level corresponds to ~ 350 km at solar minimum and ~ 500 km at solar maximum due to the difference in scale heights.

THE PARTY OF THE PROPERTY OF THE PARTY OF TH

Figure 2.2 - Same as figure 2.1 except showing global-mean profiles of the most important and reactive minor species (after Roble et al., 1987b).

constituents are considered to be Maxwellian and the thermospheric temperatures are assumed to reflect the average kinetic energy of the neutral-gas particles. At the exobase, the mean free path becomes long enough that collisions become infrequent. Consequently, the velocity-distribution function is no longer Maxwellian. Further, the exobase is located in the isothermal region where solar radiation can no longer be sufficiently absorbed to create significant temperature gradients. Temperatures above the exobase can also be expressed by the mean translational kinetic energy (Banks and Kockarts, 1973),

$$KE = m(v_{mean})^2/2 = 3kT/2$$
 (2.10)

where $(v_{mean})^2 = \int v^2 f(r,v) dV / \int f(r,v) dV$, f(r,v) is the velocity-distribution function, and dV is the elemental volume of velocity space.

2.3.2 The Mean State of the Ionosphere and its Relation to the Thermosphere

The ion density and ion-drift velocity are important inputs to the ion-drag force (equations 2.2 and 2.3). For these reasons, it is important to know the mean state of the F-region ionosphere.

The base of the F_2 -region is near 225 km (Banks and Kockarts, 1973), just above the F_1 -region peak. The daytime peak of the F_2 -region is near 300 km where the competing processes of vertical diffusion and chemistry are in balance. The height of the F_2 -peak is known to vary diurnally and with solar cycle. The global-mean vertical profiles of ion densities for solar maximum and solar minimum (Roble et al., 1987b) are contrasted in figure 2.3. According to this figure, the global-mean F_2 -region is dominated by O^+ with a peak ion density of 10^6 cm⁻³ at solar maximum. At solar minimum, the global-mean F_2 -region is still dominated by O^+ , now however, the peak ion density is almost an order of magnitude less.

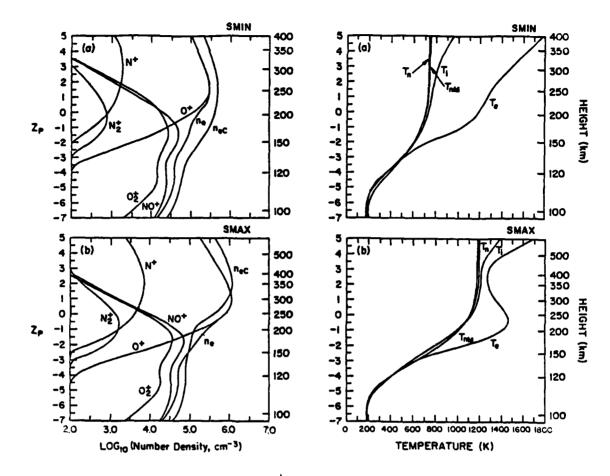


Figure 2.3 - Same as figure 2.1 except showing global-mean ion densities (after Roble et al., 1987b). The profiles with the subscript "c" refer to electron densities provided by the analytical Chiu (1975) model.

TO INCOCCOUNT DESCRIPTION OF STREET STREET STREET STREET, STREET, STREET, STREET, STREET, STREET, STREET, STREET,

Figure 2.5 - Same as figure 2.1 except showing global-mean profiles electron, ion, and neutral temperatures (after Roble et al., 1987b). The double hump in the electron temperature at solar maximum is due to increased coupling between the electrons and ions/neutrals at F2-region peak altitudes caused by higher ion/electron densities. results in more heat being provided to the ion and neutral gas and cooling of the gas. electron In addition, at approximately 200 km, the photoelectron flux is increased by a factor of 3 to 5 during solar maximum, contributing to an increase in temperature at those altitudes.

The F_2 -region also experiences a diurnal ion-density variation. The peak F-region concentration declines by an order of magnitude at night since the loss route for O^+ ions via charge exchange followed by dissociative recombination is still working, but the largest source, photoionization, has been cut off. Unlike the E or F_1 -regions, which essentially are Chapman ion-production layers, the location of the F_2 -peak concentration is governed by chemical production and loss below the peak and ambipolar diffusive transport above.

An important consideration for input to the high-latitude ion-drag force is the spatial variation of ion density. There are several well-known features of the high-latitude ionosphere. From figure 2.4, the auroral zones, both diffuse and discrete, can be seen as regions of enhanced ion density. In these regions the mapping of the ion drifts onto the neutral gas can be expected to be most efficient. However, inside the polar cap, the ion densities are somewhat lower, leading to a smaller ion-drag force. In the winter hemisphere, a polar-cap density depletion, or polar hole, is often found. Here, the ion densities are substantially depleted, since this region is constantly in darkness and does not receive fresh ions through transport processes. In the region of the polar hole, the ion-drag force can be expected to be very small.

The ion-neutral velocity difference is also a very important input into the ion-drag force. The result of the interaction between the solar wind and the magnetosphere is the high-latitude convection-electric field, which forces the ions to convect in the $\mathbf{E} \times \mathbf{B}$ direction. The ion-drift velocities at high latitudes follow either a two-cell or four-cell convection pattern, depending on the interplanetary-magnetic-field (IMF) orientation (figures 3.8 and 3.9). The influence of the solar wind on ionospheric convection is the primary topic of chapter III, and will be covered in more detail there.

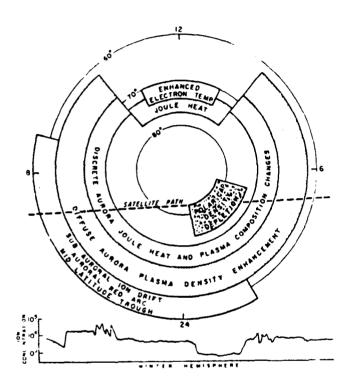


Figure 2.4 - Schematic of high-latitude ion-temperature and density features seen by satellite measurements (Heelis, 1982).

good respond to control control besitting to prove the control to the property of the control of

2.3.3 The Mean Thermal Structure of the Thermosphere

The pressure-gradient force is dependent, to a large part, on the temperature distribution in the thermosphere. For this reason, an understanding of the thermal structure of the thermosphere is necessary, in order to gain insight into the neutral winds of both hemispheres. However, the thermal balance of the thermosphere is slightly more complex than previous sections because there are several heat sources and sinks.

A well-known feature of the thermosphere is the increase in neutral temperature with height. Based on the 1D calculations of Roble et al. (1987), the global-mean temperature increases rapidly with altitude from a value of approximately 200 °K, at the base of the thermosphere, to a value between 700 and 1200 °K, depending on the solar cycle, and then increases very slowly with altitude (figure 2.5). At altitudes where the neutral temperature varies very slowly with height, the neutral temperature is known as the exospheric temperature. The asymptotic approach to the exospheric temperature effectively reduces the vertical temperature gradient in the upper thermosphere to zero. The thermosphere is dynamically stable with respect to vertical convection (Rishbeth and Garriott, 1969), due to the increase of temperature with height, except near regions of intense local heating, such as near aurora. This is in contrast to the troposphere which has large amounts of overturning and turbulence.

The upper thermosphere receives heat from three main sources, solar-EUV radiation, Joule heating due to ion-neutral collisions, and particle precipitation. However, the thermosphere is hot because it is inefficient at reradiating heat (Banks and Kockarts, 1973; Mayr et al., 1978). The main heat sink is the cold mesosphere. Heat is transported down to the mesosphere by molecular heat conduction, where it is radiated away by CO_2 and NO.

2.3.3.1 Thermospheric Heating Due to Absorption of Solar-EUV Radiation

Solar-EUV radiation (λ < 102.7 nm) is the largest global heat source in the upper thermosphere, under most circumstances. In a similar manner, solar-UV radiation (102.7 < λ < 200.0 nm) is the largest heat source for the lower thermosphere. Photoionization and photodissociation are the primary processes by which solar-EUV/UV radiation is absorbed in the thermosphere, since solar energy is stored by the products of these reactions and will later be released to the thermosphere through follow-on exothermic reactions.

Photoionization results in complete absorption of wavelengths shorter than 103 nm (Massey, 1982). In the case of photoionization, the ionization potential is that energy required to strip off an electron. Ionization potentials for thermospheric constituents, as well as the altitudes where the solar-EUV/UV flux is reduced by a factor of e⁻¹, or ~ 37%, are shown in figure 2.6. Photodissociation is the process of splitting a molecule into fragments by a photon with energy above the dissociation threshold of the molecule. Once a photon is absorbed, the molecule enters an excited state and will break apart if the dissociation threshold energy is exceeded. Photodissociation arises primarily from solar-UV radiation in the Schumann-Runge continuum (Massey, 1982). Furthermore, every ionization reaction eventually results in the dissociation of an O₂ molecule (Stolarski, 1976). However, the energy stored in breaking the O₂ bond is released in the lower thermosphere or mesosphere, after the atomic oxygen diffuses downward to regions where total number densities are sufficiently high for three-body recombination processes to occur. This represents a significant amount of stored chemical energy which is lost from the upper thermosphere.

During collisions, kinetic energy is often transferred between species. If the energy transferred is significant, but not enough for ionization, then excitation may occur. A neutral gas atom or molecule must receive sufficient excitation energy to raise it from the ground state to a higher electronic state. Once in an excited state, two follow-

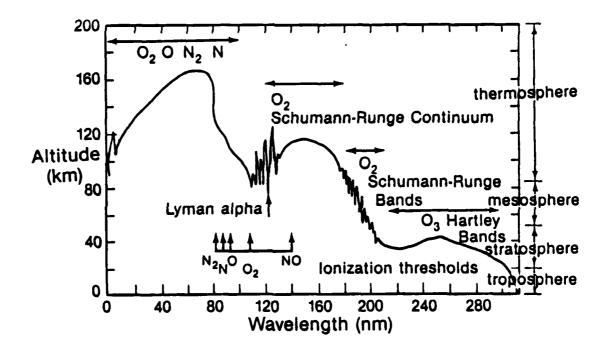


Figure 2.6 - Diagram of ionization thresholds for thermospheric constituents and altitude at which solar flux in different UV intervals is attenuated by a factor of e⁻¹ (adapted from Chamberlain, 1978).

on reactions are possible. First, the excited atom or molecule may radiate at a wavelength corresponding to the energy lost in the transition to a lower energy state. If this radiation is in the visible wavelengths, then it is lost to space. The alternative is for the excited atom or molecule to be quenched by subsequent collisions with other species.

When either of these endothermic processes (photodissociation or photoionization) occur, chemical energy is stored in the products of the reaction. A schematic diagram of the flow of energy from solar-EUV radiation to the thermospheric neutral gas, due to Torr et al. (1980b), is presented in figure 2.7. Almost all solar-EUV photons result in photoionization of O (λ < 91.0 nm), N₂ (λ < 79.6 nm), or O₂ (λ < 102.6 nm) which produce primary, fast photoelectrons and ions with the liberated energy being divided almost equally between them (Stolarski et al., 1975). The primary photoelectrons participate in elastic and inelastic collisions with the neutral gas. This can result in excitation or additional ionization and the production of secondary energetic electrons, all of which eventually lead to heating of the neutral atmosphere. The thermospheric heating from this process is equivalent to about 5% of the total incoming solar-EUV radiation, based on calculations by Stolarski (1976). This value is currently used in thermospheric models (Roble et al., 1987b).

The mean thermospheric-heating processes resulting from absorption of solar-EUV/UV radiation have been summarized by Roble et al. (1987) for both solar-minimum and solar-maximum conditions (table 2.1).

	Solar minimum	Solar maximum
EUV (primarily absorbed in	2.1 the upper thermosphe	6.33 ere)
S-R Continuum (UV) (primarily absorbed in	12.0 the lower thermosph	15.20 ere)

Table 2.1 Global-mean solar energy absorbed in the thermosphere in units of 10¹¹ watts (Roble et al., 1987b).

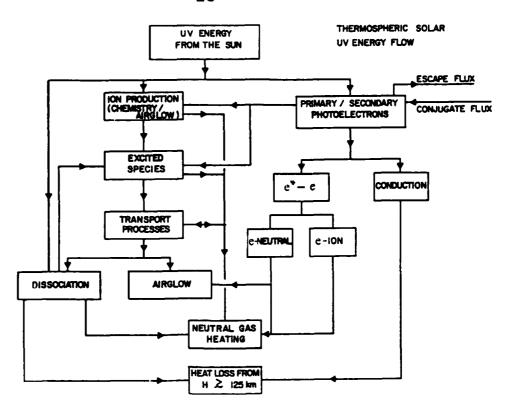


Figure 2.7 - Schematic diagram of the major solar-UV radiation energy flow channels in the thermosphere (Torr et al., 1980b).

PROCESSOR SERVICES BURNINGS CONTROL CONTROL STATEMENT ST

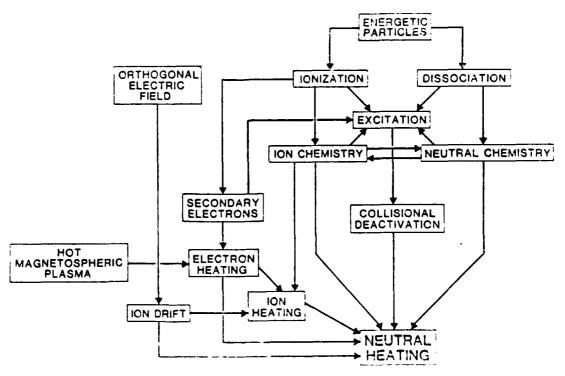


Figure 2.9 - Schematic diagram of energy flow in the thermosphere due to high-latitude processes (Rees et al., 1983).

2.3.3.2 Joule Heating of the Thermosphere

esse homese suscuse suscesse manage suscesses sympas and and participated suscesses suscesses and suscesses a

While the contribution to global heating from absorption of solar-EUV/UV radiation is spread over the entire sunlit thermosphere, the contributions from Joule heating and particle precipitation are more localized. These heat sources are of solar-wind/magnetospheric origin and occur primarily within the polar regions of both hemispheres. The energy deposition rates of both Joule heating and particle precipitation can exceed that of solar-EUV/UV absorption, but because they are localized heat sources, they generally provide a smaller percentage of the global-heat input. However, these heat sources have a significant effect on the neutral-gas dynamics of the high-latitude regions.

The magnetospheric-electric field is the result of the dynamical interaction between the solar wind and magnetosphere. It is mapped down along highly-conducting geomagnetic-field lines into the high-latitude ionosphere. Here the polar-cap electric field forces the ions to convect rapidly, in the $\mathbf{E} \times \mathbf{B}$ direction, through the slower-moving neutrals. This provides a significant high-latitude heat source for the thermosphere which is called frictional or Joule heating. The accompanying collisions heat both the ion and neutral gases at a rate proportional to the ion-neutral collision frequency, which is heavily dependent on the square of the ion-neutral velocity difference (St. Maurice and Schunk, 1981).

$$Q_{Joule} = \left\{ n_n m_n v_{ni} \left[\ 3k \left(T_i - T_n \right) \ \right] / \left(m_i + m_n \right) \right\} + \left\{ n_i \ m_i^2 \, v_{in} \, (V_i - V_n)^2 \, \right] / \left(m_i + m_n \right) \right\} \ (2.11)$$

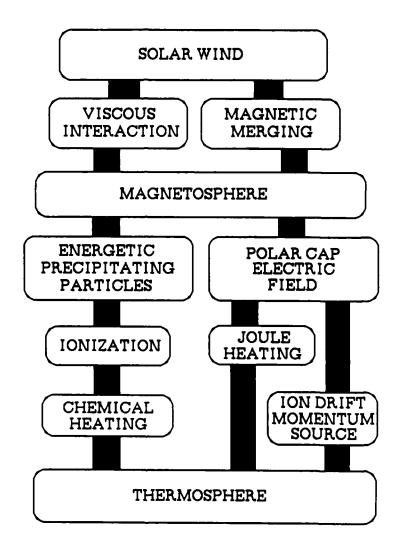
Rees et al. (1983) have stated that Joule heating is also closely coupled to particle precipitation. The source of high-latitude Joule heating is ion convection. For Joule heating to be effective, significant ionization levels are required. A substantial portion of the total ionization in the winter hemisphere is provided by particle precipitation.

2.3.3.3 Thermospheric Heating Due to Particle Precipitation

Particle precipitation also contributes to thermospheric neutral-gas heating. There are several sources of the particles which precipitate along field lines. For example, once IMF and geomagnetic-field lines have merged, the charged particles of the solar wind can be transferred to the terrestrial magnetosphere (figure 2.8). Charged particles of solar-wind origin penetrate along open field lines and are accelerated to high energies in the magnetosphere. These charged particles can move along field lines to thermospheric altitudes where they heat the thermosphere as a result of numerous elastic and inelastic collisions. This occurs directly in two regions, the polar-cap region poleward of the auroral oval and in the cusp region. Inside the polar cap, this particle precipitation often results in very weak aurora and is referred to as polar rain or drizzle, in an obvious analogy to the tropospheric phenomena. Cusp aurora are caused by solarwind particles which enter the magnetosphere at the magnetic-neutral points and move down toward the ionosphere along a funnel-shaped spiral path. These electrons are considered "soft" with energies in the range of 100 eV (Szuszczewicz, 1984). However, they are still sufficiently energetic to ionize the neutral constituents and create secondary-energetic electrons in much the same manner as was discussed above for solar-EUV absorption.

In addition to the direct-entry precipitation phenomena, there are charged particles of both solar-wind and terrestrial origin trapped in the magnetotail. Under steady-state IMF conditions, magnetospheric convection takes place and there is a regular flux of particles moving earthward from the tail, associated with the convecting closed-geomagnetic-field lines. Some of these particles move along field lines to the inner edge of the plasma sheet and are then accelerated into the high-latitude ionosphere, where they precipitate out, causing aurora.

Rees et al. (1983) presented local neutral-gas heating efficiencies due to energetic particle precipitation. The component processes which contribute to heating the neutral



good hassesson besseled herseled houses herseled herseled herseled herseled decesses designed besseled associated

Figure 2.8 - Schematic of the two main routes taken by solar-wind energy which is transferred to magnetosphere and then to the thermosphere (based on Hargreaves, 1979).

gas are similar to those of solar-EUV/UV radiation with the exception that instead of converting radiant energy to thermal or chemical energy through absorption, directed motion is now being converted to random thermal or chemical energy. The auroral-heating component processes considered by Rees et al. (1983) are:

- (a) exothermic ion-neutral reactions;
- (b) exothermic neutral-neutral reactions involving odd nitrogen;
- (c) quenching of metastable states;
- (d) ion-neutral collisions;
- (e) electron-neutral collisions.

A schematic diagram for thermospheric heating due to electron precipitation in the auroral regions (Rees et al., 1983) is presented in figure 2.9. Energetic electrons lose energy through collisions, which can result in ionization and/or excitation of the neutral constituents. The ionizing collisions yield secondary electrons with energies of tens of electron volts (Schunk and Nagy, 1978) which, in turn, lose energy by both elastic and inelastic collisions. Both the solar-EUV/UV absorption and auroral-particle precipitation are processes by which ions and excited species can be created and energy converted to thermospheric heat. Appendix A shows that there are many exothermic ion-neutral and neutral-neutral reactions which result in heat being released to the thermosphere.

Once the energetic electrons have lost sufficient energy so that they are no longer able to ionize or excite neutral constituents, generally less than 5 eV (Schunk and Nagy, 1978), they will heat the ambient electron gas through Coulomb collisions. This elevated-temperature electron gas will slowly heat the ambient neutral and ion gas through inelastic collisions. The slow heating takes place because of the small momentum transfer which takes place when suprathermal electrons try to impart momentum to the more massive ions and neutrals. However, ions with excess kinetic energy quickly thermalize with the neutrals.

2.3.3.4 Other Thermospheric Heat Sources

There are several smaller heat sources not directly related to the major heat sources in the upper thermosphere. They include quenching or deactivation of electronically-excited species and dissipation of waves.

Quenching refers to the heating that occurs through deactivation of excited ionic or neutral species. The most important quenching reaction, shown in appendix A, which adds heat to the thermosphere through collisional de-excitation, involves the metastable $O(^1D)$ state of atomic oxygen. This is because $O(^1D)$ has a very long radiative lifetime of 107 seconds (Froese-Fischer and Saha, 1983). Quenching of $O(^1D)$ takes place primarily with N_2 (Hernandez et al., 1972), because N_2 densities are an order of magnitude higher than O_2 densities at upper-thermospheric altitudes.

Wave dissipation, of thermal tides and upward-propagating gravity waves, is also a source of heat for the thermosphere (Rishbeth and Garriott, 1969). However, the effects of gravity-wave dissipation on the thermospheric heat budget have not been put on a quantitative basis yet (Killeen, 1987). Furthermore, global three-dimensional numerical calculations of heating by tidal motions have only recently been carried out for equinox conditions (Fesen et al., 1986). The calculations for solstice, which would have the most relevance to this work, have not been made yet. The effects of tides on the meridional wind, zonal wind, and neutral temperature at low and midlatitudes have been observed by incoherent scatter radars at Arecibo, St. Santin, and Millstone Hill by a number of investigators (Wand, 1983; Harper 1981, 1979, 1977; Hedin, 1980; Bernard, 1978; Roper and Salah, 1978; Hedin et al., 1977a, b; Salah et al., 1977; and Amayenc, 1974). However, Groves and Forbes (1985) numerically estimated that between 150 and 400 km the global heating due to tides was on the order of 7% of the solar-EUV/UV energy deposition. This is not an insignificant energy source, but it is clearly a secondary heat source.

2.3.3.5 Cooling Mechanisms in the Thermosphere

Now turning to thermospheric heat sinks, Roble and Emery (1983) found that solar-EUV/UV heating was approximately balanced by downward heat conduction during solar-cycle minimum. However, during solar maximum, cooling due to NO was required to bring model temperatures down to levels near those observed. In addition to NO cooling, there are two other thermospheric cooling mechanisms. They were: (1) 63 μm cooling from the fine-structure of atomic oxygen, and (2) ${
m CO_2}$ cooling in the lower thermosphere (Roble et al., 1987b). Another energy loss occurs through downward transport of constituents, such as atomic oxygen with its dissociation energy safely stored and waiting to be released at lower altitudes via three-body recombination. The upper thermosphere energy loss, due to the 630.0 nm optical emission (resulting from the O(1D) \rightarrow O(³P) transition), was considered to be minimal. This radiative loss was on the order of a few percent of the total heating and varied significantly with latitude and local time. The global-mean calculation of Roble et al. (1987) neglected this loss. What was considered important, as a global scale heat sink, was the 63 µm infrared emission of atomic oxygen from $O(^3P_1) \rightarrow O(^3P_2)$ in the optically-thin upper thermosphere. The heat sink from CO2 infrared radiational cooling was only important in the lower thermosphere. However, the importance of including the NO 5.3 µm infrared emission in numerical calculations is just beginning to be appreciated (see chapter IV).

2.3.4 Global-Thermospheric Neutral Winds

The mean vertical temperature profiles, shown earlier in figures 1.1 and 2.5, are not the same in all local-time planes. Obviously, the thermosphere is hotter on the dayside and cooler at night. This local-time-dependence of mean thermospheric temperatures results in a global-temperature distribution much like that shown in figure 2.10. This temperature distribution produces a global day-to-night pressure-gradient

force which drives neutral winds away from the dayside and toward the nightside. Twenty years ago, it was thought that the day-to-night pressure gradient was the main driving force for global-thermospheric neutral winds, even at high latitudes. If the global-scale pressure gradients were the only driving force for thermospheric neutral winds, the resulting theoretically-modeled high-latitude neutral winds would be similar to those shown in figure 2.11. Note that at the time, there were thought to be no high-latitude perturbations in the high-latitude, just uniform day-to-night flow across the polar cap.

However, since the early 1970s, ground-based observations have shown that the high-latitude neutral winds (figure 2.12) were not similar to those resulting from solar-EUV-driven pressure gradients alone. A strong sunward component on the duskside of the polar cap indicated that the high-latitude horizontal ion convection was mapping itself onto the neutral gas through ion-neutral collisions. This ion convection is driven by the high-latitude electric fields which originate from the solar-wind/magnetospheric interaction, which will be discussed in more detail in chapter III.

The NASA-funded Dynamics Explorer-2 (DE-2) satellite, launched into a polar orbit during August 1981, was the first to measure vector neutral winds from space. The neutral winds obtained by DE-2, complemented the wind data being collected by ground-based instrumentation and provided a global view of the neutral winds along the track of the satellite orbit. Using DE-2 ion drifts and neutral winds together, the efficient mapping of the high-latitude ion drifts onto the neutral gas was quickly seen (figure 2.13).

It is now clear that the mean neutral winds, away from the high-latitude processes which are approximately centered on the geomagnetic pole, are mainly driven by the day-to-night pressure-gradient force. However at high latitudes, the ion convection clearly maps itself onto the neutral gas through the ion-drag force, via ion-neutral collisions.

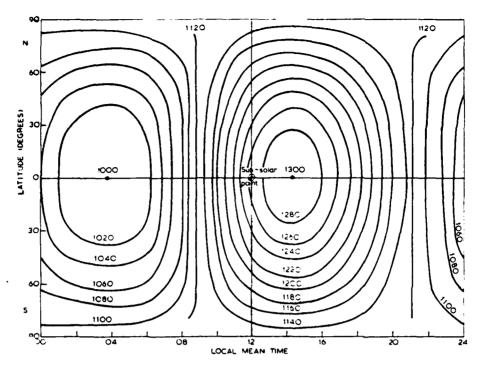


Figure 2.10 - Global temperature distribution in the thermosphere due to solar-UV/EUV processes at equinox during moderate solar activity (Jacchia, 1965).

Social moreovers has 2000 miles on the Social Additional Contractor of C

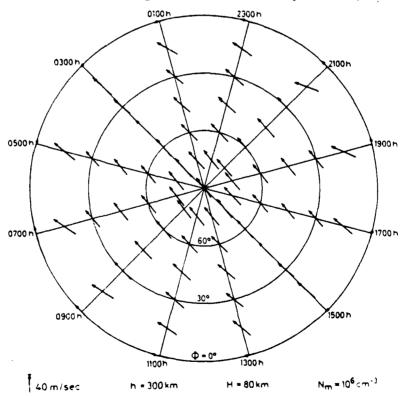
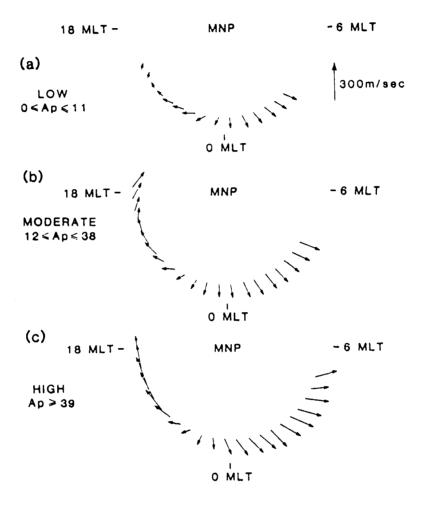


Figure 2.11 - Theoretical high-latitude neutral winds at 300 km under the influence of solar-EUV/UV heating only, no high-latitude heating processes are considered. In response to this type of forcing, the neutral winds show strictly day-to-night flow (Kohl and King, 1967).



THE PERSON CONTROL OF THE PROPERTY OF THE PROPERTY OF THE PROPERTY OF THE PROPERTY OF THE PERSON OF

Figure 2.12 - Plots of averaged neutral-wind data from a ground-based Fabry-Perot interferometer at College, Alaska for various levels of geomagnetic activity (Sica et al., 1986a). The sunward neutral winds on the duskside of the polar cap indicate that ion convection is mapping itself on the neutral-wind field through ion-neutral collisions.

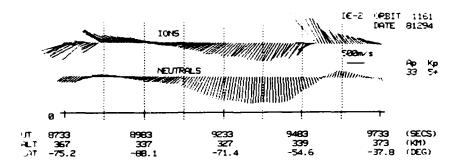


Figure 2.13 - DE-2 satellite measurements of vector ion drifts and neutral winds along the track of the satellite at high latitudes (Killeen et al., 1984b). There is significant velocity agreement between the ions and neutrals indicating the existence of a high degree of coupling.

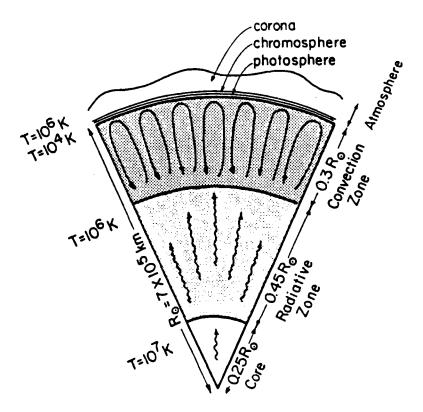


Figure 2.14 - Cross-sectional view of the solar interior and atmosphere (adopted from Noyes, 1982). The solar atmosphere conceptually begins at the base of the photosphere. The transition region is located between the chromosphere and corona but is too thin to be shown at this scale.

2.4 Perturbations From the Mean Thermospheric State

2.4.1 Variations in Solar-EUV Heating

Thermospheric temperatures are known to vary with both the 11-year and 27-day solar cycles. The reason for this is because emissions from the sun, in the wavelengths to which the thermosphere is sensitive, vary with solar activity. These variations effect the global-scale temperature distribution and the levels of ionization in the sunlit summer hemisphere.

The response of the thermospheric neutral temperature to changes in solar activity can be monitored in a number of ways. The solar-activity monitoring methods, which have provided the longest data records, are all ground-based. They include sunspot counts, solar-flare observations, and solar-radio emissions (Hargreaves, 1979). The most popular, but not necessarily the best, indicator of the general level of solar activity, which is supposed to represent the wavelengths which are absorbed in the thermosphere, is the solar-decimetric $(F_{10.7})$ radio flux. The $F_{10.7}$ index is the most popular because it can be observed at the surface of the Earth regardless of the cloud cover.

The $F_{10.7}$ index is a measure of the full solar-disc emission and not localized active regions on the sun (Lean, 1987). Furthermore, the 10.7 cm thermal radio flux originates in the narrow solar transition region, which is less than 500 km thick and located between the chromosphere and corona. The transition region is too small to be shown in figure 2.14, but the $F_{10.7}$ index is most representative of emissions from that region. However, most of the solar-UV radiation, at all but the shortest wavelengths, originates from regions deeper in the solar atmosphere. The far-UV wavelengths between 102.7 and 200.0 nm are called "UV" here. The "UV" wavelength interval includes the Schumann-Runge continuum, which originates in the lower chromosphere and upper photosphere (figure 2.15). These UV wavelengths provide the largest single source of energy to the thermosphere and are primarily absorbed in the lower

thermosphere. The EUV wavelengths, which lie between 10.0 and 102.7 nm and originate in the chromosphere, transition region, and corona, are of interest here since they are absorbed in the upper thermosphere. The $F_{10.7}$ index is therefore only an indirect measure of solar activity which affects the thermosphere. In spite of its drawbacks, the $F_{10.7}$ index continues to be used primarily because the solar-radio emission increases when flares and active region on the sun are observed. Furthermore, alternative potentially-better solar-activity indices, such as solar-calcium-plage data, cannot provide continuous data over long periods because they are optical measurements, which can be interrupted by tropospheric weather.

Use of the $F_{10.7}$ index as a proxy indicator of solar activity is not unjustified. Hedin and Mayr (1987) report that the $F_{10.7}$ index is strongly correlated with satellite drag from Jacchia's (1964, 1977) thermospheric models. Ion and neutral temperatures at thermospheric altitudes are also generally correlated with the $F_{10.7}$ index. However, the $F_{10.7}$ index is not the best indicator for solar output at wavelengths which have been shown to be most important for thermospheric heating. It would be better to have direct measurements of the flux at the important EUV wavelength intervals, noted in table 2.1. The significance of these wavelengths is explained below. However, the only feasible techniques to measure these radiation intervals are using rocket or satellite instrumentation. Since long-term measurements are considered crucial, satellites are a better choice, with rockets used for satellite-instrument calibration.

The Atmosphere Explorer (AE) spacecraft measured the solar-EUV flux from 10.0 - 102.5 nm in 0.1 nm intervals. These measurements were compressed into 37 wavelength intervals by Torr et al. (1979). Using these 37 EUV-wavelength intervals, Emery and Roble (unpublished manuscript, 1983) have shown that for both solar maximum and solar minimum, the thermospheric neutral temperature was most sensitive to the chromospheric He II emission at 30.378 nm. Furthermore, when the 37 EUV-wavelength intervals were ranked by their order of importance in heating the

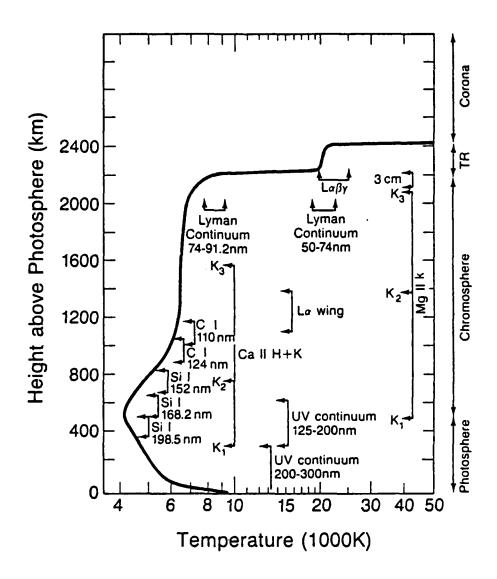


Figure 2.15- Approximate height in the solar atmosphere from which various solar emissions originate (adapted from Vernazza et al., 1976; 1981).

thermosphere, only the first five EUV intervals were required to maintain 50% of the global-thermospheric neutral temperature at solar cycle maximum. For solar minimum, only the first four EUV-wavelength intervals were necessary to maintain the global thermospheric neutral temperature at the 50% level. The EUV wavelength bands and lines referenced above, are listed in table 2.2 in order of their contribution to thermospheric heating. A comparison between the solar flux at different UV wavelengths near solar maximum for solar-cycle 21 and the $F_{10.7}$ index is presented in figure 2.16. The $F_{10.7}$ was seen to most closely represent the 28.4 nm emission, which is reasonable since they both originate in the transition region. It was also seen that the EUV flux in many of the individual wavelength intervals followed a similar but not identical trend as the $F_{10.7}$ index, indicating that a linear relationship between $F_{10.7}$ and UV radiation does not exist.

Order of importance	Solar cycle maximum	Solar cycle minimum
1.	30.378 nm	30.378 nm
2.	25.0 - 30.0 nm	15.0 - 20.0 nm
3.	20.0 - 25.0 nm	85.0 - 90.0 nm
4.	15.0 - 20.0 nm	20.0 - 25.0 nm
5.	30.0 - 35.0 nm	

Table 2.2 Comparison of the solar-EUV wavelength intervals or lines, in order of importance, necessary to maintain 50% of the thermospheric neutral temperature for different parts of the solar cycle. Only a small number of the 37 wavelength intervals, compiled from AE-E satellite measurements, provide the major fraction of heat for the thermosphere (data from Emery and Roble, unpublished manuscript, 1983).

When any of the methods of monitoring solar activity, mentioned above, are employed over long periods of time, they display different time-scales of variability. The 27-day solar cycle is related to the average rotation period of the sun. A much longer time scale of solar variation is the 11-year solar cycle, which occurs because more magnetic flux is injected into the solar atmosphere at solar maximum. According to Lean (1987), the variation in magnetic flux reaching the solar atmosphere is thought to be caused by

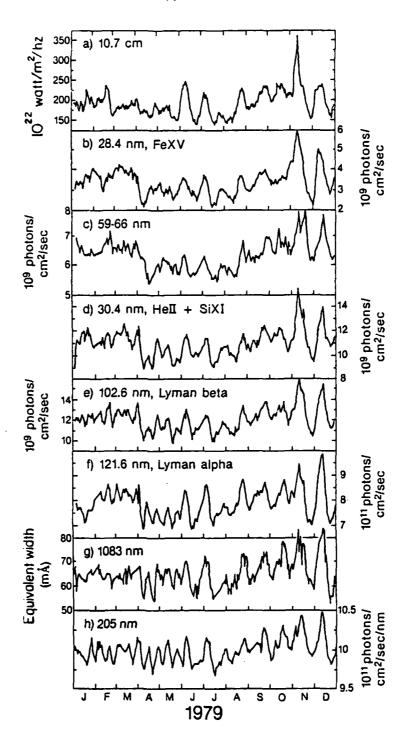


Figure 2.16 - Variation of selected solar-UV emissions and the $F_{10.7}$ index during solar-cycle 21 (Lean, 1987).

the interaction of the toroidal magnetic fields at different solar-magnetic latitudes with the poloidal-magnetic fields associated with the convection zone (figure 2.14). The interaction twists and stretches the poloidal field so that after about three years of horizontal shearing, strong magnetic-flux ropes are brought to the sun's surface by the convection. The flux ropes then form bipolar regions at low and midlatitudes. Mass can be ejected from the sun along the open magnetic-field lines and an increase in the radiative flux is also observed. The long-term cycle is thought to be modulated by a small poloidal component, which arises from the twisting of the toroidal-magnetic field through the action of many rising convection cells. This builds the poloidal field and renews the long-term solar cycle.

One might expect the solar-EUV/UV wavelength intervals, which heat the thermosphere, to vary with solar activity. However, the long-term variation of solar-EUV/UV flux is not well known because good measurements do not exist for sufficiently long periods. However, short-term variations in the solar-UV radiation are well understood and can be related to evolution of plage regions during their lifetime on the solar disc. Solar-UV radiation in the Schumann-Runge (S-R) continuum, which originates from the upper photosphere and the temperature minimum region of the photosphere-chromosphere, is primarily absorbed in the lower thermosphere and has been shown to vary by 1 to 16% over the solar-rotation period. Solar-EUV radiation, which originates in the chromosphere, transition region, and corona is mainly absorbed in the upper thermosphere and has been shown to be much more variable. The short-term variations in solar-EUV flux range from 40 to 200%, over the period of a 27-day solar rotation (Lean, 1987). The heating of the upper thermosphere is more sensitive to solaractivity variations than the lower thermosphere, since the more-variable EUV radiation is primarily absorbed in the upper thermosphere, and the less-variable UV wavelengths are absorbed in the lower thermosphere. The long and short-term variation of solar-EUV/UV radiation for selected wavelengths is shown below:

Wavelength/ region of origin	Long-term variations (~ solar cycle)	Short-term variations (~ month)
300.0 nm (photosphere)	< 1.0%	< 1.0%
250.0 nm (photosphere)	1.5 - 4.0%	2.5%
200.0 nm (photosphere)	2.5 - 9.3%	6.0%
150.0 nm (chromosphere)	16.0 - 100.0%	16.0%
121.6 nm (chromosphere)	80.0 - 155.0%	40.0%
102.6, 30.4 nm (chromosphere)	~ 100.0%	60.0%
28.4 nm (transition region and c	orona)100.0 - 1000.0%	200.0%

Table 2.3 Compilation of short-term and estimated long-term variation of solar-EUV/UV radiation at different wavelengths, based on available rocket and satellite data (adapted from Lean, 1987).

Based on the time-dependent variations known to be present in the solar-EUV flux, one can expect variations in the global-thermospheric temperature distribution. Increases in the day-to-night temperature gradient could result in significant variations in the thermospheric winds. However, higher levels of solar-EUV radiation also result in increased ionization. Furthermore, away from the high-latitude convection electric field, the ion-drag force is generally directed in a sense opposite to the pressure-gradient force. This means that the increase in the pressure-gradient force is, to a large extent, offset by ion drag. Therefore, an increase in solar-EUV/UV flux will result in larger magnitude day-to-night neutral winds, but the increased ion drag does not allow the low and midlatitude neutral winds to increase in the same proportion as the neutral temperatures (Hedin and Mayr, 1987). This is supported by a survey of the individual DE-2 satellite orbits which provided neutral winds in both hemispheres for the solarmaximum December-solstice conditions used in this research. In addition, past research using DE-2 zonal neutral winds has shown that the day-to-night component of the neutral winds, away from the region of high-latitude ion convection, are relatively constant at approximately 150 m/s (Spencer et al., 1982).

2.4.2 Variations in the Coupling Between the IMF and Magnetosphere

THE PRODUCTION OF THE PRODUCTI

Absorption of solar radiation in the UV/EUV spectrum provides the largest contribution to global-thermospheric heating. However, in the high-latitude regions of interest for this work, energy transmitted, either directly or indirectly, from the solar wind is commensurate and sometimes of greater significance. Solar-wind energy, transmitted to the magnetosphere, eventually reaches the thermosphere by two main routes, shown by a simplified schematic in figure 2.8. Both viscous interaction and antiparallel magnetic merging will be covered in more detail in chapter III. The main result of the interaction between the solar wind and magnetosphere is a dawn-to-dusk-directed magnetospheric electric field in the polar regions and energetic-particle precipitation. The variation in the IMF/magnetospheric coupling results in variation of the high-latitude electric field and levels of particle precipitation.

Large variations in the IMF/magnetospheric coupling occur when there is a change in IMF orientation, such as a sudden southward-turning of the IMF. Under these conditions there is increased magnetic merging, accompanied by increased magnetospheric convection. This is an unstable growth phase during which the magnetotail builds in size, but the plasma sheet thins. The auroral oval expands equatorward and rapid particle precipitation occurs. Reconnection at the magnetotail neutral point proceeds quickly, allowing the higher-latitude lines to spring back in towards the Earth (Vallance-Jones, 1974). This also compresses and heats the plasma on high-latitude field lines, resulting in the time-dependent diffuse and discrete aurora (figure 2.17). The energy of the precipitating electrons is sufficient to ionize neutral constituents which, in turn, produces secondary electrons that can start the procedure outlined above over again, or may provide sufficient energy for excitation. Each precipitating electron may have many collisions during its lifetime. It has been established that the energy dissipated in the formation of each ion-electron pair is about

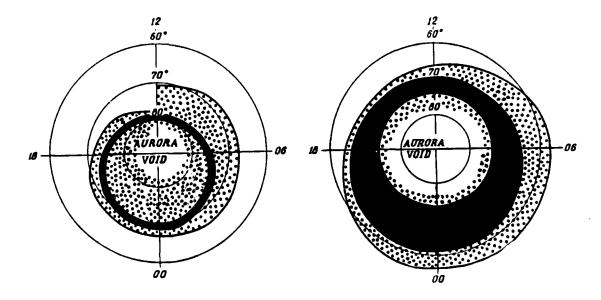


Figure 2.17 - Regions of diffuse and discrete aurora at different levels of geomagnetic activity (after Feldstein and Galperin, 1985). The black region indicates the boundaries of the auroral oval in geomagnetic coordinates. Irregular but discrete aurora are known to occur in this region. Diffuse aurora also occur in the auroral oval, as well as poleward and equatorward of the oval and are indicated by dots.

35 eV (Hargreaves, 1979). As a result, ionization in regions of particle precipitation increases.

There is an additional consequence of a sharp southward turn in the IMF B_z component. It was mentioned above that the coupling between the IMF and the magnetosphere increases and the polar-cap radius expands. However, the cross-cap potential also intensifies and the resulting $E \times B$ ion-drift velocities increase sharply. This means that the ion-neutral velocity differences become greater. Together, the increased ionization and larger ion-neutral velocity differences provide for a much larger ion-drag force (equations 2.2 and 2.3), which permits the ion convection to have an additional influence on the thermospheric neutral winds.

The opposite occurs when the IMF B_z component turns sharply northward. In general, the $E \times B$ ion-drift velocities decrease and the ion densities also fall off. Under these conditions the ion-drag force decreases and it takes longer for the ion-convection pattern to map itself onto the neutral gas.

2.5 Summary

Basic properties of the thermosphere have been reviewed with particular emphasis on the driving forces behind the neutral winds. The ion-drag force was seen to have an important effect on the high-latitude neutral gas. In these regions, the ion convection maps itself on the neutral gas through ion drag, forcing the neutral winds to move in generally the same direction as the ions. At lower latitudes, the solar-EUV/UV-driven day-to-night pressure-gradient force is most important, since it forces the neutral winds away from the dayside and toward the nightside.

The solar-EUV emissions, which heat the upper thermosphere were seen to be highly variable. However, large increases in the solar-EUV flux result in small additions to the global-scale day-to-night neutral winds, because the oppositely-directed pressure-gradient and ion-drag forces both increase. However, particle precipitation

and high-latitude convection-electric fields are even more variable (on the time scale of several hours) and depend on the coupling between the IMF and the magnetosphere. This coupling is strictly a function of the orientation of the IMF.

CHAPTER III

REVIEW OF THE INFLUENCE OF THE SOLAR WIND, MAGNETOSPHERE, AND IONOSPHERE ON THE THERMOSPHERE

3.1 Overview of Solar-Wind/Magnetospheric/Ionospheric Interactions

The ionosphere is the weakly-ionized plasma embedded in the neutral thermosphere. Even at peak daytime ion densities, the neutral concentration exceeds that of the ions by a factor of 1000. In the polar-cap regions of both hemispheres a dawn-todusk-directed electric field has been observed (Heppner, 1972, 1977). This electric field, which results from the solar-wind/magnetospheric interaction, is mapped down into the ionosphere from the magnetopause along magnetic-field lines and forces the ions to convect horizontally in the $\mathbf{E} \times \mathbf{B}$ direction, at F-region altitudes. In a similar manner, the electric field in the equatorial magnetosphere maps along geomagnetic-field lines to the polar-cap boundary regions, resulting in a dusk-to-dawn-directed electric field which forces ions to convect in a sunward direction. Together, this motion often manifests itself as a twin-cell counter-rotating ion-convection pattern with antisunward neutral winds across the polar cap and sunward return flow at lower latitudes. These motions are then transferred by collisions to the neutral gas. To understand and accurately model the cellular motions of the neutral gas in these regions, it is necessary to understand why the high-latitude electric fields exist and how they respond to changes in the solar wind and interplanetary-magnetic-field (IMF).

3.2 Solar-Wind/Magnetosphere Interaction

In chapter II, the solar-EUV/UV radiation was seen to strongly influence thermospheric heating. However, there are other time-dependent solar emissions which also influence the thermosphere and ionosphere. Several of these emissions coincide with solar flares and include X-rays, high-energy protons, and low-energy plasma (Hargreaves, 1979). The X-rays have about an eight-minute transit time from the Sun to the Earth and cause sudden-ionospheric-disturbances (SIDs), which are characterized by increased daytime ionization in the lower ionosphere (D and E region), resulting in increased high-frequency (HF) radio-communication signal loss for periods of 10 to 30 minutes. The high-energy protons are in the energy range of 1 to 100 MeV and have a several-hour transit time from the Sun to the Earth. One consequence of a high-energy proton emission may be a polar-cap-absorption (PCA) event, meaning that enhanced electron and ion densities in the high-latitude D-region will result in the blackout of HF communications and degradation at low frequencies in the polar cap lasting for several days (Fisk et al., 1984). While solar-flare effects are of practical importance, the solar phenomenon that routinely controls upper-thermospheric dynamics is the low-energy plasma emission.

The Sun's low-energy plasma emission, which consists of a quasi-neutral mix of ions and electrons, is emitted along open magnetic-field lines from coronal holes in the Sun's outer atmosphere. This plasma outflow is called the solar wind and on average consists of electrons and ions. About 96% of the solar-wind ions are protons, with the remainder consisting of alpha particles and heavy nuclei (Hargreaves, 1979). A flare-enhanced plasma emission takes one to two days to reach the Earth where it can then effect the thermosphere. Some of these low-energy particles, with characteristic energies on the order of a few hundred keV (Akasofu, 1985), will enter the magnetosphere on open geomagnetic-field lines and precipitate into the thermosphere, while others will populate the magnetosphere and be lost to particle precipitation during geomagnetic storms. Solar

flares also have the ability to change the magnitude and direction of the IMF (Fisk et al., 1984), which has important consequences, since this directly effects the dynamo coupling between the IMF and the magnetosphere. While all flare-associated plasma emissions, which arrive in the vicinity of the Earth, cause changes in the solar-wind ram pressure on the dayside magnetopause resulting in sudden impulses (SI), only those plasma emissions which also are associated with a sharp southward-directed change in the direction of the IMF, in general, cause large geomagnetic storms.

The solar wind becomes supersonic as it expands and cools moving away from the Sun. In the region between the Sun and one astronomical unit (AU), the magnetic Reynolds number, R_m , provides a measure of the ratio of the solar-wind kinetic energy to magnetic energy.

$$R_{\rm m} = L V_{\rm sw} / D_{\rm B} \tag{3.1}$$

$$D_{B} = \eta / \mu_{0} \tag{3.2}$$

$$\eta = m_e v_e / n_e e^2 \tag{3.3}$$

$$\mu_0 = |e|/mv \tag{3.4}$$

where L is the length scale of the plasma, V_{sw} is the velocity of the solar wind, D_B is the magnetic-diffusion coefficient, η is the plasma resistivity, μ_0 is the charged-particle mobility, m is mass, v is the collision frequency, n_e is the electron number density, and e is the electron charge (Sonnerup, 1984). A large magnetic Reynolds number, much greater than one, such as is the case for the solar-wind plasma, means the solar-wind plasma kinetic energy exceeds the magnetic energy of the IMF. Consequently, the IMF is "frozen" and therefore carried along by the solar wind. This is opposite to the

conditions in the Earth's magnetosphere where it is a strong geomagnetic field that controls motions of the plasma.

The solar wind is highly-variable in time and space. However, average values of the solar-wind parameters have been determined from over two decades of satellite measurements. The average flow velocity is 400 km/s, the average concentration is about 5 ions/cm³, the average temperature is 10,000° K, and a magnetic-field strength of 5 nT, which is about 10 times weaker than the geomagnetic field just inside the magnetopause (Hargreaves, 1979). The solar wind flows radially outward from the Sun, which is simultaneously spinning. The combination of the outward motion plus the rotation gives rise to a solar-wind spiral pattern that resembles the spiral pattern made by the water stream leaving a hose held by a spinning youngster, hence the name "gardenhose" pattern. The instantaneous IMF, carried by the solar wind, will have many small-scale fluctuations. On average however, the IMF will take on the familiar spiral pattern (Jokipii, 1972) as seen both in figures 3.1 and 3.2.

In the ecliptic plane of the Sun, different solar "sectors" have been observed. These sectors are generally classified as either "towards" or "away", referring to the average orientation of the IMF in that plane (figure 3.1). The sector structure is ultimately related to the polarity of the coronal-magnetic field (Schatten, 1971). Knowledge of solar-sector structure provides information on the x and y components of the IMF (figure 3.2), which are known to influence the distribution of the polar-cap electric field.

At approximately 13 Earth radii (R_e) from the Earth, above the subsolar point, the supersonic solar wind is forced to slow down. This is because the Earth's magnetic field represents a hard obstacle to the solar wind. A bow shock develops where the supersonic solar-wind parameters become discontinuous and plasma is forced to divert around the "hard" obstacle presented by the Earth's magnetic field (figure 3.3). The high conductivity (or low resistivity) of the plasma forces the solar wind to be "unfrozen" from

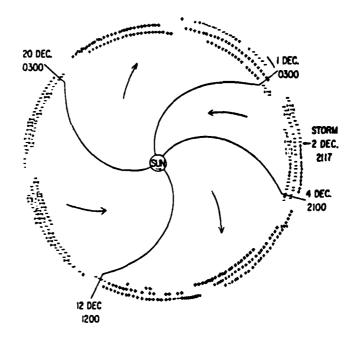


Figure 3.1 - Sector structure of the sun (Wilcox and Ness, 1965). Negative polarity sectors are also called "toward" sectors indicating that the IMF has a component pointing toward the sun. The reverse is true for positive polarity sectors which are called "away" sectors.

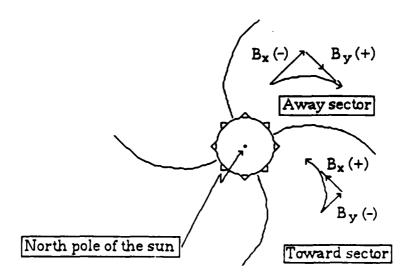


Figure 3.2 - Illustration of the anticorrelation between the interplanetary magnetic field (IMF) x and y components.

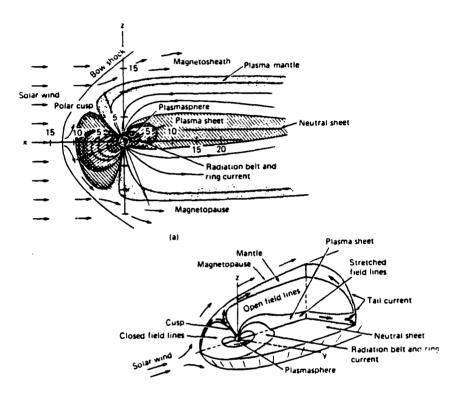


Figure 3.3 - Schematic of major regions of the Earth's magnetosphere (Hargreaves, 1979). The top diagram shows the noon-midnight plane with the Sun off to the left. The bottom diagram provides a three-dimensional perspective.

a magnetic field which has higher magnetic energy than the solar-wind particles have kinetic energy (Hargreaves, 1979).

The region where the solar-wind dynamic pressure balances the magnetic pressure of the Earth is called the magnetopause. This equilibrium may be expressed as:

$$(n_{sw} m_p V_{sw}^2) / 2 = (B^2 / \mu_0) / 2$$
 (3.5)

$$B = 0.311 \times 10^{-4} / (R_0)^3 \tag{3.6}$$

where n is the number density, m_p is the mass of a proton, V is the velocity, the subscript "sw" refers to solar-wind quantities, B is the geomagnetic-field magnitude at the magnetic equator (given by equation 3.6), R_0 is the geocentric distance in units of Earth radii, and μ_0 is the permeability of free space (Lyons and Williams, 1984). The magnetopause occurs at approximately 10 R_e from the subsolar point. This distance increases to about 14 R_e on the flanks. The region between the bow shock and the magnetopause is called the magnetosheath. Magnetosheath plasma is hotter than solar-wind plasma because kinetic energy is being dissipated as heat. The magnetosheath is also turbulent, with the levels of turbulence decreasing as the distance to the magnetopause is reduced.

The interaction of the solar wind with the Earth's magnetic field results in a teardrop-shaped cavity around the Earth called the magnetosphere. Viewing figure 3.4, it can be seen that this teardrop lies in the ecliptic plane of the Sun with the blunt end of the teardrop facing sunward. The magnetosphere protects the Earth from direct interaction with solar-charged-particle radiation. The boundary of the magnetosphere is located perhaps several-hundred Earth radii behind the Earth in the magnetotail. There are two types of interaction of the solar wind with the Earth's magnetosphere that result in an

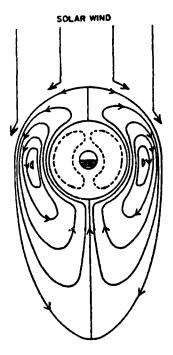


Figure 3.4 - Illustration of the equatorial plane of the Earth's magnetosphere as viewed from above the north pole in the closed-magnetosphere model (Axford and Hines, 1961). No solar wind plasma penetrates the magnetosphere. However, the motion depicted in the magnetosphere is induced by an unspecified viscous interaction. Note the teardrop shape of the magnetosphere in this plane with short magnetotail.

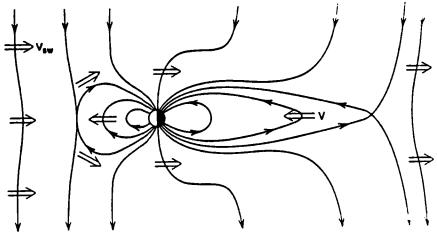


Figure 3.5 - The noon-midnight plane of the Earth's magnetosphere depicting magnetic merging of the IMF with the field lines of the Earth (Dungey, 1961). Once a field line opens to the solar wind, it begins to be swept back over the polar cap toward the magnetotail where it will reconnect and begin to rotate toward the dayside to begin the process again. The teardrop shape is evident in this plane also but is much more elongated than in figure 3.4. Also note the motion of the solar wind around the magnetosphere and the sunward motion in this plane inside the magnetosphere.

electric field being mapped down to the high-latitude regions of thermosphere. These two types of interaction are: (1) viscous interaction and (2) magnetic-field-line merging.

The closed-magnetosphere model was originally suggested by Axford and Hines (1961) as a way in which some of the solar-wind momentum was transferred to the magnetospheric plasma through a viscous-like interaction even though the solar wind does not penetrate the magnetosphere (figure 3.4). Several physical processes have been proposed to explain this transfer of momentum from the solar wind to the magnetosphere across the closed magnetopause (Reiff and Luhmann, 1986). These processes are analogous to the transfer of momentum across a turbulent boundary layer which does not violate the "frozen-in flux" concept. However, most of these processes transfer particles as well as momentum, which does violate the frozen-in flux concept, so this subject is still controversial. The quasi-viscous mechanisms fall under three main categories and simply listed here: the non-linear Kelvin-Helmholtz instability, impulsive penetration, and diffusive entry.

In the closed-magnetosphere theory, one or more quasi-viscous interaction processes occur, which allow the solar wind to impart momentum to the magnetosphere. The momentum imparted by the solar wind, in turn, moves magnetospheric plasma down the sides of the magnetosphere in an antisunward direction in the equatorial plane, with return flow near the center of the tail (figure 3.4). This convection in the equatorial plane maps itself into the high-latitude ionosphere, along magnetic (equipotential) field lines with arbitrarily-high conductivity. The resulting ion-neutral collisions result in antisunward neutral winds over the polar cap and sunward return winds at lower latitudes. The closed-magnetosphere model cannot describe all the observed phenomenology of high-latitude ionospheric and magnetospheric convection and currents, so it is mainly of historical interest. However, there is still a small fraction of the cross-polar-cap potential (~ 6 to 13 kV) which is not attributable to the open-

magnetospheric processes (Reiff and Luhmann, 1986). Therefore, the concept of a closed-magnetosphere cross-cap potential contribution has not completely faded from view.

The theory which is currently favored is the open-magnetosphere model, originally proposed by Dungey (1961). This process involves the "thawing" of IMF lines out of the solar wind in the magnetopause where the magnetic Reynolds number is approximately equal to one. The IMF lines then merge along an X-line with the geomagnetic-field lines (figure 3.5). Magnetic-field-line merging theory is helpful in explaining observed features in the magnetosphere. For example, only 10 - 20% of the Earth's field lines are expected to merge with the IMF (Stern, 1977), so that a correspondingly small fraction of the solar-wind kinetic energy is transferred to the magnetosphere and ionosphere.

The magnetic-field-line merging or magnetic reconnection concept refers to the joining of magnetic-field lines from topologically-different origins. While the process(es) by which magnetic merging takes place are still controversial, there are some theoretical aspects of magnetic merging which are reasonably-well understood. However, the actual merging process is difficult to observe since it occurs in a narrow channel of small physical dimensions and "we do not know (precisely) what plasma signatures to look for" (Sonnerup, 1984). There are two regions where magnetic merging is likely, the dayside magnetopause and the magnetotail.

The main assumption in magnetic-merging theory is that the radius of curvature of the X-line (along which antiparallel magnetic-field lines merge) is very large compared to the microscopic-length scales at which the magnetohydrodynamic (MHD) approximation, given in equation 3.7, breaks down (i.e., a gyroradii). If this assumption is true, then there is an intermediate-length scale, which is macroscopic, but still local. This intermediate-length scale is called the characteristic length, $\lambda_{\rm ch}$.

$$\mathbf{E} + \mathbf{V} \times \mathbf{B} / \mathbf{c} \cong \mathbf{0} \tag{3.7}$$

The separator divides volumes with topologically-different magnetic fields, such as those of geomagnetic origin and those of interplanetary (solar) origin. The separator and the X-line both exist in the magnetopause, which is usually marked by an electric-current sheet (Sonnerup, 1984). More than one characteristic length from the X-line, the MHD approximation holds. This also means that the "frozen-field" theorem holds in the regions more than one characteristic length from the X-line.

The motion of the solar-wind plasma across the separator surface implies a non-zero electric field across the separator line (Vasyliunas, 1984). However, the component of the $\mathbf{V} \times \mathbf{B}$ field along the X-line is assumed to go to zero (Vasyliunas, 1975). Therefore, a breakdown in the MHD approximation occurs in which terms on the right-hand-side of the full-generalized Ohm's law (3.8), which are normally negligible (notably the resistivity term), become locally-dominant (Axford, 1984).

$$\mathbf{E} + \mathbf{V} \times \mathbf{B} / \mathbf{c} = \eta \mathbf{J} + \mathbf{m_e} \left[\frac{\partial \mathbf{J}}{\partial t} + \nabla \cdot (\mathbf{J} \mathbf{V} + \mathbf{V} \mathbf{J}) \right] / ne^2 - (\nabla \cdot \mathbf{P^{(e)}}) / ne + \mathbf{J} \times \mathbf{B} / nec$$
 (3.8)

where: η is the electrical resistivity, e is the elementary charge, m_e is the mass of an electron, n is the number density of ions or electrons, c is the speed of light, and $P^{(e)}$ is the electron pressure tensor.

This means that equation 3.7 can be rewritten in the form of equation 3.9 below:

$$\mathbf{E} + \mathbf{V} \times \mathbf{B} / \mathbf{c} = \eta \mathbf{J} \tag{3.9}$$

Note that \mathbf{E} is non-zero if magnetic merging is occurring (Vasyliunas, 1975). Also, within a characteristic length of the neutral line, $\mathbf{V} \times \mathbf{B}$ is non-zero, but very small compared to c \mathbf{E} . It is here that the resistive term is important. This describes theoretically, the processes which occur when magnetic merging is taking place.

Sonnerup (1984) also notes that magnetic reconnection or merging may occur whenever the magnetic field exhibits a strong shear. Since the magnetosphere is open in regions of magnetic merging, there should be a rotational discontinuity of the $\mathbf B$ field in the merging region. At the rotational discontinuity, there is a small, but non-vanishing component of the $\mathbf B$ field, normal to the separator surface. In the merging region, the non-zero $\mathbf B_n$ results in a change in the tangential plasma momentum, caused by the $\mathbf J \times \mathbf B_n$ force as the plasma crosses the current layer. The net effect, for a southward IMF, should be a plasma acceleration to velocities twice the Alfven speed, just inside the magnetopause (Sonnerup, 1984). The Alfven speed is the characteristic velocity at which Alfven waves propagate along magnetic-field lines.

While the finer details of magnetic merging are still being investigated, there is confidence that magnetic merging is the primary solar-wind/magnetospheric interaction which influences high-latitude ion convection (Slavin and Kamide, 1986). For example, the observed polar-cap electric fields vary in a manner consistent with variations in the north-south component of the IMF, leading to confidence in the open-magnetosphere theory. Observed polar-cap potential drops range from 10 to 240 kV (Reiff and Luhmann, 1986). Hemispheric asymmetries in the distribution of the polar-cap electric fields can also be explained by the magnetic-field-line merging model (Crooker, 1979).

Changes in the polar-cap electric fields have been observed to correlate with varying orientations of the IMF (Heppner, 1972; Burke et al., 1979). For example, the total polar-cap potential drop has been shown to be a function of the north-south (B_z) component of the IMF. Furthermore, the hemispheric asymmetries in the potential drop are related to the east-west (B_y) component of the IMF. The geocentric coordinate system x-axis points toward the Sun and lies in the plane of the Earth's orbit. The y and z components can be in either geocentric-solar-ecliptic (GSE) or geocentric-solar-magnetic (GSM) coordinates. The selected coordinate system for this work is GSM. The reason for this is

that the Earth's magnetic-dipole axis alters the otherwise cylindrical symmetry of the solar-wind flow (Russell, 1971). For displaying magnetosheath and magnetotail magnetic fields and magnetosheath solar-wind velocities this coordinate system reduces the three-dimensional motion of the Earth's dipole in GSE coordinates to motion in the x-z plane. This simplifies calculations of IMF to geomagnetic-field-line orientation used in magnetic-merging theory. For the remainder of this work, By or Bz will implicitly mean By(GSM) and Bz(GSM), unless specified otherwise. The positive direction for the z-component is northward, along the magnetic-dipole axis, for the GSM coordinate system. For the y-component, the positive direction is toward dusk with the y-axis in GSM coordinates resting in the plane of the Earth's magnetic equator and perpendicular to the x-axis (figure 3.6). Both GSE and GSM coordinates are orthogonal-curvilinear coordinate systems.

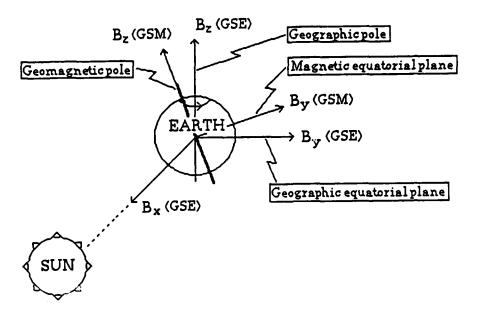
The B_z-component of the IMF has a significant influence on the coupling between the solar wind and the magnetosphere. This relates to the efficiency of antiparallel magnetic merging (Crooker, 1979) between the IMF and geomagnetic field and is a measure of coupling between the IMF and magnetosphere. Higher levels of IMF/magnetospheric coupling occur when the IMF has a southward component $(B_z < 0)$ since the IMF and Earth's magnetic field are then antiparallel. Antiparallel or nearlyantiparallel field lines favor the merging process while parallel field lines $(B_{\rm z}>0)$ decrease the efficiency of magnetic merging. A closed magnetosphere was originally theorized to occur for strictly Bz-northward conditions, such as shown by figure 3.7 (Russell, 1972). More current literature indicates that this is not true (Reiff and Burch, 1985), although during $B_z > 0$ periods, the amount of magnetic merging and therefore the IMF/magnetospheric coupling is greatly reduced. The result, for IMF $B_z < 0$ conditions, is a polar-cap electric field at thermospheric altitudes which forces the ions to convect in a two-cell counter-rotating "egg-beater" pattern, in which ion drifts are parallel to equipotential lines (figure 3.8). This provides a momentum source for the neutral gas 

Figure 3.6 - Illustration of the positive direction for each component in both the geocentric-solar-ecliptic (GSE) and geocentric-solar-magnetic (GSM) orthogonal coordinate systems (based on Russell, 1971).

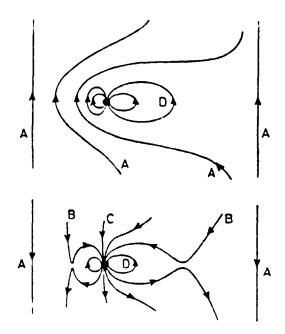


Figure 3.7 - Direct comparision of field-line configurations in the noon-midnight plane between the closed magnetosphere for strictly IMF B_z -northward conditions with no magnetic merging and the open magnetosphere for strictly IMF B_z -southward conditions (Russell, 1972).

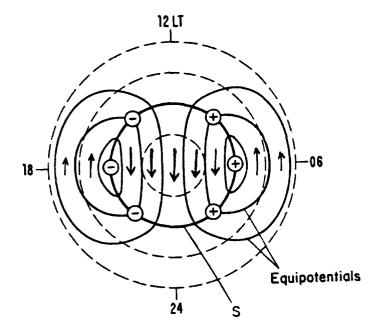


Figure 3.8 - Illustration of polar-cap equipotential contours which map down along field lines from the magnetosphere under $B_z < 0$ and $B_y = 0$ conditions (Lyons and Williams, 1984) The figure is shown in geomagnetic coordinates. The condition of $E_y = 0$ results in a symmetric ion-convection pattern. Also shown are the classical two-cell ion-drift motions which parallel the equipotential lines.

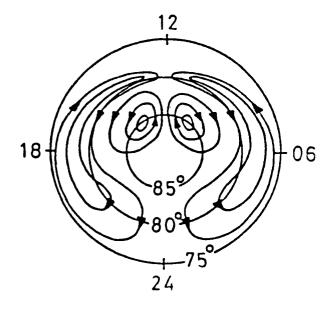
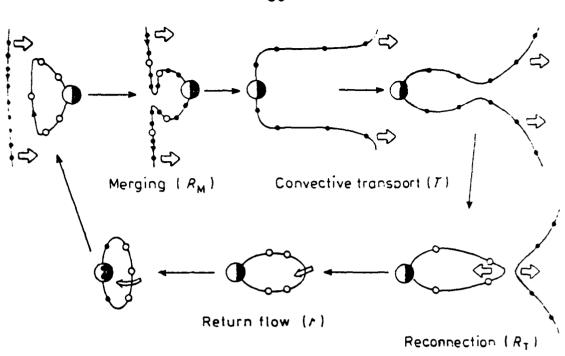


Figure 3.9 - Same as figure 3.8 but for $B_z > 0$ and $B_y = 0$ conditions (Cowley, 1981).

through collisions. When $B_z > 0$ conditions prevail, the two-cell ion-convection pattern changes to a four-cell pattern (figure 3.9) with a smaller polar-cap radius and lower total cross-cap potential. Both figures 3.8 and 3.9 show symmetric ion-convection patterns, which do not show the effects which the IMF B_y -component can have on ion convection.

The following is an illustration of the magnetic-merging process for $B_z < 0$ conditions in terms of the motion of a magnetic-flux tube. As a closed flux tube rotates around the dawnside of the Earth, it moves into a position where magnetic merging can take place. When the configuration of both the IMF and the geomagnetic field are proper for merging, then the flux tube opens in both hemispheres and begins to be swept back toward the magnetotail, at a speed corresponding to the solar-wind velocity. Once in the magnetotail, both ends of the flux tube will reconnect and begin rotating again toward the dayside. Cowley (1981) estimated that the entire cycle (figure 3.10), including opening of the field lines, transport of open-field lines toward the magnetotail, reconnection in the tail, and movement of the field lines back to the dayside so that they might be in a position to open again, would take approximately half a day.

The By-component offers information about which cell in each hemisphere will experience the largest electric-potential drop and hence preferentially influence the neutral winds through ion drag. It was originally thought that magnetic merging took place in a single region, called a neutral point, near the subsolar point (Dungey, 1961). It was later discovered topologically, that two high-latitude neutral lines exist, one in each hemisphere (Crooker, 1979). This is partially due to the draping of the IMF over the magnetopause, creating additional opportunities for the field lines to be antiparallel or nearly so. It is also caused by preferential orientation of the antiparallel merging in each hemisphere due to the IMF By-component (Crooker et al., 1985). When the IMF By-component is positive, the magnetic merging of the IMF and open-geomagnetic-field lines occurs along a neutral line, primarily over the dusk sector in the northern hemisphere and over the dawn sector in the southern hemisphere (figure 3.11). For By-



- Solar wind particle
- o Plasma sheet or Van Allen particle

Figure 3.10 - The history of a single field line during the magnetic-merging (reconnection) process for $B_z < 0$ conditions (Akasofu, 1973)

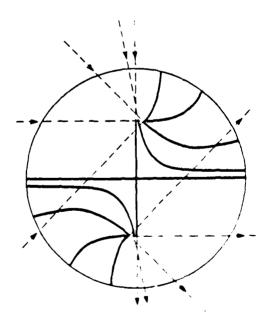


Figure 3.11 - The variation in magnetic merging line solid in each homeory corresponding to various orientations of the IMF dashed lines has been transfer Sun (Crooker, 1979).

negative conditions, the opposite occurs (Reiff and Burch, 1985). It can also be noted that the B_x-component is generally anticorrelated with the B_y-component, due to preferred flow directions in each solar sector (figure 3.2). Then, as the IMF B_y varies, the neutral line will move to a position where the geomagnetic and IMF lines are antiparallel.

Between the regions of open and closed geomagnetic-field lines on the dayside of the Earth, there is a region in each hemisphere where the total magnetic field is zero. Here, in the region called the polar cusp or cleft, charged particles of solar origin are able to enter and move along field lines down to thermospheric altitudes. The cusp itself is often pictured to have a funnel shape while the footprint of the cleft is depicted as a thin oval on the dayside of the Earth located at about 78 degrees north and south geomagnetic longitude. The cleft boundaries can range from the 0800 to the 1500 local time (LT) planes in both hemispheres (figure 3.12). The position of the cusp varies with geomagnetic activity. The position of the cusp, like the polar cap, moves equatorward during periods when the coupling between the magnetosphere and the IMF are increased. One of the effects of the cusp on the thermosphere is relatively low-energy particle precipitation and subsequent neutral atmospheric heating. It has also been shown by Van Allen et al. (1971) that the access of solar-wind particles to both cusps is not the same, but depends on the IMF B_x-component. For B_x-negative, the IMF coming from the Sun connects to the northern hemisphere while the IMF going away from the Sun connects preferentially to the southern hemisphere. Consequently, cusp particle precipitation is greater in the northern hemisphere for $B_x < 0$. Cusp particle precipitation should then be greater in the southern hemisphere for $B_x > 0$. Of course, these observations and cusp particle precipitation can only take place if the magnetosphere is open, lending more credibility to that theory.

For $B_z < 0$ conditions, the magnetic tension on newly-opened flux tubes near the dayside cusp has been shown to be dependent on the sign of the IMF B_y -component. Figure 3.13 illustrates the asymmetric shift of the magnetotail lobes in opposite

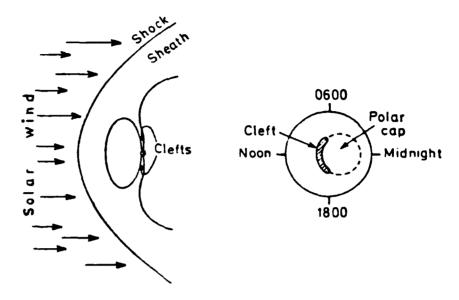


Figure 3.12 - Location and shape of the geomagnetic cusp or cleft footprint at thermospheric altitudes (Vasyliunas, 1974).

recession assessed avalages subsessed executives bearings assessed assessed

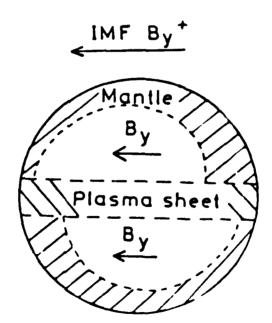


Figure 3.13 - A magnetotail cross-section of asymmetric addition of magnetic flux to the magnetospheric tail lobes for $B_z < 0$ and $B_y > 0$ conditions (Cowley, 1981)

hemispheres due to IMF $B_y > 0$ conditions. The opposite shift in position of the tail lobes is expected for $B_y < 0$ conditions. For a $B_y = 0$ condition, the magnetic tension applied to the geomagnetic-field lines is symmetric in the both hemispheres, resulting in a symmetric tail-lobe placement in both hemispheres. The $B_y = 0$ condition would also produce a symmetric ion-convection pattern like the one in figure 3.8.

3.3 IMF Effects Seen at Ionospheric Altitudes

At ionospheric altitudes, with a B_y -positive component, magnetic tension pulls the newly-opened geomagnetic-field lines toward the dawnside in the northern hemisphere and toward the duskside in the southern hemisphere. The effect of the preferred azimuthal magnetic merging near the cusp region has the effect of enlarging the size of the dusk cell in the northern hemisphere and the dusk cell in the southern hemisphere. This process asymmetrically adds particle flux to the dawnside of the magnetotail in the northern hemisphere and the duskside in the southern hemisphere for $B_y > 0$ conditions (figure 3.14a). Another result of the tension on the geomagnetic-field lines, for $B_y > 0$ conditions, is the shift of the antisunward ion drifts toward the dawnside of the polar cap in the northern hemisphere. Likewise, the maximum antisunward ion drifts are shifted toward the dawnside in the northern hemisphere for $B_y > 0$ conditions, because the highest dawn-dusk electric field is now on that side. The results, mentioned above for $B_y > 0$ conditions in the northern hemisphere, are expected to asymmetrically mirror onto the southern hemisphere. Under $B_y < 0$ conditions, the basic $B_y > 0$ effects are expected to be reversed (or asymmetrically mirrored) in both hemispheres according to Cowley (1981).

Heppner (1972) was the first to see the connection between the high-latitude electric field and the orientation of B_{y} . Theoretical model patterns of ion convection for different IMF B_{y} conditions are shown in figure 3.15. The dayside ion-convection pattern is well established. However, on the nightside and especially during winter, the measured

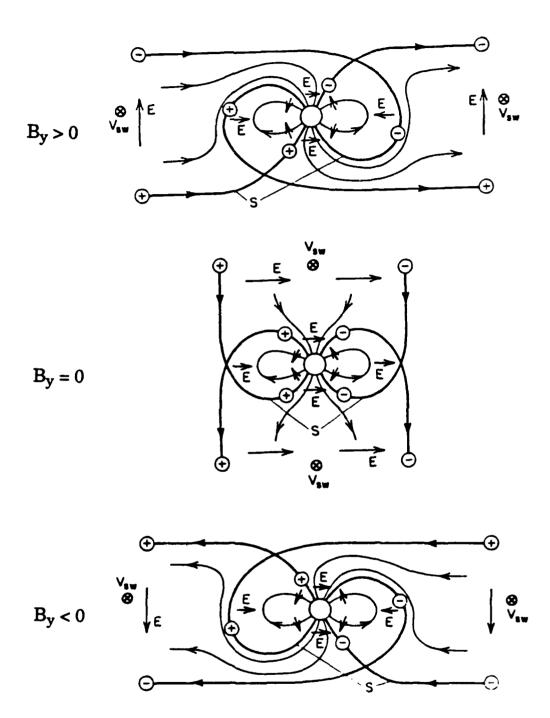


Figure 3.14 - The IMF and geomagnetic-field topology for various B_y orientations under $B_z < 0$ conditions (Stern, 1973). The view is from the Sun looking out toward the Earth with dusk on the left and dawn on the right. The $B_y > 0$ depiction is on top, followed by the $B_y = 0$, and then the $B_y < 0$ patterns.

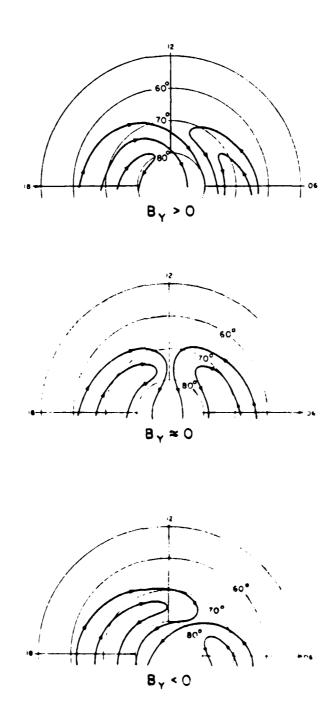


Figure 3.15 - The dayside ion-convection pattern in the northern hemisphere for various B_y conditions and $B_z < 0$ (Heelis, 1984). Once again, the $B_y > 0$ depiction is on top, followed by the $B_y = 0$, and then the $B_y < 0$ patterns.

electric fields have substantial irregularities and closure of equipotentials on the nightside is uncertain.

Heppner also noted that rotational boundaries between the antisunward and sunward ion-drift flow regions were most common in the northern summer hemisphere, while shear reversals were very common in the northern winter hemisphere. The shear reversals occur most frequently on the side of the two-cell ion-convection pattern which had the highest-magnitude antisunward flow. In the northern hemisphere, this would be the dawnside for $B_y > 0$ and the duskside for $B_y < 0$. The reversal region, where antisunward flow becomes sunward, is the boundary between open and closed geomagnetic-field lines.

The effects of the day-to-night conductivity gradient on the ion convection, introduced by Atkinson and Hutchison (1978), have not been incorporated in the wellestablished high-latitude ion-convection models (Volland, 1978; Heelis, 1982). However, after analyzing ion-drift measurements for over 10 years, the subtle effects are now being noticed. The day-to-night conductivity gradient was shown theoretically by Atkinson and Hutchinson (1978) to squeeze the antisunward ion convection toward the dawnside in both hemispheres (figure 3.16). This explains why ratios of the averaged dusk/dawn cell potential drop favor a larger potential drop in the dusk cell of both hemispheres. Heppner and Maynard (1987) used DE-2 electric-field measurements to see how the ratio of the potential drop in the dawn and dusk cells varied with By. The results, shown in table 3.1 for the northern hemisphere, demonstrate that even though the dawn/dusk cell structure was thought to flip over symmetrically in the same hemisphere for opposite signs of the IMF $\mathbf{B_v}$ -component and mirror asymmetrically between hemispheres, that the electric potentials do not. A recent example of a simple ionosphericconvection model which has incorporated the day-to-night conductivity-gradient effects can be found in Moses et al. (1987).

	$B_{y} \leq 0$	$B_{y=0}$	$B_{y \ge 0}$
Percentage of dusk/dawn electric-potential drop	53% / 47%	58% / 42%	63% / 37%

Table 3.1 The percentage of the averaged dusk and dawn potential drops for the northern hemisphere using DE-2 electric-field measurements (Heppner and Maynard, 1987).

The topology of magnetic merging is different for IMF $B_z > 0$ conditions, but magnetic merging still occurs according to Burke et al. (1979). Instead of merging along an X-line on the front side of the magnetopause, such as during $B_z < 0$ conditions, the merging takes place on the poleward boundary of the dayside cleft (Maezawa, 1976). The magnetotail portion of open field line is swept back and away, lost to the magnetosphere (figure 3-17). Burke et al. theorized that geomagnetic-field lines inside the magnetosphere must move sunward toward the magnetopause, in order to replace the field lines which have already merged. By doing so, sunward motion of the closed field lines implies sunward convection over the polar cap. It has become obvious in recent years that many researchers in global magnetospheric and ionospheric modeling (Potemra et al., 1984, Lyons, 1985, Reiff and Burch, 1985, Sojka, et al., 1986) believe that a multicell pattern exists when $B_z > 0$ based on published observations and qualitative models. However, a different view is held by Heppner and Maynard. 1987, who feel that satellite ion drift data represents a rotated and deformed two cell pattern.

It has been established that smaller cross cap potential drops exist during periods when $B_z>0$ and the entire ion convection pattern retreats to higher latitude regions. Smaller ion drift velocities are also observed. The multicell ion drift pattern is much less well-defined then the two cell ion convection, especially on the nightside. The sunaligned theta aurora, which has been a hot topic for study in recent years, is only observed under $B_z>0$ conditions (Akasofu, 1985).

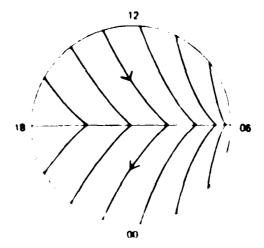


Figure 3.16. The weighting of ion convection toward the dawnside of the polar cap in both hemispheres resulting from the day to night conductivity gradient. Atkinson and Hutchinson 1978.

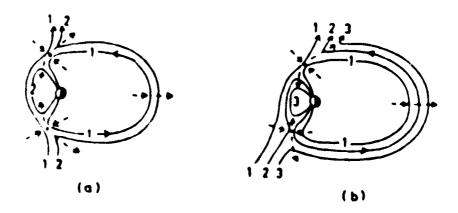


Figure 3.17. The history of a single magnetic field line for $B_\chi \to 0$ condit in Cowley, 1981. The picture on the left corresponds to strictly northward B_χ which shows field lines on the poleward side of the cusp merging with the IMF simultaneously. The illustration on the right shows merging in the northern hemisphere first followed by merging in the southern hemisphere when a $B_\chi \to 0$ component is introduced.

The effects of the other IMF components on ion convection, can also be introduced when B_z is northward. Under the conditions of $B_x > 0$, figure 3.17b shows that merging of an IMF line with a geomagnetic-field line takes place in the northern hemisphere first. This is followed by magnetic merging in the southern hemisphere. In addition, IMF B_y -effects can be introduced, with results slightly more complicated than when B_z was negative. According to Reiff and Burch (1985), when the B_y -component is positive, the larger of the two sunward-convecting cells is on the dawn-side in the northern hemisphere (figure 3.18). As might be expected, this condition approximately mirrors asymmetrically between hemispheres and is opposite for $B_y < 0$ conditions. It should also be noted that the sunward-convecting cells are much smaller than the two-cells considered for B_z -southward IMF conditions. Both sunward-convection cells are entirely contained within the polar cap.

3.4 The Influence of High-Latitude Electric Fields and Ion Densities on the Thermosphere

The main reason for attempting to understand all the different topologies of magnetic merging and IMF orientations is to understand the polar-cap electric-field distribution. The polar-cap potential drop, along the track of the satellite, can be evaluated either from in-situ measurements of the electric field or measured E×B ion drifts. It is desirable to relate the polar-cap potential drop to IMF conditions. The potential drop associated with ϵ typical measured ion-convection pattern is seen in figure 3.19. Following the rules suggested by Reiff et al. (1981), the total cross-cap potential is measured as the difference in voltage between points D and A. Evaluation of the cross-cap potential from winter or nighttime satellite-derived electric-field measurements is often difficult due to numerous irregularities in the field (Heppner, 1977). The electric-field distribution can be derived from the ion-drift velocity measurement by:

$$-\nabla \phi = \mathbf{E} = -\mathbf{V}_{ion} \times \mathbf{B}_{earth} \tag{3.10}$$

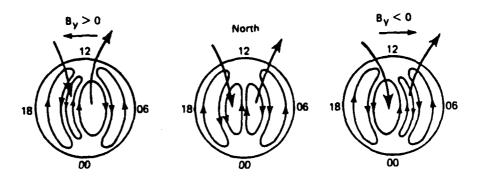


Figure 3.18 - Ionospheric-convection patterns for $B_z > 0$ conditions corresponding to variations in the B_y -component (Potemra et al., 1984).

ALEXACTOR DESCRIPTION OF THE PROPERTY OF THE P

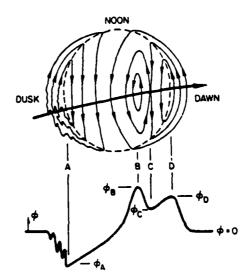


Figure 3.19 - Illustration of the cross-cap potential measured by a satellite and the corresponding ion-convection pattern (Reiff et al., 1981).

If the polar-cap electric field is measured, then the horizontal ion and electron drifts can be found by 3.11 below. This is true for both ions and electrons because, in the upper thermosphere, the collision frequency of ions and electrons is less than the gyrofrequency for each, meaning that each will convect along at the same direction.

$$\mathbf{V} = \mathbf{E} \times \mathbf{B} \tag{3.11}$$

If measurements of both the ion drift and neutral winds are available, then evaluation of ion-neutral difference vectors are possible. The magnitude of the difference vector is found by equation 3.12, where the u component is the zonal velocity, the v component is the meridional velocity, and the subscripts "i" and "n" refer to ions and neutrals respectively.

$$V_{dif} = [(U_i - U_n)^2 + (V_i - V_n)^2]^{1/2}$$
(3.12)

For the neutral gas, the direction of the ion-drag force is opposite to the direction of the neutral flow if the neutral velocity exceeds the ion velocity, meaning that the ions are holding the neutrals back by presenting a source of drag for the neutral gas to overcome. However, if the ion drifts exceed the neutral velocities (with both flowing in the same direction), then the ion-drag force is in the same direction as the neutral and ion drifts. Here, the ions are a momentum source and can be interpreted as dragging the reluctant neutrals along with them.

Once the difference vectors are evaluated, the only unknown quantity needed in the calculation of the ion-drag force is the ion-neutral collision frequency. However, to get the collision frequency in the polar cap, knowledge of the spatial and temporal variation in ion density is required. F-region ion densities has been the subject of many studies, both theoretical and empirical. Several important points are well established as a result. At F-region altitudes, the plasma of the Earth's ionosphere displays different dynamics depending on the latitude range. At midlatitudes, the plasma tends to corotate with the Earth. The plasma is frozen-in to specified magnetic flux tubes and stays with them as they rotate around the Earth. The plasma in each flux tube is enhanced during the day as photoionization of atomic oxygen takes place. At night, the ion and electron densities decay as production is reduced, but losses, such as through recombination, continue. In the midlatitude evening sector, where the fringe of the magnetospheric electric field still exists, competition begins between the sunward-directed E × B drifts and the corotation velocity. This results in stagnation over the local-time range of about 1700 - 0200 (Heelis, 1982). This means that ionization regions, which stagnate in darkness, will slowly become depleted. This region is called the mid-latitude trough and occurs at 50 to 60 degrees of geomagnetic latitude (figure 2.4).

Inside the winter-hemisphere polar cap, in the early-morning sector is a region often referred to as the polar-cap density depletion or polar hole. The polar hole was mapped during solar minimum in the southern winter hemisphere using Atmosphere Explorer-C data by Brinton et al. (1978). The polar hole is the result of long transport time for flux tubes from sources of dayside ionization. During this time, the horizontally-transported ionization decays appreciably. Sojka et al. (1981) theoretically modeled the high-latitude ionosphere at 300 km for solar minimum and found the polar-hole ionization to be maintained by production mainly due to resonantly-scattered radiation and downward diffusion of O+ and NO+ f-om higher altitudes.

Sojka et al. (1979) found a substantial universal-time effect in the ionization due to offset geographic and geomagnetic poles. Sojka et al. (1981) noted a "tongue" of high levels of ionization extending over the polar cap, during periods of strong convection, due

to plasma transport in the antisunward direction over the polar cap. The extent of the tongue of ionization was seen to be highly universal-time-dependent.

During a study of seasonal effects, Sojka et al. (1982) found that, on average, the high-latitude electron densities, or total ion densities if charge neutrality is assumed, were lower in winter than in summer. However, the dayside polar-cap electron density was larger in winter than in summer. This produced a "winter anomaly" such that the F_2 -region peak densities in the winter hemisphere exceed those of the summer hemisphere. This occurred because the ionization produced on the dayside did not have sufficient time to decay before it gets advected across the polar cap under strong ion-convection conditions. Note that the winter anomaly occurred only in O^+ densities, the NO^+ and O_2^+ densities were higher in the summer hemisphere.

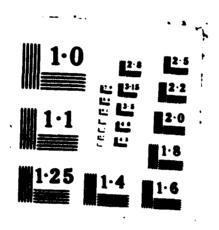
Sojka et al. also found the mid-latitude trough to have lower ion densities and a greater longitudinal extent in the winter hemisphere. In addition, the electron density had a much larger variation with altitude in winter than in summer. The polar hole was also found to appear on the nightside polar cap in both hemispheres, although it exhibited strong universal-time variations. It should also be noted, that the polar hole was less apparent during periods of strong ion convection, unless the polar hole was also associated with large downward electrodynamic drifts. Large downward drifts would send the ionization to lower levels where recombination occurs more rapidly. The downward drifts were more likely to occur in or near the aurora, so the polar hole would appear in a different location, if it was associated with downward drifts instead of horizontal transport.

Another finding, this time from Sojka and Schunk (1985), was that for periods of low magnetic activity during solar-maximum solstice, the ion-convection radius remained so small that it was always behind the terminator. Under these conditions, the mid-latitude trough extended across the dayside. Furthermore, for winter solstice in the southern hemisphere, the universal-time effects in that hemisphere were more

pronounced due to the increased offset between the geomagnetic and geographs p_i as P_i is not surprising that the effects of alread contains were tought be moreous to the summer bemisphere because of dominators by some $P_i(V)$ is rather than the winter bemisphere.

Other features of the concepters, which could affect the neutral thermisphere were long lived, ocalized ion tensity, rregularities, both enhancements and depletions Several researchers have recently studied these teatures, but have let to agree on the most kers cause for the resistance. Refer et al. 1982, used rocket and radar data as exidence that high latitude smaller scale, up to 13 km, on decists progularities were caused mainly by particle precipitation and transported by convection. Weber et a 1984, studied ion enhancement patches in the 1989 km scale size using both DE 2 and ground based optical and ionosonde data. Their conclusion was that plasma patches were convecting in an antisumward direction away from the point of creation near the dayside aurora, was. This was explained as being caused by solar EUV produced plusmus being asymmetrically convected across the pole, due to the rotating Earth with a d spiaced geomagnetic pole. De la Beaujardiere et al 1985, explained the occurrence of plasma, blobs, as a universal time dependent background ion densities which were cause 1 to pregular decay with regions of higher decay surrounding the blob location. Sojka and Schunk (1986a) theoretically modeled 100 km size blobs and explained them as being caused by localized particle precipitation in the aurora and transported around the polar cap, which is not too different from what was stated by Kelley et al. (1982). Of course, vertical motions along field lines and variations in chemistry can not be ignored either. It can be seen that ion densities in the polar cap are highly-structured and the morphology of ionization certainly has an effect on ion drag.

UPPER-THERNOSPHERIC OBSERVATIONS AND NEUTRAL-GAS DYMMHICS AT HIGH LATITUD. (U) AIR FORCE INST OF TECH MRIGHT-PATTERSON AFB OH C R TSCHAN 1987 F/G 4/1 AD-8188 858 2/4 UNCLASSIFIED



TONOMINE TO THE PROPERTY OF TH

3.5 Summary

We have seen that the solar-wind energy is transmitted all the way down to the polar ionosphere. Here, in the form of a convection-electric field, it causes a variety of ion-convection patterns and ion-drift velocities, based on the orientation of the IMF. The fact that the horizontal neutral winds at high-latitudes follow the ion drifts closely (figure 2.13), has only become well established, on a large-scale, using DE-2 satellite measurements over the past five years (Killeen et al., 1984b). The mechanism by which this occurs is ion drag. Through repeated inelastic collisions, the $\mathbf{E} \times \mathbf{B}$ -drifting ions collide with the neutral-gas particles and impart their momentum.

The reverse is also thought to occur. After having a gained a significant amount of momentum, the thermosphere acts as a flywheel, particularly at lower-thermospheric altitudes (Lyons et al., 1985). If the convection-electric field is weak, the high-latitude thermosphere will force the ions to move with the neutral gas, again through inelastic collisions.

CHAPTER IV

REVIEW OF THEORETICAL MODELING OF THE THERMOSPHERE

4.1 Overview

Thermospheric models have proven to be indispensable in developing our theoretical understanding of the neutral upper atmosphere. Global models provide a realistic view of the thermosphere at all desired locations, at any selected time, and for any specified geophysical conditions. However, in order to understand the NCAR thermospheric general-circulation model (TGCM), which is used in subsequent chapters of this thesis, a description of the model and its characteristics is given. Before any theoretical model is exercised, a basic understanding of hydrodynamical and thermodynamical underpinnings, upon which the model is based, is required. Once this is established, a brief review of the historical, as well as recent developments by thermospheric models is presented.

4.2 Transport Equations for a Weakly-Ionized Multi-Constituent Collision-Dominated Gas

The NCAR-TGCM uses a macroscopic set of transport equations, based on the continuum approach to neutral-gas dynamics. However, in this section, the transition from the basic microscopic set of gas-kinetic equations to the set of continuum-transport equations used in the NCAR-TGCM is outlined. The reasons for this are two-fold. First, the terms in the NCAR-TGCM hydrodynamic equations, in spherical coordinates, are much easier to understand, after the processes they represent are conceptualized in simpler form. Second, the use of a hydrodynamic set of equations should be justified for a

region where the neutral-gas density is on the order of 10⁹ cm⁻³, which is considered rarefied compared to the concentrations found at the surface of the Earth.

The proper set of equations to start with can be obtained by multiplying Boltzmann's equation by the zeroth (1), first $(m_s V_s)$, and second $(m_s V_s^2/2)$ moments of the velocity-distribution functions, integrating over velocity space, and simplifying. This results in the gas-kinetic continuity, momentum, and energy equations, shown below:

$$\partial \mathbf{n}_{\mathbf{g}}/\partial \mathbf{t} + \nabla \cdot (\mathbf{n}_{\mathbf{g}} \mathbf{V}_{\mathbf{g}}) = 0$$
 (4.3)

$$\rho_{\mathbf{s}} \mathbf{D}_{\mathbf{s}} \mathbf{V}_{\mathbf{s}} / \mathbf{D} \mathbf{t} + \rho_{\mathbf{s}} 2 \Omega \times \mathbf{V}_{\mathbf{s}} + \rho_{\mathbf{s}} \{ \Omega \times (\Omega \times \mathbf{R}) - \mathbf{G}^* \} + \nabla \mathbf{P}_{\mathbf{s}} = -\rho_{\mathbf{s}} \Sigma_{\mathbf{t}} \mathbf{v}_{\mathbf{s} \mathbf{t}} (\mathbf{V}_{\mathbf{t}} - \mathbf{V}_{\mathbf{s}})$$
(4.4)

$$D_{s}(3P_{s}/2)/Dt = -\rho_{s} \Sigma_{t} v_{st} \left[3k(T_{t} - T_{s}) + m_{t}(V_{s} - V_{t})^{2} \right]/(m_{s} + m_{t})$$
(4.5)

Looking first at the continuity equation (4.3), the zero on the right-hand-side represents conservation of mass. The dependent variable n is the number density and V is the velocity of species s. Moving now to the momentum equation (4.4), the convective or substantial derivative of velocity is the first term on the left-hand-side. The second term on the left-hand-side of equation 4.4 represents the Coriolis force. This is an apparent force which arises when a rotating coordinate system is used. The Coriolis force simply deflects the parcel to the right of its current velocity vector in the northern hemisphere and to the left in the southern hemisphere. The third term on the left-hand-side of equation 4.4 contains both the centrifugal $\{\Omega \times (\Omega \times \mathbf{R})\}$ and gravitational forces (G*). These two forces will be combined to form the apparent-gravity force (G) in equation 4.7. The centrifugal force is also due to the rotating Earth. The fourth term on the left-hand-side is the pressure-gradient force. The only term on the right-hand-side is the ion-drag force, which is proportional both to the collision frequency between species t and s, as well as the

velocity difference between those species. The species density, ρ_s , is the product of the species density and mass $(n_s m_s)$. The subscript "s" indicates the species of neutral-gas particle being evaluated, while the subscript "t" indicates the species with which the species "s" particle is colliding. Finally, moving to the energy equation (4.5), the term on the left-hand-side is the total derivative of pressure. The term on the right-hand-side of the energy equation is proportional to both the species temperature and velocity difference.

Once the transition is made from the above microscopic gas-kinetic equations to the continuum approach, then hydrodynamic computations on a global scale become possible. The continuum approach is valid whenever the Knudsen number, $\mathbf{K_n}$, is much less than one. The Knudsen number is defined as the ratio of the mean free path to the characteristic length of the gas (Vincenti and Kruger, 1982). For atmospheric applications, the quantity used to represent the characteristic length is the scale height, which is given by equation 2.1. When the Knudsen number approaches one (i.e., the scale lengths are on the same order as the mean free path), then the definitions of macroscopic parameters, such as pressure and temperature, break down (Bird, 1976). When the Knudsen number greatly exceeds one, the gas is considered collisionless. The altitude where the mean free path equals the neutral-gas scale height is defined as the exobase (Chamberlain, 1973). To check that use of the hydrodynamic equations was justified, the quantities which comprise the Knudsen number were computed. Using representative upper-thermospheric solar-maximum neutral-gas values (i.e., $T_n = 1500^{\circ}$ K, $n = 10^9$ cm⁻³), and the mean molecular mass is 16 amu), the neutral scale height was calculated to be on the order of 80 km, while the mean free path was on the order of a few kilometers. Therefore, it is clear that for the upper thermosphere, the Knudsen number is much less than one.

To make the transition from the gas-kinetic equations to the hydrodynamic equations, the summation over all neutral and ionic species is taken. The resulting is

equations (4.6 through 4.8) are shown below, where the subscripts "i" and "n" refer to ions and neutrals, respectively.

$$\partial \rho / \partial t + \nabla \cdot (\rho \mathbf{V}_{\mathbf{p}}) = 0$$
 (4.6)

$$\rho(\partial \mathbf{V}_{n}/\partial t + \mathbf{V}_{n} \cdot \nabla \mathbf{V}_{n}) + \rho 2 \Omega \times \mathbf{V}_{n} - \rho \mathbf{G} + \nabla \mathbf{P}^{*} = -\rho v_{in}(\mathbf{V}_{i} - \mathbf{V}_{n})$$
(4.7)

$$3/2(\partial P^*/\partial t + V_n \cdot \nabla P^*) = -\rho v_{in} \left[3k(T_i - T_n) + m_i(V_i - V_n)^2 \right] / (m_i + m_n)$$
 (4.8)

where $P^* = \Sigma_s P_s$ in the above equations.

The hydrodynamic equations, suited for use in the three-dimensional, time-dependent (3DTD) NCAR-TGCM were described by Dickinson et al. (1981). They are shown in spherical coordinates with a log-pressure vertical coordinate below, where equations 4.9 through 4.13, are the continuity, eastward-momentum, northward-momentum, energy, and hydrostatic equations, respectively.

$$1/(r\cos\phi) \,\partial(v\cos\phi)/\partial\phi + 1/(r\cos\phi) \,\partial u/\partial\lambda + e^z \,\partial(e^{-z}w)/\partial z = 0 \tag{4.9}$$

$$\frac{\partial \mathbf{v}}{\partial t} = g e^{\mathbf{z}} / P_0 \frac{\partial (\mathbf{u}}{\partial t} \frac{\partial \mathbf{v}}{\partial z} - f \mathbf{u} + (\lambda_{yy} (\mathbf{v_I} - \mathbf{v}) + \lambda_{yx} (\mathbf{u_{I^-}} \mathbf{u})) + (-\mathbf{V} \cdot \nabla \mathbf{v} - \mathbf{u}^2 / r \tan \phi) - 1 / r \frac{\partial \phi'}{\partial \lambda} - \mathbf{w} \frac{\partial \mathbf{v}}{\partial z}$$
(4.11)

$$\partial \mathbf{T}'/\partial \mathbf{t} = \mathbf{g} e^{\mathbf{z}}/P_0 c_p \partial (\mathbf{K}_T/\mathbf{H} \partial \mathbf{T}'/\partial \mathbf{z})/\partial \mathbf{z} - \mathbf{a} \mathbf{T}' - \mathbf{V} \cdot \nabla \mathbf{T}' - \mathbf{W} \cdot \nabla \mathbf{T}'$$

$$\partial \phi' / \partial z = R(T_0 + T')/m$$
 (4.13)

The terms in the momentum equations, 4.10 and 4.11, have units of force per unit mass and are, listed from left to right: the total acceleration at a fixed geographic latitude and longitude grid point, the force due to vertical viscosity, the Coriolis force, the ion-drag force, the non-linear momentum-advection force, the pressure-gradient force, and the vertical-advection force. The terms in the thermodynamic-energy equation, 4.12, are: the total heating rate at a fixed grid point, downward heat conduction, radiative cooling, heat advection, adiabatic heating and cooling due to expansion or contraction of thermospheric gases, solar-EUV/UV heating, Joule heating, and heating due to auroral particle precipitation.

The independent variables are time, t; latitude, ϕ ; longitude, λ ; and constant pressure level, $z = \ln{(p_0/p)}$, where p is pressure, $p_0 = 5 \times 10^{-4}$ µbars, and 1 bar = 1 Pascal. The dependent variables are eastward velocity, u; northward velocity, v; vertical motion, w = dz/dt; temperature, T; and geopotential, ϕ . The geopotential at height z is defined as the work required to raise a unit mass from mean sea level, $\phi = \int_{z'=0,z} g \, dz'$ (Holton, 1979). Primes indicate departures from the global-mean values which are denoted by the subscript zero.

Other parameters in the final set of equations, (4.9 through 4.13) are:

the radiative-damping coefficient, a;

the specific heat per unit mass, C_p ;

B is the magnitude of the Earth's geomagnetic field;

the Coriolis parameter, $f = 2\Omega \sin \phi$;

the Earth's angular velocity, Ω ;

the acceleration due to gravity, g;

the mean scale height, $H(\lambda, \phi, z) = R T_0 / g$;

the thermal-conductivity coefficient, $K_T(\lambda, \phi, z)$;

I is the dip angle between the geomagnetic field and the local horizontal;

k is the Boltzmann constant;

the ion-drag tensor components are,

$$\lambda_{xx} = \sigma_p B^2 (1 - \sin^2 \delta \cos^2 I) / \rho$$

$$\lambda_{xy} = \lambda_{yx} = \sigma_P \; B^2 \; (\sin\delta \; \cos\delta \; \cos^2 \! I) + \sigma_H \; B^2 \; \sin \! I/\rho, \label{eq:lambda_xy}$$

and
$$\lambda_{yy} = \sigma_P B^2 (1 - \cos^2 \delta \cos^2 I) / \rho;$$

ρ is the neutral-gas density;

Pederson conductivity, $\sigma_P = e / B \Sigma_i \{ N_i \Sigma_n (v_{in} / \omega_i)^2 / (1 + \Sigma_n (v_{in} / \omega_i)^2) \};$

Hall conductivity, $\sigma_{\rm H} = e/B \Sigma_{\rm i} \{ N_{\rm i} \Sigma_{\rm n} (v_{\rm in}/\omega_{\rm i})/(1 + \Sigma_{\rm n} (v_{\rm in}/\omega_{\rm i})^2) \};$

 $m(\lambda, \phi, z)$ is the mean molecular mass;

 $\mu(\lambda, \phi, z)$ is the coefficient of viscosity;

r is the radial distance from the center of the Earth;

R is the gas constant for air;

 $u_I(\lambda, \phi, z)$ is the zonal ion-drift velocity;

 $v_I(\lambda, \phi, z)$ is the meridional ion-drift velocity;

the static stability, $S = (\partial T_0/\partial z) + (RT_0/mC_p)$;

 $T_0(z)$ is the global-mean temperature;

 $Q_0(z)$ is the global-mean net-heating rate per unit mass;

the rate of Joule heating per unit mass, $Q_J = [\lambda_{xx}(u_I - u)^2 + \lambda_{vv}(v_I - v)^2];$

Qs is the rate of solar heating per unit mass;

Qp is the rate of auroral-particle-precipitation heating per unit mass;

and the horizontal-advective operator, $\mathbf{V} \cdot \nabla = (\mathbf{u}/\mathbf{r} \cos \phi)(\partial/\partial \lambda) + (\mathbf{v}/\mathbf{r})(\partial/\partial \phi)$.

From equations 4.9 through 4.13 it can be seen that there are five equations in five unknowns; u, v, w, T', and ϕ '. Three of the variables are prognostic: T', u, and v. In addition, the thermodynamic-energy, eastward-momentum, and northward-momentum equations are second order in z. Therefore, two boundary conditions are required for each of these equations, one at the bottom boundary and one at the top. This accounts for six boundary conditions. Furthermore, the continuity and hydrostatic equations are first

order in z, each requiring one boundary condition. To summarize this, eight boundary conditions are required to solve the five equations in five unknowns. The four upperboundary conditions, from Dickinson et al. (1981), are: $\partial T'/\partial z = \partial u/\partial z = \partial v/\partial z = \partial w/\partial z = 0$. According to Dickinson et al. (1984), the prognostic variables are in near diffusive equilibrium in the vertical as the top of the model is approached. The bottom-boundary conditions can be prescribed if known. However, at the bottom boundary, the variables o', T", u, and v are usually set to zero, except in cases where vertically-propagating semidiurnal tidal waves are being simulated (Fesen et al., 1986). For use later in this work, only TGCM calculations from the $Z = ^{+1}$ level (~ 300 km at solar maximum) will be shown. This level is about equally-spaced from the boundaries and therefore any effects due to unrealistic boundary conditions are unlikely to significantly effect the results at that altitude. An additional point, regarding the stability of vertical integration of the TGCM hydrodynamical equations, was brought up by E. C. Ridley (personal communication, 1987). Once u and v are determined, the continuity equation can be integrated vertically. However, this integration must be done moving down in altitude for stable results. The hydrostatic equation may be integrated from the bottom up.

4.3 Review of the Contribution from Individual Terms

The influence of individual momentum-forcing terms above on the neutral circulation of the low and mid-latitude thermosphere was considered in an early review by Rishbeth (1972). The ion drag force was thought by Rishbeth to be the major factor limiting the neutral thermospheric wind speeds because the ion motion was strongly impeded by the Earth's magnetic field. At that time, little was known about the influence of high-latitude ion convection on the neutral thermosphere. However, the analytical work of Rishbeth and colleagues is still valid and can now be evaluated using two present-day tools: satellite neutral-wind measurements and 3DTD TGCMs. Since it is

the momentum equation which is of primary interest in this work, a look at the contribution of individual forcing terms is presented in order of their importance.

Recent work on individual momentum-forcing terms by Killeen and Roble (1984), using DE-2 data, has shown that in the high-latitude upper thermosphere, the ion-drag force is generally dominant. Then, in descending order of important, for steady-state conditions, are: the pressure-gradient force, Coriolis force, non-linear momentum-advection force, and viscous-drag force. Momentum advection is significant only in regions where significant velocity gradients exist. In the upper thermosphere, these velocity gradients normally occur along the boundary of the magnetospherically-driven ion-convection pattern. The contribution of the momentum-advection force tends to be localized near these regions. The contribution due to the viscous force is usually smaller than either the Coriolis or momentum-advection terms. However, the theoretical simulations of the thermospheric-momentum force balance, published to date, where individual-forcing terms have been examined, have all been made using steady-state diurnally-reproducible TGCM runs (Killeen and Roble, 1984, 1985, 1986).

To provide a better feel for the relative importance of the individual momentumforcing terms, a steady-state neutral-wind simulation by Killeen and Roble (1984) using
the NCAR-TGCM was carefully analyzed. The region studied by Killeen and Roble was
the upper thermosphere of the southern hemisphere during October 1981. This was
considered a near-summer-solstice solar-maximum case. Data corresponding to two
universal times (0300 and 1500) were presented. The first universal time, 0300 UT,
corresponded to a period when the southern-hemisphere ion-convection pattern had
rotated to a point near local noon, due to the displaced invariant-magnetic pole. At the
other universal time, 1500 UT, the invariant south pole was crossing the midnight local
time plane, hence the ion-convection pattern was its maximum displacement away from
the dayside. As a result, ion drag was reduced by a factor of two, due to the lower ion
densities at night. To provide a feeling for the relative importance of the maximum force

value in the southern hemisphere at both universal times, the maximum value of each upper-thermospheric force is shown in table 4.1.

<u>Force</u>	Simplified term	<u>03 UT</u>	<u>15 UT</u>
Ion drag	$v_{ni} (V_i - V_n)$	0.619	0.373
Pressure gradient	-∇Ρ/ρ	0.135	0.133
Momentum advection	$-(\mathbf{V}\cdot\nabla)\mathbf{V}$	0.119	0.075
Coriolis	$-2(\Omega \times \mathbf{V})$	0.053	0.057
Viscous drag	$\mu(\partial^2 \mathbf{V}/\partial^2 \mathbf{h})/\rho$	0.046	0.025

Table 4.1 - The relation between the maximum values of individual upper-thermospheric momentum forces (in units of m/s²) at different universal times in the southern hemisphere, for near-summer-solstice conditions (Killeen and Roble, 1984).

Examining table 4.1, it is apparent that ion-drag has the highest maximum individual momentum-forcing magnitude of any of the forces, at both universal times. However, ion drag is modulated diurnally by its rotation into dayside regions of high ion density, followed by rotation into nightside regions of lower ion density. By comparison, the maximum pressure gradient displays little diurnal variation. At 0300 UT, when the invariant pole is near the noon-local-time plane, the ion-drag force has a magnitude approximately five times higher than the pressure-gradient force. However, at 1500 UT, the ion-drag force has fallen to only about three times the magnitude of the pressure-gradient force. The obvious conclusion is that the pressure gradient is expected to play a more important part in modifying the neutral-wind flow at 1500 UT.

THE PROPERTY OF THE PROPERTY AND THE PROPERTY OF THE PROPERTY

At high latitudes, the ions often drift at velocities more than twice as great as the neutral gas, due to the influence of the magnetospherically-driven ion convection. In these regions, the ion gas provides a momentum source for the neutral gas. However, outside the polar cap, the neutral winds often have higher velocities than the ions. Here the ions attempt to reduce the velocity of the neutral gas, hence the name ion "drag".

Away from the high-latitude regions, the neutral winds generally have higher velocities at night because of reduced ion drag (Roble, 1986).

It can be seen in equations 4.10 and 4.11, that ion drag in the high-latitude upper thermosphere is dependent on both the ion-drag tensor and the velocity difference between ions and neutrals. These two parameters vary independently. It has already been shown that even under steady-state conditions, ion drag exhibits a diurnal variation. Ion drag also varies seasonally. Under realistic time-dependent simulation conditions, the spatial and temporal variations of ion drag and the ion-neutral velocity differences are expected to be very complicated. This has been the subject of several recent studies which compared neutral winds observed by DE-2 to those computed by TGCMs. One of the main conclusions of Hays et al. (1984) was that the current first-order forcing functions for the models were too elementary and must be improved before significant point-by-point comparisons can be carried out. In addition, Killeen et al. (1986) stated that future neutral-wind modeling efforts should carefully consider asymmetries in ion convection, which are governed by the IMF orientation.

The pressure-gradient force, as was already noted, is generally directed from dayside at about 1400 local time to the nightside near 0200 local time. This is the background pressure field, which has both noon-to-midnight and dusk-to-dawn components. There are also local high-latitude pressure gradients caused by Joule (ohmic) heating (Rishbeth, 1979) and precipitation of low-energy electrons (Hays et al., 1973).

The momentum-advection force, being non-linear, was difficult for simple models to evaluate. However, large global-scale models which numerically solve the full set of coupled momentum and energy equations have been able to accomplish this task.' The horizontal-momentum-advection force can be envisioned as having the prevailing neutral winds carry in either larger or smaller momentum values than were

previously associated with a particular grid point. The previous momentum values at the grid point are simultaneously advected downstream.

The Coriolis force is simple to understand and visualize. As an apparent force arising from the choice of a rotating reference frame, it is required for Newton's second law to remain valid (Holton, 1979). The Coriolis force simply modifies the direction of the neutral-wind velocity and is always perpendicular to it. When looking up at the northern-hemisphere sky from the Earth's surface, the Coriolis force is directed to the right of the neutral-wind velocity. If the southern-hemisphere sky is also viewed from the surface, then the Coriolis force is directed to the left of the neutral-wind velocity. For the southern-hemisphere data depictions used in this work, the southern hemisphere sky is projected up onto the northern hemisphere sky. This is done so that the individual forces and neutral winds in the northern and southern hemispheres can be directly compared, by redefining the southern hemisphere data display conventions to be the same as those in the northern hemisphere. Under these conditions, the Coriolis force for the southern hemisphere displays the same behavior as in the northern hemisphere.

The viscous or viscous-drag force tends to smooth out vertical gradients of neutral-wind velocity. It is non-linear since it is proportional to second derivative of velocity with respect to height (equations 4.10 and 4.11). Kinematic viscosity, used in the expression for viscous drag (equation 2.6), is simply molecular viscosity divided by the density (\(\mu/\rho\)). In regions where the temperature lapse rate is small, such as in the upper thermosphere, the molecular viscosity is approximately constant with height (Dalgarno and Smith, 1962). Since density decreases exponentially with altitude, kinematic viscosity increases exponentially with altitude. This is interpreted to mean that the thermosphere becomes stiffer with height and therefore, very little vertical wind shear is anticipated. Viscous drag will be seen to simply subtract in a very minor way from the ion-drag velocity vector in chapter V. The viscous force may become very important at high latitudes during transient forcings. However, away from high-latitude

phenomena, viscous forces are expected to have an increased influence in reducing neutral-wind speeds at night, in regions where ion drag is greatly reduced.

Before presenting in depth details of the NCAR-TGCM, it is appropriate to review the development of our general understanding of global-thermospheric circulation, based on the results of earlier modeling. A good review of early theoretical models which places emphasis on contributions of each in a historical perspective was provided by Mayr et al. (1978).

4.4 One-Dimensional Numerical Models of the Thermosphere

The first numerical model of the thermosphere was that of Harris and Priester (1962). This was a global-mean thermospheric model, so it had only one-dimension (1D), the vertical. Early 1D models assumed the thermosphere was in diffusive equilibrium and the gases were locked into position, unable to move. This is obviously not realistic. In the original 1D models, the only physical process allowed was downward heat conduction. The nature of 1D global mean models made computation of diurnal variations impossible. The increase in available computing power, the need to incorporate dynamics, and the need to explain why the temperature results of 1D models were lower than observed led to the development of two and three-dimensional theoretical thermospheric models. However, changes in the global-mean structure of the thermosphere for different parts of the solar cycle are still being studied by 1D models as evidenced by Roble et al. (1986) using up-to-date parameterizations. Data from the Roble et al. work was shown in figures 2.1 through 2.3 and 2.5.

Several properties of the thermosphere became well known as a result of 1D modeling efforts. For instance, the concept that the thermospheric temperature was largely the result of a balance between the absorption of solar-EUV/UV radiation and thermal heat-conduction downward. The scale height of individual constituents in regions where molecular diffusion dominates over eddy mixing, above the turbopause,

was simply determined by the neutral temperature and species mass. In addition, for regions where horizontal transport was not important, the vertical-composition profile was largely effected by the eddy diffusion properties near the turbopause.

4.5 Two-dimensional Numerical Models of the Thermosphere

POSSESSE RESERVED RESERVED BUNNING RECERCION BEREINS BUNNING B

Applying the simple properties which resulted from theoretical investigations using 1D models, the upper-thermospheric diurnal temperature and pressure distributions, with the daytime pressure bulge, were given by the empirical neutral-thermospheric-density model by Jacchia (1965) based on satellite-drag measurements (figure 2.10). The post-noon bulge was known to be caused by the absorption of solar radiation in the Schumann-Runge continuum (102.6 - 175.0 nm), in the optically-thick lower thermosphere which results in the dissociation of O₂. This created a diurnal pressure and temperature bulge in the lower thermosphere, which maximized near the subsolar point at about 100 km.

Contributions to this diurnal temperature bulge are made primarily by Fourier wave numbers one and two of the perturbation temperature. In the lower thermosphere, the amplitude of the both wave numbers one and two were comparable and in phase. In the optically-thin upper thermosphere, where solar-EUV radiation is absorbed, the heating is fairly uniform across the dayside thermosphere with an abrupt transition at the terminator. In addition, the magnitude of wave number one dominates over wave number two in the upper thermosphere and wave numbers one and two are out of phase. Numerical simulations have shown that the maximum temperature perturbation in the upper thermosphere occurs in the late afternoon for both equinox and solstice. Jacchia's satellite-drag model of neutral densities and temperatures also demonstrated that diurnal, seasonal, magnetic storm, solar-activity variations of the thermosphere occurred.

At this poi vo-dimensional (2D) models became useful in investigating the thermosphere. One of the most useful models was the zonally-symmetric model of Dickinson et al. (1975, 1977), which was also applied to the thermosphere of Venus. By revealing the latitudinal differences in thermospheric dynamics, these models provided a look at meridional circulation in the thermosphere.

More was learned about the structure of the thermosphere from 2D models. Examples of the results of 2D modeling by Dickinson et al. (1975, 1977) and Roble et al. (1977) are now presented. Comparing the results of 2D models with three-dimensional (3D) empirical databases, such as the satellite-drag model of Jacchia (1965) or the OGO-6 thermospheric model from Hedin (1972), it was found that the 2D models did not closely match the observed data for solar-maximum or minimum conditions and solstice or equinox, without the inclusion of a high-latitude heat and momentum source. With a crude approximation of high-latitude heating, which included both Joule heating and particle precipitation, the results moved within the boundary of experimental error. The thermospheric circulation was found to be mainly solar-driven, during undisturbed geomagnetic conditions at solar maximum (figure 4.1). However, as geomagnetic activity increases the influence of the high-latitude heat and momentum source became apparent for both equinox and solstice (figure 4.1). For periods of average activity, the influence of ion convection reached to mid-latitudes. During geomagnetic storms, the influence of the high-latitude momentum source could even reach to the low latitudes. The 2D zonally-symmetric model was also used by Hernandez and Roble (1978) to successfully simulate the effects of meridional-traveling waves following large geomagnetic storms with $K_p > 8$, where ground-based winds and temperatures from the Fritz Peak Observatory were available for comparison with the model. Therefore, 2D zonally-averaged numerical simulations have been very useful in analyzing the effects of geomagnetic activity on the boundaries of meridional-circulation cells and showing

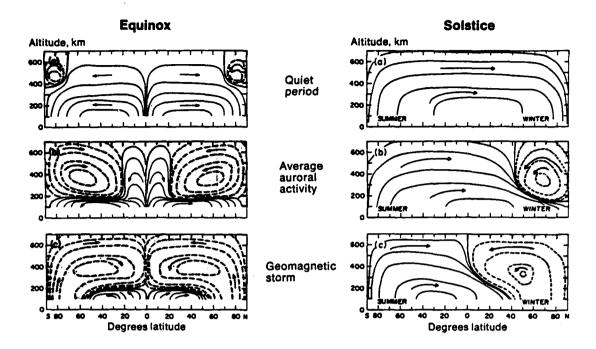


Figure 4.1 - Theoretical zonally-averaged meridional-circulation patterns calculated for solar maximum with differing levels of geomagnetic activity and seasons (Roble, 1986).

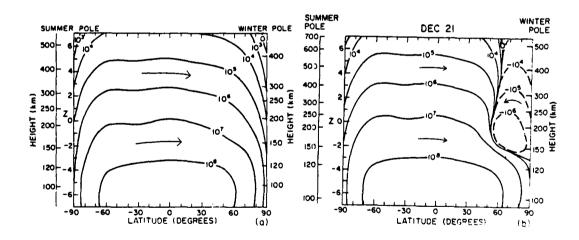


Figure 4.2 - Comparison between meridional circulation calculated during solstice for (a) solar-cycle minimum and (b) solar-cycle maximum (Roble et al., 1977). Note that the coupling between the ionsophere and thermosphere appears to be non-existent during undisturbed geomagnetic conditions.

saasi eeeeeeeee

that the most-variable portion of the thermospheric circulation was located at high latitudes.

For 2D solstice simulations, it was discovered that the high-latitude heat and momentum source had a negligible effect on the summer-to-winter flow, during periods of low-geomagnetic-activity levels at solar-cycle maximum (Dickinson et al., 1977). It was also discovered that the solstice-type neutral-flow patterns prevailed until one or two weeks before equinox. The zonally-averaged flow pattern then quickly made the transition into the equinox-circulation pattern. The neutral winds made the transition back to the solstice-circulation pattern one to two weeks after solstice (Roble et al., 1977). Therefore, for the majority of the year, the most-likely zonally-averaged neutral-windcirculation pattern to be observed, was that associated with the solstice conditions. When experimenting with the high-latitude heat and momentum source, required to bring the model into line with the measured data for solstice conditions, it was discovered that an asymmetric heat source was required. The heat source in the summer hemisphere had to be 2.5 times larger than the corresponding northern-hemisphere heat source (Dickinson et al., 1977). This idea was consistent with data which showed that the effects of geomagnetic activity were greater in the summer hemisphere than the winter hemisphere. In addition, the Pederson conductivity was shown to be 25 times higher in the summer hemisphere (Roble and Matsushita, 1975), which is another example of hemispheric asymmetries that can effect thermospheric dynamics.

Comparisons were also made between 2D thermospheric simulations for solar-maximum and solar-minimum conditions. Results from Roble et al. (1977), show that the coupling between the ionosphere and the thermosphere is much weaker during solar minimum. For undisturbed-geomagnetic conditions, the existence of a high-latitude meridional-circulation cell was not even seen (figure 4.2).

4.6 Three-dimensional Numerical Models of the Thermosphere

Additional insight into thermospheric dynamics was provided by early global-thermospheric models such as the 3D spectral model developed by the Aerospace Corporation group (Creekmore et al., 1975). This model provided reasonably accurate representations of the neutral winds and temperatures using a phenomenological temperature from the Jacchia (1971) satellite-drag model. Neutral winds, densities, and temperatures were then produced by this model using early solar-EUV parameterizations (Straus et al, 1975a). Later, the effect on the global neutral winds of a crude high-latitude heat source, were shown to be necessary to get good qualitative results with observations (Straus et al., 1975b). An advantage of this model was the relatively small amount of CPU time needed on a large mainframe computer, because only low order terms, up to order four, of the vector-spherical-harmonics expansion were retained. An example of the upper-thermospheric winds from this model are shown in figure 4.3.

Three-dimensional semi-empirical thermospheric-dynamic models were used in a series of paper by Hernandez and Roble (1976a, 1976b, 1977) to calculate the neutral winds for comparison with ground-based neutral winds and temperatures over Fritz Peak. The composition and neutral winds for these studies were provided by either the J71 (Jacchia, 1971) or OGO-6 (Hedin et al., 1974) empirical models. High-latitude ion drag was determined using the empirical electron-density model of Ching and Chiu (1973). In general, the models agreed reasonably well with the averaged data and were helpful in providing an overall global-scale picture of the neutral winds.

The next step was the development of full non-linear three-dimensional global-circulation models. There are two well-developed TGCMs in existence today. They are the National Center for Atmospheric Research (NCAR-TGCM) originally described by Dickinson et al. (1981) and the University College, London (UCL-TGCM) first described by Fuller-Rowell and Rees (1980). The main differences between tropospheric and thermospheric GCMs are the modifications which allow fast vertical diffusion of heat

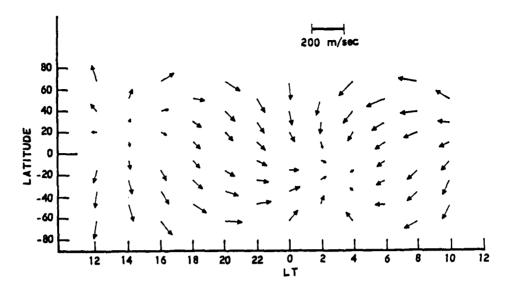


Figure 4.3 - Horizontal neutral winds for June solstice at 300 km produced by the Straus et al. (1975a) three-dimensional spectral model. The neutral winds shown here are due only to solar-EUV/UV heating, no high-latitude processes were included.

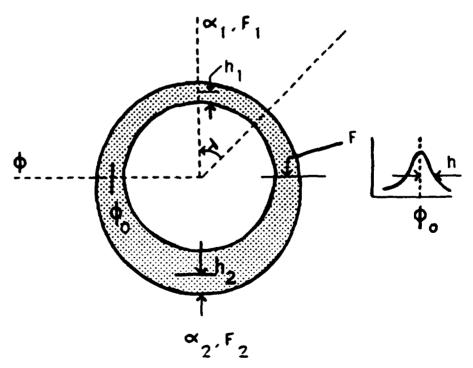


Figure 4.4 - Schematic of the analytic auroral-oval enhancement to the ion densitites provided by the Chiu model (Roble et al., 1986b). An explanation of the parameters describing the width and characteristic energy of the particle precipitation are provided in the text.

and momentum as well as the incorporation of thermospheric physics and chemistry.

This work used the NCAR-TGCM, so details provided here are relevant to that particular model.

The NCAR-TGCM is a 3DTD finite-difference model with 24 constant-pressure surfaces in the vertical from approximately 97 to 500 km. The latitude and longitude grid-point spacing is five degrees in the geographic coordinate system. The time steps used are 150 seconds. Over the past six years, the NCAR-TGCM has been updated and improved. The original version of the NCAR-TGCM, described by Dickinson et al. (1981), did not have coupling between the dynamics and composition incorporated. It also used the Sojka et al. (1979, 1981) symmetric ion-convection model. The second version of the NCAR-TGCM (Dickinson et al. 1984) included the coupling between the dynamics and composition. The version two NCAR-TGCM also utilized the Heelis et al. (1982), ion-convection model, which added greater flexibility. However, at the time the second version of the NCAR-TGCM was developed, an analytical auroral-particle-precipitation enhancement to the high-latitude ion densitites did not yet exist. The third and current version of the NCAR-TGCM (Roble and Ridley, 1987) does have auroral particle precipitation incorporated. As might be expected, large numerical models such as the NCAR-TGCM require 3DTD input parameterizations of neutral densities, ion drifts, solar-EUV/UV fluxes, and particle precipitation. The sources of such inputs are discussed below.

The initial neutral densities and temperatures are provided by the semiempirical mass spectrometer and incoherent scatter (MSIS) model of Hedin (1983) which is based to a large extent on Atmosphere Explorer spacecraft data. Global neutral densities and temperature perturbations from 85 to over 500 km are provided by a spherical-harmonics expansion. The set of coefficients, to which the harmonic expansion applies, has been determined so that they will reasonably accurately reproduce the original data with the following effects over mean values: (a) annual, (b) semiannual, (c) diurnal, (d) semidiurnal, (e) terdiurnal, (f) universal time, (g) longitudinal, (h) solar activity, and (i) magnetic activity. Satellite data was only available down to altitudes of approximately 140 km. Theoretical calculations were used to extrapolate down to the desired altitude.

An analytical global-ionospheric model which produces both ion densities and drifts would be ideal for use in the NCAR-TGCM. There is only one self-consistent global-scale ionospheric model (Sojka and Schunk, 1985). Unfortunately, this model is much too CPU-intensive for use with the NCAR-TGCM. As a result, regional ionospheric models are currently used in TGCMs. One such alternative, the "Sheffield" ionospheric model (Quegan et al., 1982), is available to provide high-latitude ion densities. The "Sheffield" model does provide very reasonable high-latitude ion densities for the UCL-TGCM. However, ion densities for the NCAR-TGCM are specified by the phenomenological model of Chiu (1975) with a high-latitude ion-density enhancement to Chiu ion densities provided by an analytical auroral model due to Roble and Ridley (1987). The low and mid-latitude ion drifts for the NCAR-TGCM are specified by the model of Richmond et al. (1980), while the high-latitude ion drifts are calculated by the analytical ion-convection model of Heelis et al. (1982). More detail is provided in the following paragraphs.

The current (third) version of the NCAR-TGCM does not solve for the ion number densities self-consistently, although this is a future goal. Instead ion densities are usually supplied by the Chiu model originally described in Ching and Chiu (1973) and updated in Chiu (1975). A new, alternative ion-density model, the empirical International Reference Ionosphere (IRI) (Bilitza, 1986) is now also available to provide global ion densities, not due to particle precipitation. There have not been any papers published yet where TGCM neutral winds were simulated using the IRI as an input, and this option was not available at the time of the neutral-wind simulations shown in chapters V and VII. However, a direct comparison between Chiu model ion densities and

Atmosphere Explorer (AE) ion-density data for solar-minimum conditions or DE-2 ion-density data for solar-maximum conditions, was made by Ponthieu et al. (1987). They were able to show that reasonably-accurate total ion densities are provided by the Chiu for solar-maximum conditions. The agreement between the AE satellite data and the Chiu model had much lower levels of agreement under solar-minimum conditions. In addition, discrete high and mid-latitude features, such as the polar hole, mid-latitude trough, and auroral oval (figure 2.4) were absent from the Chiu ionosphere for both solar-cycle maximum and minimum. Therefore, for use in the NCAR-TGCM, it is necessary to use the auroral ion-density enhancement (Roble and Ridley, 1987), which is superposed on the Chiu ion densities. This auroral ion-density enhancement is described briefly below.

The shape of the analytical auroral oval associated with the ion-density enhancement to the Chiu model was given by Roble and Ridley (1987). The center of the particle precipitation, at any angular position around the oval, is tied to the boundary between the antisunward and sunward ion drifts in the Heelis model. Furthermore, the auroral oval uses the same radius, $heta_0$, as the ion-convection pattern. When plotted in geographic coordinates, the entire auroral oval moves with the ion-convection pattern in universal time. The half-width of the auroral oval, at any position around the oval, can be determined if the half-width is known at both local noon, h₁, and local midnight, h₂, as shown in equation 4.14. In addition, the characteristic energy of the precipitating particles at both noon, α_1 , and midnight, α_2 , must be specified. The half-width position in the oval corresponds to the position where the maximum energy particles are precipitated. The energy of the precipitating particles about the maximum center of the precipitation channel, ϕ_0 , is distributed as a Gaussian function (figure 4.4), oriented in a meridional direction. Only one more parameter is required for full specification of the auroral-oval enhancement to the ion density. The energy flux of particles in the center of the auroraloval precipitation channel at both noon, F₁, and midnight, F₂.

$$h = \{(h_1 + h_2)/2\} [1 - \{(h_2 - h_1)/(h_2 + h_1)\} (\cos \lambda)]$$
(4.14)

$$\alpha = ((\alpha_1 + \alpha_2)/2) [1 - ((\alpha_2 - \alpha_1)/(\alpha_2 + \alpha_1)) (\cos \lambda)]$$
 (4.15)

$$F = \{(F_1 + F_2)/2\} [1 - \{(F_2 - F_1)/(F_2 + F_1)\} (\cos \lambda)] \exp [-\{(\phi - \phi_0)/h\}]^2]$$
 (4.16)

In equations 4.14 through 4.16, λ indicates the clockwise angular distance around the auroral oval, looking down from above the northern hemisphere, starting with $\lambda=0$ at local noon (figure 4.4). In equation 4.16, ϕ is invariant-magnetic latitude and ϕ_0 is the latitudinal center of the auroral oval.

The above parameters also provide general polar-cap particle precipitation referred to as "polar rain or drizzle." The polar rain is assumed to have a uniform flux over the magnetic polar cap which decreases in the vicinity of the auroral oval (Roble and Ridley, 1987). In addition, an additional source of soft particle precipitation is provided at the cusp. The region of cusp precipitation is approximately 5 degrees of latitude by 30 degrees of longitude (Killeen and Roble, 1985) while the energy flux for both the zonal and meridional-magnetic directions of the cusp are specified by Gaussian shapes (Roble and Ridley, 1987). For realism, the position of the cusp moves with the position of the dayside entry to the two-cell ion-convection pattern, which responds to the direction and magnitude of the IMF By component.

The auroral-ionization enhancement can then be used at each grid point in the NCAR-TGCM to calculate the auroral contribution to: (1) high-latitude energy input due to particle precipitation, (2) the production of ion-neutral chemical species, (3) electrical conductivity, and (4) production of airglow emissions. For example, equation 4.17 gives the total ionization rate due to a monodirectional beam of electrons, with a Maxwellian

energy distribution. This ionization rate has been parameterized for the TGCM by a least-squares fit as shown in equation 4.18 (Roble and Ridley, 1987).

$$q = (F \rho) / (\Delta \epsilon \alpha^2) \begin{cases} \infty \\ d(\chi) E^2 / (4.6 \times 10^{-6} E^{1.65}) \exp(-E / \alpha) dE \end{cases}$$
 (4.17)

$$q = \{ F \alpha [(\{ \rho H/4 \times 10^{-6} \}^{1/1.65})/\alpha]^{3}/\Delta \epsilon H \}$$

$$\times 2.11685 \{ [(\{ \rho H/4 \times 10^{-6} \}^{1/1.65})/\alpha]^{3} \} 2.97035$$

$$\times \exp \{ -2.09710 [(\{ [\rho H/4 \times 10^{-6}]^{1/1.65} \}/\alpha)^{3}]^{0.74054} \}$$

$$+ 0.58795 \{ [(\{ \rho H/4 \times 10^{-6} \}^{1/1.65})/\alpha]^{3} \} 1.72746$$

$$\times \exp \{ -1.37459 [(\{ [\rho H/4 \times 10^{-6}]^{1/1.65} \}/\alpha)^{3}]^{0.93296} \}$$

$$(4.18)$$

For equations 4.17 and 4.18 the flux, F, is now given by $N_0 \alpha^2$ (in cm²/s), where N_0 is a normalization factor for the mean energy of the Maxwellian distribution and α is the characteristic energy of the particles, specified in equation 4.15. In addition, H is the scale height, ρ is the density (in gm/cm³), E is the energy (in keV), $\Delta \varepsilon = 35$ eV for the ionization of air specified by Roble (1986). It is important to keep in mind that the TGCM uses ionospheric input at grid points spaced five degrees of geographic latitude and longitude apart. With this grid-point spacing, the fine-structure associated with some high-latitude ionospheric features, such at those seen in the global ionospheric model of Sojka and Schunk (1985), are unlikely to ever be fully incorporated into the TGCM.

Richmond et al. (1980) provided the formulation for low and mid-latitude ion drifts for use in the NCAR-TGCM. However, it is the high-latitudes which are of interest here. The high-latitude electric fields and ion drifts are supplied by an analytical model due to Heelis et al. (1982). The Heelis ion-convection model has 13 adjustable parameters which can be used to simulate ion drifts under a variety of IMF $B_z < 0$ conditions. These parameters are outlined in table 4.2 and pictured in figure 4.5. The Heelis model is

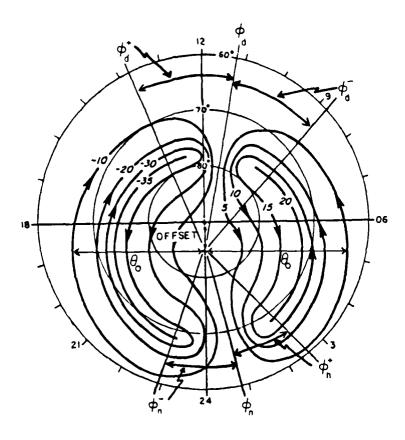


Figure 4.5 - Diagram showing some of the 13 variables which must by specified in the Heelis et al. (1982) ion-convection model and the ways they are measured.

necessary to calculate the high-latitude ion-drag momentum source and the Joule heating rates at each grid point.

Parameter Purpose

Offset R_1	number of degrees the polar cap is displaced toward midnight, in degrees of latitude exponent for variation of electric field outside the auroral oval
R_2	exponent for variation of electric field inside the polar cap
θ_0	half-width of antisunward flow region, measured in degrees
θ_{c}	phase angle within the auroral oval, measured in degrees
$\Phi_{\mathbf{d}}$	angle which the zero-potential line is oriented on the dayside
ϕ_n	angle which the zero-potential line is oriented on the nightside
$\phi_{\mathbf{d}}^{+}$	angular limit of the dayside convergence zone measured counterclockwise
ϕ_n^+	angular limit of the nightside divergence zone measured counterclockwise
Φd^{-}	angular limit of the dayside convergence zone measured clockwise
ϕ_n^-	angular limit of the nightside divergence zone measured clockwise
$\psi_{\mathbf{m}}$	morning cell maximum electrostatic-potential drop in kV
$\Psi_{\mathbf{e}}$	evening cell minimum electrostatic-potential drop in kV

Table 4.2 - Description of the 13 adjustable parameters in the Heelis et al. (1982) ion-convection model. Each parameter can be varied with universal time.

The Heelis ion-convection model can simulate ion-drift patterns for symmetric cells, $B_y = 0$, or $B_y > 0$ and $B_y < 0$ as well as other realistic ion-convection features, such as the dayside "throat" and Harang discontinuity. The Heelis et al. (1982) ion-convection model is an improvement over the symmetrical dawn-dusk electric-potential distribution in the Volland (1978) ion-convection model because of the additional variable parameters (Sojka and Schunk, 1986). These additional parameters add the flexibility required for realistic time-dependent prescriptions of the convection-electric field and ion-drift boundary conditions. However, the Heelis et al. model still has several shortcomings that have been relieved in this work. First, the ion-convection pattern must remain centered on the invariant-geomagnetic pole. This is because in the model the zero-potential line is constrained to pass through the invariant-pole position. This is seen not to be true for most cases, based on empirical studies by Heppner (1972,

1977) as well as Heppner and Maynard (1987). This is a disadvantage that we have attempted to circumvent in chapter VI. Next, while the potentials applied to the dawn and dusk cells do not have to be equal, and the shape of the cells can be varied, the radius of both cells must be the same. This is not realistic, based on past studies. The Heelis et al. model only provides shear reversals, even though some rotational reversals are observed in ion-drift data in chapter VI. The justification for this constraint was that a 180-degree shear reversal implies an equipotential surface (Heelis et al., 1976). Finally, the Heelis et al. ion-convection model can not simulate the multi-cell ion-convection patterns associated with northward IMF. Since the Heelis model became operational in the NCAR-TGCM, other ionospheric modelers have come up with new models which correct some of the above deficiencies. One of the most recent models of the ionospheric convection electric field, which appears to be capable of numerically simulating $B_z > 0$ conditions with only modest CPU expenditures, was described by Sojka et al. (1986). Unfortunately, this model is not at the stage of development where it can be easily incorporated into the NCAR-TGCM.

A simple method of prescribing both the 13 standard parameters in the Heelis et al. (1982) high-latitude ion-convection model and the required parameters in the auroral ion/electron-density enhancement was developed by Roble and Ridley (1987). This scheme requires only three measured quantities/indices and can then analytically specify all the model-ion-convection parameters. The three quantities are: the By component of the IMF, the cross-cap electrostatic potential, and the hemispheric precipitating particle flux (or hemispheric power) index. This method will be discussed in more detail in section 7.3.2.

There are other parameters which must be specified to run the NCAR-TGCM. For example, for solar-EUV/UV heating, the solar fluxes in the appropriate wavelength ranges and their variations with solar cycle must be specified. The 37 EUV wavelength intervals of Torr et al. (1979), which were based to a large extent on Atmosphere Explorer

satellite measurements, have been simplified down to 7 wavelength intervals, such that for any portion of the solar cycle, the proper solar fluxes can be quickly specified. Ongoing developments at NCAR will further reduce the number of wavelength intervals needed to fully specify the solar flux in the NCAR-TGCM down to two (Emery, private communication, 1987), following successful use of this scheme in the global-mean 1D model of Roble et al. (1987). Finally, a representative solar-cycle 21 maximum value of the 10.7 cm solar flux ($F_{10.7}$) was 200×10^{-22} W m⁻² Hz⁻¹. Using this $F_{10.7}$, the solar-UV flux values from Torr et al. (1980) can be used. The solar-EUV flux values are then obtained from Hinteregger (1981). With the solar-EUV/UV fluxes specified, the solar-heating distribution and O_2 photodissociation can be calculated.

4.7 Results of and Improvements to the NCAR-TGCM

The initial results from the NCAR-TGCM (Dickinson et al., 1981) were encouraging. A temperature pattern similar to Jacchia's was produced for equinox when heating only due to solar-EUV/UV was considered (figure 4.6). The resulting global temperature and pressure gradients put the entire thermosphere in motion with horizontal flow away from the pressure bulge on the dayside and toward the pressure minimum on the nightside of the globe. This was the main source of horizontal neutral winds outside the polar cap and contributed to a background day-to-night neutral-wind field within the polar cap. Also note that the meridional flow at high latitudes in figure 4.7 was stronger in the winter northern hemisphere than in the southern summer hemisphere. This was due to a stronger day-to-night pressure gradient in the winter hemisphere when comparing regions of similar geographic latitude and local time

At high latitudes, a plot of early model neutral winds at 300 km (Kohl and King, 1967), which were due only to the day-to-night pressure gradient, is shown in figure 2.11. The basic post-noon to post-midnight polar-cap neutral-wind pattern was revealed, although the magnitude of the flow is quite low at about 40 m/s. In the early 1970s, it was

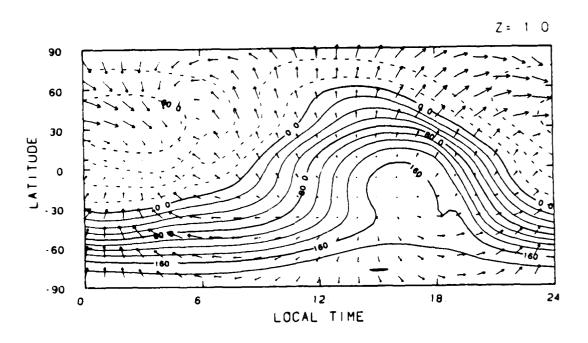


Figure 4.6 - NCAR-TGCM global neutral-wind pattern due only to solar-EUV/UV heating for solar-maximum conditions at equinox (Dickinson et al., 1981).

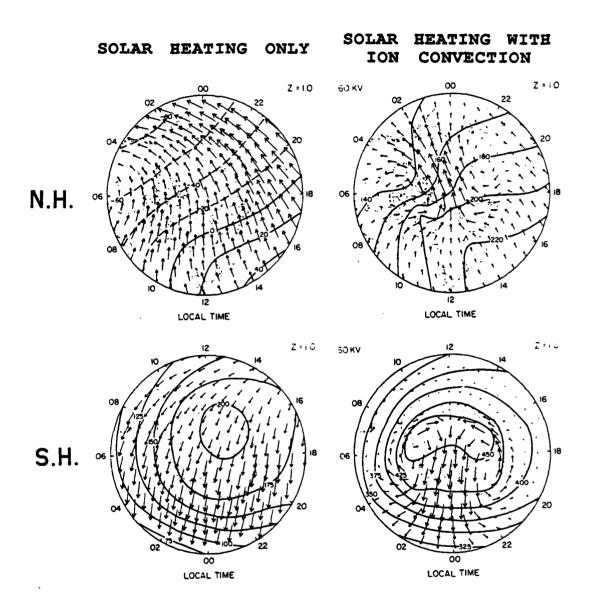


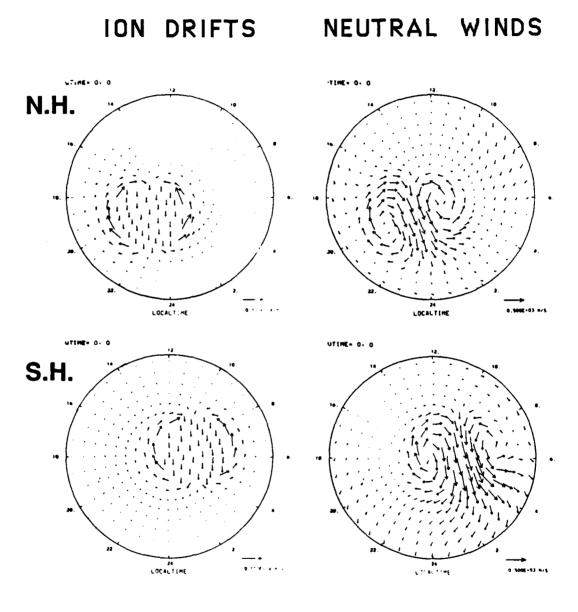
Figure 4.7 - High-latitude neutral winds in both hemispheres due only to solar-EUV/UV heating for solar-maximum December-solstice conditions (Roble et al., 1983). The maximum neutral-wind vector in the northern hemisphere is 181 m/s, while the maximum neutral-wind vector in the southern hemisphere is 110 m/s. Note the changes from the standard orientation of local-time planes used throughout this work.

CALLACON PARESESSON DAVOCOC

recognized from theory (Cole, 1971; Fedder and Banks, 1972) and experimental data (Nagy et al., 1974) that the neutral winds of the upper thermosphere were heavily influenced by the motions of the convecting ions. When the high-latitude neutral winds were numerically-modeled using a simple, symmetric high-latitude analytical ionconvection model, originally due to Volland (1978), as a source of additional momentum through ion drag, the neutral winds displayed a much different flow pattern. The highlatitude neutral-wind pattern (figure 4.8) was quite similar to the two-cell ion-drift pattern. The duskside neutral winds appeared to make nearly a closed loop. However, the dawnside neutral circulation did not appear to make the same closed loop. This failure to exhibit closed-dawnside circulation was more pronounced in the southern hemisphere. At the time, these NCAR-TGCM model results (Roble et al., 1982) could not be verified because there was no large-scale data base of neutral-wind measurements available. Since then, global neutral winds for the 1981 - 1983 period have been collected from DE-2. At the same time, global-thermospheric simulations, for both equinox (Roble et al., 1982) and solstice (Roble et al., 1983), were accomplished with high-latitude ion convection which featured displaced geographic and geomagnetic poles. The work by Roble et al. (1983) showed several orbits of DE-2 neutral-wind data to demonstrate qualitatively that the measured neutral winds followed the two-cell circulation pattern of the ions.

THE POST OF THE STATE OF THE POST OF THE P

The NCAR-TGCM was made more realistic by coupling the dynamics and the composition. This was achieved by solving the mass-continuity equations for each constituent, including their vertical molecular diffusion through each other. Results for equinox during solar-cycle minimum were shown by Dickinson et al. (1984). The differences between the computational results, with coupled composition versus composition prescribed by the MSIS model, were interesting, but small for the solar-minimum 60 kV cross-cap potential case.



AND REPORTED ASSESSED FOR THE PROPERTY OF THE

Figure 4.8 - NCAR-TGCM high-latitude symmetric ion convection and corresponding solar-maximum neutral-wind circulation due to both solar heating and ion convection in both hemispheres for December solstice.

The NCAR-TGCM provides global values of neutral winds, perturbation temperatures, and composition at all grid points. However, insight into thermospheric dynamics was expanded greatly with the introduction of the NCAR-TGCM post-processor diagnostic package of Killeen and Roble (1984). The diagnostic package allowed individual momentum-forcing and heating terms to be plotted independently, which provides a look at the temporal and spatial variation of these terms. The capabilities of the diagnostic package were further enhanced by the capability to provide forward and backward trajectories in a variety of reference frames (Killeen and Roble; 1985, 1986). Furthermore, the forces and heating along the neutral-parcel trajectory could be analyzed. Output from the diagnostic package was used in this research to analyze the momentum forcing for the solar-cycle-maximum, December-solstice case (chapter V).

A unique comparison between DE-2 data and both the UCL and NCAR-TGCMs was shown by Hays et al. (1984). The neutral winds of both models were similar to the individual orbits shown and both showed the same trends. The differences between the neutral-wind fields, generated by the models, were due to the differences between the ion-convection parameterizations, so that a quantitative test of which TGCM more accurately simulated thermospheric neutral winds was not possible without the ion-convection input parameters being the same. To further extend the ability to compare observed neutral winds with TGCM output, DE-2 satellite measurments were merged with observations from several ground-based (GB) FPI locations in a manner similar to surface observations which create a weather map (Killeen et al., 1986). This was done only for the northern hemisphere during the November - December 1981 period. The spatial separation between ground stations demonstrated that coordinated observations can fill in missing parts of the neutral-circulation picture, away from the plane of the satellite orbit.

The second secon

Magnetospheric cusp heating by a "soft" (~ 100 eV) flux of electrons, with an energy peak of 10 erg cm⁻² s⁻¹, was shown to be an integral part of the high-latitude

thermal structure of the thermosphere for a solar-maximum summer-southern-hemisphere case. This was done using both the NCAR-TGCM and DE-2 satellite data. Emery et al. (1985) used another orbit of solar-maximum summer-southern-hemisphere DE-2 data to show that satellite measurements of the magnetic field, ion drifts, and auroral-energy spectra could be used to calculate the structure of the thermosphere and ionosphere below the satellite. In turn, these calculations are used to provide input to the TGCM.

Additional work is still required on several aspects of the TGCM. Use of the Chiu model inhibits realistic ion densities, which are crucial to proper modeling of ion drag. Efforts are already underway to incorporate a self-consistent ionosphere into the NCAR-TGCM. In addition, the inclusion of nitric oxide (NO) cooling is also a high priority for geomagnetic-storm studies (such as in chapter VII). Currently, the heat deposited in the high-latitude thermosphere during a geomagnetic storm does not have all the naturally-occurring sinks available to dissipate it. This primarily effects the TGCM neutral temperatures and composition.

4.8 Summary

CONSCIONS PROPERTY CHARACTER CONTROL SOCIONAL SOCIONAL POSSESSIONAL CONTROL SOCIONAL POSSESSIONAL POSSESSIONA

Global-dynamical models are available today that can provide the three-dimensional time-dependent variation of neutral-gas momentum forcing in the thermosphere. These models have greatly benefitted thermospheric research because they have the ability to simulate the atmosphere in regions or for times where measured data are unavailable. Many improvements have taken place in recent years to make these models more realistic. However, several areas for further development have also been noted.

CHAPTER V

DIURNALLY-REPRODUCIBLE NCAR-TGCM NEUTRAL-GAS FORCE ANALYSIS

5.1 The Solar-Maximum December-Solstice Diurnally-Reproducible NCAR-TGCM Calculations

THE PARTY OF THE P

The goal of this research effort is to observe and theoretically understand the global dynamics of the high-latitude thermosphere. Subsequent chapters will analyze thermospheric neutral-gas momentum forcing seen in Dynamics Explorer-2 (DE-2) data (chapter VI) and three-dimensional time-dependent (3DTD) neutral-wind simulations (chapter VII) using the National Center for Atmospheric Research thermospheric-general-circulation model (NCAR-TGCM). These cases are complex, so this chapter provides the foundation for understanding the more-complex dynamics by analyzing a simple, diurnally-reproducible NCAR-TGCM solar-maximum December-solstice case.

The term "diurnally-reproducible" means, in part, that external geophysical parameters, such as the interplanetary-magnetic-field (IMF) or solar-extreme-ultraviolet (EUV) fluxes, are held constant. This means that the input parameters which govern the high-latitude ion convection in the TGCM, such as the cross-cap electric potential, do not vary with universal time. If the geomagnetic and geographic poles were not displaced, the constant external geophysical parameters would result in a steady-state neutral-wind simulation (i.e., $\partial \mathbf{V}/\partial t = 0$). However, due to the rotation of the geomagnetic pole around the geographic pole, the local time-rate-of-change of the neutral wind at a grid point is not zero. This means there is a universal-time (UT) dependence. However, at the end of 24 hours, the thermospheric fields at each grid point, return to those

corresponding to the same universal time during the previous day. This is the reason for the coining of the term "diurnally-reproducible."

A thermospheric diurnally-reproducible state is somewhat idealized and probably does not occur in nature, due to continually-varying outside influences, such as the IMF and solar wind. However, analysis of a diurnally-reproducible case provides the global universal-time-varying background neutral-wind and momentum-forcing fields upon which the naturally-occurring perturbations can be superimposed. In addition, the analysis of the diurnal variation of forces in both hemispheres for a single, solar-maximum diurnally-reproducible day contained in this chapter alone has, in its own right, substantially improved our theoretical understanding of the morphology and differences between high-latitude thermospheric circulation in opposite hemispheres during December solstice. Therefore, it represents a natural starting point for these investigations.

and becaused any series recommended the series of

A COLUMN TEACHER OF THE ASSOCIATION TO A SECURITION OF THE ASSOCIATION OF THE ASSOCIATION

In this chapter, the diurnal variation of TGCM neutral winds, ion drifts, and neutral-gas momentum-forcing terms in both hemispheres, at selected universal times are examined. The diurnally-reproducible neutral-gas force analysis was made on a generic solar-maximum December-solstice "run" of the NCAR-TGCM with a 60 kV dawn-dusk electric potential applied to produce a symmetric two-cell ion-convection pattern, usually associated with IMF B_z southward and $B_y = 0$ conditions. It should be noted that this diurnally-reproducible force analysis utilized the second version of the NCAR-TGCM, which had both heating due to soft particle precipitation, in the cusp and Joule heating incorporated, as well as a simplified ion-drag enhancement in the auroral regions, but not the auroral-particle-precipitation parameterization due to Roble and Ridley (1987), which was described in chapter IV. The individual forces which result in the TGCM neutral winds were decomposed by extending the NCAR-TGCM post-processor diagnostic package first introduced by Killeen and Roble (1984). The results of these calculations are presented in both hemispheres at four universal times; 04, 10, 16, and 22

UT. These universal times were selected for two reasons. One, the symmetric six-hour spacing provides insight into the diurnal variation of the forces. Next, based on the position of the invariant-magnetic poles (see table 5.2), the asymmetrically-offset invariant poles of both hemispheres are closest to the noon-midnight local-time plane at approximately 04 and 16 UT, while both invariant poles are closest to the 0600/1800 local-time plane at approximately 10 and 22 UT. This UT selection will be seen to be important for comparing forces between hemispheres in this and subsequent chapters.

Highlights of the results from this chapter include a theoretical understanding of TGCM neutral-wind observation that the dawn-cell neutral circulation is more organized in the winter northern hemisphere than in the summer southern hemisphere. This is due to the polar-cap pressure-gradient force, which has an orientation conducive to producing sunward neutral winds on the dawnside of the winter northern hemisphere polar cap. The more-divergent summer-hemisphere neutral flow was confirmed by neutral-parcel-trajectory calculations, where the parcels of air were tracked from the location of the invariant pole in both hemispheres. In addition, the TGCM neutral winds and momentum forces along a simulated satellite track are shown and the importance of using TGCM model data in this satellite-track format, in order to understand the neutral-gas momentum forces behind DE-2 neutral winds, is emphasized.

Plots of the individual component forces are presented in figures 5.3, 5.4, and 5.6 through 5.8. All the polar-stereographic projections in this chapter, unless specifically noted otherwise, are in geographic coordinates viewing from the solar-inertial reference frame, so that the times around the perimeter of the polar dial represent local-solar time, and include geographic latitudes poleward of 40 degrees, in each respective hemisphere. All model data shown apply to gridpoints at and between the latitudes of 42.5 and 87.5 degrees, again in their respective hemispheres. In addition, the TGCM neutral-wind and ion-drift velocities, in these figures, do not have the corotation velocity of the Earth added in. The TGCM forces on these figures can be readily compared between

hemispheres, over a 24-hour period, because the southern-hemisphere plots are projected up onto the northern hemisphere. This means that local-time planes of both hemispheres line up identically in these figures. For ease in making comparisons, the scale length of the velocity and force vectors are held constant among the plots in each figure. In addition, the relation of the scale-arrow length on each figure to other figures is seen in table 5.1, allowing easy determination of the relative influence of each of the individual forces.

Neutral winds (figure 5.1)	500 m/s
Ion drifts (figure 5.2)	1000 m/s
Ion-drag force (figure 5.3)	0.2 m/s^2
Pressure-gradient force (figure 5.4)	0.2 m/s^2
Coriolis force (figure 5.6)	0.1 m/s^2
Inertial or horizontal-momentum-advection force (figure 5.7)	0.1 m/s^2
Viscous-drag force (figure 5.8)	0.1 m/s^2

Table 5.1 - Compilation of diurnally-reproducible NCAR-TGCM velocity and force plots designed for easy comparison between hemispheres and also between figures. The scales used for velocity and force plots can be seen to vary by factors of two.

Finally, for the December-solstice case analyzed in this research, both hemispheric and seasonal differences influence the neutral-gas dynamics of the thermosphere. The hemispheric differences refer to the dissimilar offsets of the invariant-geomagnetic poles from the geographic poles, in opposite hemispheres (figure 5.2). Furthermore, this research examines only the conditions of summer southern hemisphere and winter northern hemisphere. Therefore, it is impossible to conclusively distinguish the hemispheric from the seasonal differences in the neutral-gas dynamics, without examining a solar-maximum June-solstice case. For this reason, although some observations in this and subsequent chapters may refer to "seasonal differences", this really refers to what appears to be a seasonal difference in neutral winds or forces, but which has not yet been proven to be such.

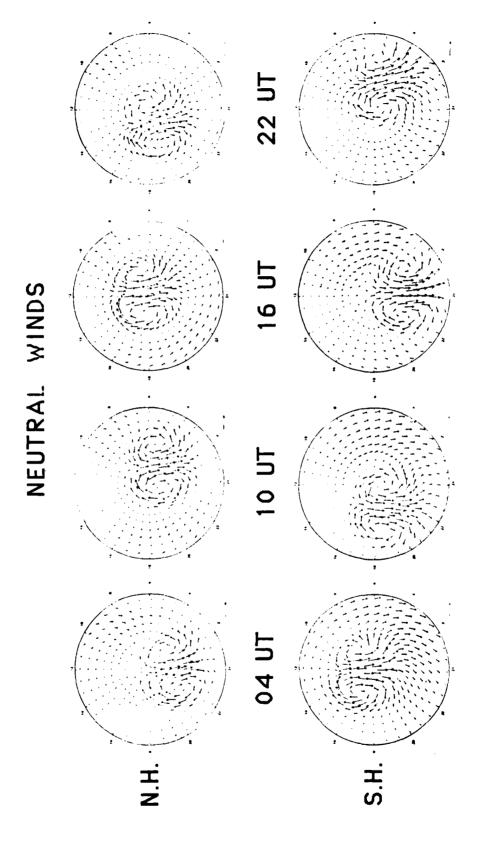
5.2 Diurnally-Reproducible Neutral Winds and Ion Drifts

ROSE HOUSESON POROLINA PARAMENTALISMO OCCURSON RAMAMA MANAMENTALISMO PARAMENTO PROCESSOR PROCESS

The high-latitude neutral-wind field (figure 5.1) has been shown to be controlled to a high degree by horizontal ion convection (figure 5.2). This was originally shown using the NCAR-TGCM by Killeen and Roble (1984), but here is extended through an entire 24-hour period to show the full diurnal variation of forces with "snapshots" of the neutral winds, ion drifts, and neutral-gas forces shown in both hemispheres at selected universal times. Since the center of ion convection in this version of the NCAR-TGCM is physically tied to the position of the displaced invariant-geomagnetic poles, which is also offset five degrees toward the nightside, the ion-convection cells in both hemispheres can be seen to rotate around the geographic pole with a period of 24 hours (figure 5.2). The ion drift velocity in the antisunward regions generally ranges from 250 to 300 m/s with maximum-sunward ion drifts of approximately 1000 m/s in all cases. Since previous experimental and theoretical studies (see chapter IV) have demonstrated the importance of ion drag between the ions and neutrals at high latitudes, it is not surprising to see the neutral winds flow in a manner similar to that of the ions.

Now viewing the neutral-wind fields more closely, it can be seen that the dusk cell is well-formed in both hemispheres and at all universal times. Furthermore, the dusk-cell neutral flow gives the appearance of being practically non-divergent (i.e., $\nabla \cdot \mathbf{V} \equiv 0$). By this it is meant that, qualitatively, the circulation appears to be closed. However, this will be quantified in section 5.6.2. In contrast, the dawn-circulation cell appears smaller in both hemispheres and is less well-formed. The dawn cell gives the impression of being much more divergent in both hemispheres, especially when the invariant pole passes through the noon local-solar-time plane. This would correspond to 16 UT in the northern hemisphere and 04 UT in the southern hemisphere.

The portion of the dawn cell which appears to have the highest divergence is the nightside half of the cell. When the invariant pole is at or near the noon-local-solar-time plane, the neutral winds in the nightside half of the dawn cell are equatorward, rather



THE PROPERTY AND PROPERTY OF THE PROPERTY OF T

DESTRUCTION OF THE PROPERTY OF

Figure 5.1 - NCAR-TGCM diurnally-reproducible neutral winds in both hemispheres and at selected universal times for solar-maximum December solstice. Vector length indicated by scale arrow in bottom right of each plot is 500 m/s.

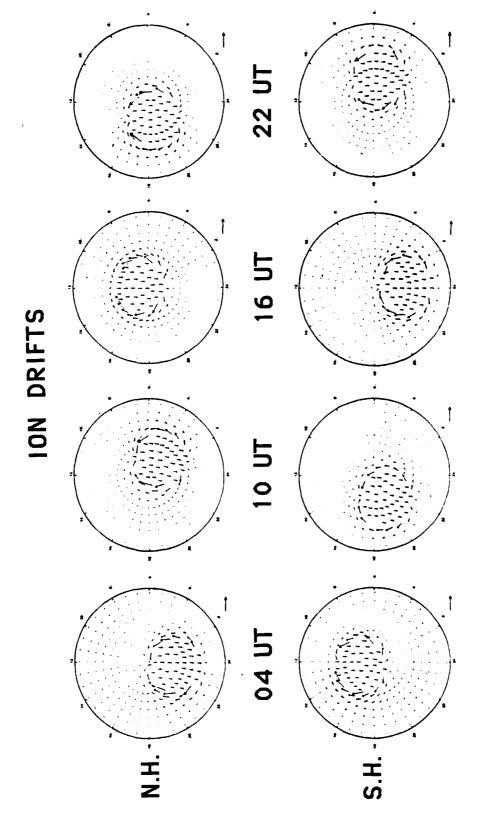


Figure 5.2 - Same as figure 5.1, except ion drifts are plotted and vector length indicated by scale arrow in bottom right of each plot is 1000~m/s.

than sunward. Sunward flow would be expected if ion drag was the dominant force. Also note that the dawn-cell circulation in the summer southern hemisphere appears to be more divergent than the neutral flow in the winter northern hemisphere. This is contrary to what would be expected intuitively, since the higher ion densities in the summer southern hemisphere should provide for more tightly-coupled ions and neutrals, but this does not appear to be true. These observations are discussed in more detail in sections 5.3.2 and 5.6.2.

5.3 Individual Force Analysis

5.3.1 The Ion-Drag Force

STATE OF THE PROPERTY OF THE P

The second

The most important force at high latitudes is usually the ion-drag force. Figure 5.3 shows that the highest ion-drag force values occur in the regions of sunward ion convection (figure 5.2). In these regions, the ion-drag forces can be three to four times larger than the next-largest contributing force. Here, the ions are clearly a momentum source and are drifting under the control of a dusk-dawn electric field which maps along closed field lines, from the equatorial magnetosphere (chapter III). The sunward-convecting ions are drifting in a direction opposite to that for the solar-EUV/UV-driven day-to-night neutral flow, which further enhances the ion-neutral velocity difference (equation 2.2), on which the ion-drag force directly depends.

In each hemisphere, the universal-time modulation of the ion-drag force can be most easily seen by observing the magnitude of the sunward-ion-drag-force vectors (figure 5.3). When the invariant pole is near or within several hours after local noon, the ion-drag force peaks, due to higher ion densities. This is shown in the northern hemisphere by higher ion-drag values at 16 and 22 UT. Lower ion-drag values are present in the northern hemisphere at 04 and 10 UT, due to the fact that the main ion-convection pattern is now in regions of lower ion densities. An analogous situation occurs in the southern hemisphere, except that this polar cap is experiencing summer

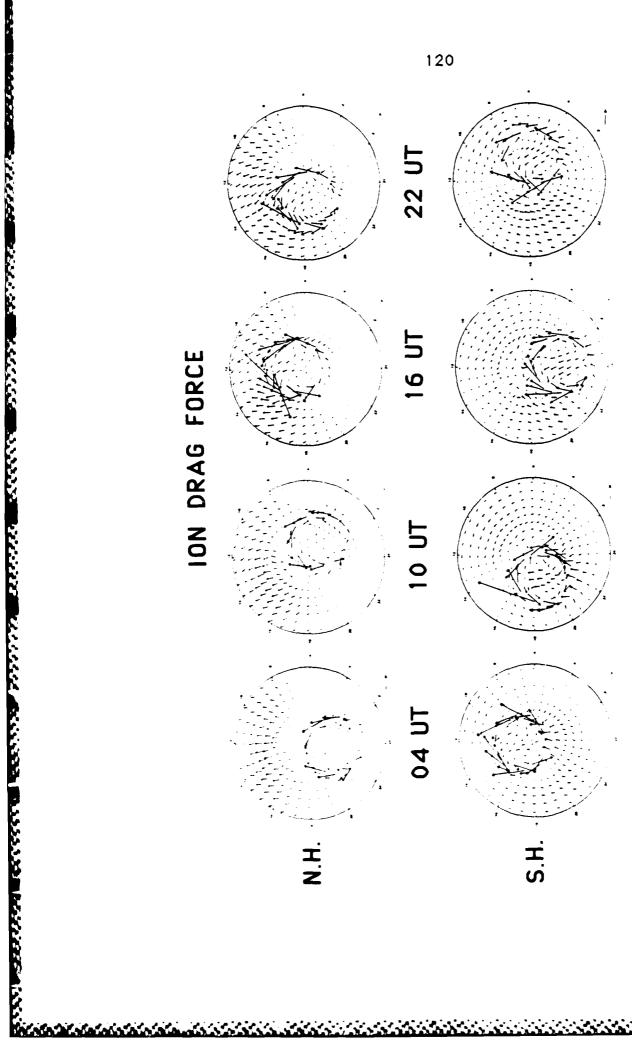


Figure 5.3 - The ion-drag force shown for the same conditions as given in figure 5.1, except vector length indicated by the scale arrow is 0.2 m/s².

Therefore, high ion densities are present at most universal times, with the lowest ion drag occurring at 16 UT, when the invariant pole is close to local midnight.

Large, generally antisunward ion-drag forces can also be found along the inner boundary of the sunward-ion-reversal drifts, although they are generally not as large as the maximum ion-drag force at the outer boundary, associated with the sunward reversals. This large ion drag occurs because the two-cell ion-convection pattern is always slightly out-of-phase with the neutral-wind circulation, due in part to the relatively long ion-neutral momentum-coupling time constant (-hours), which keeps the highly-viscid neutral thermosphere from responding immediately to inputs from ion convection. When the ion-convection pattern moves into a region where the neutrals have previously been set in motion by oppositely-directed ion drifts, there are large velocity differences, which results in high ion drag. This was first pointed out by Killeen and Roble (1984).

Inside the polar-cap, the effect of the ion-drag force is less clear. The ion-drag force, in regions where the ions are drifting in an antisunward direction, is obviously important in accelerating the neutral gas in order to first establish the basic two-cell motion. However, at least one other force (see section 5.3.2) is at work providing additional momentum for the antisunward-flowing neutrals. Therefore, once the antisunward-neutral-wind velocities exceed the ion-drift velocity, the ion-drag force must be in the opposite (sunward) direction, in an effort to retard the antisunward-neutral-gas flow.

Away from the high-latitude, magnetospherically-driven ion convection, the ion-drag force is highest on the dayside in the northern hemisphere, where the solar-driven day-to-night neutral winds would like to flow from the dayside pressure bulge centered near 1400 local time to the region of the post-midnight pressure minimum. In these regions, the ions are holding the neutrals back and so the ion-drag force is directed opposite to the direction of the neutral flow. A similar situation occurs in the southern

hemisphere, except the region of maximum ion drag at lower latitudes has a primary maximum in the early-evening local-time hours, with a secondary maximum in the prenoon-local-time hours. As pointed out by Killeen and Roble (1984) and as is shown in figure 5.4, the pressure-gradient force in these regions is largely offset by ion drag, so the net result is lower-magnitude neutral winds.

5.3.2 The Pressure-Gradient Force

hadd hooddag sanddag gaadhaa hagansaa baddaas baddaan sandahaan sandahaa badhaan baddaan baddaan bada

In terms of magnitude, the pressure-gradient force is the next most important force at high latitudes. From figure 5.4, the pressure-gradient force, at midlatitudes in sunlit regions, is seen to have roughly comparable values to the ion-drag force, but is oppositely-directed. Even at high latitudes, the pressure gradient is a moderating force, without the sharp spatial gradients which characterized the ion-drag force in regions of sunward-reversal drifts. In all other regions shown, except the regions of high ion-drag force associated with sunward reversals, the pressure-gradient force has comparable magnitude to the ion-drag force for this specialized diurnally-reproducible case. Away from the high latitudes, the pressure gradient is basically directed outward from the dayside pressure bulge, centered near 1400 local-solar time, and toward the post-midnight region of lowest pressure. The maximum values of the southern-hemisphere pressure gradient, away from the high latitudes, occur in the early evening and pre-noon hours. The pressure-gradient force converges on the nightside in the mid-latitude, post-midnight region.

In the dayside northern hemisphere, away from the high-latitude processes, there is a strong meridional component in the pressure-gradient force, which is almost entirely offset by oppositely-directed ion drag. In the midnight sector of the winter northern hemisphere, the pressure-gradient force is much smaller (too small to be seen clearly for the force scales used in figure 5.4). However, in this same region the ion-drag force is even smaller (figure 5.3). Here, the neutral winds respond primarily to and flow

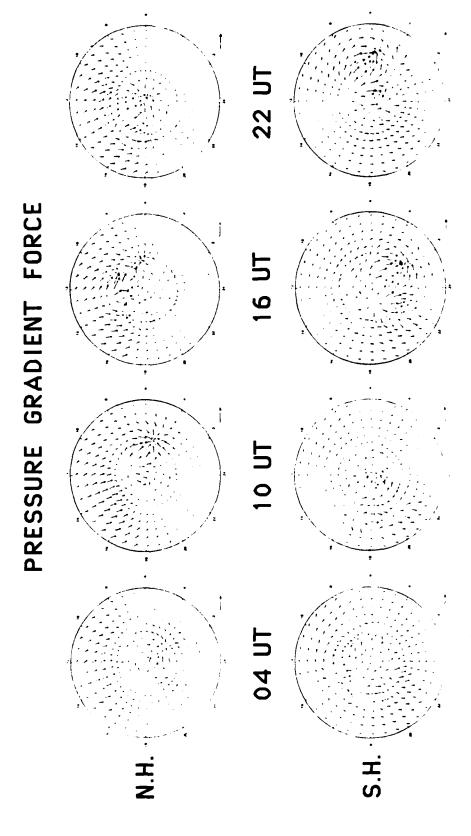


Figure 5.4 - Same as figure 5.3, except the pressure-gradient force is plotted. Vector length indicated by the scale arrow is 0.2 m/s^2.

in the direction indicated by the pressure-gradient force (figure 5.4), largely unopposed by the very-weak mid-latitude ion-drag force. Similar phenomena occur in both the noon and midnight sectors of the summer southern hemisphere, but the vector magnitudes are large enough so that the ion-drag and pressure-gradient forces can be seen in figures 5.3 and 5.4.

The largest-magnitude pressure-gradient forces are a factor of about two above the normal background field and are associated with the high-latitude processes. The polar-cap pressure-gradient force is divergent away from the warm duskside "high" and convergent into the cold dawnside "low", in both hemispheres. The point from which the divergent polar-cap pressure-gradient force originates is farther sunward in the warm high, than the point in the cold low to which the pressure-gradient force is converging. This leads to a pressure-gradient force, inside the polar cap, which is generally oriented in almost the same direction, along the 1400/0200 local-time meridian, as the day-tonight pressure-gradient flow outside the polar-cap. This provides both a noon-tomidnight-directed component, which is responsible for boosting the neutral-wind speed above that which could be achieved strictly by the ion-drag force and a dusk-to-dawndirected component, which becomes maximum near the local-midnight portion of the high-latitude neutral-circulation pattern and is responsible for the diurnally-modulated counterclockwise "twist" of the neutral-wind pattern above that induced by any rotation of the ion-convection cells. As shown by figure 5.4, the summer southern hemisphere has the largest dusk-dawn polar-cap pressure-gradient force component. However, the southern hemisphere thermosphere also is more tightly-coupled to the ionosphere. Even though the maximum value of both the ion-drag and pressure-gradient forces is lower in the winter northern hemisphere, the importance of the pressure gradient is enhanced relative to ion drag, especially during the hours that the invariant pole crosses the postmidnight-local-time planes. This leads to a larger angular variation of the antisunward neutral-wind flow axis from the noon-midnight local-time plane due to a

larger relative contribution from the dusk-to-dawn-directed zonal component of the pressure-gradient force.

Perhaps an even more important observation is related to the differences, between hemispheres, of the orientation of the pressure-gradient force on the dawnside of the polar cap. In the same region as the dawnside divergent neutral flow (noted in section 5.2), the pressure-gradient force in the southern-summer-hemisphere polar cap has a strong meridional component oriented toward the early-morning local-time planes (i.e., the pressure-gradient force has both an antisunward and a meridional component), at all universal times. However, the pressure-gradient force in corresponding dawnside regions of the northern winter hemisphere, is seen to have a slight sunward component. It will be seen in section 5.4.2 that the pressure-gradient force generally has the largest magnitude of any of the forces, inside the polar cap.

It has already been seen that there are differences in the orientation and magnitude of the pressure-gradient forces between the summer southern hemisphere and the winter northern hemisphere. It is also interesting to see why the pressure-gradient force varies between hemispheres. Figure 5.5 displays the TGCM diurnally-reproducible neutral-wind and pressure-gradient fields superposed on the neutral perturbation temperature contours for both hemispheres. The neutral temperature perturbations represent the variation from the global-mean temperature. The northern and southern hemispheres shown are at different universal times, 16 UT in the northern hemisphere and 04 UT in the southern hemisphere, which were selected because the invariant pole for both universal times was displaced farthest toward the dayside. The day-night terminator has also been shown on the neutral winds and temperature portion of the figure.

The spatial variations in the temperature contours are seen to correspond closely to the position of the day-night terminator, in both hemispheres. This basically represents the solar-EUV-driven temperature field. Superposed on this are the effects of

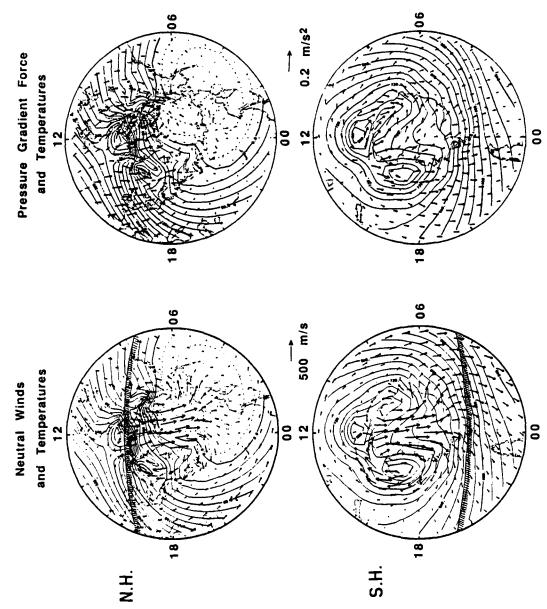


Figure 5.5 - Northern and southern hemisphere neutral-wind and pressure-gradient fields superposed on the neutral-temperature fields.

cusp and Joule heating. The cusp heating can be seen as the circular region of enhanced temperature at the entry to the two-cell neutral-wind-circulation pattern in figure 5.5. Cusp heating results in a larger perturbation to the winter-northern-hemisphere temperature field. The region of Joule heating (figure 5.5) can be seen as the "crescent-shaped" neutral-temperature perturbation regions on both sides of the polar cap. The largest Joule-heating perturbations correspond to the regions where the neutral winds reverse from the antisunward to the sunward direction, demonstrating the influence of the ion-neutral velocity difference on Joule heating (equation 2.11).

The high-latitude cusp and Joule heating can be seen to be perturbations on the global-scale solar-EUV-driven temperature distribution. Away from the high-latitude regions, the pressure-gradient force is seen to be normal to the temperature contours (figure 5.5), indicating that the global-temperature distribution is primarily the driving influence behind the pressure-gradient force in these regions. Furthermore, the high-latitude temperature distribution has a significant effect on the local polar-cap pressure-gradient force. However, the high-latitude pressure-gradient-force vectors (figure 5.5) are not always normal to the temperature contours, indicating that density changes in the polar cap also contribute to the high-latitude pressure-gradient force (see equation 2.5).

5.3.3 The Coriolis Force

THE PERSONAL PROPERTY OF THE P

The Coriolis force is next in importance based on its magnitude. The Coriolis force is an apparent force which acts to deflect a parcel moving with respect to a grid point on a rotating sphere, to the right (equation 2.6). Since the southern hemisphere is projected up onto the northern hemisphere in this work, it also forces parcels to the right of the neutral-wind vectors plotted in figure 5.1.

In figure 5.6, the universal-time variation of the Coriolis force is shown for both hemispheres. Generally, the magnitudes of the vectors are about the same in both hemispheres. Away from the high-latitude processes, the neutral-wind velocities are

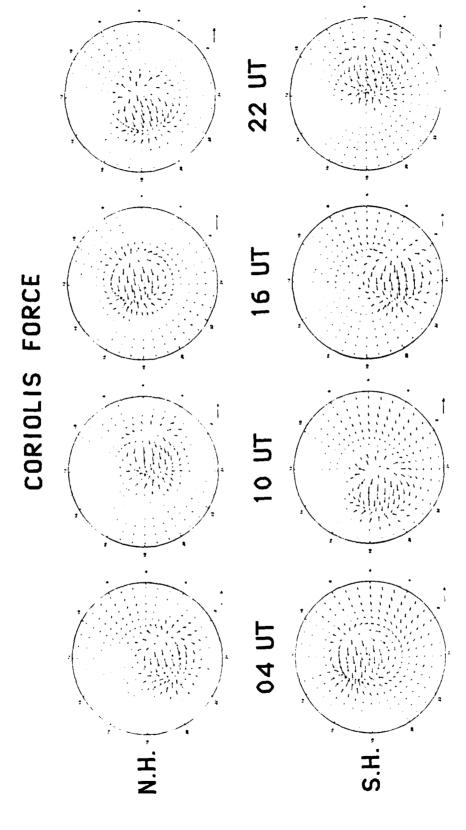


Figure 5.6 - Same as figure 5.3, except the Coriolis force is plotted and the vector length indicated by the scale arrow is 0.1 m/s 2 .

small enough that the Coriolis force does not seem significant. However, a clear pattern develops at high latitudes, where the Coriolis force is always divergent and directed away from the clockwise-circulation cell on the dawnside, while the Coriolis force converges into the counterclockwise dawn cell. It should also be noted that the Coriolis-force vectors shown in figure 5.6 are actually half the size of the ion-drag and pressure-gradient forces, shown in figures 5.3 and 5.4, due to the change in scale-arrow length. Therefore, from a synoptic force balance point-of-view the Coriolis force has a relatively small influence on the neutral-wind dynamics of both hemispheres.

5.3.4 The Horizontal-Momentum-Advection Force

The inertial or non-linear horizontal-momentum-advection force is given in equation 2.8. The inertial force is negligible in many mid-latitude regions in figure 5.7, especially on the dayside of both hemispheres. However, at high latitudes, the inertial force is directed away from the center of both the dawn and dusk circulation cells. On the dawnside of the high-latitude neutral circulation, the inertial force works together with the Coriolis force to carry momentum outward and spread it over a larger area. On the duskside, the inertial force works against the Coriolis force. However, since the scale-arrow length is the same for the Coriolis and inertial forces and the inertial force is seen to have a larger magnitude, the inertial force overcomes the Coriolis force. The summation of the Coriolis and inertial force vectors leads to a small outward-directed force on the duskside of the polar cap. Looking ahead to figures 5.18 and 5.19, where the diurnally-reproducible forces along a simulated satellite track are shown, with all forces using the same scale-length arrow, it can be seen that the inertial force may be comparable in magnitude to (or even exceed) the pressure-gradient force in the areas of antisunward to sunward-neutral-flow reversals.

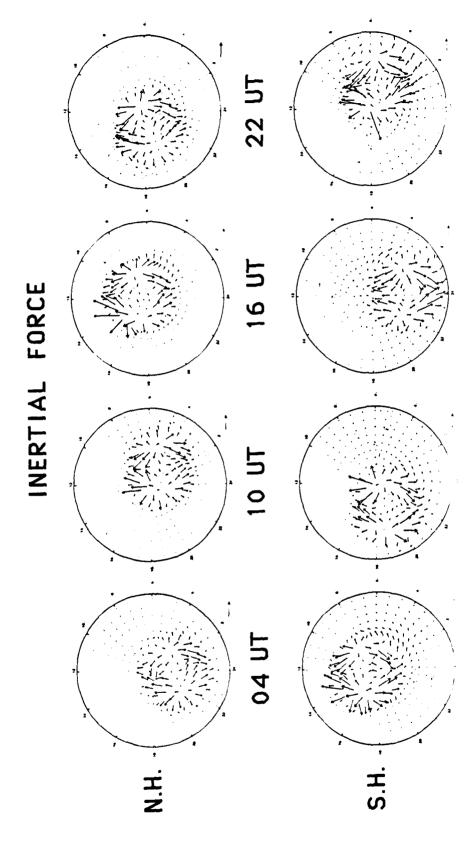


Figure 5.7 - Same as figure 5.3, except the inertial or horizontal-momentumadvection $(\mathbf{V}\cdot \mathbf{V}\mathbf{V})$ force is plotted and the vector length indicated by the scale arrow is 0.1 m/s^2 .

المدعدة والمحمد والمحمد المحمد المحمد

5.3.5 The Viscous-Drag Force

The viscous-drag force, shown in figure 5.8 and given in equation 2.7, appears to be the smallest and least important of the five forces shown in this chapter. However, it is important to remember that this is a diurnally-reproducible case, without time-dependent changes in the parameters which drive the high-latitude ion-convection pattern. As such, viscosity has and is continuing to do an efficient job of smoothing vertical-neutral-wind shears. However, the differences in the horizontal neutral wind with altitude are small. Consequently, the viscous-drag force works slowly but continuously, with the result being small viscous-drag vectors which generally work in an opposite direction to the high-latitude neutral-wind flow. Away from the high latitudes, the viscous-drag force is even smaller.

5.4 Balance of Neutral-Gas Forces

5.4.1 Diurnal Variations of the Maximum Forces in Each Hemisphere

The diurnal variation of the maximum forces at each universal time, and in each hemisphere, is of interest since the maximum forces are usually located in the high-latitude regions. The plots in this section do not represent the force balance at a point, since each maximum-force value, even at the same universal time, may come from a different grid point. Rather, the purpose of this section is to provide a relative "feel" for the diurnal variation of the maximum-force values, which leads up to the force balance at particular locations in the next section. To more clearly see the similarities in the diurnal variation of forces in this (figure 5.9), and similar subsequent plots which use local solar time as the abcissa, the local-solar times of the invariant-pole longitude are appropriately phased between hemispheres.

The locations of the invariant poles, in geographic coordinates (table 5.2), indicate that they are not just offset from the geographic poles, but displaced by different amounts. It can be seen that the southern-hemisphere invariant pole is at a lower

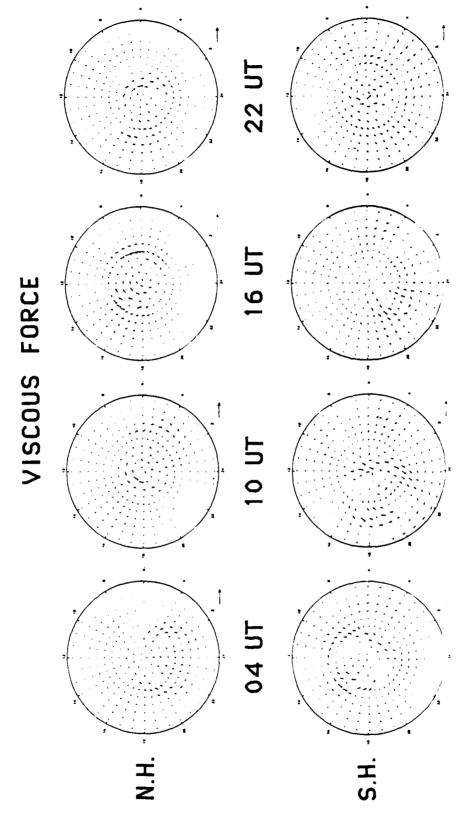


Figure 5.8 - Same as figure 5.3, except the viscous-drag force is plotted and the vector length indicated by the scale arrow is 0.1 m/s².

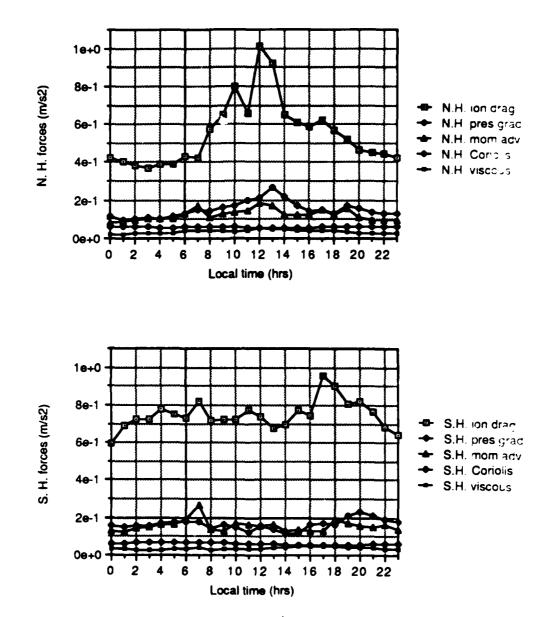


Figure 5.9 - The maximum forces on neutral-gas parcels in the northern hemisphere (top) and southern hemisphere (bottom) as a function of local solar time of the longitude of the invariant pole.

geographic latitude than the northern-hemisphere invariant pole. Furthermore, the geographic longitudes of the invariant poles are not separated by 180 degrees. Since the TGCM computations were saved at each universal-time hour, it was decided that the best way to crudely phase the local-solar times of the TGCM data in both hemispheres, was to put the northern-hemisphere data corresponding to 04 UT in the 00 local-time (LT) bin while putting the 16 UT southern-hemisphere data in the 00 LT bin. When the data is binned in this manner, and plotted with respect to the local-solar time of the invariant-pole longitude, the diurnal variations between hemispheres can be readily compared.

	Latitude	Longitude	Local Noon(UT)	Local Midnight(UT)
Northern hemisphere	+78.3	69.0 W	16:36	04:36
Southern hemisphere	-74.5	127.0 E	03:32	15:32

Table 5.2 - Locations of the offset invariant-geomagnetic poles and the universal times at which each invariant pole experiences local noon and midnight.

In general, the maximum ion-drag force in the summer southern hemisphere, at each universal time, is higher than the maximum ion-drag force in the winter northern hemisphere. The daily average of the maximum ion-drag force is 0.748 m/s² in the southern hemisphere and 0.548 m/s² in the northern hemisphere. The diurnal variation in the summer southern hemisphere is also less (~ 0.35 m/s²) while in the winter northern hemisphere the diurnal variation is almost twice as great (> 0.60 m/s²). All the other forces have maximum values in each hemisphere and at each universal time of less than 0.25 m/s². The most-important secondary forces are the pressure-gradient and non-linear horizontal-momentum-advection forces. Both of these secondary forces experience peaks at the same universal times as the ion drag peaks and are usually minimal when ion drag is minimal, although there is no indication which force is responding to another force yet. (i.e., which force is the cause and which is the effect).

The universal-time effect can be clearly seen in figure 5.9. For example, the northern hemisphere is mostly dark in the winter, with low levels of ionization, resulting in minimal levels of ion drag. However, when the invariant pole rotates around to the dayside and approaches the noon-local-time plane, the maximum ion drag increases significantly, since the position of the ion-convection pattern on the dayside and the higher levels of ionization, in unison, enhance the ion-drag force on the neutral thermosphere. However, just a few hours later, when the ion-convection pattern has rotated to a position behind the solar terminator, the maximum ion-drag force returns to pre-noon levels.

22238

NAMES AND A PROPERTY OF THE PR

In the summer southern hemisphere, the situation is more complex. In this case almost the entire polar region is sunlit, and the lowest daily values of maximum ion drag are approached only when the invariant pole moves near local midnight, with maximum values that are 50% higher than the lowest values of the maximum ion-drag vectors in the winter hemisphere near local midnight (figure 5.9). Unlike the winter hemisphere, there are no clear maximum ion-drag values near local noon. Instead. there are two maxima when the invariant pole passes through 0700 and 1700 local-solar time. This can be interpreted as a response to the meridional pressure gradient. Figure 5.4 reveals that the pressure-gradient force in the summer southern hemisphere maximizes in the early-morning and early-evening local-time sectors. This is also reflected in figure 5.9. However, the pressure-gradient force is generally oppositelydirected to the sunward-ion-drag force in the regions of the sunward-ion-drift reversals where the ion drag is maximum (figure 5.3). Therefore, the maximum ion drag in these regions is higher at 0700 and 1700 UT, because the ion-neutral velocity difference is greater, since the neutral gas in adjacent regions has the highest-antisunward neutralwind speeds where the day-to-night pressure gradients are strongest.

Looking back at the northern hemisphere now, in figure 5.4, the northern-hemisphere day-to-night pressure gradient maximizes in approximately the 1300 local-

solar-time plane. This is seen as the early-afternoon pressure maximum in figure 5.9. In a similar manner to the southern hemisphere, ion drag also maximizes at that time, although clearly the dominant factor in the diurnal ion-drag variation in the winter northern hemisphere is the rotation of the ion-convection pattern into the sunlit section of the polar cap.

Of the other secondary forces, the maximum values of the horizontal momentum advection exceeds the maximum pressure-gradient force, most notably at 07 UT, as shown in both hemispheres of figure 5.9. The maximum Coriolis force is always less than the maximum ion-drag, maximum pressure-gradient, or maximum momentum-advection forces for all universal times and both hemispheres, being approximately half the average value of either the maximum pressure-gradient or the maximum momentum-advection forces. The maximum viscous-drag force is even less than the maximum Coriolis force, owing to the efficiency with which it limits vertical neutral wind shears. Both the maximum Coriolis and the maximum viscous-drag forces have very small diurnal variations.

5.4.2 Force Balance Over the Invariant Poles

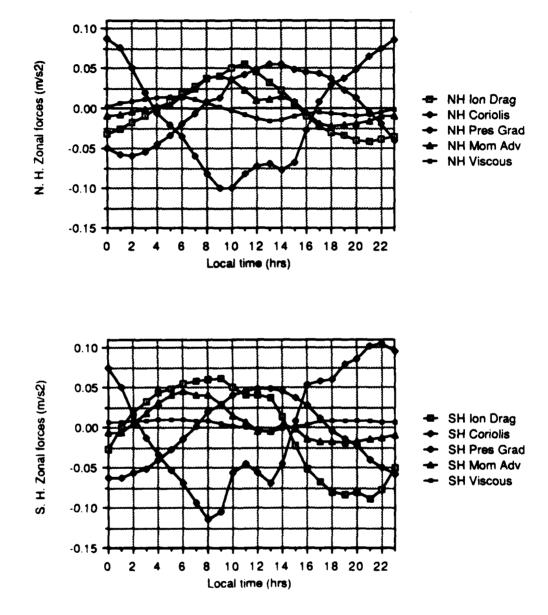
NASTERIOR STATES SECRETARION S

The invariant poles in both hemispheres are unique and interesting locations at which to perform a diurnal neutral-gas force-balance analysis, because they both rotate around the geographic pole in universal time, and are expected to experience similar diurnal momentum-forcing variations. These locations are special because the diurnal variation of the neutral-gas forces can be compared between hemispheres with mainly "seasonal" differences apparent in the momentum-forcing histories. The hemispheric and universal-time-effect differences have been virtually eliminated by choice of the location and by displaying the data in both hemispheres as a function of local-solar time (LST) of the invariant pole in geographic coordinates, which provides phasing for the diurnal variations along a common LST abcissa, as shown in the previous section.

This momentum-force-balance analysis is also interesting because it allows us to see the force balance inside the polar-cap, where the scale of the vectors in figures 5.3, 5.4, and 5.6 through 5.8 was large enough to show the larger-magnitude forces associated with the ion-convection-reversal boundaries, but did not resolve the mid-polar-cap forces well. Finally, it is reasonable to assume that any difference in the momentum forcing as a function of local-solar time between hemispheres at these points is mainly attributable to "seasonal" differences.

The zonal and meridional components of the individual forces in both hemispheres, at the location of the invariant pole, are presented in figures 5.10 and 5.11 as a function of local-solar time. It was quite surprising to see that the diurnal variation of each of the individual components of both the zonal meridional forces was quite similar in both hemispheres. The diurnal variation of the both the zonal and meridional components was generally slightly higher in the summer southern hemisphere than in the winter northern hemisphere, except for the viscous-drag forces which generally had a larger diurnal variation in the winter northern hemisphere. Furthermore, the maxima and minima in each hemisphere are out of phase by about one hour, probably due to the crude phasing the local-solar times of the data, explained above.

The magnitude of the vector sum of the individual neutral-gas forces over the invariant poles in both hemispheres is presented in figure 5.12. When the components are vectorially added together, the slight differences in individual components between hemispheres is magnified and the resultant individual forces no longer have many similarities between hemispheres. The pressure-gradient force is generally the most important force inside the polar cap, in both hemispheres. During the post-midnight hours, the pressure-gradient force is often twice as strong as ion drag. During the day, the ion-drag forces approaches the magnitude of the pressure-gradient force and in the summer southern hemisphere even exceeds it for several early evening hours.



PERSONAL LINESCHER SPRINGS PRINCESS

CONTRACTOR CONTRACTOR RECEIVED TO CONTRACTOR OF THE CONTRACTOR OF

Figure 5.10. The diurnal variation of the individual zonal neutral-gas momentum-forcing components for both hemispheres. The positive direction is eastward.

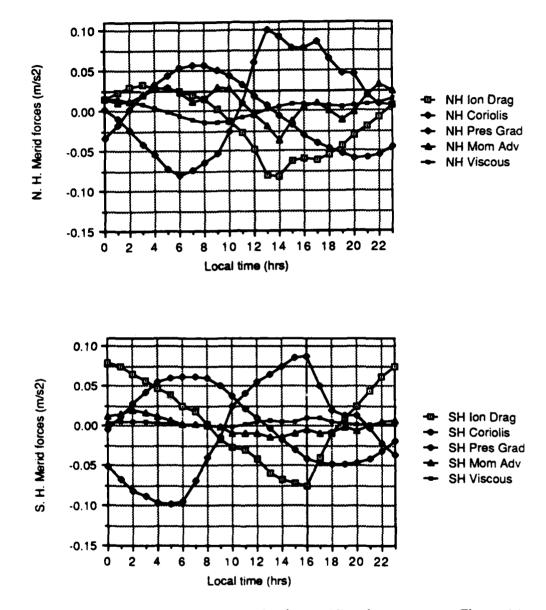


Figure 5.11 - Same as figure 5.10, except for the meridional components. The positive direction is northward.

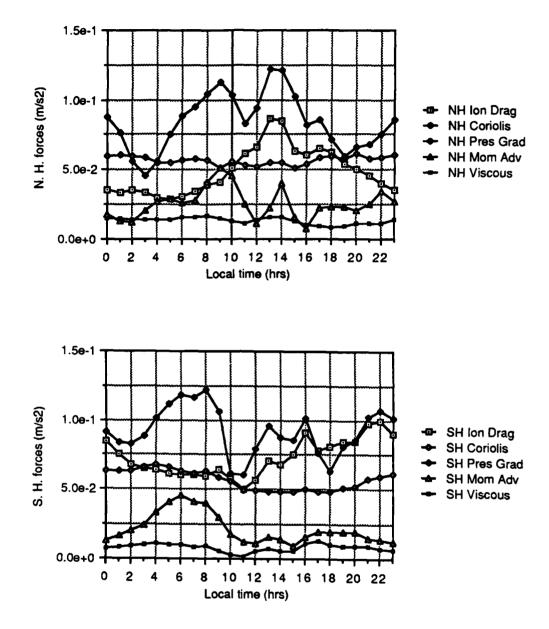


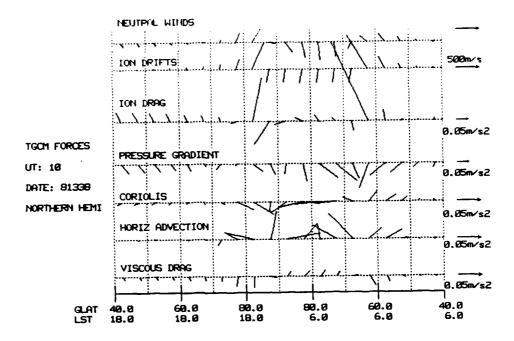
Figure 5.12 - Same as figure 5.10, except for the total individual forces.

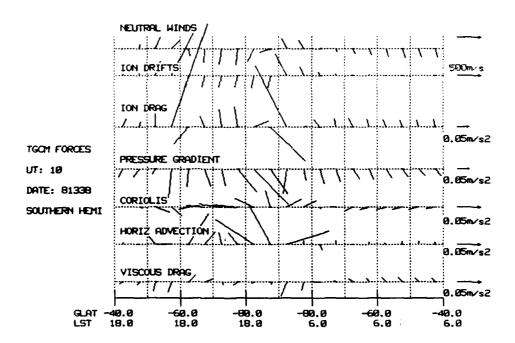
A close balance in magnitude between the pressure-gradient and ion-drag force is apparent in the southern hemisphere between 1000 and 0100 local solar time (figure 5.12). However, this close balance between the pressure-gradient and ion-drag forces never develops in the winter northern hemisphere, due to the weaker ion densities. The ion-drag force approaches the magnitude of the pressure-gradient force in the northern hemisphere in the 1100 through 1900 local-solar-time hours, but is generally lower in magnitude.

5.5 NCAR-TGCM Neutral Winds and Forces Along a Simulated Satellite Track

It was desirable to use this diurnally-reproducible model run to help understand the neutral winds which will be seen in the DE-2 satellite data in the next chapter. Only the ion-drag and Coriolis forces can be accurately depicted along the satellite track using the measured data. Therefore, the ability to depict the remaining forces in a similar manner, from the model, can aid in the neutral-gas forcing analysis of satellite-measured neutral winds. To do this, an additional capability was developed for the NCAR-TGCM diagnostic processor which allowed neutral winds, ion drifts, and neutral-gas forces along selected longitudes, in both hemispheres, to be displayed along a satellite track. The neutral winds, ion drifts, and forces in both hemispheres, are shown for 10 and 22 UT in figures 5.13 and 5.14 where the sun is at the top of each figure. These universal times correspond to periods when the invariant poles in both hemispheres are close to the 0600/1800 local-time plane. This means that similar portions of the dynamics are sampled in both hemispheres. This concept is referred to as "conjugate-region" sampling and will be covered in greater depth in chapter VI.

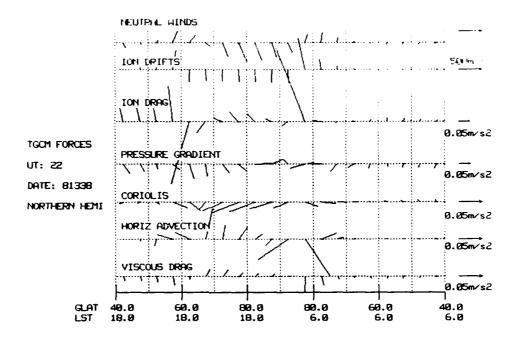
Figures 5.13 and 5.14 show that there is a difference in the directions of the antisunward ion drifts and neutral winds. The antisunward neutral winds are angled slightly more toward the post-midnight sector than the ion drifts. The amount of "twist" in the direction of the antisunward neutral winds is universal-time dependent, and this





REAL PRODUCTION OF THE PRODUCT OF THE PROPERTY OF THE PROPERTY

Figure 5.20 - comparison of TGCM forces in high latitudes of opposite hemispheres at Z=1 pressure level in the 0600/1800 local-time plane at 10 UT.



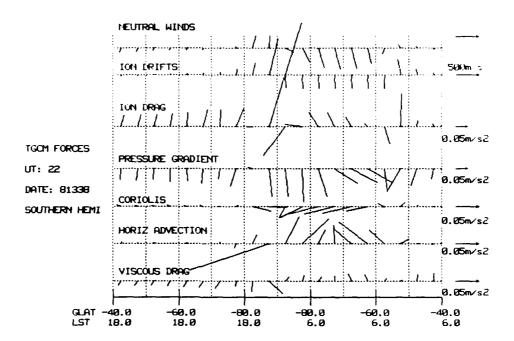


Figure 5.14 - Same as figure 5.13, except at 22 UT.

universal-time effect seems to dominate the "seasonal" effects, since the "twist" is most pronounced in both hemispheres at 22 UT. The full diurnal variation of the antisunward ion-drift and neutral-wind orientation will be discussed further in the next section.

It can also be noted that the model ion drifts along the satellite track, for these universal times (figures 5.13 and 5.14), typically show only shear reversals, while the model neutral winds show both shear and rotational reversals in regions of transition from sunward to antisunward flow. The antisunward neutral winds are seen to exceed the ion drifts in the region of high-latitude antisunward flow in both hemispheres. Further, the duskside neutral-wind reversal is always stronger than the dawnside reversal in both hemispheres, as mentioned in preceding sections. The maximum duskside ion-drift reversal in the southern hemisphere exceeds the dawnside ion-drift reversal while the opposite is true in the northern hemisphere. This may be due to the choice of grid points for the display of ion vectors in these figures.

PERSONAL PROPERTY AND PROPERTY AND PROPERTY.

CONTRACT BUTTORS WINDOWS WASSING

Depictions of the neutral-gas forces along the track of a satellite were generally easier to understand after viewing the polar plots of the forces in both hemispheres, which provided the "big picture". The maximum ion-drag forces in figures 5.13 and 5.14 directly reflect the ion-drift reversals mentioned in the previous paragraph. As expected, ion drag is generally stronger in the summer southern hemisphere, inside and outside the polar-cap. It was also be noted, that the ion-drag force in the center of the antisunward polar-cap neutral-wind region was small, compared to the other forces of figures 5.13 and 5.14, especially when compared to the pressure-gradient force at 10 UT in the northern hemisphere. This indicates that the pressure-gradient force often has a significant influence on the polar-cap neutral winds, even though they generally follow the two-cell motions of the ions. The polar-cap pressure gradient, in both hemispheres, has a component which is oriented toward the early-morning local-time sector. The pressure gradient along the simulated satellite track is stronger in the summer southern hemisphere, but so is the ion-drag force.

The Coriolis force shows convergence in the vicinity of the dusk cell and divergence in the vicinity of the dawn cell, with only small variations between hemispheres or with universal times. Finally, viscous drag is usually small in all the frames shown, usually opposing ion drag outside the polar-cap and working in unison with ion drag inside the polar-cap. The exception to this is in the southern hemisphere at 10 UT where an extremely small viscous-drag force is oriented in the opposite direction to the ion-drag force, but with little consequence. Again, all of these observations are consistent with the hemispheric plots of individual forces, which make interpretation of the forces along a simulated satellite track much easier.

5.6 Observations of 'Seasonal' and Diurnal Neutral-Wind Variations

5.6.1 Universal-Time Variation of the Orientation of Polar-Cap Neutral Winds

Examination of the neutral winds in figure 5.1 led to a number of significant points. For example, the two-cell ion-drift patterns in figure 5.2 are basically sunaligned, with a small diurnal variation (< 20 degrees) in the angle of the antisunward ion drifts with respect to the noon-midnight plane of approximately equal magnitude in both hemispheres. However, while the antisunward neutral winds, in figure 5.1, exhibit a diurnal variation in the angle of the antisunward winds with respect to the noon-midnight local-time plane, which is similar to the ion drifts, there is an additional "twist" of the antisunward neutral winds in the counterclockwise direction, which differs depending on the hemisphere (see figures 5.13 and 5.14). The diurnal variation of the antisunward orientation for the ions and neutrals, in both hemispheres and for all universal times, is shown in figure 5.15. It should be remembered that this diurnally-reproducible TGCM model run provides data for an IMF $B_z < 0$, $B_y = 0$ case, and the measured antisunward ion drifts, which will be seen in chapter VI, are rarely oriented in the same direction in both hemispheres, at the same universal time.

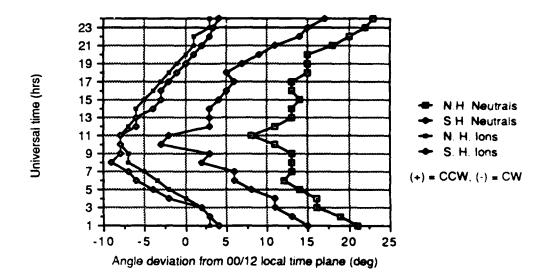


Figure 5.15 - Angular variation in universal time of the antisunward ion drifts and neutral winds from the noon-midnight local-time plane for the diurnally-reproducible NCAR-TGCM run. Positive departures indicate the counterclockwise direction, starting from 0000 local time.

The universal-time variation of the angle the antisunward ion drifts make with respect to the noon-midnight local-time plane is essentially the same in both hemispheres for this diurnally-reproducible model run. The antisunward neutral winds generally follow the diurnal variation the ions make with respect to the noon-midnight local-time plane, indicating the influence of the ion drifts on the neutral winds. However, the "twisting" effect seen in the antisunward neutral winds in figure 5.15 is more pronounced in the winter northern hemisphere where the coupling between the ions and neutrals, as measured by the ion-neutral momentum-coupling time constant (equation 6.1), is less than in the summer hemisphere, due to lower ion densities. This indicates that forces, other than ion drag, are beginning to have a substantial impact on the high-latitude dynamics within the polar cap.

5.6.2 Dominance of the Duskside Neutral-Circulation Cell

THE PROPERTY OF THE PROPERTY O

Another observation is that the dusk neutral-circulation cell, in both hemispheres, seems to be more well developed than the dawn cell (figure 5.1). The sunward-return flow in the neutral circulation is clearly established on the duskside in both the summer and winter hemispheres. However, the dawnside sunward-return flow is not so well established. In the winter northern hemisphere, sunward neutral winds in the dawn sector exist, but have lower magnitudes and cover a smaller-latitude region than in the dusk sector. In the summer southern hemisphere, dawnside sunward neutral winds at certain universal times, such as 04 and 22 UT, are essentially non-existent. The sunward-return flow on the dawnside that does exist is much less organized than the dawnside flow in the winter northern hemisphere. Hence, the dawnside sunward return flow in the 0600/1800 local-time plane, in either hemisphere, would be minimal in latitudinal size and magnitude of the neutral winds, compared to the sunward return flow in the dusk sector. This is consistent with the neutral-wind data shown in figures 5.1, 5.13, and 5.14

To go further, at all the universal times shown in figure 5.1, the duskside northern-hemisphere sunward-return flow appears to be less divergent than the dawnside neutral flow in the southern hemisphere. To confirm this, the divergence of the neutral-wind field in each hemisphere was calculated, using the coefficients resulting from a vector-spherical-harmonic (VSH) analysis of the neutral wind field. To do this the VSH model of Killeen and Roble (1986) was employed on the NCAR-TGCM output neutral-wind field. Based on these calculations, the nightside of the dawn and dusk neutral-wind circulation cells, in each hemisphere and at each universal time, was characterized by its maximum neutral-wind divergence $(\nabla \cdot \mathbf{V})$ value. The results, seen in figure 5.16, show that the dawn cell has larger divergence values in both hemispheres. However, when the invariant pole is between the 0700 and 1900 local time planes, it is apparent that the summer-southern-hemisphere dawn cell generally has much higher levels of divergence than the dawn cell in the winter northern hemisphere. From the pre-noon through early evening local-time planes, the summer-southernhemisphere dusk cell also has higher divergence than the corresponding dusk cell in the winter northern hemisphere. However, when the invariant-pole longitude passes through the post-midnight through prenoon local-solar-time hours, the divergence values of the dusk cell in both hemispheres are comparable. Furthermore, for the post-midnight sector, the divergence values of the dawn cells in both hemispheres are also similar.

CONTRACTOR CONTRACTOR CONTRACTOR

VIVINE USSESSANDINES DESCRIBE RELECTION

To see the effects of difference in neutral-wind-field divergence between hemispheres, a forward trajectory was run from the NCAR-TGCM grid point closest to the location of the invariant pole in both hemispheres. Both trajectories were begun at 00 UT and run for 24 hours for this diurnally-reproducible December-solstice solar-maximum case. Plotted in geomagnetic coordinates, these trajectories reveal that a neutral parcel starting in the antisunward-neutral-flow region in the summer southern hemisphere does not stay in the two-cell circulation pattern but is forced out of the post-

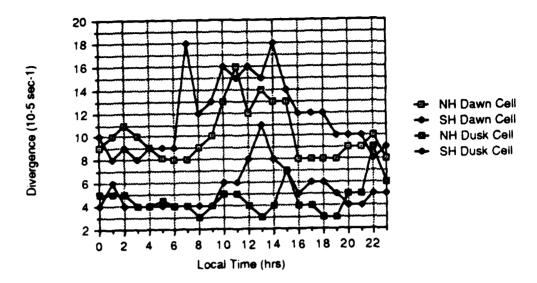


Figure 5.16 - The divergence of the nightside portions of the dawn and dusk cells of the neutral-wind field (10⁻⁵ s⁻¹), at each universal time and in both hemispheres for the diurnally-reproducible NCAR-TGCM run, evaluated using the VSH model of Killeen and Roble (1986). The data here are presented with local solar time of the invariant pole as the abcissa.

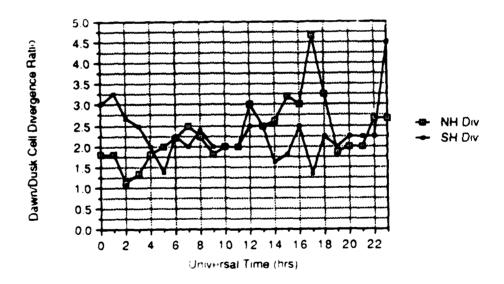


Figure 5.18 - The dawn/dusk ratio of the neutral-wind divergence $(\nabla \cdot \mathbf{V})$ on the nightside portions of the neutral-circulation cells, calculated using the data in figure 5.16 and presented as a function of universal time for use in analyzing the neutral-parcel trajectories in figure 5.17.

midnight sector, where it moves to lower latitudes and corotates. However, a parcel started at the same invariant latitude and longitude in the northern hemisphere has quite a different trajectory. Now, the neutral parcel, also started in the antisunward flow region, is trapped and follows the dawn-cell circulation through more than one complete cycle during the 24 hours of the simulation.

To understand the neutral-parcel trajectories in figure 5.17, the ratio of the dawn-to-dusk-cell divergence was taken at each universal time. The results, which are plotted in figure 5.18, show that at the time the trajectories began, the southern-hemisphere dawn cell had significantly more divergence than the southern-hemisphere dusk cell. A comparison between hemispheres shows that for the first four hours of the trajectory runs, the ratio of the dawn-to-dusk-cell divergence in the summer southern hemisphere was almost twice that of the winter northern hemisphere. By 04 UT, when this dawn-to-dusk divergence ratio was similar in both hemispheres, the neutral parcel in the summer southern hemisphere had already moved to mid-latitudes.

In general, during the mid-day local-solar times, the summer-southern-hemisphere dawn and dusk cells were more divergent than the corresponding winter-northern-hemisphere neutral-circulation cells, with the dawn neutral cell always more divergent than the dusk cell. The neutral-wind trajectories in opposite hemispheres show that differences in the neutral-wind momentum forcing exist between the winter northern hemisphere and the summer southern hemisphere. They also provide an intuitive feel for the differences in the levels of neutral-wind divergence.

5.6.3 Diurnal Variation of the Maximum Polar-Cap Neutral Winds

Unlike the ion convection, which generally has the largest ion-drift velocities associated with the regions of sunward convection, the maximum neutral-gas velocities occur in the antisunward polar-cap flow regions. The diurnal variation of the maximum-antisunward neutral-wind speeds, in both hemispheres, is shown in figure

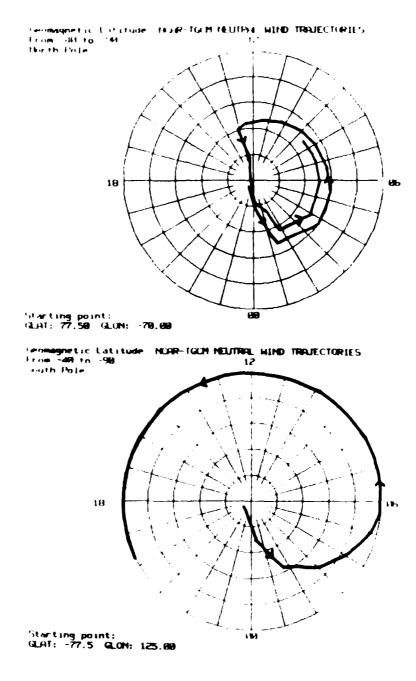
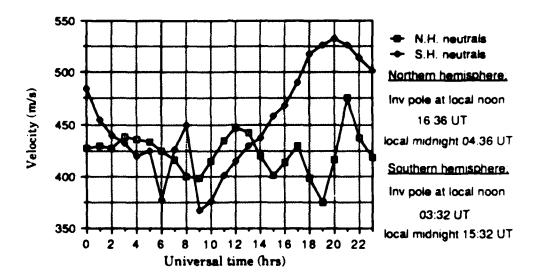


Figure 5.17 - NCAR-TGCM neutral-parcel trajectories, for both the northern and southern hemispheres, with the strating point at the invariant-pole location and plotted in invariant-geomagnetic coordinates.

5.19. The summer southern hemisphere generally had slightly-higher maximum-antisunward neutral winds, with a mean value of 453 m/s and a standard deviation of 50 m/s over the 24 hour period, than the winter northern hemisphere, which had a mean maximum-antisunward neutral-wind speed of 423 m/s and a standard deviation of 20 m/s. The higher mean antisunward neutral winds in the summer southern hemisphere are due to greater ion densities, resulting in a higher-average ion-drag momentum source, as well as higher-average pressure-gradient forces in the the summer hemisphere polar cap. However, the maximum-antisunward neutral-wind velocities are modulated by the rotation of the invariant-geomagnetic pole around the geographic pole, often referred to as "the universal-time effect." Local midnight at the location of the invariant pole in the northern (southern) hemisphere occurs at 04:36 UT (15:32 UT).

The reason for the large diurnal variation is the maximum antisunward neutral winds, in figure 5.19, can be understood in terms of the polar-cap ion-drag and pressure-gradient-force distributions at different universal times. Looking back at figure 5.14, it can be seen that at 22 UT, when the invariant pole in the summer southern hemisphere is approximately passing through the 0600 local-solar-time plane, the antisunward-pressure-gradient force is much stronger than the oppositely-directed ion-drag force. At this universal time, the dominant polar-cap pressure gradient forces the antisunward neutral winds to higher velocities.

In contrast, at 10 UT, the summer southern hemisphere polar-cap ion-drag and pressure-gradient forces are more closely balanced, resulting in lower antisunward neutral-wind velocities. This case is somewhat idealized because, as shall be shown in chapter VI, the antisunward-convecting ions frequently exceed the velocity of the antisunward neutrals, providing a source of antisunward momentum, which increases the neutral velocities instead of retarding them as in the diurnally-reproducible case for the antisunward-circulation region.



CALLEDON TO CONTRACT CONTRACTOR CONTRACTOR

TO SECOND TO SECUL AND SECOND TO SECOND SECO

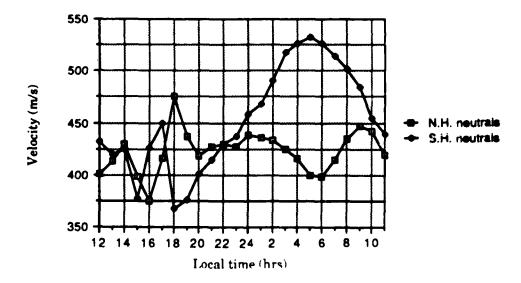


Figure 5.19 - The values of the maximum antisunward neutral winds in both himispheres plotted as a function of universal time (top) and local-solar time of the invariant-pole longitude (bottom).

5.6.4 Size Comparison Between Ion-Convection Pattern and Neutral-Wind-Circulation System

Another observation which can be made is that the size of the neutral-circulation system is larger than the ion convection. A 30-degree radius circle, in geographic coordinates, will enclose the majority of the neutral-circulation pattern and a 25-degree radius circle encloses the ions (figure 5.20). The area of the neutral-circulation pattern is larger than the ions due to the pressure-gradient force, when viewing the total acceleration on the neutral gas from inertial space. The relative size of the neutral-circulation system relative to the ion-convection pattern shows little universal-time variation or differences between hemispheres. In addition, the high-latitude ion-convection pattern and neutral-wind-circulation pattern boundaries always coincide on the duskside of the polar cap, with the neutral-wind-circulation pattern extending past that of the ion convection on the dawnside. This also does not vary between hemispheres or with universal time.

In the inertial-reference frame, the simple-horizontal neutral-gas equation of motion (equation 2.1) can be rewritten so that the total acceleration is on the left-hand-side of the equation. Furthermore, the Coriolis force is non-existent in this reference frame. The resulting equation is shown below:

$$DV/Dt = v_{ni} (V_i - V_n) - \nabla P / \rho + \mu (\partial^2 V / \partial^2 h) / \rho$$
 (5.1)

The pressure-gradient force inside the polar cap, as seen in figures 5.12 to 5.14, is the primary neutral-gas momentum source. Since the polar-cap pressure-gradient force generally has both an antisunward and a dusk-to-dawn component, it forces the neutral gas in those directions (figures 5.4, 5.13, and 5.14). In these polar-cap regions, the ion-drag force and viscous-drag forces generally work to decelerate neutral-gas parcels. It was seen in the previous section that the diurnal variations in magnitude of the pressure-gradient force had a large impact on the diurnal variation in the maximum-

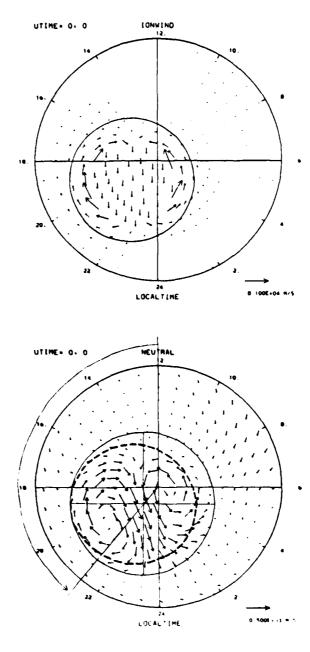
antisunward neutral winds. The point is now made that the dusk-to-dawn component of the polar-cap pressure gradient helps to spread the neutral-gas circulation over a larger area, resulting in the difference in size between the ion-convection and neutral-wind-circulation patterns shown in figure 5.20.

To summerize this section, the only force capable of enlarging the size of the highlatitude neutral-wind-circulation system, in the inertial-reference frame, is the pressure gradient force. In this reference frame, the Coriolis force does not exist and the non-linear momentum-advection force has been incorporated into the total derivative.

NOTIFICATION OF THE CONTRACTOR OF THE CONTRACTOR

5.6.5 Phase Difference Between Ion-Convection and Neutral-Wind-Circulation Systems

Roble et al. (1982) estimated the time (or phase) lag between the high-latitude ion-convection and neutral-wind-circulation systems to be two hours, based on solar-maximum-equinox calculations made using the NCAR-TGCM. This estimate was obtained by subtracting the neutral-wind field without high-latitude ion-convection from the neutral-wind field with ion convection. The resulting neutral-wind difference field is presumed to be due entirely to ion convection. The neutral-wind difference field is then compared to the current ion-convection pattern and the angular distance between the center of the two circulation patterns noted. More recent estimates of the phase lag are 0.5 - 1.0 hour (Roble et al., 1987a). The phase lag exists because of the time it takes the neutrals to respond to both the ion drifts and the movement of the ion-convection pattern. This will be discussed further in section 6.2.5, which deals with the time constant for ion-neutral momentum coupling. However, since the ion-convection pattern is rotating with the geomagnetic pole and is not stationary, the neutral-wind circulation at any particular time is expected to be more representative of the position of the ion-convection pattern at some previous time.



the recognitive consists expected and the second an

Figure 5.20 - Illustation of the relative sizes and positions of the neutral-wind and ion-convection patterns for the northern hemisphere at 00 UT. The majority of the neutral circulation is enclosed by a 30-degree radius circle, while the ion convection is primarily enclosed by a 25-degree radius circle. The circle enclosing the ion-convection pattern is also drawn on the neutral-circulation system in a dashed line to provide an idea of the approximate relative sizes. Note how the center of the neutral-circulation system is measured.

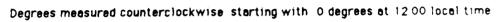
Due to a stated interest in comparing the dynamics of opposite hemispheres, it was desirable to compare the phase lag between the ion-drift and the neutral-wind-circulation patterns of the winter northern hemisphere to those of the summer southern hemisphere. However, a different technique was used. This technique consisted of calculating the angular position of the ion-convection pattern in the model based on the position of the invariant pole but with a five-degree antisunward offset of the convection pattern toward midnight. The equations used to analytically calculate the angular position of the center of the ion-convection pattern with the five-degree antisunward offset from the invariant-pole location, are given below:

$$\theta_{NH} = [111. + (UT \times 15.)] + [5. \times \sin\{69. - (UT \times 15.)\}]$$
 (5.2)

$$\theta_{SH} = [307. + (UT \times 15.)] + [5. \times \sin(233. - (UT \times 15.))]$$
 (5.3)

where UT is the universal time in hours. In equations 5.2 and 5.3, the angular position is measured in a counterclockwise direction from local noon. The result is a very-slight sinusoidal variation in the angular rotation of the center of the ion-convection pattern, which can hardly be detected in figure 5.21 but is present in the NCAR-TGCM whenever the five-degree antisunward offset of the ion-convection pattern is instituted.

Once the position of the center of the ion-convection pattern was known, the position of the center of the neutral-circulation pattern was determined. A different method was used to contrast the results of Roble et al. (1982). This technique consisted of overlaying a 30-degree of geographic-latitude radius circle on the neutral-circulation system of both hemispheres, as described in the preceding section. The circle was intended to contain as much of the high-latitude neutral-wind circulation as possible, even though the outer boundary of the high-latitude neutral-wind-circulation pattern does not represent a circle. The fit of the circle to the outer boundary of the dusk-cell sunward



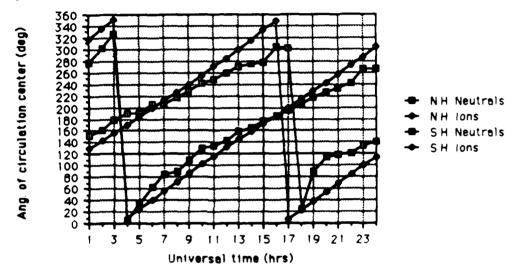
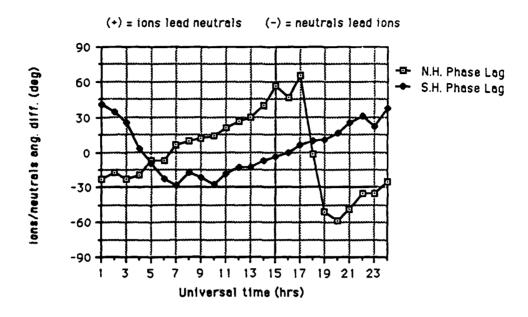
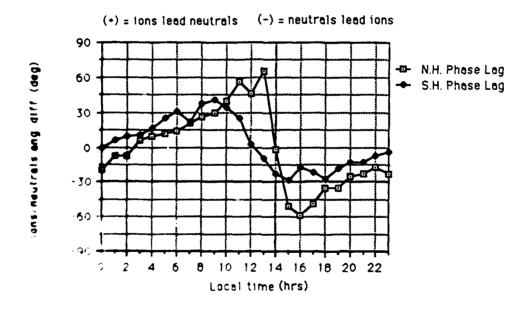


Figure 5.21 - The angular position of the center of the ion-convection and neutral wind-circulation pattern as a function of universal time for both hemispheres

circulation, the dawn-cell sunward circulation on the dayside, and the increased neutral-flow divergence on the nightside exit of the two-cell circulation provided the clearest indication for placement of the circle. The fit of this circle was surprisingly easy, but slightly subjective, although the exact same technique was used to fit each of the 48 neutral-wind-circulation patterns (24 for each hemisphere), making the data set self-consistent. This can be considered to be a less accurate technique than that used by Roble et al., but is better suited for application to averaged sets of measured neutral-wind data provided by DE-2 (Thayer et al., 1987; McCormac et al., 1987). However, the results of the two different techniques should not be quantitatively compared.

The angular location of the position of the centers of both the ion-convection and neutral-wind-circulation patterns, for both hemispheres and at all universal times, are shown in figure 5.21. The angle is measured in a counterclockwise direction starting from the noon-local-solar-time plane. The angular position of the geometric centers of the high-latitude ion-convection and neutral-circulation systems rarely coincided. Unexpectedly, the center of the neutral-circulation system was found to be ahead of the center of the ion-convection pattern for a portion of the day in both hemispheres. The phase difference between the ions and the neutrals can be examined in figure 5.22, where the data are presented as a function of either universal time or local-solar time of the invariant poles. In the summer southern hemisphere, the two-cell ion-drift pattern leads the neutral-circulation pattern for twelve hours of the day and by amounts of up to three However, when the center of the summer-southern-hemisphere neutralcirculation pattern moves from the local-noon through local-midnight hours, the center of the neutral-circulation pattern is ahead of the ion convection by up to two hours. In the winter northern hemisphere, the two-cell ion-drift pattern leads the neutral-circulation pattern for only eight hours a day, but by amounts which can exceed four hours. During the remaining hours of the day, the center of the neutral-circulation pattern leads the ions by up to four hours. From the phase-lag plot for both hemispheres as a function of local-





The phase lag or lead of the ion-convection pattern with respect to the Anti-creatation for both hemispheres as a function of universal time (top) the inversal time of the invariant-pole longitude (bottom). A positive value of the ions are leading the neutrals.

solar time, it can be seen that both hemispheres show the same trend, but the variations are larger in the winter northern hemisphere, presumably because the ionosphere is not as tightly-coupled to the thermosphere. It is also important to mention that the uncertainty in neutral-wind-circulation-pattern position is not the same for all data points shown in figures 5.21 and 5.22. It was more difficult to find the center of the neutral-circulation pattern accurately when the invariant pole was near local noon because the neutral-wind-circulation pattern is also offset in the antisunward direction. This means the separation of the center of the neutral circulation from the geographic pole was very small. This results in the appearance that the center of the northern-hemisphere neutral-circulation pattern covered over 80-degrees of angular distance in one hour (17 to 18 UT), as seen in figure 5.21. This angular-rotation rate seems to be too high, but this discrepancy could not be more accurately resolved using this technique.

The angular-phase differences between the centers of the ion-convection and the neutral-wind-circulation systems are subtle and not as dramatic as figure 5.22 might lead one to believe. When overlaying the 25-degree-radius ion-convection pattern and 30-degree-radius neutral-wind-circulation pattern, discussed in the previous section, it has been found that the ion-convection pattern remains inside the 30-degree-radius circle of the neutral-wind circulation. Furthermore, the duskside boundaries of the neutral-wind-circulation and ion-convection patterns are coincident. The large angular-phase difference between the centers of the ion-convection and neutral-wind systems is ascribed to the path the center of the neutral circulation takes. Since the neutral-circulation system has been extended over a larger area than the ion-driven system on the dawnside, the center of the neutral-circulation system, for this diurnally-reproducible model run, is displaced toward the dawnside as well. This helps to produce the large angular phase difference, in addition to the pressure-gradient force described above.

5.7 Summary

This chapter represents the fundamental first step in a comprehensive understanding of the solar-maximum December-solstice neutral-gas momentum-force analysis, since the full diurnal variation of forces influencing the neutral-gas dynamics was presented in a manner which allowed easy inter-comparison with all universal times and between hemispheres. The analysis of the diurnally-reproducible TGCM force balance has direct application to understanding the forces driving the neutral winds measured by DE-2. However, this diurnally-reproducible analysis represented IMF $B_y = 0$ conditions (i.e., symmetric ion-convection cells), but was most helpful in isolating "seasonal" and diurnal variations in the forces.

It was also noted that to truly isolate seasonal differences, a similar simulation corresponding to the June solstice must also be analyzed. In addition, there are several more diurnally-reproducible cases which could provide additional insight into thermospheric dynamics. These cases correspond to the four categories of satellite neutral-wind signatures cited in the next chapter; 1) $B_z < 0$, $B_y > 0$, 2) $B_z < 0$, $B_y < 0$, 3) $B_z > 0$, 4) $B_z >> 0$. The first two (B_z -southward) cases should be attempted almost immediately. The B_z -northward cases require the development and installation of a new more-capable ion-convection model in the NCAR-TGCM.

CHAPTER VI

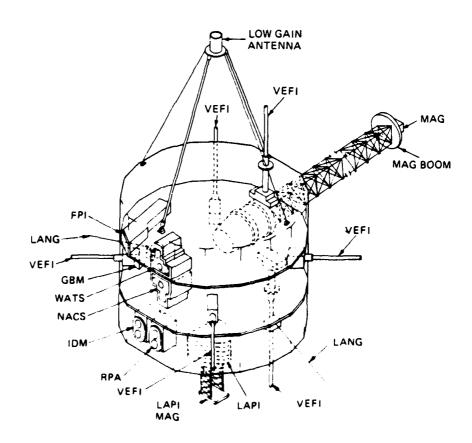
DYNAMICS EXPLORER-2 DATA ANALYSIS

6.1 Overview of the DE-2 Dataset

The Dynamics Explorer-2 (DE-2) neutral wind and supporting thermospheric/ionospheric dataset, used in this research, is the first global-scale database with coverage of both polar regions on the same orbit. To put the importance of this database in perspective, a brief review of the neutral-wind data available before the existence of this dataset is in order.

Measurements of thermospheric neutral winds and temperatures have been available from ground-based Fabry-Perot interferometers (GBFPIs) for almost two decades. A recent example, from a GBFPI in Alaska, is shown in figure 2.12. The first simultaneous determination of high-latitude neutral winds and ion drifts was reported by Nagy et al. (1974). The neutral winds were derived from GBFPI measurements and the ion drifts were deduced from incoherent-scatter radar measurements. This data has greatly enhanced our understanding of thermospheric processes including horizontal transport, because the neutral winds were seen to generally follow the motions of the ions at high latitudes.

One unavoidable consequence of ground-based remote sampling is that different local time planes are sampled at a fixed geographic latitude. The result is a fixed local time-to-universal-time relationship, due to the unique portion of either the ion-convection or neutral-wind-circulation pattern which is sampled. This occurs because the observing location rotates around the geographic pole in universal time and makes a



PRODUCES PARAMETER ASSOCIATE PRODUCES PRODUCES ACCORDE ANDIVINIA CARDONNE

Figure 6.1 - Schematic of the DE-2 spacecraft showing the placement and orientation of the various instruments.

circular track with respect to the ion-convection pattern (when plotted in invariant-geomagnetic coordinates), due to the antisunward offset of the entire ion-convection and neutral-wind-circulation pattern. Therefore, the morphology of ion convection or neutral winds, at a particular latitude and longitude, is not necessarily directly applicable to other local-time-to-universal-time relationships defined by a different latitude and/or longitude. Furthermore, the measurements apply only to that region of the atmosphere within the line-of-sight of the station and usually are limited to periods of darkness. Using only ground-based thermospheric neutral wind measurements from a sparsely-populated observation network, it is difficult to build a large-scale picture of neutral-wind transport within the thermosphere, although there are new attempts by the Coupling, Energetics, and Dynamics of Atmospheric Regions (CEDAR) program to do just that (Romick et al., 1987).

ACCUPATION RESISTANCE

During August 1981, when the NASA DE-2 satellite was launched, a "new" source of data from the thermosphere became available. The word "new" is used because DE-2 was the first satellite capable of determining vector neutral winds along the satellite track, providing a global slice of this neutral-wind data. In addition, DE-2 was launched into a true polar orbit which allowed it to sample conjugate regions of the thermosphere. Note that the definition of conjugate regions used in this work was given in section 1.3.

A stated purpose of the DE-2 mission was to study the coupling between the magnetosphere, ionosphere, and thermosphere (Hoffman and Schmerling, 1981). This coupling was expected to be greatest during solar maximum, which occurred during 1981—1982. For the above reasons, DE-2 has provided a dataset with more useful information on polar-thermospheric neutral-gas dynamics than any previous satellite mission. For example, the last previous major NASA thermospheric satellite which was launched into a polar orbit was Atmosphere Explorer (AE-D) during late 1976. This mission was flown during solar minimum rather than solar maximum and did not have the capability of measuring vector neutral winds.

To review briefly the success of the DE-2 mission, some of the many research studies published over the past five years using DE-2 neutral-wind data are listed below. For instance, neutral-wind vectors from DE-2 have been found to be well suited for collecting global-climatological data (Killeen et al., 1986) and morphological studies (Hays et al., 1984; Killeen et al., 1982, 1983). Comparison of DE-2 neutral-wind data with general-circulation models was done by Emery et al. (1985), Killeen and Roble (1984), Roble et al. (1983, 1984), and Rees et al. (1983). Some other studies, using DE-2 neutral-wind data, included coordination of observations between GBFPI and DE-2 neutral-winds (Killeen et al., 1984a), ion-neutral coupling (Killeen et al., 1984b), neutral-parcel transport (Killeen and Roble, 1985), and neutral-wind signatures under various interplanetary-magnetic-field (IMF) conditions (Killeen et al., 1985; McCormac et al., 1985).

Given the maturity of the DE-2 data-processing effort and the latitude sampling of the satellite, it is now possible to conduct a global study which would examine slices of DE-2 data, including thermospheric winds and temperatures, over an entire orbit, with coverage in both hemispheres. This novel database was envisioned as consisting of multi-instrument two-piece datasets; the first which could essentially be considered as a "snapshot" of the polar thermosphere along the track of the satellite in one hemisphere followed by another "snapshot" in the opposite hemisphere. To the author's knowledge, this is the first dataset of its kind. These "snapshots" would be separated only by the time it took the DE-2 satellite to travel to the opposite pole, which was 50 minutes from pole to pole. This is the best that can be done with a single satellite attempting to measure data in both polar regions. The satellite transit time of 50 m nutes can be considered relatively short compared to the ion-neutral momentum-coupling time constant, \(\tau\), (equation 6.1) which ranges from several tens of minutes to several hours, depending on the ion density (Baron and Wand, 1983). The ion-neutral momentum-coupling time constant is an estimate of the time required for the neutral gas to approach the ion-drift velocity

following an instantaneous ion-drift velocity change (Killeen et al., 1984b). Ion drag is often considered to be the primary momentum source near and inside the polar cap, although the diurnally-reproducible model results in chapter V have shown this not to true near the invariant poles. However, the ion-neutral momentum-coupling time constant, shown below (from Killeen et al., 1984b), is still a useful approximation.

$$\tau = 1 / v_{ni} = n_n / (n_i v_{in})$$
 (6.1)

where n is the number density (#/cm³), the subscripts n and i represent the neutral and ionic species respectively, V_{in} represents the neutral-ion collision frequency (collisions/sec), and V_{ni} is the ion-neutral collision frequency (collisions/sec). The neutral-ion collision frequency is the sum of the O⁺ - O and the O⁺ - N₂ collision frequencies, which are given by Schunk and Nagy (1980).

With a multi-instrument dataset, such as described above, there are many new things to look for, since comparison of thermospheric parameters in conjugate regions of both hemispheres, on the same orbit, has never been previously attempted. One example is the influence of the IMF on the high-latitude ion-convection pattern in opposite hemispheres, as seen through the neutral winds. In addition, the "seasonal" differences between thermospheric parameters measured on the same orbit are of interest. Furthermore, there has been no global-scale thermospheric-neutral-wind data available with which to verify the thermospheric-general-circulation models (TGCMs). This is why few realistic, three-dimensional, time-dependent (3DTD) TGCM simulations have been attempted, until now. With data to initialize and verify the performance of a GCM, the time response of global-thermospheric winds to substorms is also of interest.

With the above studies in mind, an initial estimate of possible DE-2 orbits which might provide coverage of both hemispheres was conducted. The maximum number of orbits was estimated at less than 100 orbits for the following reasons:

- (a) Of the entire 18-month mission of DE-2, only during the last three months was the satellite orbit low enough to make in-situ measurements over the entire orbit.
- (b) Only during a fraction of the total possible orbits per day (more than 14) were the instruments on long enough to cover both poles. These orbits will be referred to as "long" orbits.
- (c) During some of the potential "long" orbits, the DE-2 Fabry-Perot Interferometer was not configured to provide meridional neutral winds from the 630.0 nm O I emission, but was instead collecting data from other emissions.

The local-time-plane coverage of the orbit range considered, orbits 7073 through 8273, is shown in figure 6.2. The orbits which eventually provided coverage of both hemispheres are listed chronologically in appendix B. Coverage by some orbits is better than others, therefore some comments are included.

Macacan account with the district Kindson

TOTAL COMMISSION OF THE PROPERTY OF THE PROPER

To investigate the influence of the IMF on the thermosphere, through the coupled magnetosphere/ionosphere/thermosphere system, measurements of the IMF must exist. Unfortunately, for some orbits listed near the end of appendix B the IMF data is missing. This is because the IMF data was normally supplied by two satellites, the International Sun-Earth Explorer-3 (ISEE-3) and the Interplanetary Monitoring Platform-8 (IMP-8). However, from the end of December 1982 through the rest of this solution period, ISEE-3 was inside the Earth's magnetosphere (figure 6.3). This resulted ir data from ISEE-3 which is not representative of true IMF conditions. Unfortunately, the remaining IMF data from IMP-8, supplied by the National Space Science Data Center (NSSDC), is less than complete.

The data which constitutes this unique dataset was compiled from six instruments on the DE-2 satellite. A brief description of these instruments and their measurement uncertainties is provided in the next section.

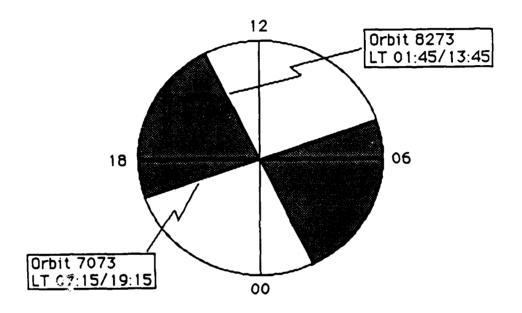


Figure 6.2 - Diagram of the local-time-plane coverage (shaded) of the DE-2 orbits which provided coverage of both hemispheres on the same orbit.

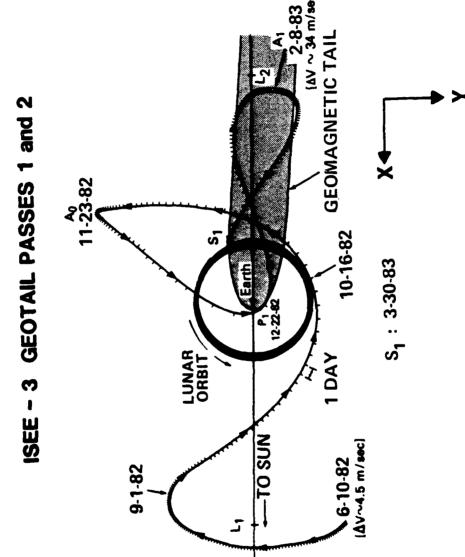


Figure 6.3 - Diagram of the orbital path of the ISEE-3 satellite during 1982 and early 1983 (Slavin et al., 1986).

6.2 The DE-2 Spacecraft Instrumentation

6.2.1 The DE-FPI Instrument

THE PARTY OF THE P

The DE-2 Fabry-Perot Interferometer (DE-FPI) was the first space-based interferometer to remotely sense the neutral winds in the Earth's thermosphere. The DE-FPI provided altitude profiles of the meridional neutral-wind component, determined from the Doppler shift of the 630.0 nm O(¹D) emission, below the spacecraft altitude (Killeen et al., 1982; Hays et al., 1981). Since little altitude structure was seen in the wind field, the meridional winds over the altitude region sampled were averaged to provide a mean upper-thermospheric meridional neutral-wind component (Killeen et al., 1982).

The DE-FPI was not as sensitive to errors in spacecraft attitude information as other DE-2 instruments, such as the DE-WATS and DE-IDM. The typical statistical uncertainty for DE-FPI measurements was ± 30 m/s (Killeen et al., 1982), which was based on the statistics of individual photon-counting observations (Hayes et al., 1981). Estimates of the DE-FPI measurement uncertainty, for daytime measurements with optimum photon-counting statistics, were ± 15 m/s.

6.2.2 The DE-WATS Instrument

The DE-2 Wind and Temperature Spectrometer (DE-WATS) provided in-situ measurements of the zonal and vertical components of the neutral wind, by measuring the arrival angle of a beam of neutral atoms entering the aperture of a quadropole mass spectrometer using the baffle technique (Spencer et al., 1981). Since the incoming stream was modulated by an oscillating baffle, knowledge of the baffle position was also necessary to determine the angle of the incoming stream precisely. The DE-WATS instrument also supplied the neutral temperatures used in this research.

The DE-WATS instrument had a typical statistical uncertainty in its measurement of the neutral-wind components of less than 10 m/s (Killeen et al., 1982),

once it had been determined that the DE-2 attitude was generally known to better than +1 of a degree. The neutral-temperature measurement uncertainty was $\sim 5\%$ K. Spencer et al., 1981).

6.2.3 The DE-RPA Instrument

The DE-2 Retarding Potential Analyzer DE-RPA furnished the meridional component of the ion-drift velocity and ion temperature. The DE-RPA measured currents caused by ions striking a single collector at the back of the instrument. The measurement parameters were derived from a least-squares fitting technique by finding the mean energy separation between ions of different mass and comparing this to the energy expected from just the spacecraft velocity itself (Hanson et al., 1981).

The errors in the DE-RPA temperature measurements were less than 2%, based on experience with previous RPA devices (Hanson et al., 1973). However, knowledge of the spacecraft velocity and attitude were critical to achieve an uncertainty in the meridional component of the ion-drift velocity of less than 50 m/s (St. Maurice and Hanson, 1984).

6.2.4 The DE-IDM Instrument

The DE-2 Ion Drift Meter (DE-IDM) produced the zonal and vertical components of the ion-drift velocity (Heelis et al., 1981). The DE-IDM is similar to the DE-RPA in operation, except it has four sectional collectors at the back of the instrument. The DE-IDM requires the total ion-drift velocity, measured by the DE-RPA, and then determines the remaining velocity components by analyzing the ratio of the currents at the different collector plates. The currents at the four collector plates were not the same unless the ion drifts were exactly normal to the face of the instrument. The uncertainty in DE-IDM measurements were \pm 10 m/s (Heelis et al., 1981), since knowledge of the spacecraft attitude was better than 0.1 degrees.

625 The DE-NACS Instrument

The DE-2 Neutral Atmosphere Composition Spectrometer (DE-NACS) was a quadropole mass spectrometer which measured the abundances of molecular nitrogen and atomic oxygen, as well as trace neutral constituents, such as helium and argon Carignan et al., 1981). The DE-NACS instrument had an absolute uncertainty of \pm 15% in its measurements, with a relative uncertainty between measured species of \pm 5% Carignan et al., 1981). Final monthly NACS data calibration values for the entire DE-2 mission became available during late 1986 (A. E. Hedin, private communication ,1986).

6.2.6 The DE-LANG Instrument

The DE-2 Langmuir probe (DE-LANG) supplied the electron densities and temperatures (Krehbiel et al., 1981). The DE-LANG operated by measuring the probe current, resulting from attracted charged particles, as the applied voltage was swept from negative to positive. Typical errors in the density and temperature measurements, when N_e exceeded 10³ cm⁻³ and T_e exceeded 1000⁰ K were less than 5% (Brace et al., 1973).

6.3 Individual-Orbit Dual-Hemisphere DE-2 Datasets for Different IMF Configurations6.3.1 General Observations

Of the 67 orbits which actually supplied neutral-wind data in the high-latitude regions of both hemispheres, 57 orbits also had ion and other supporting data. From this dataset, several orbits of data were chosen to represent the different categories of neutral-wind signatures in both hemispheres, according to the prevailing IMF configuration before and at the time of the orbit. As shown in chapter III, individual orbits of DE-2 neutral winds in the northern hemisphere have previously been shown to correlate well with the sign of IMF B_y, for southward-IMF conditions (McCormac et al., 1985). In addition, northern-hemisphere DE-2 neutral winds have been compared under IMF B_z northward (positive) and southward (negative) conditions (Killeen et al., 1985).

AD-0188 858		UPP	UPPER-THERMOSPHERIC OBSERVATIONS AND NEUTRAL-GAS DYMANICS AT HIGH LATITUD. (U) AIR FORCE INST OF TECH HRIGHT-PATTERSON AFB OH C R TSCHAN 1987 AFIT/CI/NR-87-1350 F/G 4/1								TECH	3/4	
UNCLA	SIFIE	ĀFI	T/CI/	W-87-	1350		, K 130	-INN 4.		F/G	4/1	ML	
							*						
	~					: :	= :	#: :≢		.» II.	ii - ii		22°
iz īr		18	15			25	49						



And I was a second of the seco

The neutral-wind signatures fit best into four categories. They are: B_y positive and B_z negative, B_y negative and B_z negative, B_z slightly positive, and B_z much greater than zero. The third category, B_z slightly positive, is new and may represent a transient neutral-circulation state because a survey of existing IMF data during the DE-2 lifetime indicated no prolonged period when B_z remained slightly positive. The multi-instrument data sets for these four categories are shown in figures 6.5 through 6.8.

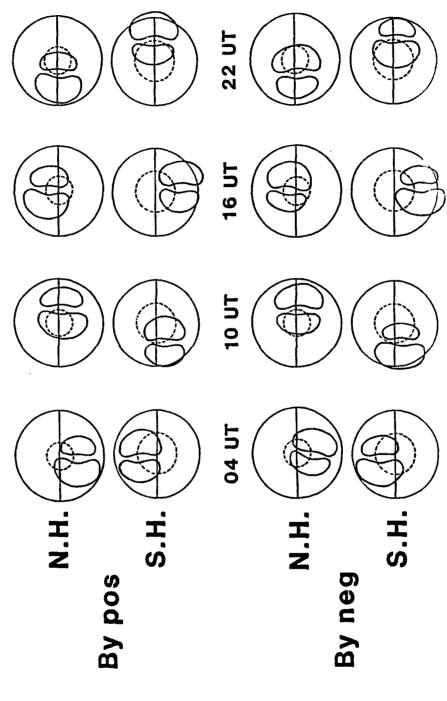
Before viewing these figures several conventions should be explained. The preferred coordinate system for this work is geographic latitude and longitude. Staying in this coordinate system has several advantages. First, the effects of rotation of the displaced-geomagnetic poles around the geographic poles will be important in understanding the universal-time variations of the antisunward neutral-wind signatures. Also, numerical models of the thermosphere, such as the National Center for Atmospheric Research (NCAR)-TGCM, use geographic coordinates. Next, the DE-2 spacecraft flew in a solar-inertial polar orbit. This means that plots of the satellite track in geographic coordinates will be a straight line, which is easier to visualize.

The rotation of the invariant-geomagnetic pole around the geographic pole with universal time had an important effect on the neutral winds sampled by the DE-2 spacecraft, because the ion-convection pattern generally followed the position of the invariant-geomagnetic pole, with a slight offset of three to five degrees toward midnight (Roble et al., 1987b). The ion convection was driven by both the dawn-to-dusk-directed convection-electric field mapping directly from the open field lines at the magnetopause-merging points and dusk-to-dawn-directed electric fields, which map along closed-field lines, from the equatorial magnetosphere. Since both sets of electric fields map along magnetic-field lines, which were assumed to have arbitrarily high conductivity, it was reasonable to expect the ion-convection pattern and the electric fields which drive them to translate, with the position of the invariant pole, through the neutral thermosphere with a period of 24 hours.

Since the DE-2 spacecraft was in a polar orbit and the ion-convection pattern moves with the invariant pole as it rotated around the geographic pole, the satellite sampled different slices of the ion-convection pattern every orbit. This can be visualized in figure 6.4 for both IMF By positive and By negative cases, when Bz was negative. Due to oppositely-displaced geomagnetic poles, the satellite track, indicated by a horizontal line in the dawn-dusk local-time plane, passed through the dayside cusp of the two-cell pattern in one hemisphere and the midnight sector in the other, at the universal times of 04 and 16 UT. Only at certain times, approximately 10 and 22 UT, did the satellite track pass through similar or conjugate regions in both hemispheres. Furthermore, the geometry was most favorable for conjugate measurements in both hemispheres when the DE-2 satellite orbit was situated near the 0600/1800 local time plane. This meant that orbits in the 0600/1800 local-time plane and within one hour of 10 or 22 UT had special importance for conjugacy studies.

Figures 6.5 through 6.8 fall into this category and are presented, explained, and analyzed below. There are two sets of data to every figure. The northern hemisphere data is plotted at the top, the southern hemisphere is on the bottom. The large rectangular plot represents the DE-2 data, with all the scales on the right-hand-side. Information regarding time and location of the spacecraft are indicated along the bottom of each rectangular plot. Every plot displays as much data as was available, from 40 degrees latitude through the corresponding geographic pole and back to 40 degrees latitude. This places the position of the geographic pole close to the center of each of the large rectangular plots. The plots are arranged so that the duskside is always to the left and the dawnside is on the right-hand-side, with the sun at the top of each plot, in both hemispheres. This means that the data is plotted with universal time increasing from left to right in the southern hemisphere and from right to left in the northern hemisphere. In all rectangular plots, the sunward direction is toward the top of the paper. This was done so that comparisons between the two hemispheres could be accomplished most easily. The

Model ion convection pattern positions



polar-orbiting satellite, such as DE-2, for various selected universal times and under different IMF ${\bf B_y}$ configurations, when the satellite orbital plane is aligned with the Figure 6.4 - Schematic of the high-latitude ion-convection-pattern sampling done by a 0600/1800 local-time plane.

derived parameters on the large rectangular plots are the ion-drag force, Coriolis force, the ion-to-neutral momentum-coupling time constant, and the neutral and plasma scale heights.

To the top left of each large rectangular plot is a polar-geographic projection with the neutral winds plotted, as viewed from above the northern hemisphere. In both the polar and large rectangular plots, corotation velocities have been removed from both the ion-drift and neutral-wind velocities. Local times are plotted around the outside of the dial. Also, the position of the day-to-night terminator is indicated by a hashed line and the position of the invariant-geomagnetic pole is shown by a "+". The southern hemisphere plot is projected up onto the northern hemisphere, for ease of comparison of the neutral winds, between hemispheres. Viewed in this way, one can visualize the relative positions of the satellite track with respect to the terminator, and the meridional shift of the neutral-wind signatures with respect to the geographic pole, as universal time progresses, and with respect to the invariant-geomagnetic pole, in response to IMF By variations.

Also to the left of each of the large rectangular plots, is a smaller rectangular plot displaying the time history of selected geophysical parameters, at the time of the DE measurements and for the previous 23 hours. At the top of this plot, the auroral electrojet index is shown. The auroral-electrojet index is a measure of the average horizontal electrojet activity (currents) as indicated by perturbations in the H component (in the local-magnetic meridian plane) of the geomagnetic field in the auroral zone, measured at several ground stations (Rostoker, 1972). The scale, on the right hand side, varies from 0 to 1500 nT. The values plotted are three-minute averages. Next, hourly-averages of overall geomagnetic activity are shown using the linear K_p index. The scale, shown on the left-hand-side, varies from 0 to 10, although the index only goes up to 9. Finally, the magnitude of the three components of the IMF; B_x , B_y , and B_z ; in geocentric-solar-magnetic (GSM) coordinates, are shown.

Slavin et al. (1986) noted that the solar maximum portion of solar-cycle 21, as measured by the solar flux, was stronger than the previous solar maximum for which satellite IMF data is available. Another finding was that the maximum IMF | Btotal | lagged behind the solar flux maximum by over a year. The maximum | B_{total} | occurred at the same time as the DE-2 period of interest, late 1982 and early 1983. This implies that the range of IMF fluctuations, including those of B_z , were greater during this period than any time since satellite IMF measurements have been available. Therefore, this study may encompass a period when the IMF-magnetosphere-ionosphere-thermosphere system was very highly-coupled. This would be a fortunate coincidence, but would also imply that higher values of the ion-neutral momentum-transfer time constant might apply to other, less active solar-maximum periods. Additionally, the higher coupling from the IMF to the ionosphere during solar-cycle 21 might also explain why elevated cross-cap potentials, in excess of 200 kV, were required in chapter VII to duplicate ion-drift velocities. Typical published ranges of observed cross-cap potentials during solar minimum are 23 to 140 kV (Heppner, 1977) and other estimates, such as those of Stern (1977), present more conservative cross-cap potential ranges (i.e., 44 to 76 kV) then Heppner.

6.3.2 The Four-Characteristic Neutral-Wind Signatures

Four-basic neutral-wind signature groups have been identified and categorized, according to the orientation and magnitude of the IMF. For the categories displayed, only orbits occurring at conjugate-sampling universal times were selected, greatly restricting the number of available orbits of data. For the southward-IMF cases, several orbits were available to choose from and the best (i.e., most representative) orbits were selected. For the northward-IMF cases, only one or two orbits fit the selection criteria, so the orbits selected are not the best, but the only ones available. More data will be required to see if these orbits are truly representative of the IMF categories shown for solar-

maximum December-solstice conditions. A description of the neutral-gas circulation for each of these categories is described below.

For all B_z < 0 conditions, there is a two-cell structure seen in the neutral circulation in both hemispheres with a well-established dusk cell and a weaker dawn cell. Under B_z < 0, B_y > 0 IMF conditions (figure 6.5), the maximum antisunward neutral winds are clearly located on the dawnside of the polar-cap flow in the northern hemisphere and on the duskside of the polar-cap flow in the southern hemisphere. There is a small velocity decrease near the center of the antisunward flow in both hemispheres and the comparison of the polar-cap neutral winds between hemispheres shows an asymmetric mirroring of neutral flow between hemispheres. The data shown in figure 6.5 correspond to moderate levels of K_p and the dusk reversals are larger in magnitude and latitudinal extent than the dawnside reversals.

For $B_z < 0$, $B_y < 0$ IMF conditions (figure 6.6), the maximum antisunward neutral winds are now located on the duskside of the polar-cap flow in the northern hemisphere and on the dawnside of the polar-cap flow in the southern hemisphere, although this hemispheric asymmetry is not as clearly pronounced as in the $B_z < 0$, $B_y > 0$ case. This case corresponds to low levels of K_p . The velocity decrease in the center of the polar-cap flow is only recognizable in the northern hemisphere. It can be seen that the dawnside reversals are non-existent in the southern hemisphere and are just barely noticeable in the northern hemisphere. The duskside reversals are even more prominent than for the $B_z < 0$, $B_y > 0$ case.

For $B_z > 0$ conditions, a transitory neutral-wind state exists, where the neutral wind signatures are quite different in opposite hemispheres (figure 6.7). In the winter northern hemisphere, the antisunward neutral-wind speeds are diminished across much of the center of the polar cap. The northern-hemisphere neutral winds appear to presage a change to sunward flow in the center of the polar cap. However, in the summer southern hemisphere, the neutral circulation retains the two-cell circulation structure with the

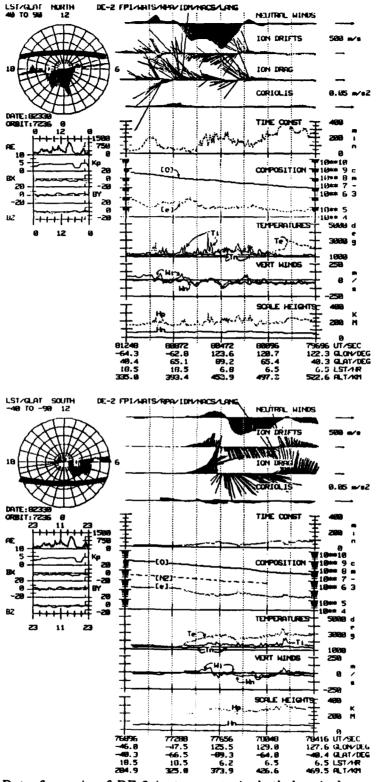


Figure 6.5 - Data from six of DE-2 instruments in both hemispheres, as well as derived quantities and neutral-gas momentum-forcing terms, representative of $B_z < 0$, $B_y > 0$ conditions.

UE-2 FPI/MAIS/RPA/IDH/NACS/LANG

LST/GLAT NORTH 40 TO 90 12

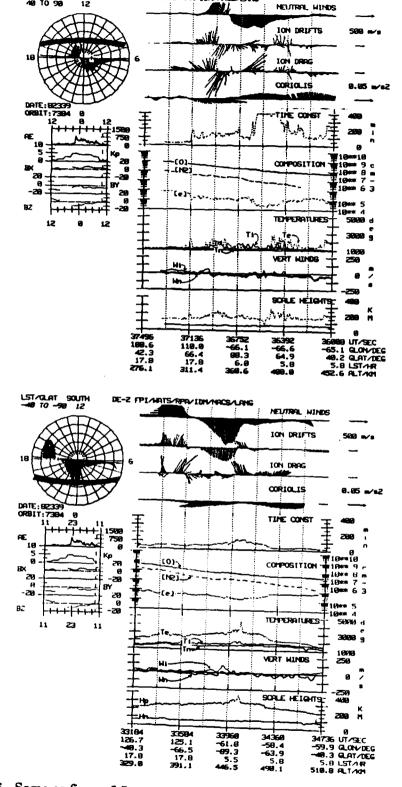
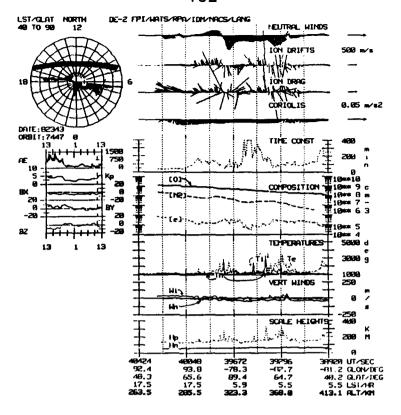


Figure 6.6 - Same as figure 6.5, except representiative of $B_z < 0$, $B_y < 0$ conditions.



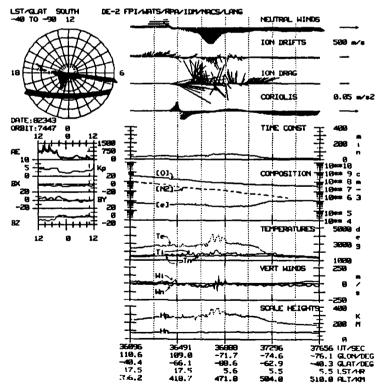
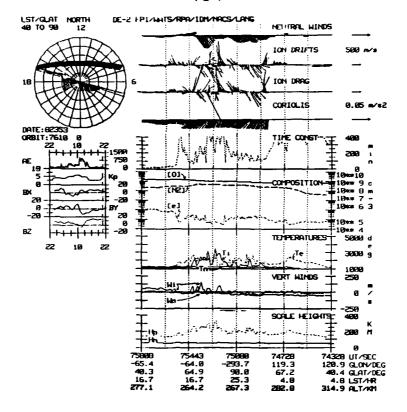


Figure 6.7 - Same as figure 6.5, except for $\rm B_{\rm z} > 0$ conditions.

maximum antisunward neutral winds located in the center of the polar cap. The sunward-reversal flow on the duskside is much weaker in the winter northern hemisphere, and there is virtually no sunward flow on the dawnside in either hemisphere (a very small dawnside sunward reversal exists in the northern hemisphere).

For the IMF $B_z >> 0$ case, a selection to present here was difficult to find. There were only two candidate (stable $B_z >> 0$) periods during the three months when DE-2 neutral-wind data were available in both hemispheres. One $B_z >> 0$ period occurred on November 24, 1982. This is the period which is studied in detail in chapter VII. Unfortunately, there were multicell neutral winds in both the northern (figure 7.11) and southern (figure 7.12) hemispheres, but there were no orbits with coverage of both hemispheres, during the $B_z >> 0$ period. The best example, during this period, provided northern-hemisphere multicell neutral winds on one orbit (7213) and southern-hemisphere multicell neutral winds on the next orbit (7214). This resulted in neutral-wind measurements in both hemispheres which were separated by more than two hours, clearly more than one ion-neutral momentum-coupling time constant for the summer southern hemisphere. The second $B_z >> 0$ period occurred on December 19, 1982. Here, several orbits of $B_z >> 0$ neutral-wind data were obtained and one orbit of data, shown in figure 6.8, not only corresponded to the universal-time range for conjugate region sampling in both hemispheres, but also provided neutral winds in both hemispheres.

For $B_z >> 0$ IMF conditions (figure 6.8), the neutral winds in the southern hemisphere exhibit multicell structure. The northern-hemisphere neutral winds appear to be turning sunward but there is no sunward flow in center of the polar cap. However, the sunward flow is clearly visible in southern-hemisphere data. Also, by late December 1982, the plane of the satellite orbit shown in the polar-dial plot (figure 6.8), had precessed away from the 0600/1800 local-time plane which is desirable for conjugate sampling in both hemispheres. Therefore, the satellite orbit was not in the optimum local-time plane



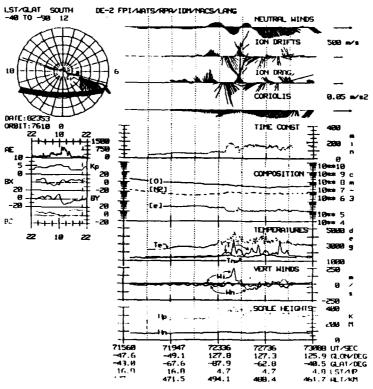


Figure 6.8 - Same as figure 6.5, except for $B_{\mbox{\scriptsize z}} >> 0$ conditions.

for observing the small sunward-return flow section of the neutral-wind-circulation system. However, the existence of lower electron/ion densities, and hence lower ion-neutral momentum exchange, in the winter-northern-hemisphere sunward-ion-convection region, is a more likely reason that the sunward neutral winds were not seen in the northern-hemisphere polar cap.

6.3.3 DE-2 Ion-Drift Data

Figures 6.5 through 6.8 show ion-drift vectors which correspond to the four-characteristic groups of neutral-wind data discussed in the previous section. In general, the figures show that the ion convection was more organized in the summer southern hemisphere than in the winter northern hemisphere, with irregularities and fine structure in the ion drifts more noticeable for the B_z -northward cases, than the B_z -southward cases. The irregularities in the ion convection apply to both the antisunward and sunward return drifts.

It can be seen that the ion drifts, under $B_z < 0$ conditions (figures 6.5 and 6.6), had a tendency to point away from the noon-madnight local-time plane. For $B_z > 0$ IMF conditions (figure 6.7), the sunward ion convection is generally weak in both hemispheres. For the $B_z >> 0$ conditions, the sunward ion convection is stronger, but it is still relatively weak compared to the antisunward ion convection in the center of the polar cap that dominates under $B_z < 0$ conditions.

6.3.4 Neutral-Gas Momentum Forces Derived From DE-2 Data

Only two neutral-gas vector forces can be calculated along the track of the satellite, with the data provided. These forces are the ion-drag force and the Coriolis force, which are shown in figure 6.5 through 6.8. Some of the reasons why the other forces cannot be determined are outlined below.

The component of the pressure-gradient force along the track of the satellite can be calculated in principle, but the satellite is unlikely to be orbiting in the direction of the maximum pressure gradient. Furthermore, test computations of the polar-cap pressure gradient along the track of the satellite were extremely noisy. Outside the polar cap, the along-the-track pressure gradient was dominated by the vertical component of the satellite motion, which has not been removed successfully. To evaluate the horizontal-momentum-advection term requires knowledge of the horizontal-velocity field in a cross-satellite-track direction. This is not known. Finally, evaluation of the viscous-drag term requires knowledge of the second derivative with respect to altitude (i.e., information above and below the satellite), which also is not known.

The ion-drag force inside the polar cap gives a quick indication of whether the ion or neutral-wind velocities are greater. For example, in the $B_z < 0$, $B_y > 0$ case, the southern-hemisphere data shows the ion-drag force to be oriented in the same basic direction as the ion drifts. This means that the ion drifts exceed the neutral winds and that therefore, the ions are a momentum source for the neutral gas. However, in the northern hemisphere, the ion-drag force has a sunward component even though both the ions and the neutrals are moving in an antisunward direction. This is ascribed to neutral-wind velocities that are greater than the ion-drift velocities, so that the ion-drag force works against the neutral gas in an attempt to slow it down. Since the sunward ion drifts are generally larger than the sunward neutral-wind reversals, the ion-drag force in these regions is normally directed sunward, on both the dawn and dusk sides of the ion-convection system and in both hemispheres.

For the $B_z < 0$, $B_y < 0$ case, the reverse of the $B_z < 0$, $B_y > 0$ case is true. The northern-hemisphere ion-drag force is a direct reflection of the ion drifts. However, in the southern hemisphere, the ion-drag force has sunward-directed components inside the polar cap. The ion-drag force in the sunward-ion-convection regions is also directed sunward for this case in both hemispheres and on both sides of the polar cap. Based on the

limited sample provided by the DE-2 dataset, the ion-drag signature along a dawn/dusk satellite track appears to be influenced by the sign of the IMF B_y component. That is, when the ion convection is indicative of IMF $B_z < 0$, $B_y > 0$ conditions, the southern-hemisphere ion-drag force directly reflects the ion drifts in that hemisphere, while the ion-drag force in the northern hemisphere does not show a resemblance to the ion convection. For IMF $B_z < 0$, $B_y < 0$ conditions, the observations are similar, but the hemisphere in which the ion-drag force directly reflects the ion drifts has reversed. These observations are probably not completely symptomatic of the IMF category, meaning that while no exceptions to these observations have been noted yet, they will undoubtedly be found.

For the transitory $B_z>0$ case, the ion-drag force also has different signatures, when comparing the summer and winter hemispheres. In the winter northern hemisphere, the ions are convecting in an ill-defined multicell pattern with sufficient drift velocity that the ion-drag force is in the same direction as the ion drifts. However, in the southern hemisphere, it can be speculated that the "neutral-wind flywheel" may be affecting the ion drifts (Lyons et al., 1985) and hence the ion-drag force. Figure 6.7 shows that the electron density is an order of magnitude higher in the summer-hemisphere polar cap than in the winter hemisphere. With higher electron densities come higher ion-neutral collision frequencies, which might contribute to a feedback system where the neutrals drag the ions along. Under these conditions, the weak $B_z>0$ electric field may not be strong enough to resist the motion of the southern-hemisphere neutrals. The result is a confused, but mainly sunward-directed ion-drag force in the summer-southern-hemisphere polar cap.

The $B_z >> 0$ case is much simpler. Only when these IMF conditions are stable for several hours do they provide the proper conditions for the neutral gas to follow the ion drifts. As a result, the morphology of the ion-drag force is a direct reflection of the morphology of the ion drifts in both hemispheres.

6.3.5 The Ion-Neutral Momentum-Coupling Time Constants

As discussed in chapter III, the ions move in response to the high-latitude convection-electric field, continually colliding with neutral gas particles. If the highlatitude electric fields are slowly-varying, then after one e-folding time scale for ion-toneutral momentum transfer (equation 6.1), the neutral gas should have gained enough momentum to change it from the velocity it had previously had. The new velocity, to a first order approximation, is along the direction of the mean ion drift during the efolding time period. The neutrals should therefore display a similar signature to that of the ions. This is indeed what has been found previously (Killeen et al, 1982), and is also what is seen here in both hemispheres (figures 6.5 - 6.8). In most cases, the similarities between the ion and neutral vectors are greater in the summer southern hemisphere. This is because the ion-neutral momentum-coupling time constant is lower in the sunlit summer hemisphere (table 6.1), due to higher ion densities and increased ion-neutral collisional interactions. It should also be noted that the time constant has a nonlinear dependence on altitude, due to the collision-frequency term in the denominator and neutral densities which vary exponentially in the numerator. Further, the satellite was not at the same altitudes for both the northern and southern hemisphere and the altitudes varied between orbits. Therefore, the purpose of table 6.1 is to show only that the mean time constant is shorter in the sunlit summer hemisphere.

Orbit	IMF	Кp	Winter Northern Time const (min)	-	Summer Souther Time const (min)	•
7236	$B_z < 0, B_y > 0$	3.3	157	445	49	374
7384	$B_z < 0, B_y < 0$	0.7	206	362	60	437
7447	$B_z > 0$	4.3	135	329	40	457
7610	B _z >> 0	4.7	269	277	130	476

Table 6.1 - Mean ion-neutral momentum-transfer time constants in both hemispheres by IMF category with selected geophysical parameters. Calculation of the time constant assumes ion drag is the primary momentum source for the neutrals.

The computed ion-neutral momentum-coupling time constants, shown above, are reasonable for periods of small or moderate changes in the ion-drift velocity. However, the onset of large geomagnetic storms, such as seen in the DE-2 data following a stable B_z >> 0 period in chapter VII, show that large increases in the neutral-wind velocity can occur in a period shorter than the calculated time constant. In the northern hemisphere, the polar-cap neutral winds are seen to be significantly stronger in figure 7.12 over those of three hours earlier (figure 7.11). During that three-hour period the ion-neutral momentum-coupling time constant was similar to that shown for the northern hemisphere in figure 6.8 (i.e., approximately four hours). However, figure 7.1 shows that the IMF B_z component began to turn sharply southward at 1100 UT, which is only one and a half hours before the neutral winds in the northern hemisphere of figure 7.12 were measured. This observation seems to be true mainly when the ion-drift velocities increase significantly in a very short period of time, so that the original momentum source associated with pre-storm ion drifts appears small by comparison.

6.3.6 Supporting DE-2 Data

In addition to the data and derived quantities described above, composition, temperature, and vertical-motion data are also presented in figures 6.5 through 6.8. The neutral-gas number densities in both hemispheres generally decrease from dusk to dawn because the satellite orbit was near apogee on the dawnside of the Earth for this period. The electron densities in the sunlit summer southern hemisphere usually show a slight dip inside the polar cap, probably due the lack of particle precipitation in the appropriate energy ranges and increased recombination rates at higher temperatures. In the winter northern hemisphere, the spatial variation of the electron densities is much more complicated and highly-structured. The nightside electron densities, away from auroral processes, are very low. The structure of the polar-cap electron density is the

result of a combination of horizontal and vertical transport, uneven ionization decay, and temporal/spatial variation in auroral processes.

The electron, ion and neutral gas temperatures are also shown. The three temperatures have similar values far from the high-latitude processes. However, inside the summer-hemisphere polar cap, the electron temperature is generally about 1000^0 higher than the neutral-gas temperature. The ion temperature generally has features like the electron temperature, but is only a few hundred degrees warmer than the neutral-gas temperature. The minimum neutral temperature in the summer polar cap is approximately 1500^0 K. In the winter hemisphere, the minimum neutral temperature is about 1100^0 K. The ion and electron temperatures have similar minimum temperatures, perhaps a few hundred degrees warmer.

The composition and temperature data were used to calculate both the ion-neutral momentum-coupling time constant and the ion-drag force. The vertical neutral and ion motion, as well as the neutral and plasma scale height values were not required for analysis in this thesis, although they are interesting. They were included in these figures only for completeness, since they were readily available.

6.4 Observations of Similarities and Differences in the High-Latitude Neutral-Wind Systems of Opposite Hemispheres

6.4.1 Width of the Polar-Cap Antisunward Neutral Flow

Using individual orbits of DE-2 neutral winds, such as were shown in section 6.3.2, an observation often made at the conjugate-sampling times of 10 and 22 UT was that the polar-cap neutral flow was wider in the northern hemisphere. Specifically, the width of the antisunward winds in the northern hemisphere was measured to be more than 30-degrees (of geographic latitude) wide, while in the southern hemisphere the width of the polar-cap flow was only 25-degrees wide (figure 6.5). This hemispheric asymmetry was initially unexpected, but was discovered to be due to the differences in the geomagnetic-field topology between hemispheres. The non-dipolar terms are more

significant in the northern hemisphere than in the southern hemisphere. To demonstrate this, figure 6.9 is presented with the neutral-wind data from figure 6.5. In addition, a selected geomagnetic-latitude line was also drawn on figure 6.9. In the northern hemisphere, the lines of geomagnetic latitude are elongated, along the 90 degrees east to 90 degrees west geographic-longitude direction, by about six-degrees of geographic latitude over the other direction. In the elongated direction, 30-degrees of geomagnetic latitude corresponds to 36-degrees of geographic latitude. This effect is maximum during the time ranges for sampling conjugate regions in both hemispheres, so a greater width of antisunward flow can be expected in the northern hemisphere, when measured in geographic coordinates. In general, the conjugate orbits in the dual-hemisphere database had polar-cap flow of two to six degrees wider in the northern hemisphere than in the southern hemisphere. The differences in the width of the polar-cap antisunward neutral winds between hemispheres is a naturally-occurring phenomena, caused by differences in the magnetic-field topology, which are not currently incorporated into ion-convection models or the TGCMs, but should be.

6.4.2 The Influence of IMF-Controlled Ion Convection on Averaged High-Latitude Neutral Winds

From individual orbits of DE-2 neutral winds, it was also common to observe higher antisunward neutral winds in the winter northern hemisphere, rather than in the summer southern hemisphere where higher levels of ionization should result in stronger ion-neutral coupling. To study this further, averaged DE-2 neutral winds in the 0600/1800 local-time plane and at conjugate-sampling universal times were used. Specifically, the data criteria were that the orbit plane had to be within one-and-a-half hours of the 0600/1800 local-time plane and only the universal times at which conjugate sampling occurs (i.e., 09 - 11 and 21 - 23 UT), were averaged. An additional criterion which was specified required generally southward-IMF conditions. To increase the number of orbits available, the requirement for data in both hemispheres, on the same

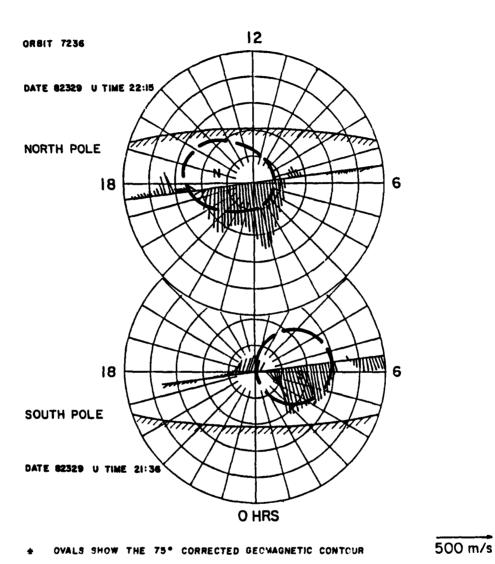


Figure 6.9 - Diagram of neutral winds from DE-2 orbit 7236 in both hemispheres with a single of line of invariant-geomagnetic latitude is superimposed to explain the discrepancy in the width of the antisunward neutral flow in the northern hemisphere at certain universal times.

orbit was relaxed, so that all orbits in the November 1981 - January 1983 and November 1982 - January 1983 periods were included in the averaging process. In the northern hemisphere 75-orbits of data were available. In the southern hemisphere only 46-orbits of data fit the selection criteria. The results (figure 6.10), were binned at a resolution of two degrees of geographic latitude and were separated into IMF $B_y > 0$ and $B_y < 0$ cases, whenever $B_z < +1$. Similar selection and binning criteria for averaging the DE-2 neutral winds, separated by IMF B_y conditions, were used by Thayer et al. (1987). The invariant pole location is indicated by an "N" or "S" depending on the hemisphere. In addition, a small diagram to the upper right of each polar-dial plot indicates schematically the general shape of the two-cell ion-convection pattern anticipated. The satellite passes through the two-cell pattern along the 0600/1800 local-time plane.

Even with relaxed selection constraints, used to boost the number of available orbits in this averaged study, the number of input orbital passes which were used in creating each neutral wind vector was about 20, but was much lower in some frames. The averaged neutral winds faithfully reproduce features seen in the individual orbits, increasing confidence in the selection criteria and averaging process. However, it will be shown below, that there are a number of subtle features in the neutral-wind fields which indicate three different influences simultaneously affecting the antisunward neutral winds. These influences can be categorized as the IMF-controlled ion convection, universal time, and the season. Due to heavy reliance on the distibution and magnitudes of these averaged neutral winds for the results in this section, coupled with an insufficient number of input datasets, as well as a mixture of all geomagnetic activity levels in the averaged data, the results in this section are considered "preliminary indications."

A gross feature which can be immediately seen in the averaged neutral winds is that magnitude of the antisunward neutral winds are approximately commensurate. In addition, when comparing neutral-wind signatures at different universal times, it is

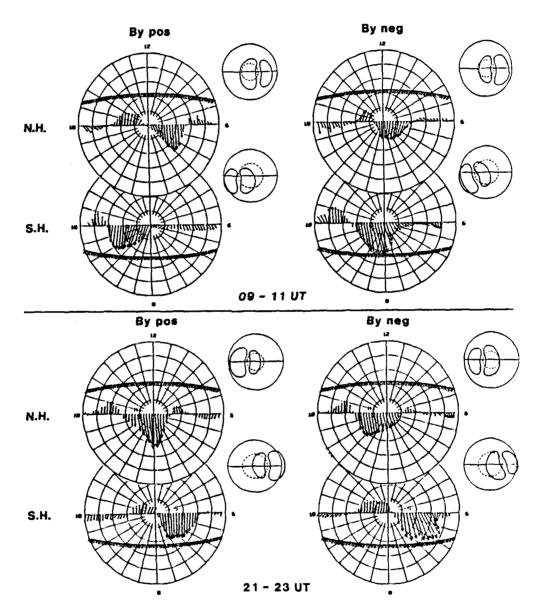


Figure 6.10 - High-resolution averaged DE-2 neutral winds in both hemispheres at the conjugate-sampling universal times and sorted according to IMF conditions.

important to remember that the invariant-pole location has moved, since the plots are in geographic coordinates. This means that a large shift in the position of the high-latitude neutral-wind signature is primarily due to the change in the position of the ionconvection pattern. However, there are a number of more subtle features which rely on the actual magnitude of the antisunward neutral winds. For example, the averaged neutral winds (figure 6.10) show that the northern (southern) hemisphere antisunward neutral wind velocities are greater than the southern (northern) hemisphere antisunward neutral winds under IMF $B_v > 0$ ($B_v < 0$) conditions. This means the antisunward neutral wind velocities in the southern hemisphere should be larger than those of the northern hemisphere under IMF B_v negative conditions (table 6.2). However, in the northern hemisphere, the antisunward neutral winds should be stronger than those of the southern hemisphere whenever IMF By positive conditions prevail, meaning the dusk cell is again dominant in the northern hemisphere. This was an unexpected result for solstice conditions since it was anticipated that higher levels of ion-neutral coupling in the summer southern hemisphere, as a result of greater ionization, would result in higher levels of momentum transfer from the antisunward drifting ions to the neutrals.

		$B_y > 0$	$B_y < 0$
09 - 11 UT	N.H.	524 m/s	367 m/s
	S.H.	462 m/s	634 m/s
21 - 23 UT	N.H.	682 m/s	463 m/s
	S.H.	514 m/s	529 m/s

Table 6.2 - Maximum antisunward zonal component of neutral winds, categorized by IMF conditions, hemisphere, and universal times when conjugate-region sampling is possible. Note that there are not enough available orbits of DE-2 neutral winds to provide confidence that these results are conclusive or show meaningful standard deviations.

Both the DE-2 data and TGCM neutral-wind predictions, in the dawn/dusk local-time plane, show that the dusk cell was usually the dominant of the two neutral-circulation cells, in both size and magnitude of sunward return flow. For IMF $B_y > 0$ ($B_y < 0$) conditions, the largest magnitude DE-2 dusksiae neutral winds were usually found in the northern (southern) hemisphere. From figure 6.10, the magnitude of the maximum duskside sunward neutral winds averaged 260 m/s and extended over a 25-degree-wide region, in the hemisphere where the dusk cell was dominant. However, during times when the dawn cell was dominant in either hemisphere, the maximum duskside sunward neutral winds were approximately the same at 230 m/s, but extended over only a 17-degree-wide region. An insufficient number of input data points once again prohibits display of meaningful standard deviations to accompany these neutral-wind values. As with the antisunward neutral flow, the IMF B_y configuration is known to influence the ion convection which, in turn, controls the duskside sunward neutral flow to a large extent with only minor "seasonal" variations.

Control of the Contro

6.4.3 Universal-Time Variations in the Averaged High-Latitude Antisunward Neutral Winds

A universal-time-dependence of the antisunward-neutral-wind speeds can also be seen in the winter northern hemisphere in figure 6.10 and table 6.3. For example, the northern-hemisphere antisunward neutral winds are stronger at 21 - 23 UT than for the same IMF conditions at 09 - 11 UT. This universal time dependence in the winter hemisphere is attributed primarily to the access the ion-convection pattern has to dayside-ionization processes when the invariant pole moves through its extreme dayside position. At these universal times, the flux tubes become enriched with ions, which are then convected in an antisunward direction. The neutral parcels in the same vicinity as the antisunward-flowing ions are then subject to greater ion-drag and more of the antisunward momentum is transferred, resulting in the higher neutral-wind velocities in the northern hemisphere seen in both figures 6.5 and 6.9. It should be noted that figures

6.5 and 6.9 represent conjugate-region-sampling universal times, which are approximately six hours after the invariant pole passed its most sunward position. This means that the dayside of the two-cell ion-convection pattern had flux tubes entering for several hours which contained dayside levels of ionization. This must have been the case, although it can be seen in figure 6.5 that at the time of the DE-2 measurement, the electron density in the southern-hemisphere polar cap was already a factor of four higher than in the northern hemisphere. However, the 22 UT electron density was approximately constant across the northern-hemisphere polar cap, without the large electron-density trough seen in the center of the northern-hemisphere polar cap at 10 UT (figure 6.6).

There is another universal-time variation in the DE-2 averaged antisunward neutral winds, which changes in both hemispheres according to the sign of the IMF B_v component. This is the diurnal variation of the angle the averaged antisunward neutral winds make with respect to the noon/midnight local-time plane. Unfortunately, there has always been insufficient DE-2 ion-drift data available, so that it has been impossible to compare the averaged DE-2 antisunward ion-drift angle with those of the neutral winds, such as was done for the diurnally-reproducible TGCM neutral-wind simulation in chapter V. However, it can still be noted that the universal-time variation of the angle the averaged DE-2 antisunward neutral winds make with respect to the noon-midnight local-time plane is IMF dependent (figure 6.11). Note that the same caveat, mentioned above regarding use of the averaged DE-2 neutral winds with a low statistics, applies here as well, and this result is also considered preliminary. In addition, the only values of the angle the antisunward neutral winds make with respect to the noon/midnight localtime plane that exist are at the conjugate-region-sampling universal times of 10 and 22 UT. The lines used to join these data points are only intended to illustrate the trend with universal time, not reflect the actual angles at other universal times. Under IMF $B_{\nu} > 0$

Seed because consists freezest and seeds and seeds the seeds deserved because because because by

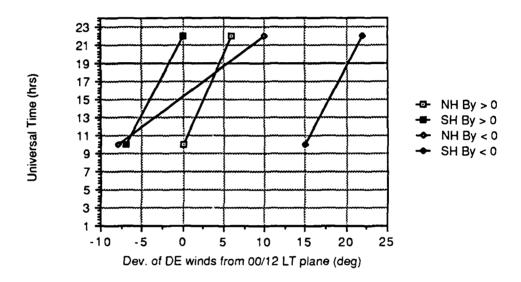


Figure 6.11 - Universal-time variations of the averaged DE-2 high-latitude antisunward neutral-wind direction with respect to the noon-midnight local-time plane and separated according to IMF conditions.

 $(B_y < 0)$ conditions, the counterclockwise twist of the antisunward neutral winds in the northern (southern) hemisphere is greater than in the opposite hemisphere.

6.4.4 "Seasonal" Differences in the High-Latitude Neutral Winds

In this subsection, differences between the neutral-wind circulation, measured by DE-2 in the summer southern hemisphere, are contrasted with DE-2 neutral winds from the winter northern hemisphere, for solar-maximum December-solstice conditions. Also recall from section 5.1, that a qualification was made about the preliminary nature of the determination of "seasonal" differences in the neutral-wind-circulation features, based on analysis of December solstice only. This qualification is re-introduced here. This work cannot claim to distinguish the seasonal features from the hemispheric features of the neutral winds, without examining neutral-wind data for a solar-maximum June solstice. Therefore, all findings which are expected to eventually be labelled true seasonal variations, are here labelled "seasonal," to acknowledge the preliminary nature of the findings.

The sunward neutral winds on the dawnside of the polar cap exhibit significant differences, between the summer southern hemisphere and the winter northern hemisphere. The dawn-cell neutral circulation, characterized by the latitudinal extent and magnitude of the sunward neutral flow, while noticeably weaker than the duskside-neutral-wind-circulation cell in both hemispheres, was found to be stronger and more organized in the winter northern hemisphere than in the summer southern hemisphere in both individual orbits (figures 6.5 - 6.8) and averaged data (figure 6.10). The DE-2 averaged maximum dawnside sunward-neutral-wind velocity was 120 m/s in the northern hemisphere and was virtually non-existent in the summer southern hemisphere. This "seasonal" effect was also identified using the diurnally-reproducible model data in chapter V. Furthermore, the summer-hemisphere dawn cell, in the DE-2 data, appears to be more divergent than the winter-hemisphere dawn cell,

even though the summer hemisphere is more tightly coupled to the non-divergent twincell ion convection. From modeling studies (chapter V), these relationships are ascribed to the orientation of the polar-cap pressure-gradient force, which is dusk-to-dawn-directed in the summer hemisphere and has a small sunward-directed component in the winter hemisphere. The organization and strength of the dawn-cell portion of the thermospheric-neutral-wind circulation is seen to be largely controlled by "seasonal" differences in both the DE-2 measured and TGCM model data.

6.5 Summary

The first dual-hemisphere database of neutral winds and supporting data, from DE-2, has produced a number of interesting results in addition to observing the morphology of the neutral winds and momentum forcing of the thermospheric neutral gas. The ion-drag force, calculated from individual orbits of DE-2 measured data, is much more complex than shown in the diurnally-reproducible model results. Under IMF $B_z < 0$ conditions, the ion-drag force reflects the ion drifts in the hemisphere which has the large duskside ion-convection cell. The ion-neutral momentum coupling time constants were found to be twice as large in the winter northern hemisphere then in the summer southern hemisphere. The dawnside DE-2 neutral winds, for solar-maximum December-solstice conditions, do not seem to influenced by the IMF B_y component but rather by "seasonal" differences. This is consistent with the diurnally-reproducible model results, discussed in chapter V.

Some of the findings in this chapter relied on averaged data, for which there were an insufficient number of DE-2 orbits for the results to be considered conclusive. However, these results provide preliminary indications of the relative importance of factors influencing the magnitude and extent of the sunward duskside and antisunward polar-cap neutral-wind features. For example, the polar-cap and duskside neutral winds were seen to be influenced by the configuration of the IMF B_{ν} component when B_{z} is

southward. Furthermore, there were insufficient data to characterize the neutral winds according to IMF B_y conditions, during B_z -northward periods. Together, the neutral-gas momentum forces based on the NCAR-TGCM diurnally-reproducible results (chapter V), and the IMF-dependent results from DE-2 (chapter VI) have begun to build a coherent "big picture" view of the high-latitude neutral-wind circulation in both hemispheres.

CHAPTER VII

TIME-DEPENDENT NCAR-TGCM NEUTRAL-WIND SIMULATIONS

7.1 Time-Dependent Thermospheric Neutral-Wind Simulation Background

Seven years ago, the first thermospheric-global-circulation models (TGCMs) appeared (Fuller-Rowell and Rees, 1980; Dickinson et al., 1981). Since then the TGCMs have been steadily improved with the intention of becoming more realistic. Thermospheric modelers have spent considerable time and effort trying to realistically simulate the thermosphere (Roble et al., 1987, 1984, 1983, 1982; Killeen et al., 1986; Emery et al., 1985; Hays et al, 1984; Rees et al., 1983; Fuller-Rowell and Rees, 1981). However, most of the model simulations, attempted to date, have tried to simulate averaged ground-based neutral-wind data (Killeen et al., 1986; Sica et al., 1986; Roble et al., 1982), averaged space-based neutral-wind data (Killeen et al., 1986; Hays et al., 1984; Roble et al., 1984), make gross comparisons with individual orbits of space-based neutral-wind data (Emery et al., 1985; Rees et al., 1984, 1983; Roble et al., 1983), or examine idealized case studies (Rishbeth et al., 1985; Roble et al., 1983, 1982; Fuller-Rowell and Rees, 1981). Only one study used a long-term ground-based thermospheric-neutral-wind database to establish and model the climatology over Fritz Peak for an entire solar cycle (Hernandez and Roble, 1984).

Qualitative comparisons between satellite or ground-based neutral winds and model neutral winds have shown that the TGCMs have correctly incorporated the proper atmospheric physics, to first order. However, only two papers, both referring to the same time period, have attempted to directly simulate a series of orbits of satellite-derived

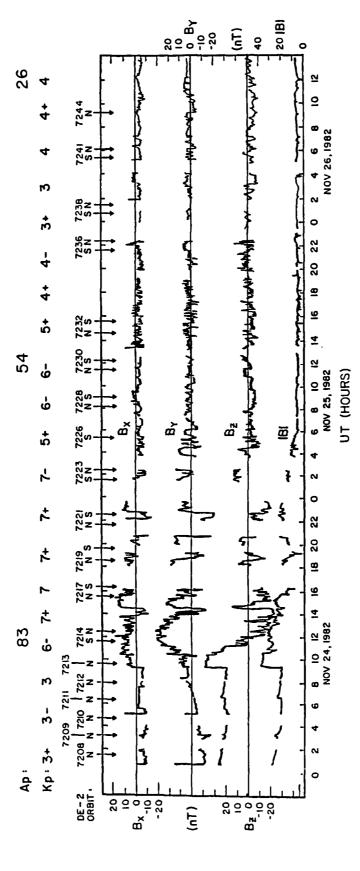
thermospheric neutral winds in a truly time-dependent manner (Roble et al., 1987; Forbes et al., 1987). There may have been problems in determining the neutral winds from the satellite triaxial accelerometer used for that study (Roble, private communication, 1986). Further, this time-dependent simulation did not conclude with a quantitative comparison of the TGCM versus satellite-derived neutral winds. This means there has not yet been a quantitative validation of the NCAR-TGCM with time-dependent neutral winds on a global scale. Models, such as the TGCM, have the potential to provide extensive insight on time-dependent physical processes by displaying the velocity and forcing fields simultaneously at all latitudes, longitudes, and altitudes. However, before reliance is placed on model output, it should be compared to measured neutral winds, such as those from the DE-2 satellite, on a global scale. This is the primary goal of the work described in this chapter.

7.2 Description of the Time-Dependent Simulation Period

pervices essentially accesses advantage

After the dual hemisphere neutral-wind database (appendix B) was established, the opportunity to select a period for simulation by the NCAR-TGCM arose. This new database provided the first opportunity to validate the performance of the TGCM in both high-latitude regions. The choice of a simulation test period was simple because the period selected (November 24 - 26, 1982) had the highest concentration of neutral wind and supporting data in both hemispheres (see figure 7.1).

The selected period was an ambitious one to simulate. It began with a $B_z >> 0$ period for about the first twelve hours of November 24, 1982. During this time, multicell neutral wind signatures were seen in both hemispheres, but not on the same orbit. The antisunward neutral-wind on both sides of the polar cap approached 400 m/s, with 200 m/s sunward flow in the center of the polar cap. The neutral-wind data corresponding to this period are displayed in the top line of figure 7.11, which shows three consecutive orbits of northern-hemisphere neutral winds (7211, 7212, and 7213). The only southern-



\$5505508 | B0000000 | Beekeekee | beekeekee

magnitude measured by ISEE-3 for the simulation period November 24 - 26, 1982. The Figure 7.1 - High-resolution IMF components in GSM coordinates and total field time corresponding to DE-2 orbit numbers are indicated by arrows at the top. three-hourly K_p index and 24 hour A_p are also indicated at the top of the figure.

hemisphere coverage was provided shortly after the storm began. This orbit was 7214 and still showed a multicell neutral-wind pattern (figure 7.12).

The B_z >> 0 period was followed by a large geomagnetic storm. The effects of the onset of the storm (figure 7.1) were seen in the thermospheric neutral winds shortly after the IMF turned sharply southward. The radius of the polar cap increased and the antisunward neutral winds quickly assumed the southward-IMF-associated two-cell wind pattern. The neutral-wind speeds increased significantly over the next several orbits (orbits 7214, 7217, and 7219). The highest velocity neutral winds were seen in the northern hemisphere during orbit 7217 (figure 7.13), when they and reached approximately 1200 m s⁻¹. These were the highest-velocity neutral winds seen during the entire DE-2 mission.

According to figure 7.1, the IMF B_y component was less than zero during the time period corresponding to orbit 7221 (figure 7.15). However, the neutral-wind signature seen in the figure 7.15 corresponds to IMF $B_y > 0$. Apparently, the $B_y < 0$ IMF condition did not persist for a long enough period of time to effect the neutral winds. Also, by the time of orbit 7221, the neutral winds had already decreased significantly from the stormtime peaks. The maximum antisunward neutral winds, for orbit 7221, were 700 m/s in the summer southern hemisphere and approximately 500 m/s in the northern hemisphere, significantly less than during the storm.

Orbit 7223 was the first orbit of November 25th, 1982. For this orbit, the ISEE-3 satellite indicated that IMF $B_z > 0$ conditions existed, but the neutral winds in both hemispheres continued to follow the $B_z < 0$ two-cell neutral-wind-circulation patterns. At the universal time of orbit 7223 (figure 7.16), the invariant poles were approaching the noon/midnight local-time planes. In the northern hemisphere, the DE-2 satellite passed through the sunward entry portion of the neutral-wind-circulation pattern. In the southern hemisphere, the divergent exit region of the neutral-wind-circulation pattern

was sampled by the DE-2 spacecraft. This is the reason that the DE-2 neutral-wind signatures in opposite hemispheres look so different.

For the remaining 24 hours of the TGCM simulation (Nov. 25/12 UT through Nov. 26/12UT), there were no residual effects of the storm, which were seen 12 to 24 hours before. During this period, the velocity of the antisunward neutral winds in both hemispheres appeared to be fairly constant at about 500 m/s. These orbits, 7230 through 7244, appear in figures 7.17 to 7.22. The IMF $B_y > 0$ signature is easily seen on most of these figures with the maximum antisunward flow on the dawnside (duskside) in the northern (southern) hemisphere.

7.3 The Time-Dependent TGCM Simulations

7.3.1 Overview of the Ion-Convection Prescriptions

With the dual-hemisphere database and selection of the simulation period, it became apparent that there was sufficient data to do more than test the ability of the NCAR-TGCM to simulate neutral winds. The time-dependent ion-convection parameters, which go into the TGCM, are normally prescribed analytically by a series of routines devised at NCAR. However, since DE-2 ion-drift data in the dawn-dusk plane existed, it could also be used to provide a second time-dependent set of ion-convection parameters. So two different time-dependent runs of the NCAR-TGCM were planned. The first run would use the standard TGCM ion-convection parameterization and was primarily used to test the time-dependent neutral wind simulation capability. The second run was executed in an effort to look for an alternative method of obtaining the time-dependent model ion convection parameters, hopefully, in a more realistic way. Both runs simulated the identical November 24 - 26, 1982 period, for which DE-2 neutral winds were available. Therefore, the DE-2 measured neutral winds in both hemispheres can be quantitatively compared with TGCM-simulated neutral winds.

7.3.2 The Analytical High-Latitude Ion-Convection Parameterization

The Roble and Ridley (1987) analytical high-latitude parameterization for the first TGCM run depends solely on three quantities; IMF measurements (B_y) , the hemispheric-power index (H_p) of Evans (Foster et al., 1986), and the cross-cap potential (ϕ) calculated by an empirical formula (Reiff and Luhmann, 1986) shown below:

$$\phi(kV) = \phi_0 + A_0 \times V_{sw}(km/s) \times B \times \sin^3(\theta/2)$$
 (7.1)

where $\phi_0 = 6.7 (kV)$

 $A_0 = 0.047 \text{ (kV s/km nT)}$

 $B = min [9, B_{total}] (nT)$

 $\theta = \arccos (B_z / B_{total})$

This parameterization was introduced in chapter IV. While this is a simple method of estimating the values for the 20 parameters necessary to fully specify both the analytical auroral oval and ion convection (chapter IV), there may be times when these three quantities are unavailable. There may also be times when measured quantities such as the electrostatic-potential difference across the polar cap are available from thermospheric satellite measurements. The auroral oval portion of the high-latitude parameterization is common to both the analytical NCAR-developed and the experimental ion-convection parameterization schemes and will be covered in this section.

As a result of the two time-dependent TGCM runs, the neutral winds from the simple NCAR-developed high-latitude ion-convection parameterization used in the first run was compared against the neutral winds which resulted from the alternate experimental ion-convection parameterization method, used in the second run. The results show that neither method produces a sufficiently-accurate simulated neutral wind (i.e., simulated neutral-wind magnitude consistently within 20% of the measured

neutral-wind magnitude). Of the two high-latitude parameterization techniques tested here, the analytical method resulted in TGCM-simulated neutral winds which were closer to the DE-2 measured neutral winds more often than the TGCM simulated neutral winds which were produced using the experimental technique of determining ionconvection parameters. This was partially-attributable to the frequency with which input to the analytical ion-convection routine can be updated. For example, updated IMF values, for use in determining the cross-cap potential in the first TGCM simulation, were available every few minutes. However, DE-2 measured ion drifts, used to determine the cross-cap potential in the second TGCM test, were updated typically about six times a day in each hemisphere. This was due to instrument-duty-cycle restrictions, which meant that when the DE-2 satellite instrumentation was turned on for long periods, in order to cover both hemispheres on the same orbit, data was generally only available for alternating orbits. This meant that the analytical technique for determining the ionconvection parameters was quite possibly able to more closely detect and follow changes in the IMF, which influence the ion convection. Even with much lower frequency of the DE-2 satellite measurements, there were a few orbits where the alternate, experimental method was clearly superior. This was ascribed to the repositioning of the model-ionconvection pattern to line up with the measured ion drifts. Therefore, it is recommended that elements of both methods be combined in the future, whenever possible, to increase further the TGCM neutral-wind-simulation accuracy.

To partially alleviate differences between the frequency of the input data to the different techniques for determining the ion convection parameters, both sets of input (the empirical and derived cross-cap potentials) were combined to produce an average time-dependent cross-cap potential variation, which was used as input to both simulations. However, the cross-cap potential was the only parameter which was "shared" between the two TGCM simulations.

The actual time history of IMF components (in nanotesla), cross-cap potential (in kilovolts), and hemispheric-power index (in gigawatts) for the simulation period are shown in figures 7.1, 7.3, and 7.4. The IMF measurements in figure 7.1 are from the ISEE-3 satellite. Figure 7.1 is a composite of several original data plots at 64 second resolution (Russell, 1982). All components; B_x , B_y ,and B_z , are shown in GSM coordinates (described in chapter III). In figure 7.2, hourly-averaged IMF values are shown, along with a smoothed fit to this averaged data, which represents the variation of the B_v component actually used as input to this test run of the NCAR-TGCM. At the beginning of this simulation test (figure 7.1), strongly-positive B_{z} (northward) IMF conditions existed, which were fairly-stable and lasted over 12 hours. This positive Bz period began at approximately 2200 UT on 82327 and continued until about 12 UT on 82328. At that time, a large geomagnetic disturbance began in response to the sharp southward turning of the IMF Bz component. This geomagnetic storm can be seen more clearly in figure 7.3, where the three-hourly K_p index jumped from 3 to 7⁺ in six hours. The K_p index then took the next 36 hours to return to its former level of 3. During this period the IMF was predominantly $B_z < 0$ and $B_v > 0$, but there were also numerous instances, shown by figure 7.1, where this was not seen to be true.

The empirical formula used by Roble and Ridley (1987) for the determination of the cross-cap potential drop was chosen from several available formulas, due to Reiff and Luhmann (1986), and is shown in equation 7.1. Roble and Ridley caution that if this formula is used during periods when the IMF is swinging rapidly back and forth between strongly B_z southward and northward, the resulting cross-cap potential values rise and fall quickly (solid line on figure 7.4). Roble and Ridley go on to state that because "the convection can speed up rapidly, but apparently can't slow down rapidly," a linear combination of calculated-cross-cap potentials, from the current and the past two hours, should be used to smooth the potential values for use in the TGCM (dashed line on figure 7.4). This smoothing process involves weighting the potential for the current hour by

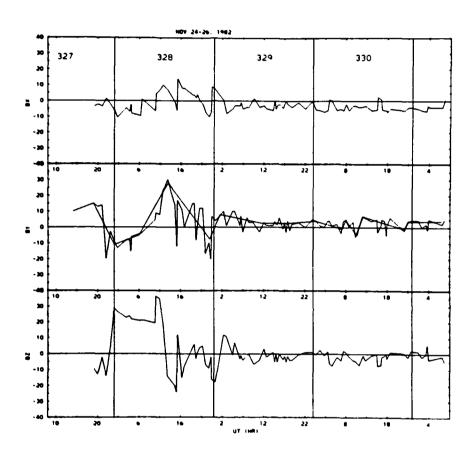


Figure 7.2 - Hourly-averaged values of the IMF components for the November 24 - 26, 1982 period. The smooth line indicates the fit to the one-hourly IMF B_y data which was used as input to the NCAR-TGCM.

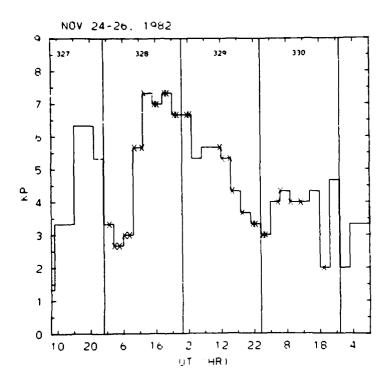


Figure 7.3 - Diagram of the variation of the geomagnetic activity, as shown by the $\rm K_p$ index, for the November 24 - 26, 1982 period with an "X" used to indicate the time of the relevant DE-2 data.

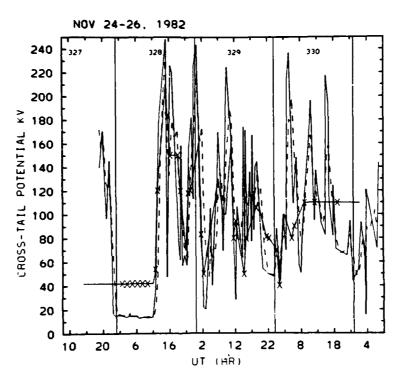


Figure 7.4 - Diagram showing measured and calculated cross-cap potentials for the November 24 -26, 1982 period. The cross-cap-potential drop was calculated from an expression from Reiff and Luhmann (1986), given by equation 7.1, and is shown as the solid line with the highest peaks and valleys. The weighted three-hour average cross-cap potential drop, also using the Reiff formula, is shown by the dashed line. Each "X" represents a cross-cap potential measured by the DE-2 satellite. The other solid line which crosses through the X(s) represents the cross-cap potential values used in the test of the alternate method of high-latitude parameterization. This line was determined both by using the points indicated by the DE-2 data and utilized the Reiff potential drops to fill in, between periods when DE-2 data was not present.

57%, the potential from last hour by 29%, and the potential value from two hours ago by 14%. The final time-dependent cross-cap potential drop used in the TGCM is shown by the other solid line which crosses through the "X" values. Since equation 7.1 utilizes solar-wind velocity, the time-dependent variation of the solar-wind velocity and plasma density for this period are shown in figures 7.5.

The hemispheric-power index of precipitating electron flux was required by both high-latitude ion-convection parameterization schemes to specify the analytical-auroral-oval ion-density enhancement to the Chiu model. The hemispheric-power index, for the period of interest, is shown by the solid line with the large spikes in figure 7.6. The values used for input to the TGCM are shown by the other solid line which again goes through the "X(s)" which indicate the times of available DE-2 data.

Since the required outside geophysical parameters have been specified, the task of specifying the ion-convection parameters for direct entry into the model is now discussed. Several of the parameters were held constant in the standard test. The exponents which control the variation of the electric potential inside and outside the polar cap were set to r^1 and r^{-4} , respectively. This means that the ion drifts inside the polar cap had a slow variation as the distance from the center of the ion-convection pattern increases (Stern, 1977). In contrast, the electric potential outside the polar cap dropped rapidly, resulting in a strong reduction in the sunward ion drifts as latitude decreased (figure 7.7). For the test of the analytical or "standard" parameterization scheme, both hemispheres had their dusk ion-convection cells assigned 60% of the total cross-cap potential drop, while the dawn ion-convection cells were assigned the remaining 40% of the polar-cap potential drop. This follows the empirical results of Heppner (1972, 1977). The radius of the auroral oval and the ion-convection pattern were determined by equations 7.2 and 7.4, the offset of both toward midnight is determined by equation 7.3, and the phase angle, ϕ_c , was determined by equation 7.5.

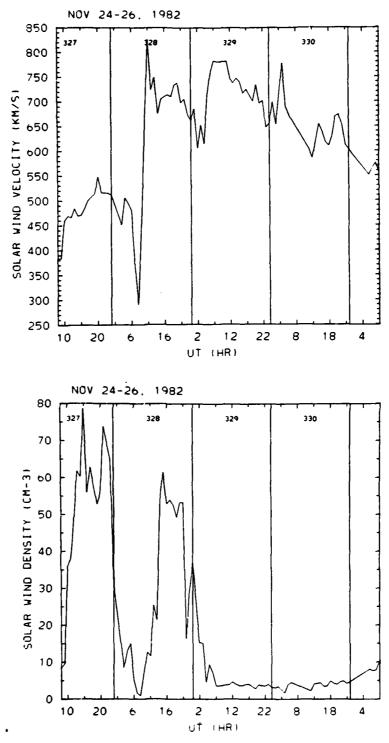
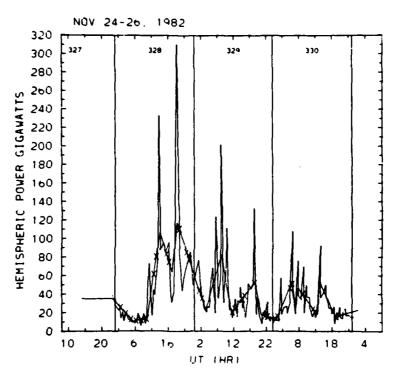


Figure 7.5 - The variation of solar-wind velocity (top) and plasma density (bottom) determined by the ISEE-3 satellite for the November 24-26, 1982 period.



SOST DESCRIPTION OF THE PROPERTY OF THE PROPER

Figure 7.6 - The hemispheric-power index, H_p (gigawatts), determined from the ion and electron precipitation flux measurements on the NOAA-6 and 7 satellites for the period of November 24 - 26, 1982.

DUSK

Orbit 7221 82328/2143 UT CROSS-CAP POTENTIAL DISTRIBUTION Northern Hemisphere

DAWN

paradas provides paradas paradas analysis aparadas

HAD ADDOMER TO COOK TO SEE

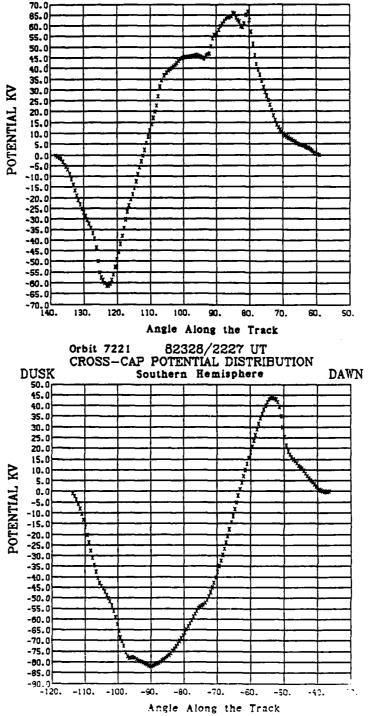


Figure 7.7 - The electrostatic-potential distribution for both the northern and southern hemispheres of orbit 7221, from which the cross-cap potential can be determined, based on the DE-2 ion-drift measurments. Orbit 7221 was selected to be shown because it is the only orbit in the study period which displays a $B_{\rm y} < 0$ cross-cap-potential pattern in both hemispheres.

$$R_{aurora} = (R_1 + R_2)/2$$
 (7:2)

where:
$$R_1 = 17.6 + 0.093 \times H_{p45} + 0.029 \times H_{p \text{ max45}}$$

 $H_{p45} = \min (H_p, 45.)$
 $H_{p \text{ max45}} = \max (0., H_p - 45.)$
 $R_2 = 17.6 + 0.093 \times H_{pcp45} + 0.029 \times H_{pcp \text{ max45}}$
 $H_{pcp45} = \min (H_{pcp}, 45.)$
 $H_{pcp \text{ max45}} = \max (0., H_{pcp} - 45.)$
 $H_{pcp} (\phi > 59.7 \text{ kV}) = 2.18 \times \phi - 86.0$
 $H_{pcp} (\phi < 59.71 \text{ kV}) = \exp ((\phi - 4.) / 14.63)$

Offset =
$$3.0 + 0.006 \times H_p$$
 (7.3)

$$R_{ion\ convection} = R_{aurora} - 3.3$$
 (7.4)

$$\Phi_{\mathbf{c}} = \mathbf{R}_{\text{ion convection}} \times 14. / 17. \tag{7.5}$$

The hemispheric-power index, $H_p(gigawatts)$, was determined from the precipitating energy flux of ion and electrons between 300 eV and 20 keV and has been available since 1978 (Foster et al., 1986). The cross-cap potential from equation 7.1 was also used to create a "pseudo-hemispheric-power" index, H_{pcp} (in gigawatts), which was also used to calculate the radius of the analytical auroral oval and subsequently the radius of the ion-convection model. Further, the departure angles (see figure 4.7); ϕ_{day} , ϕ_{night} , ϕ_{night} ; were determined analytically by equations 7.6 through 7.9:

(for
$$B_y > 0$$
) $\phi_{day}^+ = 90. + 15. \times B_y^+ / B_{yx}^+$ (7.6a)

(for
$$B_v < 0$$
) $\phi_{dav}^+ = 90. - 15. \times B_v^- / B_{vx}^-$ (7.6b)

where:
$$B_{yx}^{+} = 12$$
.
 $B_{yx}^{-} = 10$.
 $B_{y}^{+} = \min (abs(B_{y}), B_{yx}^{+})$
 $B_{y}^{-} = \min (abs(B_{y}), B_{yx}^{-})$

AND THE SECOND AND THE SECOND STATE OF THE SECOND STATES OF THE SECOND S

(for
$$B_y > 0$$
) $\phi_{day}^- = 75. + 10. \times B_y^+ / B_{yx}^+$ (7.7a)

(for
$$B_v < 0$$
) $\phi_{dav} = 75. -10. \times B_v / B_{vx}$ (7.7b)

(for
$$B_y > 0$$
) $\phi_{night}^+ = 65. -15. \times B_y^+ / B_{yx}^+$ (7.8a)

(for
$$B_y < 0$$
) $\phi_{night}^+ = 65. + 15. \times B_y^- / B_{yx}^-$ (7.8b)

(for
$$B_y > 0$$
) $\phi_{night} = 70. + 5. \times B_y + B_{yx}$ (7.9a)

(for
$$B_y < 0$$
) $\phi_{night} = 70. - 5. \times B_y / B_{yx}$ (7.9b)

The angles associated with the zero-potential lines (figure 5.7); ϕ_{day} , ϕ_{night} ; were determined using equations 7.10 and 7.11:

$$\phi_{\text{day}} = -7.5 - 37.5 \times B_y^+ / B_{yx}^+$$
 (7.10)

$$\phi_{\text{night}} = -7.5 + 22.5 \times B_y^{-} / B_{yx^{-}}$$
 (7.11)

The remaining parameters, needed to define the analytical-auroral-oval ion-density enhancement, were the values of the half-width (in degrees of latitude) of the auroral particle precipitation, h; the energy flux (in ergs cm⁻² s⁻¹ ster⁻¹ keV⁻¹), E; the mean electron energy (in keV), 2 α ; and the number flux (in cm⁻² s⁻¹), F. Each of these parameters was specified at local noon and local midnight and identified by the subscripts 1 and 2, respectively. The analytical formulae used, given the hemispheric-power index, are shown in equations 7.12 through 7.15:

$$\alpha_1 = 0.91$$
 (7.12a)

$$\alpha_2 = 0.63 + 0.039 \times H_{p33} + 0.0022 \times H_{p33max}$$
 (7.12b)

where: $H_{pcp33} = min (H_{pcp}, 33.)$ $H_{pcp \ max33} = max (0., H_{pcp} - 33.)$

$$H_1 = 1.7 + 0.0065 \times H_n \tag{7.13a}$$

$$H_2 = 2.20 + 0.029 \times H_{p45} + 0.012 \times H_{p45max}$$
 (7.13b)

$$E_1 = 0.15 + 0.090 \times H_{p50} \tag{7.14a}$$

$$E_2 = 1.20 + 0.1135 \times H_p$$
 (7.14b)

where: $H_{p50} = min (H_p, 50.)$

$$F_1 = (3.1211 \times 10^8) \times E_1 / \alpha_1$$
 (7.15a)

$$F_2 = (3.1211 \times 10^8) \times E_2 / \alpha_2$$
 (7.15b)

In this section the analytical expressions which govern the model auroral and ion convection parameters used in the NCAR-TGCM neutral-wind simulations for this chapter were covered. These expressions provide the understanding necessary to contrast the analytical and the experimental approachs to arriving at the TGCM high-latitude ion-convection parameters, covered in the next section.

Since both the standard and the experimental TGCM simulations were attempting to simulate solar-maximum neutral winds, the appropriate solar-cycle-maximum EUV fluxes from Hinteregger (1981) were used, assuming $F_{10.7} \sim 200 \times 10^{-22}$ W m⁻² Hz⁻¹. In addition, no tides, such as those simulated for equinox conditions by Fesen et al. (1986) using the NCAR-TGCM, were included in either simulation. This was done to avoid the additional complexity of deconvolving the time-dependent effects due to the high-latitude ion-convection parameterization from the effects due to tides because no solstice run of the TGCM, with tides included, has been published yet. Therefore, no established "base" run exists from which to judge TGCM solstice results with tides.

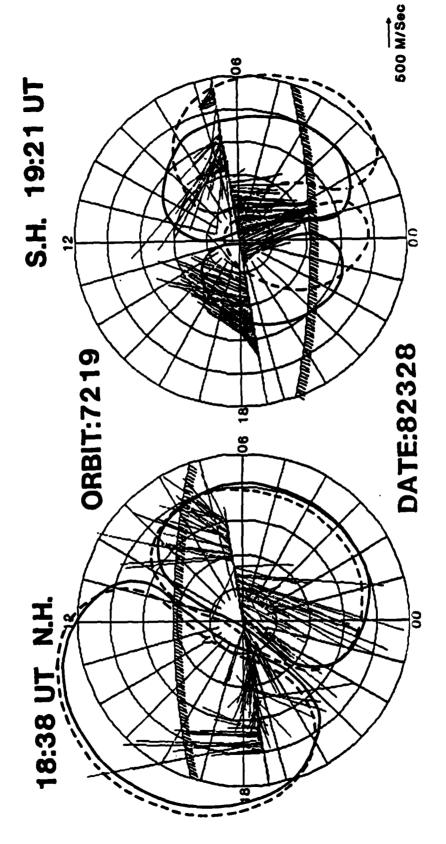
7.3.3 The Experimental High-Latitude Ion-Convection Parameterization

- Contractor and Charles of the State of the

As mentioned in the preceding sections, a new technique for providing the model-ion-convection parameters based on measured DE-2 ion drifts has been developed during the course of this research, for use in the second TGCM run. It is tested in this chapter. This alternative method of determining high-latitude ion-convection parameters may provide more realistic input into the TGCM. Furthermore, using direct ionospheric measurements to initialize an ionospheric model may allow us to more accurately simulate the thermosphere. This technique of using ion drifts to determine the model-ion-convection parameters is outlined further below.

Roble et al. (1987) state that, "the preferable method of determining the electrostatic-potential difference across the polar cap is direct measurement of the electric field by a polar-orbiting satellite in a dawn-dusk orbit." In addition, satellite ion drift measurements can be used to provide many of the other model ion convection parameters. For these reasons, an alternate method of determining the high-latitude ion-convection parameters, based on ion drifts measured by the DE-2 satellite, was developed and tested in the second time-dependent TGCM run. For example, whenever the convection-reversal boundaries of the measured ions did not line up with the standard position of the ion-convection pattern, which is approximately centered on the invariant-pole location, the model ion-convection pattern for input into the TGCM was moved to a location where the reversals did line up (see figure 7.8). The output NCAR-TGCM neutral winds, using this modified high-latitude ion-convection parameterization scheme, were compared to the DE-2 neutral winds in the same manner as the TGCM neutral winds from the first simulation to determine whether this method resulted in any improvement.

The primary assumption behind this alternate technique was that the in-situ ion drifts measured, as the DE-2 satellite passed through high-latitude regions, change slowly with time. However, the ion drifts have the ability to change significantly over



CATALOG SE

Figure 7.8 - An example of the position of the ion-convection cells when they are centered on the invariant-pole location (dashed lines) and the position when they are centered on the position given by the center of the DE-2 measured ion drifts (solid lines).

periods as short as seconds or minutes because the IMF and solar wind, which drive the polar-cap electric field through the solar-wind/magnetosphere interaction, frequently change on this time scale, especially during magnetic-storm periods. This test provided insight into the validity of this assumption.

Ion convection in the non-sunlit portion of the winter hemisphere has been known to be variable and irregular (Heppner and Maynard, 1986; Heppner, 1977). Further, Sojka and Schunk (1986) state that the model-ion-convection patterns tend to represent the average ion convection and not the structured and highly-variable instantaneousconvection patterns. An instantaneous measurement of ion drifts may or may not closely represent the average ion-convection pattern. Intuitively, one can easily believe that the measured ion drifts could more closely represent the true, averaged ion convection during periods of little or no change in the IMF and solar wind. However, this has not been substantiated. This means there might be periods when a model ionconvection pattern, which used satellite-measured ion drifts as input, could not be expected to produce more accurate neutral winds than the analytical high-latitude ionconvection-parameterization technique. Further, the IMF and cross-cap potential can be calculated almost continuously while the hemispheric-power index is provided at 30 to 90 minute intervals. As mentioned earlier, these data are supplied at much higher frequencies than the ion-drift data from DE-2, which at its very best is available only about six times per day in each hemisphere. So the analytical high-latitude ionconvection-parameterization scheme, used in the first run of the TGCM, already has the advantage of superior temporal resolution. Even with these disadvantages, the possibility of developing a practical alternate technique for determining the model-ionconvection parameters, without the need for IMF information, made this test appealing.

ASSESSMENT AND SECRETARY ASSESSMENT OF SECRETARY SECRETA

For this test, several simple concepts were tested. For example, the analytic highlatitude parameterization is well suited to producing a smoothed and averaged ionconvection patterns. For this simulation, it was desirable to make the input to the ionconvection pattern as realistic as possible. To do this, the radius of the antisunward ion convection was measured, in degrees of geographic latitude, in the 0600/1800 local-time plane, using DE-2 ion-drift data. The measured radius of the antisunward convection is only equal to the radius of the ion-convection pattern during the universal times when the satellite track is passing through conjugate regions in both hemispheres, as shown in figure 7.4. This occurs for universal times of approximately 09 - 11 and 21 - 23 UT. However, for the other universal times, the measured antisunward radius can be related to the radius of the ion-convection pattern. It should be noted that the radii used in this test, of an alternate high-latitude ion-convection pattern parameterization, often differed greatly between hemispheres. The ion-convection radii given in table 7.1 are those used in the test of the alternate, experimental-ion-convection-parameterization technique.

The state of the s

		North	Northern hemisphere		Southern hemisphere		
Date	Orbit	UT	Model radius (deg)	UT	Model radius (deg)		
82328	7211	0618	16.4				
82328	7212	0749	16.4				
82328	7213	0921	16.4				
82328	7214	1225	26.0	1136	17.5		
82328	7217	1535	26.0	1615	20.0		
82328	7219	1838	23.0	1921	16.0		
82328	7221	2143	18.0	2227	21.0		
82329	7223	0218	17.5	0133	19.0		
82329	7228	0824	17.5	0911	18.0		
82329	7230	1134	20.0	1216	18.0		
82329	7232	1439	20.0	1524	17.5		
82329	7236	2221	20.0	2140	15.0		
82330	7238	0126	17.0	0041	17.5		
82330	7241	0602	17.5	0516	17.5		
82330	7244	0907	17.5				

Table 7.1 - The radii of the ion-convection patterns, in degrees of geographic latitude, used in the NCAR-TGCM to test the experimental technique of using DE-2 ion drifts to provide model input.

Another important concept was also tested here. Upon examination of the ion-drift data, such as that seen in chapter VI, it was noticed that the center of the measured antisunward ion drifts was often offset from the position of the invariant-geomagnetic pole. If this offset of the center of the ion-drift pattern was a true representation of the

averaged ion convection, then it was possible that the analytic high-latitude parameterization scheme might not position the ion-convection pattern and the auroral oval properly. The center of the ion convection system, before this test, had always previously been assumed to be approximately centered on the invariant-pole location, with a small offset toward midnight. Placement of the ion-convection system in the improper location would ultimately lead to a poor simulation of the neutral winds by the TGCM. For the November 24 - 26, 1982 period, the migration of the center of the measured antisunward ion drifts, in each hemisphere, which was used to position the ion-convection pattern and the auroral oval is shown in table 7.2. The location of the invariant poles was given in table 5.2.

	Northern hemisphere Southern hemisphere Geographic Geographic						
Date	Orbit	UT		Longitude	UT		Longitude
82328	7211	0618	78.3 N*	69.0 W*			
82328	7212	0749	78.3 N*	69.0 W*			
82328	7213	0921	78.3 N*	69.0 W*			
82328	7214	1225	81.3 N	69.0 W	1136	74.5 S	112.0 E
82328	7217	1535	88.3 N	69.0 W	1615	87.5 S	127.0 E
82328	7219	1838	80.3 N	69.0 W	1921	84.5 S	127.0 E
82328	7221	2143	76.3 N	69.0 W	2227	78.5 S	127.0 E
82329	7223	0218	78.3 N	69.0 W	0133	73.5 S	157.0 E
82329	7228	0824	85.3 N	69.0 W	0911	74.5 S	127.0 E
82329	7230	1134	85.3 N	69.0 W	1216	69.5 S	112.0 E
82329	7232	1439	78.3 N	69.0 W	1524	69.5 S	097.0 E
82329	7236	2221	83.0 N	69.0 W	2140	78.3 S	127.0 E
82330	7238	0126	78.3 N	69.0 W	0041	74.5 S	127.0 E
82330	7241	0602	89.5 N	69.0 W	0516	74.5 S	112.0 E
82330	7244	0907	87.3 N	69.0 W			

^{*} indicates that during strongly $B_z > 0$ conditions, it was not possible to determine the center of the ion-convection pattern in the conventional $(B_z < 0)$ sense, so the invariant pole location was used.

Table 7.2 - The locations of the center of the ion-convection pattern observed using DE-2 ion-drift data for the November 24 -26, 1982 period.

The latitudes of the center of the antisunward drifts, seen in table 7.2, were used to reposition the ion-convection pattern so that the sunward reversals in the model lined up

with the reversals seen in the data. When a correct fit using this information was difficult to achieve or it was otherwise obvious that the ion-convection pattern was not centered on the longitude of the invariant pole, then the longitude of the center of the ion-convection pattern was varied, in 15 degree of geographic-longitude increments, in both directions in an attempt to better fit the model to the DE-2 ion-drift data. The longitudes which resulted in the best fit of the model-ion-convection pattern to the DE-2 data are also shown in table 7.2.

It should also be noted that the ion-convection parameters, determined in each hemisphere from the DE-2 data, were applied only in that hemisphere. This is the first time the NCAR-TGCM has been run with ion-convection parameters varied independently in opposite hemispheres, based on the measured-ion-drift data for that hemisphere. Model-ion-convection parameters for each of the 150 second time steps in the TGCM were linearly interpolated between the model-ion-convection-parameter data points determined from the DE-2 ion drifts.

ALLES CONTRACTOR CANADA

COORDINATE OF THE PROPERTY AND ADDRESS OF THE PROPERTY OF THE

One exception to the independent variation of ion-convection parameters in opposite hemispheres was cross-cap potentials. As shown in figure 7.4, the cross-cap potentials, shown by "X(s)" and derived by numerical integration of the electric field along the track of the satellite, are not distinguished by hemisphere since there was not sufficient reason to believe that different cross-cap potentials would be applied to opposite hemispheres. Since the values derived from the DE-2 satellite data were reasonably close to the values provided by the empirical cross-cap potential formula (equation 7.1), the derived cross-cap potentials from both hemispheres were joined into a single dataset, with the Reiff potentials used to fill in between gaps. Therefore, the same temporal variation of cross-cap potentials was used in both hemispheres for both the analytic and experimental tests.

The cross-cap potentials for each hemisphere of available DE-2 ion-drift data were derived by integrating the gradient of the electric potential or electric field along the

satellite track at latitudes poleward of 50 degrees magnetic latitude. This is given by equation 7.16 where the zonal component of the ion drift is provided by the DE-IDM instrument (chapter VI) and the magnetic field at the satellite altitude is provided by the MAGSAT model, which resides in the DE-2 orbit/attitude files and is available at the location and altitude of each DE-2 data value (Smith et al., 1981).

$$-\nabla \phi = \mathbf{E} = -\mathbf{V}_{\text{ion}} \times \mathbf{B} \tag{7.16}$$

An example of the results of this integration for both hemispheres of orbit 7221 is shown in figure 7.7. In this figure, dusk is always to the left and dawn to the right. The potential distribution in both hemispheres had a $B_y < 0$ signature, but the signature was more distinct in the southern hemisphere, due to a larger ratio of dusk-to-dawn potential drop in the southern hemisphere than the dawn-to-dusk potential drop in the northern hemisphere.

passi increased accorded becaused because measured measured measured increased increased increased increased in

For $B_y>0$ cases, this signature was easier to recognize in the northern hemisphere. This seems to be caused by the effect of the day-to-night conductivity gradient mentioned in chapter III, which enhances the size of the dusk cell. However, recall that the analytically-derived high-latitude ion-convection parameterization always applied 60% of the total cross-cap potential to the dusk cell, regardless of external geophysical conditions. This seemed to simulate only $B_y>0$ conditions in the northern hemisphere and $B_y<0$ condition in the southern hemisphere. In order to test different geophysical conditions, this experimental high-latitude ion-convection simulation mirrored the cell potential percentages between hemispheres, in an attempt to introduce a time-dependent IMF B_y effect into the neutral winds, such as those seen in chapter VI. That is under $B_y>0$ ($B_y<0$) conditions, the dusk/dawn ratio of cell potential drop was roughly 60%/40% (40%/60%) in the northern hemisphere and 40%/60% (60%/40%) in the southern hemisphere. This ignores an extra percentage of the total potential drop, which

might be applied to the dusk cell in both hemispheres due to the day-night conductivity gradient effect (chapter III). However, the intention of this simulation was to use more realistic ion-convection parameters than the analytical method, so when the integrated cross-cap potentials from individual orbits of DE-2 data displayed differences from the averaged dusk/dawn ratio of potential drop seen by Heppner and Maynard (1987), these ratios were used in the TGCM simulation.

The relevant potentials for all the available ion-drift data for the November 24 - 26, 1982 period are compiled in table 7.3. Unfortunately, the cross-cap potential measurements presented the same problem as the measured radius of antisunward ion convection. Only during the universal times for conjugate measurements in both hemispheres are the measured cross-cap potentials similar to the total cross-cap potentials which drive the ion convection, because the satellite does not fly through the maximum potential sections, except during conjugate sampling universal times. The final (total) cross-cap potentials, used as input to the TGCM and which are representative of the DE-2 ion drifts, are also shown below, in table 7.3.

Northern hemisphere Southern hemisphere measured final measured final					
Date Orbit U	JT dusk/dawn Tot.	dusk/dawn Tot.	UT dusk/dawn Tot.	dusk/dawn Tot.	
82328 7211 06	S18 */* 20.	-24./16. 40.			
82328 7212 07	749 */* 29.	<i>-</i> 24./16. 40.			
82328 7213 09	921 */* 41.	-24./16. 40.			
82328 7214 12	225 */* 109.	-70./50. 120.	1136 */* 62.	-20./30. 50.	
82328 7217 15	535 */* 114.	-110./70.180.	1615 -49./42. 91.	-70./80. 150.	
82328 7219 18	338 -44./64. 108.	-80./70. 150.	1921 -51./47. 98.	-50./70. 120.	
82328 7221 21	43 -62./66. 128.	-50./70. 120.	2227 -82./44. 126.	-70./50. 120.	
82329 7223 02	218 -23./5. 28.	-30./20. 50.	0133 -27./7. 34.	-35./45. 80.	
82329 7228 08	324 */* *	-60./40. 100.	0911 -56./42. 98.	-40./60. 100.	
82329 7230 11	134 */* 43.	-45./35. 80.	1216 -53./2. 55.	-40./55 . 95 .	
82329 7232 14	139 -24./30. 54.	-30./20. 50.	1524 -35./0. 35.	-40./50. 90.	
82329 7236 22	221 -23./25. 48.	-45./35. 80.	2140 -35./47. 82.	-35./45. 80.	
82330 7238 01	126 */* 23.	-25./15. 40.	0041 -6./21. 27.	-30./40. 70.	
82330 7241 06	502 -28./32. 60.	-50./40. 90.	0516 -18./15. 33.	-35./45. 80.	
82330 7244 09	007 -40./45. 85.	-65./45. 110.			

^{* -} indicates either incomplete ion data, a $B_z > 0$ ion-convection pattern, or other problem in evaluating either the dusk/dawn potential-drop percentages and/or total cross-cap potential.

Table 7.3 - The measured and final cross-cap potentials (kV) used as input to the TGCM and based on the DE-2 ion-drift measurments.

Another concept which was tested in an attempt to improve accuracy of the neutral winds simulated by the TGCM was to constrain the antisunward model ion drifts to parallel the measured antisunward ion drifts as closely as possible. This was done by adjusting the ϕ_{day} and ϕ_{night} parameters (introduced in chapter IV) so that the shape of the model equipotential lines, which the ions are assumed to drift parallel to, are tangent to the DE-2 ion drifts in the 0600/1800 local-time plane. An example of an orbit of measured ion drifts, with a model equipotential pattern overlaid, is shown in figure 7.9. The final values of ϕ_{day} and ϕ_{night} used as input into the TGCM are presented in table 7.4.

SOUTH GEOGRAPHIC LAT. DE - IDM/RPA Ion Drift Vectors

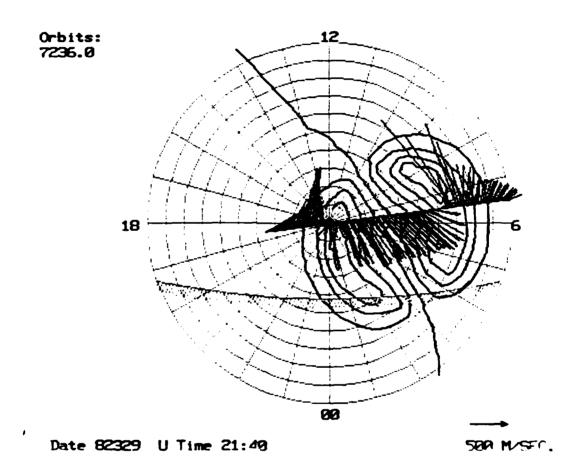


Figure 7.9 - An example of the Heelis et al. (1982) model equipotential pattern overlaid on an orbit of measured ion drifts. The object here is to show how the angles of the zero-potential lines on both the noon and midnight sides of the ion-convection pattern, can be adjusted from the noon-midnight local-time plane to get the equipotential lines tangent to the DE-2 measured ion-drift direction.

		Northern hemisphere			1Southern hemisphere		
Date	Orbit	UT	Day	Night	UT	Day	Night
82328	7211	0618	0.	+180.			
82328	7212	0749	0.	+180.			
82328	7213	0921	0.	+180.			
82328	7214	1225	-20.	+160.	1136	-20.	+155.
82328	7217	1535	-50.	+130.	1615	-30.	+145.
82328	7219	1838	-40.	+160.	1921	+15.	-170.
82328	7221	2143	+5.	+175.	2227	-30.	+150.
82329	7223	0218	+5.	+180.	0133	+15.	+180.
82329	7228	0824	-35.	+140.	0911	0.	+160.
82329	7230	1134	-20.	+150.	1216	-5.	+150.
82329	7232	1439	-50.	+135.	1524	-10.	+150.
82329	7236	2221	-55.	+130.	2140	+30.	-130.
82330	7238	0126	-10.	+165.	0041	+10.	-170.
82330	7241	0602	-20.	+165.	0516	+10.	-160.
82330	7244	0907	-20.	+165.			

Table 7.4 - The final values of the angles of the zero-potential lines, with respect to the noon-midnight local-time plane, used as input to the experimental run of the TGCM. Positive angles are measured in the counterclockwise direction.

There were several ion-convection-model parameters which were kept constant for this test. Among them were the departure angles; $\phi_{\rm day}^+$, $\phi_{\rm day}^-$, $\phi_{\rm night}^+$, $\phi_{\rm night}^-$; which were set at a constant value of 60 degrees. This constant value was chosen arbitrarily in order to simplify this test. In addition, the DE-2 ion drift data, in the 0600/1800 local-time plane provided no information on the departure angles, so any attempt to assign time-dependent values would be no better than a guess for which there was no verification. Another parameter held constant for the model ion-convection pattern was the midnight offset of the ion-convection pattern and auroral oval, which was set at five degrees (Feldstein and Galperin, 1985). Finally, the exponent which controls the variation of the electric potential inside the polar cap was changed from the value of one, set in the standard analytical run and set to a value of two, for this experimental run. This led to a slight decrease in the drift velocity of the antisunward convecting ions in the center of the polar cap (Heelis et al., 1982) which was commonly seen in the DE-2 ion-drift data.

Based on the information in this chapter regarding the analytical and experimental methods of determining the time-dependent ion-convection-model prescriptions used by the TGCM, it can be seen that both methods are complex because of the large number of model parameters which must be determined. Before comparing the TGCM neutral winds from both methods, it was useful to stand back and get the "big picture" view of what both high-latitude ion-convection-parameterization schemes were trying to achieve. The analytical technique was set up to provide the model parameters from the smallest number of geophysical indices as possible. The experimental method was developed as an alternative to the analytical technique, which could utilize measured ion drifts for input and measured neutral winds to check upper-thermospheric neutral-wind-simulation accuracy. The alternate method tested several new approaches, of which the main one was the shifting of the center of the ion-convection pattern to match the center of the measured ion-drift pattern. The advantages of doing this are apparent in figures 7.8 and 7.9. Figure 7.10 shows the measured ion drifts at the top, with the model ion drifts from the analytical technique in the center, and the model ion drifts from the experimental technique on the bottom. This example was chosen specifically to illustrate the differences in the model ion drifts, along the track of the satellite resulting from the two parameterization techniques. In this case, the experimental technique does a much better job of simulating the measured ion drifts along the satellite track because the radius of the convection pattern is closer to reality and the sunward convection reversals are better aligned. The analytical method has misaligned sunward reversals and the radius of the antisunward convection is too large.

7.4 Comparison of TGCM Neutral-Wind Simulations with DE-2 Neutral Winds

The NCAR-TGCM using the standard NCAR-developed analytical high-latitude ion-convection and auroral parameterizations took 110 seconds of Cray-1 CPU time to do

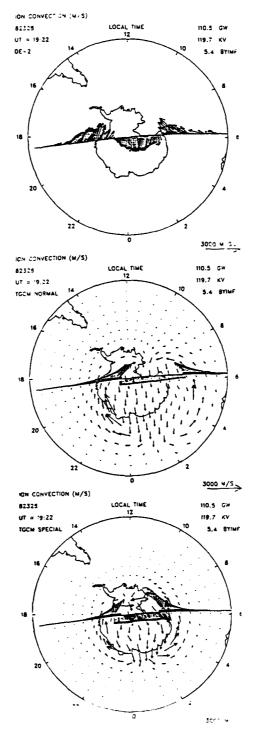


Figure 7.10 - A comparison of the DE-2 measured ion drifts (top) with the model ion drifts using the analytic high-latitude ion-convection parameterization (midule) and the ion drifts using the experimental method of ion-convection parameterization (bottom). This particular case demonstrates how measuring the proper radius and lining up the convection-reversal boundaries can bring the model ion drifts closer to the measured values. Note that the model ion drifts are interpolated to the resolution of the spacecraft data from the normal five degrees of latitude spacing.

one hour of simulation, using 150-second forward time steps. The same simulation using the experimental ion-convection parameterization took a significantly longer period of time to run, using 140 seconds of Cray-1 CPU time to simulate one hour using the same time steps as above. The DE and TGCM neutral winds for the selected simulation period are depicted both in figures 7.11 to 7.22. In an effort to quantify the accuracy of each TGCM run in simulating the neutral winds, the TGCM neutral winds at the same altitude as the DE-2 satellite and in the same local time planes, were linearly interpolated from the five degree latitude and longitude grid-point spacing of the TGCM to the same resolution as the DE-2 neutral winds. At this point there were two methods by which to judge how closely the TGCM neutral winds simulated the DE-2 measured neutral winds. A qualitative comparison was used to spot a simulation which was not an improvement over standard methods. Then there was the quantitative approach, where a difference vector was calculated between the DE-2 measured and TGCM-simulated neutral winds at each point in figures 7.11 through 7.22. Finally, the magnitude of the difference vectors at each data point were summed and normalized by the number of data points to produce an average difference-vector magnitude for each hemisphere. This can be considered as a rough estimate of the error of the model neutral winds and the relative accuracy of each high-latitude ion-convection parameterization technique.

A look at the simulated data in figures 7.11 through 7.22 shows that the experimental technique did much better than the analytical technique in the southern hemisphere of orbit 7219 (figure 7.14) and the northern hemisphere of orbit 7244 (figure 7.22). The quantitative evaluation in table 7.5 bears this out. However, there were also several orbits when the results of the experimental simulation looked good but the average difference vectors indicated the simulated neutral winds were way off. An example of this was the southern hemisphere of orbit 7221, where the failure of the reversals to line up lead to a large quantitative difference. A quick qualitative analysis

processes expresses establishes processes buildings

training (property

gesonmentation personal

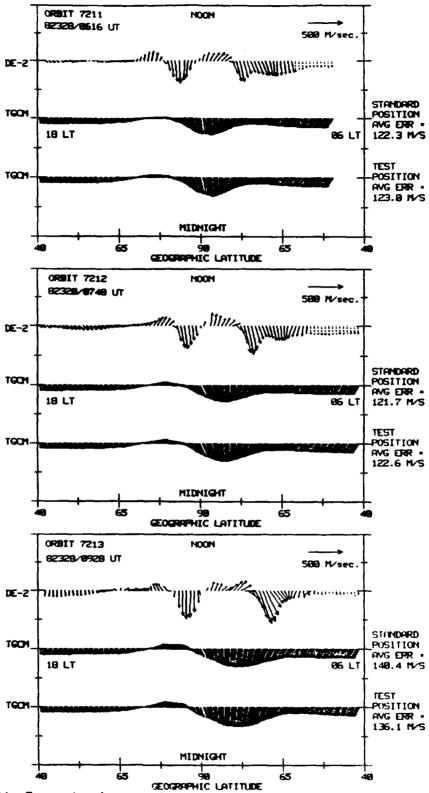
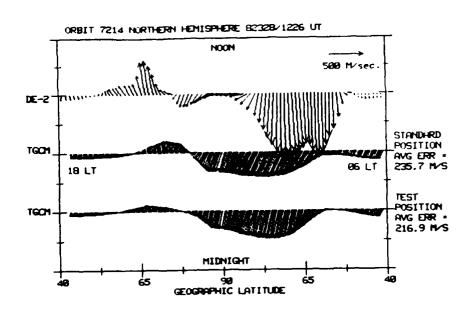


Figure 7.11 - Comparison between the measured DE-2 neutral winds in the 0600/1800 local-time plane and the standard, analytical run of the NCAR-TGCM and the new, experimental run of the NCAR-TGCM for northern hemisphere orbits 7211, 7212, 7213.



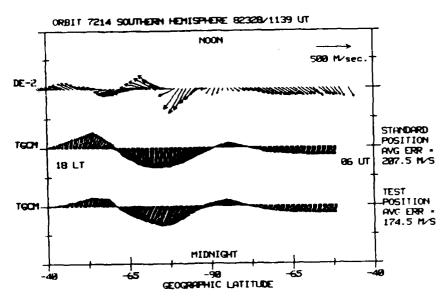
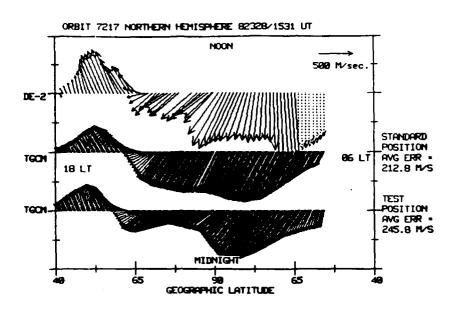
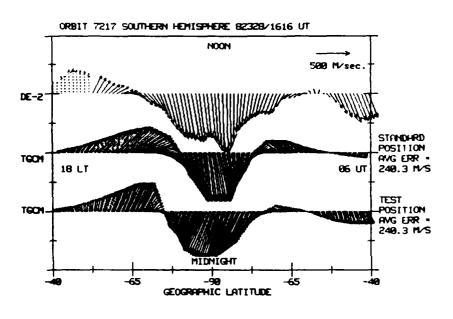


Figure 7.12 - Same as figure 7.11 but for the northern and southern hemispheres of orbit 7214.





general control of the property of the propert

Figure 7.13 - Same as figure 7.11 but for the northern and southern hemispheres of orbit 7217.

of figures 7.11 through 7.22 might not indicate that this experimental simulation of the southern hemisphere of orbit 7221 resulted in the lowest accuracy of the entire simulation.

		IN	orthern hemis	phere	1 Sou	thern hemis	phere
Date	Orbit	$\mathbf{U}\mathbf{T}$	Std. tech.(m/s) E	xp. tech.(m/s)	UT S	td. tech.(m/s) E	xp. tech.(m/s)
82328	7211	0618	122.3 T	123.0 T			
82328	7212	0749	121.7 T	122.6 T			
82328	7213	0921	140.4 T	136.1 T			
82328	7214	1225	235.7	216.9 *	1136	207.5	174.5 *
82328	7217	1535	212.8 *	245.8	1615	240.3 T	240.3 T
82328	7219	1838	215.1 T	221.5 T	1921	233.9	198.3 *
82328	7221	2143	140.1 T	136.5 T	2227	155.9 *	302.9
82329	7223	0218	154.2 *	171.6	0133	257.5	203.5 *
82329	7230	1134	128.0 *	174.9	1216	132.6 *	197.3
82329	7232	1439	131.3 *	203.5	1524	153.9 *	174.9
82329	7236	2221	120.8 *	162.7	2140	117.7 *	150.3
82330	7238	0126	107.7 T	108.3 T	0041	091.3 T	095.5 T
82330	7241	0602	148.5 T	145.6 T	0516	094.3 *	165.6
82330	7244	0907	133.3	111.0 *			

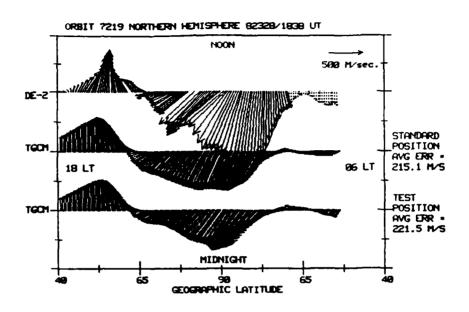
^{*} indicates the highest accuracy (lowest error) in simulating the observed DE-2 neutral winds.

T indicates an effective tie between the two high-latitude ion-convection parameterization techniques; i.e., the average difference vectors were within 5% of each other.

INCOCOCO CONTROL DESCRIPTION CONTROL DESCRIPTION CONTROL CONTROL DESCRIPTION CONTROL DESCRIPTION CONTROL DESCRIPTION

Table 7.5 - A compilation of the magnitude of the average difference vectors (m/s) resulting from a comparison between the DE-2 measured neutral winds and both runs of the NCAR-TGCM using the standard analytical and the new experimental high-latitude ion-convection-parameterization techniques.

A first look at table 7.5 shows that the average neutral-wind difference-vector magnitudes for all orbits and hemispheres were lower that one might have initially anticipated. Most of the difference-vector magnitudes lie between 100 - 200 m/s, which is not small considering that the DE-2 maximum antisunward neutral winds were approximately 500 m/s during undisturbed conditions and increased to greater than 1000 m/s during the geomagnetic storm. Furthermore, based strictly on the number of times one high-latitude-parameterization technique produced more accurate simulated neutral winds over the other technique, it can be seen that the analytical auroral-oval and ion-



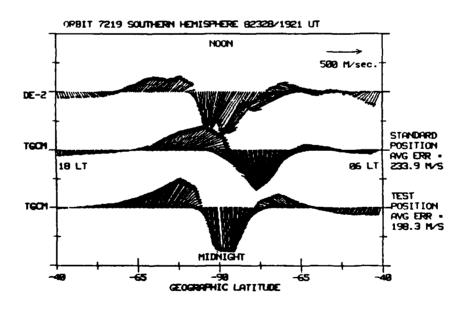
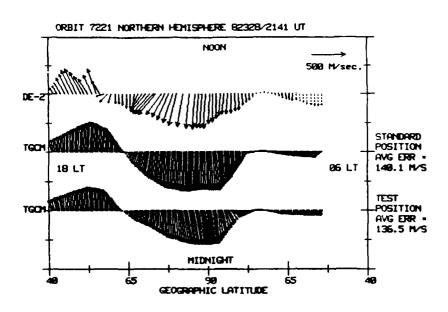
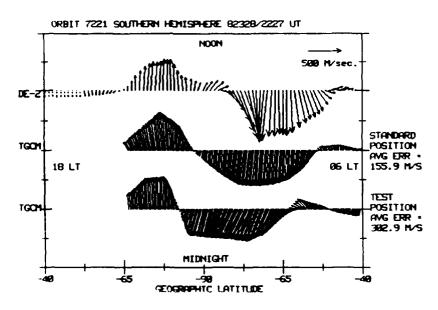


Figure 7.14 - Same as figure 7.11 but for the northern and southern hemispheres of orbit 7219.





ADTON POLICICAN STATUTE TOCKSONS PERSONS EXECUTE ELECTION SECOND SECOND MERICON STATUTE

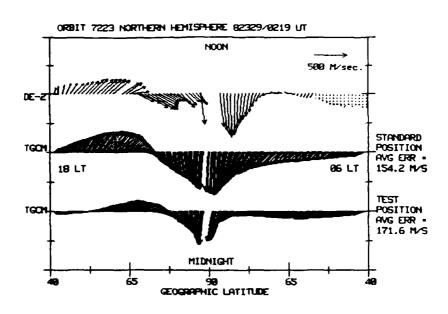
Figure 7.15 - Same as figure 7.11 but for the northern and southern hemispheres of orbit 7221.

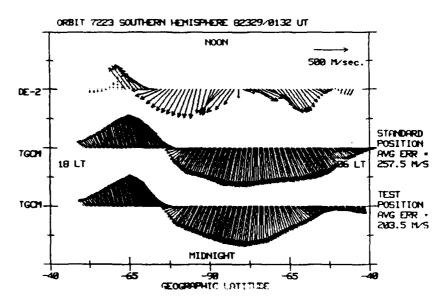
convection parameterization technique resulted in the most accurate neutral-wind simulation.

The development and test of the experimental technique was still worthwhile. Table 7.5 shows that there were two orbits, the southern hemisphere of orbit 7219 and the northern hemisphere of orbit 7244, where the experimental technique did substantially better than the standard analytical technique. What were the reasons for more accurate neutral winds on those particular orbits? Further, why was the standard analytical high-latitude ion convection parameterization technique better at simulating the neutral winds in both hemispheres for the orbit series 7230, 7232, and 7236? The answers to these questions are multi-faceted and are based solely on this single set of comparable NCAR-TGCM runs with only 10 orbits of dual-hemisphere neutral-wind data for simulation verification, so they should not be considered conclusive.

To begin, if only the ten orbits which supplied DE-2 neutral winds and ion drifts in both hemispheres are considered, orbits 7214 - 7241, then the final compilation of which method of determining the high-latitude ion-convection parameters was more accurate is shown in table 7.6. The standard analytical technique of high-latitude ion-convection and auroral-model parameterization was accurate a larger number of times (5) in both hemispheres. However, the experimental technique was accurate three times more often in the summer southern hemisphere, than in the winter northern hemisphere. This indicates that the use of DE-2 ion data to provide the model-ion-convection parameters is more likely to be successful in the sunlit summer hemisphere, where the measured ion drifts probably more closely represent the actual averaged ion convection. In the winter northern hemisphere, where ion convection is known to be more irregular (Heppner and Maynard, 1986 and DE-2 data in chapter VI), the standard analytical high-latitude ion-convection parameterization scheme is either clearly superior or of equal accuracy to the experimental technique 90% of the time. It is interesting to note that the only example for which the experimental technique was superior in both hemispheres was orbit 7214. This

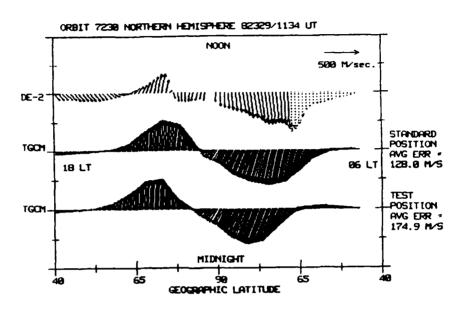
een maaaaaan beeelaan soosaal goodaan beeelaan beeelaan kaasaan kaasaan kaasaaan kaasaaaan maaaaaan maaaaan maa





TO A SECOND PROPERTY OF THE PR

Figure 7.16 - Same as figure 7.11 but for the northern and southern hemispheres of orbit 7223.



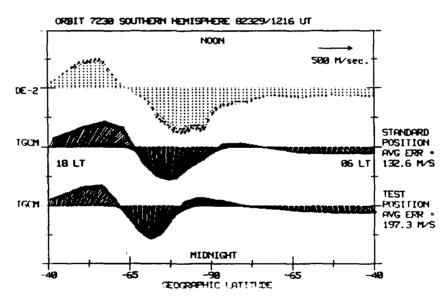


Figure 7.17 - Same as figure 7.11 but for the northern and southern hemispheres of orbit 7230.

orbit represents the onset of the geomagnetic storm after the sharp southward-turning of the IMF B_z component. Whether this result will hold for other storm simulations remains to be seen. As far as the series of orbits where the standard experimental technique resulted in more accurate neutral-wind simulations in both hemispheres for the orbit sequence 7230,7232, and 7236, the analytical high-latitude ion-convection-parameterization technique appeared to do better than the experimental technique during periods when the external geophysical parameters were slowly changing. An example of such a period is shown in figures 7.1 and 7.3, when there was a quasi-steady IMF and a slow decrease in the K_p index.

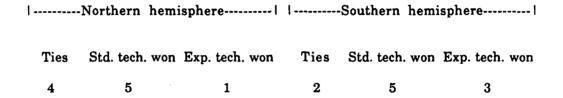
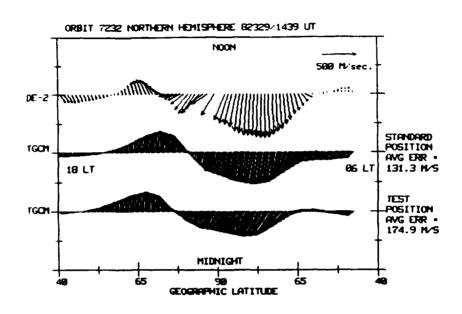
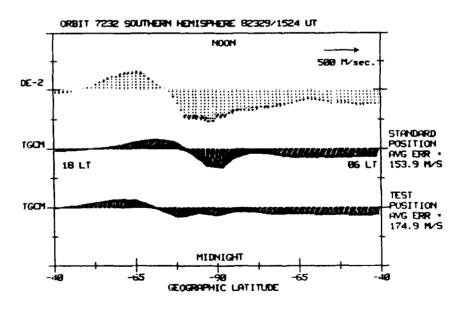


Table 7.6 - Results of the quantitative comparison between observed DE-2 and TGCM-simulated neutral winds, based on two different high-latitude ion-convection-parameterization techniques showing how many times the different techniques were more accurate or provided essentially the same results.

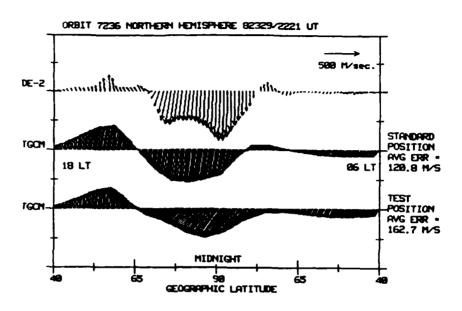
The statistics from tables 7.5 and 7.6 provide a general overview of the results of the comparisons between the measured neutral-wind data and the TGCM runs. However, a look at the actual data provided additional insight. Due to the limitations of the current version of the Heelis et al. (1982) ion convection model, it was not expected that the neutral winds during $B_z > 0$ periods would be accurately simulated. Simulation of the neutral winds by a TGCM for $B_z > 0$ conditions has not yet been achieved, because none of the ion-convection models, which attempt to simulate ion convection under $B_z > 0$ conditions (see chapter III), have been incorporated into an operational TGCM. The best that could be done was to minimize the cross-cap potential in a manner similar to that seen in the observed data above, but using the ion-convection model which corresponded to $B_z < 0$ conditions. As expected, the simulated neutral winds in the polar cap for both





Proposed Proposed Angeles and Proposed Control of the Control of t

Figure 7.18 - Same as figure 7.11 but for the northern and southern hemispheres of orbit 7232.



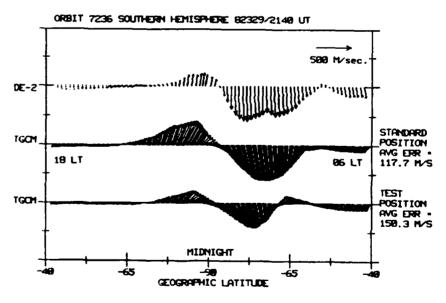
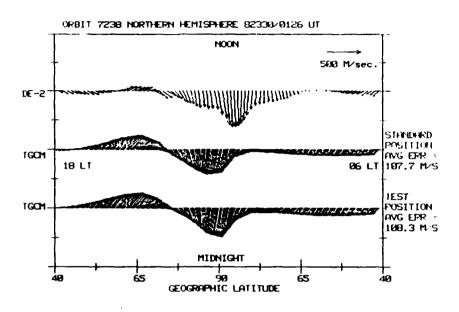


Figure 7.19 - Same as figure 7.11 but for the northern and southern hemispheres of orbit 7236.



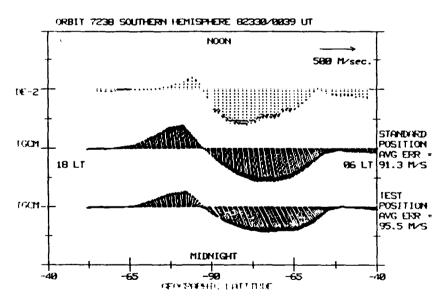
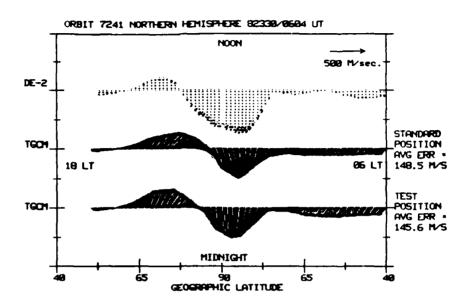


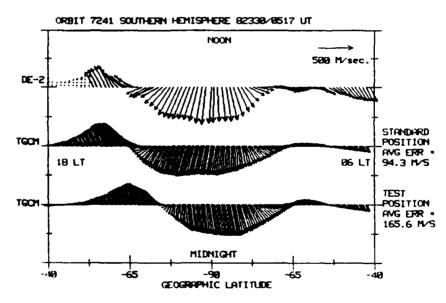
Figure 7.20 - Same as figure 7.11 but for the northern and southern hemispheres of orbit 7238.

techniques were very dissimilar to the measured neutral winds during IMF $B_z > 0$ periods, as can be seen in figure 7.11.

For other periods, such as the northern hemisphere of orbits 7230 (figure 7.17) and 7238 (figure 7.20), when the ion convection showed a $B_z > 0$ signature, the observed DE-2 neutral winds in the northern hemispheres appeared to have the lowest-latitude portions of the antisunward neutral winds decrease, but the antisunward signature of $B_z < 0$ neutral-wind circulation remained. This is presumably because the $B_z > 0$ ion convection did not persist for a long enough period (figure 7.1), such as one for ionneutral momentum-coupling time constant, which would be several hours in the winter hemisphere polar cap (chapter VI). It is also noted that it was not possible to tell what the individual-orbit neutral-wind signatures in the 0600/1800 local time plane would have looked like if there had not been a $B_z > 0$ influence (i.e., the IMF remained $B_z < 0$ for the entire post-storm period) without averaging the data for several orbits, such as was done to identify the universal-time effect in the antisunward neutral-wind magnitudes in chapter VI.

Looking again at the all the figures which show comparisons between the DE-2 neutral winds and the two simulations by the NCAR-TGCM (figures 7.11 to 7.22), there does not seem to be a significant change in the TGCM neutral winds of most orbits when the position of the center of the ion convection was changed from that of the invariant pole. In the summer southern hemisphere the only time the position of the invariant pole was changed by more than five degrees of latitude was for orbits 7217 and 7219, both of which occurred during the most intense portion of the geomagnetic storm. The movement of the center of the ion-convection pattern improved the neutral winds in both of these cases. The extent of the movement of the ion-convection cells can be judged in figure 7.8, where the dashed line represents the position associated with the center of the ion convection centered on the invariant-pole location. Since it was difficult to fit the Heelis ion-convection model to the winter-northern-hemisphere ion data, the location where the





post according to the property of the property

Figur: 7.21 - Same as figure 7.11 but for the northern and southern hemispher orbit 7241.

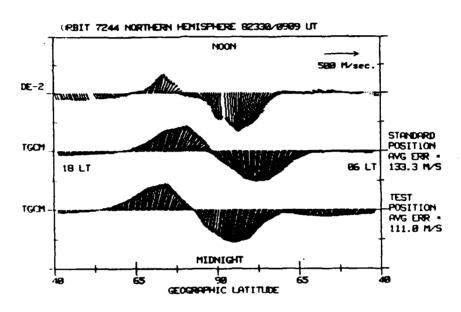


Figure 7.22 - Same as figure 7.11 but for the northern hemisphere of orbit 7244.

CONTRACT CONTRACTOR CO

center of the ion-convection model should be positioned could not be located with confidence. As a result, ion-convection-model repositioning was minimized in the winter northern hemisphere, so the analytical high-latitude technique would have been better for general use in the winter hemisphere. However, in the southern hemisphere the movement of the center of the ion-convection pattern is considerable. This is where the experimental technique excels. Also, notice the difference in the ion-convection-cell sizes between the northern and southern hemispheres. Using the analytical technique, the same ion-convection-cell radius was applied to both hemispheres, while using the experimental technique the radii were allowed to vary between hemispheres. Here again, the experimental technique based on measured ion-drift data introduced additional flexibility into global-scale numerical simulations which was shown to have the ability to improve thermospheric neutral-wind-simulation accuracy.

7.5 Summary

Contract Con

As a review of the results of this chapter, it can be seen that the NCAR-TGCM has a time-dependent neutral-wind-simulation capability, for IMF $\rm B_{z} < 0$ conditions. During the geomagnetic storm, the neutral winds increased as did the radius of the polar cap. The TGCM did not compute neutral winds which had comparable velocities to those seen in the DE-2 data, but the overall neutral-wind signature is very similar. The average difference vectors generally had magnitudes exceeding 100 m/s. This means that during quiet periods the magnitude of the neutral-wind-simulation error was on the order of 10%. However, during the peak of a storm, this increased to around 40%.

The analytical high-latitude ion-convection-parameterization technique was, in general, better at simulating the neutral winds than the experimental technique, based on a test of the use of DE-2 ion-drift data to determine the time-dependent sequence of model-ion-convection prescriptions in both hemispheres. This seemed to be due, in part, to the higher resolution of the IMF data, which helped to provide more meaningful

averages for the analytical high-latitude ion-convection parameterization scheme. In addition, a disadvantage of the experimental high-latitude ion-convection-parameterization technique was the inability to know when the ion drift data was representative of average ion-convection conditions. However, the experimental technique did seem to do better during the onset and main phase of geomagnetic storms, particularly in the summer hemisphere, where the measured ion drifts were more likely to represent the averaged ion convection. The onset of the geomagnetic storm was the time when the analytical technique was most likely to improperly position the ion-convection pattern or get the radius of the ion convection wrong. During the slow "wind-down" phase of the geomagnetic storm, the analytical technique appeared to be superior, especially if the IMF was rapidly jumping between IMF $B_{\rm Z} > 0$ and $B_{\rm Z} < 0$ conditions. The place where the experimental technique had the smallest chance of success was in the winter northern hemisphere, where it was impossible to determine whether or not the irregularities in the measured ion convection were representative of the averaged ion convection or just transient features.

CHAPTER VIII

PROSPECTS FOR NUMERICAL THERMOSPHERIC FORECASTS

8.1 Possible Methods of Forecasting the High-Latitude Ion-Convection Parameters

Based on the results of the time-dependent thermospheric modeling, it has been shown that knowledge of the interplanetary-magnetic-field (IMF) is required to simulate the high-latitude thermospheric dynamics. The most important influence on the high-latitude thermospheric circulation at high latitudes of both hemispheres is the distribution of the polar-cap electric field. Furthermore, the time-dependent morphology of the polar-cap electric field is controlled mainly by the orientation of the north-south component of the IMF. Therefore, in order to numerically forecast thermospheric circulation, one must have a series of model-ion-convection parameters which will precisely describe how the ion convection will vary with time. This requires a reasonable prediction of the IMF orientation or more simply, the future polar-cap electric-field distribution. However, there are many problems in understanding the seemingly random behavior of the IMF. Furthermore, without a prediction of the IMF orientation, accurate predictions of the polar-cap electric field are not likely.

In the search for a practical method with which to provide the model-ion-convection parameters for numerical thermospheric forecasts, a couple of different approaches were tried. These included attempts to forecast the IMF B_z component for the next 24 hours, based on its trend over the previous two hours. The approach which offered the most encouragement for use in establishing an early thermospheric-forecast capability was a mixture of statistical techniques borrowed from tropospheric

meteorology. The mix of techniques involves forecasting persistence in the IMF and polar-cap electric-field conditions during slowly-changing conditions. However, when a large and persistent change in the north-south component of the IMF was recorded over a two-hour period, then a new time-dependent series of ion-convection parameters would be used, corresponding to a historical variation of ion-convection parameters for IMF conditions most closely matching the currently-observed trends. These ion-convection parameters would be based on IMF parameters observed in real time and would be used as input to a numerical thermospheric global-circulation model (TGCM). The output of the model would be the thermospheric neutral-wind forecast.

One may also ask why a thermospheric-forecast capability be of interest? A thermospheric-forecast capability would be an excellent research tool, allowing us to test our current knowledge against the natural variability which exists in every aspect of atmospheric science. In addition, there are practical interests related to the horizontal transport of ionic and neutral species.

8.2 Attempts to Forecast the IMF

It has been known for many years that fluctuations in the IMF, ΔB , are on the same order of magnitude as the magnetic-field itself (Barnes et al., 1984). The random behavior of the IMF is similar to that measured by a surface-wind-direction recorder. With this in mind, the approach usually taken to categorize the IMF is statistical and is similar to that used in turbulent fluid mechanics.

Using statistical autocorrelation theory, Jokipii (1971) used Mariner-4 IMF data to observe the power spectra of IMF fluctuations. In figure 8.1, it is seen that most of the power is in the low-frequency oscillations. The high-frequency oscillations had very little power and were almost totally uncorrelated. The correlation time, after which the IMF has no memory of its past, is estimated to be on the order of several hours. This

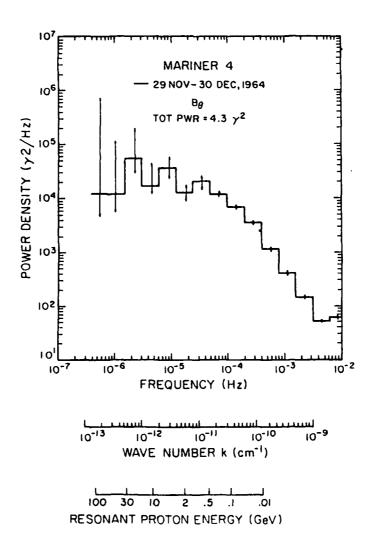


Figure 8.1 - The power spectrum of the component of the IMF normal to the solar-equatorial plane, observed by Mariner-4 (Jokipii, 1972).

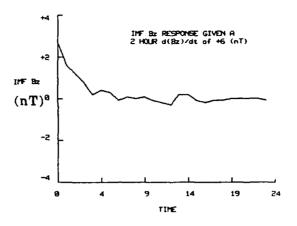
makes it virtually impossible to forecast the IMF for periods longer than one correlation time.

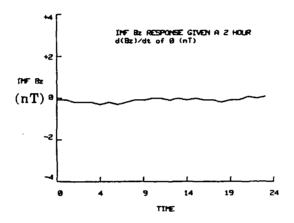
After taking the above factors into consideration, it was still considered interesting to see if the IMF B_z component, which controls the magnitude of the cross-polar-cap convection-electric field could be forecast under certain conditions. If IMF forecasting proved to be impossible for useful time periods, at least quantification of these attempts could be useful. Hourly-averaged IMF data, covering the 507 days of the DE-2 mission from August 1981 to February 1983, was used as the database from which IMF "hindcasting" was be attempted. Although use of hourly-averaged IMF data eliminated most of the higher-frequency fluctuations, this data still represents a reasonably accurate mean for each hour and its use in IMF forecasting for the 12 - 24 hour period was the goal.

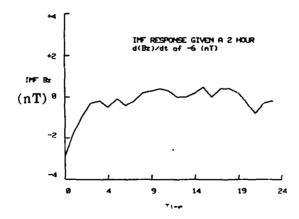
PROPERTY SEEDING CONFERENCE SOCIONOS POCOCOSOS

In order to use the hourly-averaged IMF data over the DE-2 mission, to provide insight on how the IMF B_z component responded over the next 24 hours, given an observed trend, the data must be properly binned. It was determined that the selection criteria for binning the IMF data, over a 24-hour period, would be a change in IMF B_z component over the past two hours. A one-hour trend in B_z was sometimes shown to be a false indicator of an ongoing IMF trend because the time scale of the trend and the time resolution of the averaged IMF data were the same. Thirty bins of $\partial(B_z)/\partial t$ were created, from +15 to -15 nanoTesla (nT), separated by a one nT absolute value change in B_z over two hours.

The mean values of the actual IMF B_z component at the end of the two hours were used to designate the proper bin row, then the corresponding IMF B_z values for the next 24 hours were placed in this bin row. Selected results are shown in figure 8.2. Basically, if the IMF goes up by several nT during a two-hour period, then the starting value of B_z is large and the wave train appears to move back to background levels over the next 24 hours. The same is true for a significant IMF downward trend over two hours. In that case, the B_z component returns to approximately zero after a few hours. When the $\partial(B_z)/\partial t$ value was unchanged over two hours, the follow-on hours also showed little change.





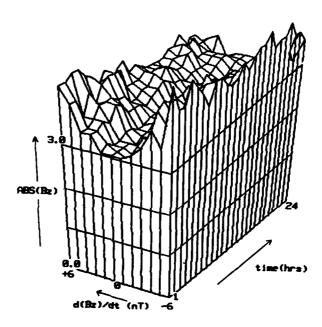


Where 8.2 - A three-panel plot of the time response of the average value of the IMF B_z -ment (in nT) to various changes in the IMF B_z -component over a two-hour with using hourly-averaged ISEE-3 data for the 507 days of the DE-2 mission.

Though the above results were intuitively expected and seemed hopeful, it was not known if the reason that the mean B_z component after several hours was close to zero was because the magnitude of B_z was decreasing, as hoped a_z at the other extreme, that random, large-scale fluctuations in B_z were cancelling each other out. To discover the answer to this question, the same procedure as above was repeated, except the mean absolute value of B_z over a 24-hour period was found. The results are also shown in figure 8.3. They show that even though most of the high-frequency oscillations are eliminated, the hourly-averaged data has little memory of past events and the absolute magnitude of the IMF varies little over the 24 hour "forecast" period. This left little hope for forecasting the IMF B_z component.

8.3 Forecasting Model-Ion-Convection Parameters

Only long-lived major changes in the IMF B_z component, not small ripples, were expected to exert a significant influence on the thermosphere by causing major changes in the ion convection. It was arbitrarily assumed that the change necessary to see a significant effect in thermospheric circulation due to a change in ion convection, is on the order of $\Delta B \sim 5$ nT or greater. Furthermore, it was assumed that this change must remain in effect for more than one hour to have a significant effect on the thermospheric neutral winds, based on the actual ion-neutral time constants (chapter VII). Therefore, it was desirable to make the connection between significant changes in the IMF B_z component, which would effect IMF/magnetospheric/ionospheric coupling, and ion-convection parameters. The intent here was to track past changes in the IMF and relate them to a set of time-dependent ion-convection parameters in both hemispheres. Then, after observing many such events, it might be possible to associate past changes in the IMF with a respective set of time-dependent ion-convection parameters, then apply this historical time sequence of ion-convection parameters as the prescription for future changes. This is based on the assumption that time-dependent model-ion-convection



grand a contract accounts becommed accounts accounts accounts accounts account accounts account accounts account

Figure 8.3 - A three-dimensional plot of the time response of the absolute value of the IMF B_z -component to various changes in the IMF B_z -component over a two-hour period, using the same ISEE-3 data as in figure 8.2.

parameters respond similarly under similar time-dependent variations in IMF conditions.

To illustrate this, assume the IMF turns sharply southward. Under these conditions, the electric field, transmitted via the magnetosphere to the polar-cap ionosphere as a result of increased magnetic merging. As a result, the ion drifts quickly increase and the polar-cap region expands, just like the storm case analyzed in chapter VIII. The thermospheric circulation is "spun-up" due to this "kick" and over the next several hours, slowly spins down. Based on observations of the DE-2 neutral winds for the time-dependent case used in the last chapter, subsequent southward turnings of the IMF or "kicks", especially if they are smaller than the original, have a little effect on the thermosphere because the difference between the ion and neutral velocities is reduced resulting in a smaller ion-drag force. Recall from figure 8.1 that there were several transitions from $B_z > 0$ to $B_z < 0$ following the onset of the large geomagnetic storm. However, the highest-velocity polar-cap neutral winds were established early in the storm and decreased with time. The polar-cap neutral winds did not appear to reach new maximum velocity levels each subsequent time the IMF turned sharply southward. This upper-thermospheric observation may be related to the thermospheric-modeling efforts of Roble et al. (1987a) where it was found that the lower-thermospheric-circulation features, once established, tended to persist several hours after the substorm forcings have subsided. The same effect is seen here for upper-thermospheric neutral-windcirculation systems. This means that the most important ion-convection parameters to model are those associated with the initial southward-turning of the IMF (i.e., the "kick").

At the other extreme, for periods when the averaged-IMF turns sharply positive, the coupling between the IMF and the magnetosphere is reduced. Ion-convection parameters corresponding to a similar northward-turning IMF case could then be used as input to the TGCM. In the case where the measured IMF B_z component was is quasi-

steady, no changes would be required. A forecast of persistence would be applied and there is no need to change the set of ion-convection parameters currently being used.

The advantage of this method is simplicity. To illustrate this see the flowchart for a tentative thermospheric-forecasting capability (figure 8.4). Only certain, directlymeasured IMF quantities are required to be monitored and the need for much of the uncertain aspects of solar and magnetospheric physics is eliminated. Further, only when significant long-lived changes in the IMF occur, would an update of the present forecast required. In addition, the thermospheric circulation has been shown (chapter VII) to display a daily periodicity and only a finite number of IMF $f B_z$ trend bins and the associated averaged time-dependent ion-convection parameters, for both storm and steady states are anticipated. The number of sets of ion-convection parameters is estimated to be on the order of 20, for the solar-maximum conditions considered here. This means all cases could be run in advance and the results stored for later use. Under these conditions, the vector-spherical-harmonics (VSH) model of Killeen and Roble (1986) could be extremely useful. The output of each run of the TGCM could be reduced to a set of truncated coefficients which can be stored on a microcomputer. When the need for a new forecast arises, the set of coefficients corresponding most closely to the IMF Bz changes measured can be used with the VSH model to regenerate the neutral winds at selected altitudes and universal times. The reconstituted neutral-wind circulation has been shown to be an almost perfect match to the original neutral-wind results. Furthermore, use of the VSH model no longer requires a significant period of time for the TGCM to be run in realtime on a supercomputer.

This tentative thermospheric-forecasting capability is quite unusual in the world of atmospheric science. The ability to quickly forecast the dynamics of the atmosphere using a finite set of pre-run coefficients is quite different from forecasting tropospheric weather. All that's required to provide the foundation for this forecasting capability is to continue the "hindcasting" process begun in the last chapter.

Flowchart of thermospheric forecasting methodology

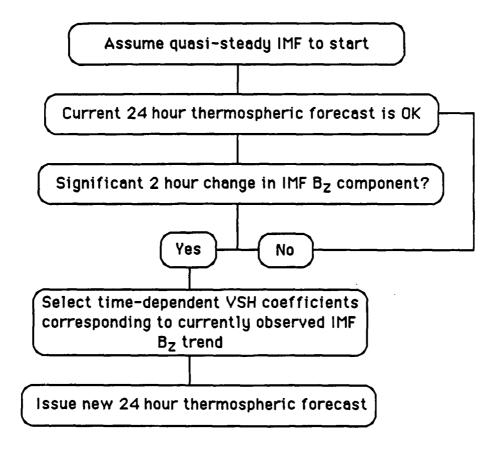


Figure 8.4 - Flowchart of the tentative methodology for a basic thermospheric-forecast capability.

8.4 Areas Requiring Additional Effort Before An Effective Thermospheric-Forecast Capability Can Be Established

It is obvious that for the methodology described above to work, additional spacecraft ion-drift and neutral-wind data is needed. Without the ion drift data, time-dependent histories of ion convection in both hemispheres cannot be determined. Furthermore, neutral-wind data is required to conduct ion-neutral coupling studies, both at solar maximum and solar minimum. The desired improvements in neutral-wind-simulation capability cannot be verified without globally-measured neutral-wind data.

There are also some ionospheric features which need to be represented in TGCMs, if the models are going to more realistically reproduce naturally-occurring thermospheric phenomena. Some of these areas include the following: (a) more realistic ion-density fields in the TGCM; (b) incorporation of the day-to-night conductivity-gradient effect, which will shift the antisunward ion-drift region more to the dawnside of the polar-cap, regardless of IMF configuration; (c) realistic ion-convection models for IMF $B_z > 0$ conditions. To the author's knowledge, efforts to incorporate items (a) and (c) into the NCAR-TGCM are underway. However, the incorporation of the day-to-night conductivity-gradient effect should be addressed by ionospheric modelers.

CHAPTER IX

RESULTS AND CONCLUSIONS

9.1 Summary of Research

Proceedings - Consistent Consiste

The primary objective of this work has been to develop a better understanding of the neutral-gas dynamics of the high-latitude regions of the Earth's upper thermosphere. To achieve this, an understanding of the morphology of the neutral winds and the forces which drive or modify them was required. To this end, a unique dataset was established which utilized satellite neutral winds and other supporting data from Dynamics Explorer 2 (DE-2), with coverage of both polar caps during the same orbit.

Analysis of these data led to the characterization of four basic neutral wind signature categories for the various interplanetary-magnetic-field (IMF) configurations, as well as observations of similarities and asymmetries in the neutral circulation between hemispheres for solar-maximum December-solstice conditions. Averaging of the neutral-wind data in various IMF categories has provided preliminary indications of the influence of IMF-controlled ion-convection on the polar-cap antisunward and duskside sunward neutral winds. Analysis of the individual neutral-gas forces from the diurnally-reproducible version of the NCAR thermospheric general-circulation model (TGCM) provided insight into the causes of "seasonal" and diurnal variations in the high-latitude neutral-wind-circulation system. This resulted in the "seasonal" differences of the polar-cap pressure-gradient force between hemispheres explaining the virtual absence of dawnside-sunward neutral winds in the summer southern hemisphere which are usually observed in the winter northern hemisphere.

The knowledge acquired above was applied to two tests of the time-dependent capabilities of the NCAR-TGCM, with the intention of evaluating the use of TGCMs for thermospheric forecasting. The first TGCM simulation was accomplished in an effort to quantitatively evaluate the ability of the TGCM to yield accurate time-dependent neutral winds. The results of this test were that the NCAR-TGCM provided good first-order time-dependent neutral winds with errors from the DE-2 measured neutral winds of 10 - 40%. A second TGCM simulation was intended to assess our ability to use DE-2 measured ion-drift data to provide a more realistic time-dependent prescription of model-ion-convection parameters in both hemispheres. Results here, show that use of DE-2 measured ion-drift data, under selected geophysical conditions, can improve the ability of the TGCM to simulate thermospheric neutral winds.

9.2 Synopsis of Major Results

appressed appropriate the property of the prop

9.2.1 Major Morphological Results

Four-basic characteristic neutral-wind signatures have been identified that may be categorized according to the orientation and magnitude of the IMF, viz: 1) $B_z < 0$, $B_y > 0$; 2) $B_z < 0$, $B_y < 0$; 3) $B_z > 0$; and 4) $B_z > 0$. For all $B_z < 0$ conditions, there was a two-cell structure to the neutral circulation in both hemispheres with a well-established dusk cell and a small weak dawn cell. Under $B_z < 0$, $B_y > 0$ IMF conditions, the maximum antisunward neutral winds were clearly located on the dawnside of the polar-cap flow in the northern hemisphere and on the duskside of the polar-cap flow in the southern hemisphere. For $B_z < 0$, $B_y < 0$ IMF conditions, the maximum antisunward neutral winds were located on the duskside of the polar-cap flow in the northern hemisphere and on the dawnside of the polar-cap flow in the northern hemisphere and on the dawnside of the polar-cap flow in the southern hemisphere, although this case was not as clearly pronounced as the $B_z < 0$, $B_y > 0$ case.

When B_z was slightly northward, a transitory neutral-wind state existed, where the neutral-wind signatures varied greatly between hemispheres. In the winter northern

hemisphere, the antisunward-neutral-wind speeds were diminished in the center of the polar cap, as though in preparation for a change to sunward flow in the center of the polar cap. In the summer southern hemisphere, the neutral circulation retained the two-cell circulation structure with the maximum-antisunward neutral winds located in the center of the polar cap. Under $B_z >> 0$ conditions, the neutral winds in both hemispheres had a multicell structure, although the region of sunward-neutral-wind speed in the center of the polar cap was small and associated with relatively small neutral-wind speeds.

In the analysis of the interhemispheric neutral-wind signatures, two universaltime periods were given special attention, namely 09 - 11 and 21 - 23 UT. During these periods, the local-time plane of the invariant-geomagnetic-pole longitude in both hemispheres, was such that the DE-2 spacecraft-sampled essentially-conjugate regions. Data obtained during these universal times enabled characteristic differences in the neutral-wind signatures of both hemispheres to be examined, without the ambiguity caused by the hemispheric differences in the displacements of the invariantgeomagnetic and geographic poles. At "conjugate-sampling" universal times, with the spacecraft in the dawn-to-dusk local-time plane, the (latitudinal) width of the antisunward polar-cap neutral winds was found to be two to six degrees larger in the northern hemisphere than in the southern hemisphere, under quasi-steady IMF conditions. This asymmetry was due to the different geomagnetic topology in the northern hemisphere, with the non-dipolar terms being of significantly greater importance in the northern hemisphere, than the southern hemisphere. For the conjugate-sampling periods, the major axis of the ellipse describing the contours of constant invariant latitude was approximately aligned with the 0600/1800 local-time plane, and therefore the spacecraft observed the maximum asymmetry at these universal times. This asymmetry between northern and southern hemispheres was not predicted by the current theoretical models. These models need to be reformulated using a more

transfer the second second second second second second second second second second

realistic magnetic-field topology in order to be able to simulate these asymmetricneutral-wind fields.

At the conjugate-sampling time ranges of 09 - 11 and 21 - 23 UT, individual orbits in the DE-2 dataset showed that the winter-northern-hemisphere polar cap had larger maximum antisunward neutral-wind speeds than the summer-southern-hemisphere polar cap when the IMF was in a $B_z < 0$, $B_y > 0$ configuration. The results were reversed for the $B_z < 0$, $B_v < 0$ IMF orientation. This finding was unexpected since the summer hemisphere generally has higher average levels of ionization and ion drag. Therefore, the summer southern hemisphere was intuitively expected to have higher convectiondriven neutral-wind speeds. Averaged DE-2 neutral winds in the dawn/dusk plane, at the conjugate-sampling UTs, provided preliminary indications that higher-velocity antisunward neutral winds were seen in the hemisphere which has the largest-duskside ion-convection cell, which is controlled by the sign of the IMF By component. The maximum-average-antisunward neutral winds were 160 m/s higher in the northern hemisphere than the southern hemisphere at 09 - 11 UT and 220 m/s higher in the northern hemisphere for 21 - 23 UT, when IMF $B_v > 0$ conditions prevailed. This was contrasted by summer-southern-hemisphere maximum-average-antisunward neutral-wind speeds which exceeded those of the winter northern hemisphere by 170 m/s at 09 -11 UT and by 15 m/s for 21 - 23 UT under IMF B_v < 0 conditions. However, the number of DE-2 neutralwind orbits available for this very selective study was not considered sufficient to provide conclusive results. It is for this reason, that the results are considered "preliminary."

reconstruction of the second services and the second secon

Both the DE data and TGCM neutral-wind calculations, in the dawn/dusk local-time plane, show that the dusk cell was usually the dominant of the two neutral-circulation cells, in both size and magnitude of sunward-return flow. Under conditions identical to those mentioned above for the antisunward neutral flow, the magnitude of the maximum-duskside sunward-return flow averaged 260 m/s and the sunward winds extended over a 25-degree-wide region in either hemisphere when the dusk ion-

convection cell was dominant (i.e., $B_y > 0$ ($B_y < 0$) in the northern (southern) hemisphere). However, when the dawn ion-convection cell was dominant in either hemisphere, the maximum-average duskside-sunward-return flow was about the same at 230 m/s, but the neutral-wind reversal extended over only a 17-degree wide region. As with the antisunward neutral flow, the IMF B_y configuration was seen to control the ion convection, which in turn influenced the sunward-duskside neutral flow to a large extent, with only minor variations between hemispheres.

The dawn-cell neutral circulation, as seen by the latitudinal extent and magnitude of the sunward neutral flow, was found to be stronger and more organized in the winter northern hemisphere than in the summer southern hemisphere in both individual orbits which covered both hemispheres and averaged data. The maximum-sunward-dawnside return flow averaged 120 m/s in the northern hemisphere and was virtually non-existent in the summer southern hemisphere. Further, the summer-hemisphere-dawnside circulation was shown to be more divergent than the winter-hemisphere-dawnside circulation, even though the summer hemisphere is more tightly-coupled to the non-divergent twin-cell ion convection. From modeling studies, these relationships were ascribed to the orientation of the polar-cap pressure-gradient forces, which were dawn-to-dusk-directed in the summer hemisphere and sunward-directed in the winter hemisphere. The dawnside portion of the thermospheric neutral circulation was seen to be largely controlled by "seasonal" differences in both the measured data and model calculations.

CONTRACTOR DECEMBER STATES CONTRACTOR CONTRA

Based on diurnally-reproducible IMF $B_y = 0$ TGCM model results, the calculated summer-southern-hemisphere antisunward neutral winds were oriented at an angle of 5 to 15 degrees counterclockwise from that of the antisunward-convecting ions. The angle from which the polar-cap antisunward neutral winds deviated from the noon-midnight local-time plane was larger in the winter northern hemisphere than in the summer southern hemisphere by an additional 5 - 10 degrees due to the increased importance of

forces other than ion drag. The diurnal variation of the angle the TGCM antisunward-drifting ions made with the noon-midnight local-time plane was followed by the TGCM neutral winds. Unfortunately, insufficient DE-2 ion-drift data was available to provide an indication of the averaged-diurnal variation of the angle the actual antisunward-drifting ions made with respect to the noon-midnight local-time plane. Using averaged DE-2 neutral-wind data, an IMF B_y -dependent difference is seen in the variation of the angle the antisunward neutral winds make with respect to the noon-midnight local-time plane. Under IMF $B_y > 0$ ($B_y < 0$) conditions, the counterclockwise twist is greater in the northern (southern) hemisphere.

9.2.2 Neutral-Gas Momentum-Forcing Mechanisms

Mean ion-neutral momentum-coupling time constants, which are an estimate of the time required for the neutral winds to approach the ion-drift velocity following an instantaneous-ion-drift-velocity change, were computed using DE-2 data for the four-characteristic neutral-wind-signature categories and for the regions poleward of 40 degrees in both hemispheres. The winter-hemisphere time constants were at least twice as large as the summer-hemisphere values, in all cases. The mean time constants for the first three cases were approximately one hour in the summer hemisphere and two to three hours in the winter northern hemisphere. However, for the $B_z >> 0$ case, the summer-hemisphere time constant exceeded two hours while the winter-hemisphere time constant increased to over four hours.

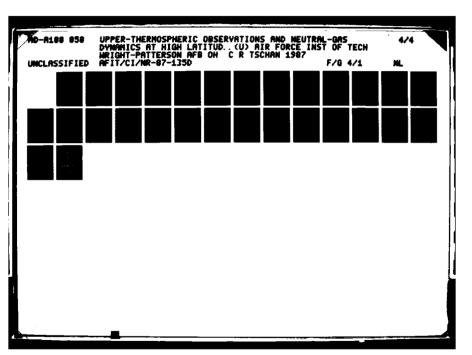
The momentum forcing over both invariant poles was analyzed from the diurnally-reproducible TGCM run. It was found that the zonal and meridional components of the individual forces in opposite hemispheres, for a solar-maximum December solstice, were remarkably similar. However, the differences between the vector magnitude of the individual forces, in opposite hemispheres, were significant. In general, the pressure-gradient force was the most important force in both hemispheres.

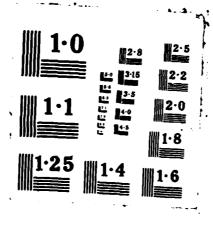
The peaks and valleys in the diurnal variation of the pressure-gradient force occurred at approximately the same local time in both hemispheres. However, the relative magnitude of the peaks varied for different seasons. During the post-midnight hours, the pressure-gradient force was often twice as strong as ion drag. During the day, the peaks and valleys of both the ion-drag and pressure-gradient forces had similar magnitudes. In addition, viscous drag was generally twice as large in the winter northern hemisphere as in the summer southern hemisphere, indicating greater vertical-neutral-wind shears in the winter northern hemisphere.

CONTRACTOR MANAGEMENT

The antisunward neutral winds from the diurnally-reproducible TGCM simulation were observed to exceed the antisunward ion drifts inside the polar cap. This occurred because the ion-drag force inside the polar cap was secondary in importance to the pressure-gradient force. Theoretical studies of the neutral-gas parcel-trajectory-forcing history over both invariant poles show this to be true in both hemispheres at solstice.

The radius of the diurnally-reproducible neutral-wind-circulation system was typically 30 degrees, while the radius of the high-latitude ion convection was typically 25 degrees. Through all 24 hours of universal time and in both hemispheres, the duskside boundary of the high-latitude ion-convection and neutral-wind-circulation systems were seen to coincide. The dawnside of the neutral-wind-circulation system was seen to extend out, past the boundary of the ion convection. This larger spatial extent of the neutral circulation over the driving non-divergent ion convection, in the inertial-reference frame, was caused primarily by the dusk-to-dawn component of the polar-cap pressure-gradient force. This polar-cap pressure-gradient force was shown to be due to both the spatial variations in neutral temperature and density. The polar-cap temperature distribution was, in turn, shown to result from the superposition of the solar-EUV, cusp, and Joule heating.





9.2.3 NCAR-TGCM Neutral-Wind-Verification Test

The first database of neutral winds, with coverage over both polar regions on individual orbital passes (~ 70 orbits), enabled the global accuracy of neutral-wind simulations from a TGCM to be critically-evaluated. Two time-dependent runs of the NCAR-TGCM, each simulating the same period in November 1982, but using different techniques to prescribe the high-latitude ion convection were compared against measured DE-2 neutral winds. The objective was twofold. First, validate the time-dependent TGCM neutral-wind-simulation capability and second, determine the weak and strong points of each of the high-latitude ion-convection-parameterization techniques. One technique analytically determined all the ion-convection parameters from a series of relationships which required knowledge of the IMF. The other technique found the ion-convection parameters by fitting the ion-convection model to experimental DE-2 ion-drift data.

The TGCM model inputs which need to be most realistically characterized at high latitudes are: the average ion convection and spatial variations in the ion densities. In this work, the search for a method to more realistically characterize the average ion convection was undertaken. Neither the analytical or experimental high-latitude parameterization techniques proved to specify the ion convection as accurately as hoped. Looking only at the number of times that one of the high-latitude parameterization techniques was more accurate than the other, the analytical technique was more accurate in simulating DE-2 satellite neutral winds in both hemispheres. However, there were several orbits when the center of the ion-convection model was moved significantly from the standard location associated with the invariant pole and the accuracy of the neutral-wind simulation was increased. In these cases, the high-altitude ion-convection-parameterization technique, which used DE-2 ion-drift data, was significantly more accurate. In general, the best way to improve TGCM neutral-wind-simulation accuracy

may be to combine the analytical and experimental ion-convection-parameterization techniques, whenever possible.

9.2.4 High-Latitude Ion-Convection Modeling

Ion-drift data from DE-2 were used to specify the time-dependent model-ion-convection parameters for an experimental run of the NCAR-TGCM. If the DE-2 ion-drift data, in the dawn/dusk plane, showed the center of the antisunward ion convection to be located some distance from the invariant-pole location, then both the ion-convection and auroral-oval models were picked up and placed in a position where the model-ion-convection reversals closely matched those of the DE-2 data, in both radius and position. In addition, the model cross-cap electric potentials were specified using the integrated potential gradients from the DE-2 satellite data in the dawn-dusk plane.

Postoces

CANTESTANI BEZZEZEGA BESCOCCE

Results of the test between the analytical and experimental high-latitude ion-convection-parameterization techniques, mentioned above, are as follows: the analytic technique should be used in the winter hemisphere, where frequent irregularities in the measured ion convection make it difficult to derive ion-convection parameters which represent the average ion-convection system. The experimental technique is more applicable to the summer hemisphere, where the measured ion drifts are more representative of the time-averaged ion convection. Furthermore, the experimental technique was superior at providing average ion-convection parameters in both hemisphere during the onset of a large geomagnetic storm.

9.2.5 Numerical Thermospheric Forecasting

To forecast the dynamics of the thermosphere, it was found that a forecast of model-ion-convection parameters was required. The methodology for an initial thermospheric-forecast capability was established, based on the hypothesis that a historical series of derived model-ion-convection parameters could be associated with a

currently-observed trend in the IMF. This historical time-dependent series of model-ion-convection parameters would subsequently become input for the TGCM ion-convection-prescription forecast. If a number of cases corresponding to different sets of historical model-ion-convection parameters were run in advance (i.e., a number of diurnally-reproducible as well as time-dependent cases corresponding to increasing and decreasing IMF B₂) these cases could be reduced to sets of VSH coefficients, which could be used to quickly regenerate the thermospheric-neutral-wind fields which would serve as a thermospheric forecast. In this way, re-issuing a 12 - 24 hour thermospheric forecast based on a change in observed IMF could become trivial, as the only task becomes selecting the proper set of VSH coefficients.

9.2.6 Future Work

The diurnally-reproducible NCAR-TGCM results have provided the insight necessary to understand the universal-time and "seasonal" variations in neutral-gas momentum forcing at solar-maximum December solstice, in both hemispheres. However, this was only done for simple IMF $B_z < 0$, $B_y = 0$ conditions. To use TGCM model data to fully interpret DE-2 data in the four-basic neutral-wind-signature categories, additional diurnally-reproducible runs need to be attempted. The $B_y > 0$ and $B_y < 0$ simulations can be run in the near future. The $B_z > 0$ and $B_z >> 0$ run require additional capabilities in ion-convection models.

To conclusively determine which variations in the high-latitude neutral-wind signatures are truly hemispheric and which are seasonal, a solar-maximum June solstice also needs to be examined. Unfortunately, neutral-wind vectors for June are not available from DE-2 because the satellite was inverted during this period, so no FPI data is available. This means that conclusive determination of "seasonal" differences in the neutral winds at solstice will have to wait at least until the next solar-cycle maximum, or later. For the same reasons, the qualifier "preliminary" cannot be removed from the

observations which resulted from the averaged DE-2 neutral winds. All available orbits of DE-2 neutral winds at the conjugate-sampling universal times and in the 0600/1800 local-time plane were used and the statistics are still low to be conclusive.

It is obvious that continuation of work on high-latitude thermospheric-neutral-gas dynamics could be fruitful, for both research and practical interests. However, the DE-2 mission supplied a tantalizing but insufficient quantity of neutral wind measurements from which to draw long-term conclusions. It is indeed unfortunate that there are no known spacecraft missions currently planned which can be expected to globally measure the neutral winds of the terrestrial upper thermosphere, either for solar maximum or solar minimum.

APPENDICES

APPENDIX A

EXOTHERMIC CHEMICAL REACTIONS IN THE NCAR GLOBAL-MEAN MODEL AND TGCM (Roble, 1986; Roble and Ridley, 1987)

Neutral-Neutral Reactions

$$N(^2D) + O_2 \rightarrow NO + O(^1D) + 1.84 \text{ eV} + \text{quenching of } O(^1D)$$

$$N(^4S) + NO \rightarrow N_2 + O + 2.68 \text{ eV}$$

$$N(^{2}D) + O \rightarrow N(^{4}S) + O + 2.38 \text{ eV}$$

$$N(^4S) + O_2 \rightarrow O + NO + 1.4 \text{ eV}$$

$$N(^2D) + NO \rightarrow N_2 + O + 5.63 \text{ eV}$$

$$N(^2D) \rightarrow N(^4S) + hv$$

$$NO + hv (Ly_{\alpha}) \rightarrow NO^+ + e$$

$$O + O + M \rightarrow O_2 + M$$

$$O + O_2 + M \rightarrow O_3 + M$$

$$N(^{2}D) + e \rightarrow N(^{4}S) + e + 2.38 eV$$

Ion-Neutral Reactions

$$\mathrm{O^{+}(^4S)} + \mathrm{O_2} \longrightarrow \mathrm{O_2^+} + \mathrm{O} + 1.555 \mathrm{eV}$$

$$O^{+(4S)} + N_2 \rightarrow NO^+ + N(4S) + 1.0888ev$$

$$N_2^+ + O \rightarrow NO^+ + N(^2D) + 0.70 \text{ eV}$$

$$N_2^+ + O \rightarrow O^+ + N_2 + 1.96 \text{ eV}$$

$$O_2^+ + N(^4S) \rightarrow NO^+ + O + 4.21 eV$$

$$O_2^+ + NO \rightarrow NO^+ + O_2 + 2.813eV$$

$$N^+ + O_2 \rightarrow O_2^+ + N(^4S) + 2.486eV$$

$$\mathrm{N^{+}} + \mathrm{O_{2}} \rightarrow \mathrm{NO^{+}} \, \mathrm{O} + 6.699 \mathrm{eV}$$

$$N^+ + O \rightarrow O^+ + N + 0.93 eV$$

$$NO^+ + e \rightarrow (20\%) N(^4S) + O + 2.75eV$$

$$(80\%) N(^{2}D) + O + 0.38eV$$

$$O_2^+ + e \rightarrow (15\%) O(^3P) + O(^3P) + 6.95eV$$

(85%)
$$O(^{3}P) + O(^{1}D) + 4.98eV + quenching of O(^{1}D)$$

$$N_2^+ + e \rightarrow (10\%) N(^4S) + N(^4S) + 5.82eV$$

$$(90\%) N(^4S) + N(^2D) + 3.44eV$$

$$NO + h\nu(Ly_\alpha) \to NO^+ + e$$

Quenching reactions

$$O(^1D) + N_2 \rightarrow O + N_2 + 1.96 \text{ eV}$$

APPENDIX B

DE-2 SATELLITE ORBITS WHICH PROVIDED NEUTRAL-WIND COVERAGE IN THE HIGH LATITUDES OF BOTH HEMISPHERES

	Orbit	Date	Univ.	Hemi. Local time	IMF B _z IMF B _y	, Comments
			time	coverage plane	_	
1.	7073	82319	09 UT	$N \Rightarrow S 07:15/19:15$	neg pos	
2.	7111	82321	21 UT	$S \Rightarrow N 07:05/19:15$	neg neg	
3.	7114	82322	02 UT	$S \Rightarrow N 07:05/19:05$	neg neg	
4.	7117	82322	06 UT	$S \Rightarrow N 07:05/19:05$	pos neg	
5.	7134	82323	08 UT	$S \Rightarrow N 07:00/19:00$	pos neg	
6.	7164	82325	06 UT	$N \Rightarrow S 06:50/18:50$	neg pos	
7.	7183	82326	12 UT	$S \Rightarrow N 06:45/18:45$	pos neg	
8.	7186	82326	17 UT	$S \Rightarrow N 06:45/18:45$	pos neg	
9.	7198	82327	11 UT	$S \Rightarrow N 06:40/18:40$	pos neg	
10.	7214	82328	12 UT	$S \Rightarrow N 06:35/18:35$	neg pos	
11.	7217	82328	16 UT	$N \Rightarrow S 06:35/18:35$	neg pos	
12 .	7219	82328	19 UT	$N \Rightarrow S 06:35/18:35$	pos neg	
13.	7221	82328	22 UT	$N \Rightarrow S 06:35/18:35$	neg neg	
14.	7223	82329	02 UT	$S \Rightarrow N 06:35/18:35$	pos pos	
15.	7228	82329	09 UT	$N \Rightarrow S 06:35/18:35$	neg pos	Missing dusk
						reversal in N.H.
16.	7230	82329		$N \Rightarrow S 06:35/18:35$	pos pos	
17.	7232	82329		$N \Rightarrow S 06:35/18:35$	neg pos	
18.	7236	82329	22 UT		pos pos	
19.	7238	82330		$S \Rightarrow N \ 06:30/18:30$	pos pos	
20.	7241	82330		$S \Rightarrow N \ 06:30/18:30$	neg pos	
21.	7287	82333		$S \Rightarrow N 06:15/18:15$	neg pos	
22.	7289	82333		$S \Rightarrow N 06:15/18:15$	neg pos	
23 .	7291	82333		$S \Rightarrow N \ 06:15/18:15$	pos pos	
24.	7331*	82336		$S \Rightarrow N \cdot 06:05/18:05$ $N \rightarrow S \cdot 06:00/18:00$	neg pos	
25.	7357	82337		$N \Rightarrow S 06:00/18:00$	neg pos	
26.	7366	82338		$N \Rightarrow S 05:55/17:55$	pos neg	
27.	7384	82339		$S \Rightarrow N 05:50/17:50$ $N \Rightarrow S 05:45/17:45$	neg neg	
28. 20.	7397 7421	82340 82341		$N \Rightarrow S = 05:45/17:45$ $N \Rightarrow S = 05:40/17:40$	pos neg	
29. 30.	7431*	82342		$S \Rightarrow N \ 05:35/17:35$	neg neg	
30. 31.	7443			$S \Rightarrow N 05:30/17:30$ $S \Rightarrow N 05:30/17:30$	neg pos	Most of N.H.
31.	1440	02040	04 0 1	5 ⇒ N 05:50/17.50	neg pos	WATS missing
32 .	7447	82343	10 UT	$S \Rightarrow N 05:30/17:30$	pos neg	
33.	7454	82343		$S \Rightarrow N 05:30/17:30$	pos neg	
34.	7462*	82344		$S \Rightarrow N 05:25/17:25$	neg neg	Partial
						coverage of N.H.
35 .	7468	82344	18 UT	$N \Rightarrow S 05:25/17:25$	neg neg	
36.	7483	82345	18 UT	$S \Rightarrow N 05:20/17:20$	neg neg	

37.	7509	82347	10 UT	$S \Rightarrow N \ 05:10/17:10$	neg	neg	Partial coverage of N.H.
38.	7559	82350	14 UT	$S \Rightarrow N 05:00/17:00$	neg	pos	
39.	7573	82351	12 UT	$S \Rightarrow N 04:55/16:55$	neg	pos	
4 0.	7588	82352	11 UT	$S \Rightarrow N 04:50/16:50$	neg	neg	
41 .	7591	82352	15 UT	$N \Rightarrow S 04:50/16:50$	neg	neg	
42 .	7593	82352	18 UT	$S \Rightarrow N 04:50/16:50$	neg	neg	
43 .	7607*	82353	15 UT	$N \Rightarrow S 04:45/16:45$	pos	neg	
44.	7610	82353	20 UT	$S \Rightarrow N 04:45/16:45$	pos	neg	
45 .	7614	82354	03 UT	$S \Rightarrow N 04:45/16:45$	pos	neg	
46.	7632	82355	05 UT	$N \Rightarrow S 04:40/16:40$	neg	pos	
47 .	7641	82355	20 UT	$S \Rightarrow N 04:35/16:35$	neg	pos	
48.	7704*	82359	20 UT	$S \Rightarrow N 04:15/16:15$	N/A	N/A	Missing part of
							dusk reversal
4 9.	7764	82363	15 UT	$N \Rightarrow S 04:00/16:00$	pos	neg	
50.	7773*	82364	05 UT	$N \Rightarrow S 04:00/16:00$	N/A	N/A	
51.	7791*	82365	08 UT	$N \Rightarrow S = 03:55/15:55$	neg	neg	
52 .	7795	82365	15 UT	$S \Rightarrow N 03:55/15:35$	neg	neg	
53.	7811	83001	15 UT	$S \Rightarrow N 03:50/15:50$	N/A	N/A	
54 .	7874	83005	15 UT	$S \Rightarrow N 03:30/15:30$	N/A	N/A	
55.	7878	83005	21 UT	$N \Rightarrow S 03:30/15:30$	pos	pos	
56.	7883	83006	04 UT	$N \Rightarrow S 03:30/15:30$	pos	pos	
57.	7924	83008	19 UT	$S \Rightarrow N 03:15/15:15$	N/A	N/A	
58.	7965	83011	10 UT	$S \Rightarrow N 03:05/15:05$	N/A	N/A	
59.	7970	83011	18 UT	$N \Rightarrow S = 03:05/15:05$	pos	pos	
60.	8000	83013	14 UT	$S \Rightarrow N 02:55/14:55$	neg	pos	
61.	8050	83016	19 UT	$S \Rightarrow N 02:45/14:45$	pos	pos	
62.	8088	83019	03 UT	$N \Rightarrow S 02:30/14:30$	neg	pos	
63 .	8129	83021	17 UT	$N \Rightarrow S 02:20/14:20$	N/A	N/A	
64.	8141*	83022	12 UT	$S \Rightarrow N 02:15/14:15$	N/A	N/A	
65 .	8148	83022	23 UT	$S \Rightarrow N 02:15/14:15$	N/A	N/A	
66.	8159*	83023	15 UT	$N \Rightarrow S 02:10/14:10$	N/A	N/A	
67.	8273	83030	19 UT	$N \Rightarrow S 01:45/13:45$	pos	pos	

^{*} indicates orbits which provided neutral wind information in both hemispheres but insufficient multi-instrument support data to be classified as a true dual hemisphere data set.

REFERENCES

POTE PARTICULAR SECTION OF THE SECTI

REFERENCES

- Akasofu, S. I. The magnetospheric currents: an introduction. *Magnetospheric Currents*. Edited by T. A. Potemra. AGU monograph 28, American Geophysical Union, 1984.
- Akasofu, S. I. The polar caps, reprinted from Memoirs of National Institute of Polar Research Special Issue No. 38, Tokyo, 1985.
- Amayenc, P. Tidal oscillations of the meridional winds at midlatitudes. Radio Sci., 9, 281-294, 1974.
- Atkinson, G. Energy flow and closure of current systems in the magnetoshere. J. Geophys. Res., 83, 1089 1103, 1978.
- Atkinson, G. and D. Hutchinson. Effect of the day night conductivity gradient on polar cap convective flow. J. Geophys. Res., 83, 725 729, 1978.
- Alexander, J. K., L. F. Bargatze, J. L. Burch, T. E. Eastman, J. G. Lyon, J. D. Scudder, T. W. Speiser, G. H. Voigt, and C.-C. Wu. Coupling of the solar wind to the magnetosphere. Solar Terrestrial Physics: Present and Future. Edited by D. M. Butler and K. Papadopoulos. Chapter 5. NASA Reference Publication 1120, 1984.
- Axford, W. I. Magnetic field reconnection. Magnetic Reconnection in Space and Laboratory Plasmas, edited by E. W. Hones, Jr. AGU monograph 30, American Geophysical Union, Wash., D. C., 1 8, 1984.
- Axford, W. I. and C. O. Hines. A unifying theory of high-latitude geophysical phenomena and geophysical storms. Can. J. Phys., 39, 1433 1464, 1961.
- Banks, P. M. and G. Kockarts. Aeronomy. Academic Press, New York, 1973.
- Barnes, A., M. Goldstein, J. Hollweg, J. Mariska, W. Matthaeus, C. Smith, E. Smith, R. Stein, G. Withroe, and R. Woo. MHD waves and turbulence in the sun and interplanetary medium. Solar Terrestrial Physics: Present and Future. Edited by D. M. Butler and K. Papadopoulos, Chapter 4. NASA Reference Publication 1120, 1984.
- Bates, H. S. W. The structure of the terrestrial atmosphere at middle latitudes. chapter 2 of Applied Atomic Collision Physics. Edited by H. S. W. Massey and D. R. Bates. Academic Press, New York, 1982.
- Bernard, R. Incoherent scatter results for coordinated special intervals as St. Santin (France), J. Atmos. Terr. Phys., 36, 1105 1120, 1974.
- Bilitza, D. International reference ionosphere: recent developments. Radio Sci., 21, 343 346, 1986.
- Blamont, J. Optical observations of the thermosphere. J. Atmos. Terr. Phys., 37, 927 938, 1975.
- Blamont, J. E. and J. M. Luton. Geomagnetic effect on the neutral temperature of the Fregion during the magnetic storm of September 1969. J. Geophys. Res., 77, 3534-3556, 1972.

- Bird, G. A. Molecular Gas Dynamics. Oxford Univ Press, United Kingdom, 1976.
- Boris, J. P., C. R. DeVore, L. Golub, R. F. Howeard, B. C. Low, N. R. Sheeley, Jr., G. W. Simon, K. C. Tsinganos. Evolution of solar magnetic flux. *Solar Terrestrial Physics: Present and Future*, edited by D. M. Butler and K. Papadopoulos, Chapter 3. NASA Reference Publication 1120, 1984.
- Brace, L. H., R. F. Theis, and A. Dalgrano. The cylindrical electrostatic probes for Atmosphere Explorer-C, -D, and -E. Radio Science, 8, 341 348, 1973.
- Brinton, H. C., J. M. Grebowsky, and L. H. Brace. The high latitude winter F-region at 300 km: thermal plasma observations from Atmosphere Explorer-C. J. Geophys. Res., 83, 4767-4776, 1978.
- Burch, J. L. and R. A. Heelis. IMF changes and polar cap electric fields and currents. Dynamics of the Magnetosphere. Edited by S. I. Akasofu, D. Reidel, 47, 1979.

remain a second designation of the second of

- Burch, J. L., P. H. Reiff, J. D. Menietti, R. A. Heelis, W. B. Hanson, S. D. Shawhan, E. G. Shelley, M. Sugiura, D. R. Weimer, and J. D. Winningham. IMF By-dependent plasma flow and Birkeland currents in the dayside magnetosphere 1. Dynamics Explorer observations. *J. Geophys. Res.*, 90, 1577 1593, 1985.
- Burke, W. J., M. C. Kelley, R. C. Sagalyn, M. Smiddy, and S. T. Lai. Polar cap electric field structures with a northward interplanetary magnetic field. *Geophys. Res. Lett.*, 6, 21, 1979.
- Carbary, J. F. and C.-I. Meng. Relations between the interplanetary magnetic field B_z, AE index, and cusp latitude. *J. Geophys. Res.*, 91, 1549 1556, 1986.
- Carignan, G. R.; B. P. Block, J. C. Maurer, A. E. Hedin, C. A. Reber, and N. W. Spencer. The neutral mass spectrometer on Dynamics Explorer, *Space Science Inst.*, 5, 429-441, 1981.
- Chamberlain, J. W. Theory of Planetary Atmospheres: An Introduction to their Physics and Chemistry. Academic Press, New York, 1978.
- Chandra, S. and A. K. Sinha. The diurnal heat budget of the thermosphere. *Planet. Space Sci.*, 21, 593, 1973.
- Chapman, S. and J. Bartels. Geomagnetism. Oxford University Press, London. 1940.
- Chapman, S. and T. G. Cowling. The Mathematical Theory of Non-Uniform Gases. Cambridge University Press, New York, 1970.
- Ching, B. K. and Y. T. Chiu. A phenomenological model of global ionsopheric electron density in the E, F₁, and F₂ regions. J. Atmos. Terres. Phys., 35, 1616 1630, 1973.
- Chiu, Y. T. An improved phenomenological model of ionospheric density, J. Atmos. Terr. Phys., 37, 1563 1570, 1975.
- Chiu, Y. T., R. Anderson, J. Fennell, L. Frank, R. Hoffman, M. Hudson, L. Lyons, P. Palmadesso, E. Ungstrup, R. Vondrak, D. Williams, and R. Wolf. Connection between the magnetosphere and ionosphere. *Solar Terrestrial Physics: Present and Future*.

Edited by D. M. Butler and K. Papadopoulos, Chapter 7. NASA Reference Publication 1120, 1984.

Cole, K. D. Electrodynamic heating and movement of the thermosphere. *Planet. Space Sci.*, 19, 59-75, 1971.

Cole, K. D. Energy deposition in the thermosphere caused by the solar wind. J. Atmos. Terr. Phys., 37, 939 - 949, 1975.

Cowley, S. W. H. The causes of convection in the Earth's magnetosphere: a review of developments during the IMS. Rev. Geophys. Space Phys., 20, 531 - 565, 1982.

Cowley, S. W. H. Magnetospheric and ionospheric flow and the interplanetary magnetic field. The Physical Basis of the Ionosphere in the Solar-Terrestrial System. NATO advisory group for aerospace research and development conf. proc. number 295, Seine, France, 1981.

Cowley, S. W. H. Magnetospheric asymmetries associated with the Y-component of the IMF. *Planet. Space Sci.*, 29, 79 - 95, 1981.

Creekmore, S. P., J. M. Straus, R. M. Harris, B. K. Ching, and Y. T. Chiu. A global model of thermospheric dynamics I. Wind and density fields derived from a phenomenological temperature. J. Atmos. Terres. Phys., 37, 491 - 516, 1975.

Crooker, N. U. Solar wind-magnetosphere coupling. Rev. Geophys. Space Phys., 13, 955-958, 1975.

Crooker, N. U. Dayside merging and cusp geometry. J. Geophys. Res., 84, 951 - 959, 1979.

Crooker, N. U. Magnetopause merging site asymmetries. J. Geophys. Res., 90, 341 - 346, 1985.

Dalgarno A. and F. J. Smith. The thermal conductivity and viscosity of atomic oxygen. *Planet. Space Sci.*, 9, 1, 1962.

De La Beaujardiere, O. B., V. B. Wickwar, G. Caudal, J. M. Holt, J. D. Craven, L. A. Frank, L. H. Brace, D. S. Evans, J. D. Winningham, and R. A. Heelis. Universal time dependence of nighttime F-region densities at high latitudes., J. Geophys. Res., 90, 4319-4332, 1985.

Dessler, A. J. Geomagnetism. Chapter 8 of Satellite Environmental Handbook. Edited by F. S. Johnson. Stanford University Press, Stanford, CA 1965.

Dickinson, D. F., S. B. Mende, and D. S. Evans. Dayside variation in auroral conjugacy. Geophys. Res. Lett., 13, 68-71, 1986.

Dickinson, R. E., E. C. Ridley, and R. G. Roble. Thermospheric general circulation with coupled dynamics and composition. *J. Atmos. Sci.,41*, 205 - 219, 1984.

Dickinson, R. E., E. C. Ridley, and R. G. Roble. A three-dimensional circulation model of the thermosphere., J. Geophys. Res., 86, 1499 - 1512, 1981.

- Dickinson, R. E., E. C. Ridley, and R. G. Roble. Meridional circulation in the thermosphere, I, Equinox conditions, J. Atmos. Sci., 32, 1737 1754, 1975.
- Dickinson, R. E., E. C. Ridley, and R. G. Roble. Meridional circulation in the thermosphere, II, Solstice conditions, J. Atmos. Sci., 34, 178-192, 1977.
- Dungey, T. N. The morphology of the polar aurora. Phys. Rev. Lett., 6, 47-48, 1961.
- Emery, B. A. and R. G. Roble. Sensitivity of the mean global thermospheric temperature to the energy flux within various solar EUV wavelength intervals. unpublished manuspeript, 1983.
- Emery, B. A. and R. G. Roble. The solar EUV neutral gas heating efficiency. unpublished manuscript, 1983.
- Emery, B. A.; R. G. Roble, E. C. Ridley, T. L. Killeen, M. H. Rees, J. D. Winningham, G. R. Carignan, P. B. Hays, R. A. Heelis, W. B. Hanson, N. W. Spencer, L. H. Brace, and M. Sugiura. Thermospheric and ionospheric structure of the southern hemisphere polar cap on October 21, 1981, as determined from Dynamics Explorer 2 satellite data. J. Geophys. Res., 90, 6553 6566, 1985.
- Evans, D. S. A hemispheric power index based on NOAA 6/7 particle flux data. unpublished manuscript, 1984.
- Fairfield, D. H. Electric and magnetic fields in the high-latitude magnetosphere. Rev. Geophys. Space Phys, 15, 285 298, 1977.
- Fedder, J. A. and P. M. Banks. Convection electric fields and polar thermospheric winds. J. Geophys. Res., 77, 2328 2340, 1972.
- Feldstein, Y. I. and Y. I. Galperin. The auroral luminosity structure in the high-latitude upper atmosphere: its dynamics and relationship to the large-scale structure of the earth's magnetosphere. Rev. Geophys. Space Phys., 23, 217 275, 1985.
- Fesen, C. G., R. E. Dickinson, and R. G. Roble. Simulation of the thermospheric tides at equinox with the National Center for Atmospheric Research thermospheric general circulation model. *J. Geophys. Res.*, 91, 4471 4489, 1986.
- Fisk, L. A., R. A. Arnoldy, L. J. Lanzerotti, R. Lin, E. Oran, J. B. Reagan, M. Schulz. Impact of flares on the solar terrestrial environment. *Solar Terrestrial Physics: Present and Future*. Edited by D. M. Butler and K. Papadopoulos, Chapter 9. NASA Reference Publication 1120, 1984.
- Forbes, J. M., R. G. Roble, and F. A. Marcos. Thermospheric dynamics during the March 22, 1979 magnetic storm. 2. Comparison of model predictions with observations. Submitted to J. Geophys. Res., 1987.
- Foster, J. C., J. M. Holt, R. G. Musgrove, and D. S. Evans. Ionospheric convection associated with discrete levels of particle precipitation. *Geophys. Res. Lett.*, 13, 656 659, 1986.
- Frank, L. A., J. D. Craven, K. L. Ackerson, M. R. English, R. H. Eather, and R. L. Carovillano. Global auroral imaging instrumentation for the Dynamics Explorer mission. Space Science Inst., 5, 369 393, 1981.

Frank, L. A. and K. L. Ackerson. Observations of charged particle precipitation into the auroral zone. *J. Geophys. Res.*, 76, 3612 - 3643, 1971.

Froese-Fischer, C. and Saha. Multiconfiguration Hartree-Fock results with Briet-Pauli corrections for for adden transitions in the 2p⁴ configuration. *Phys. Rev. A*, 28, 3169, 1983.

Friis-Christensen, E., Y. Kamide, A. D. Richmond, and S. Matsushita. Interplanetary magnetic field control of high-latitude electric fields and currents determined from Greenland magnetometer data. *J. Geophys. Res.*, 90, 1325 - 1338, 1985.

Fuller-Rowell, T. J. A two-dimensional, high-resolution, nested-grid model of the thermosphere, 2. Response of the thermosphere to narrow and broad electrodynamic features. J. Geophys. Res, 90, 6567 - 6586, 1985.

Gold, T. Motions in the magnetosphere of the earth. J. Geophys. Res., 64, 1219 - 1224, 1959.

Grad, H. On the kinetic theory of rarefied gases. Comm. Pure Appl. Math., 2, 331 - 407, 1949.

Groves, G. V. and J. M. Forbes. Mean zonal and meridional accelerations and mean heating induced by solar tides for equinox and solstice conditions. *Planet. Space Sci.*, 32, 447, 1984.

Gustafsson, G. A revised, corrected geomagnetic coordinate system. Arkiv for Geofysik, 5, 595 - 617, 1970.

Hanson, W. B., R. A. Heelis, R. A. Power, C. R. Lippincott, D. R. Zuccaro, B. J. Holt, L. H. Harmon, and S. Sanatani. The retarding potential analyser for Dynamics Explorer-B, Space Science Inst., 5, 503-510, 1981.

Hanson, W. B., D. R. Zuccaro, C. R. Lippincott, and S. Sanatani. The retarding potential analyzer on Atmosphere Explorer. Radio Science, 8, 333-339, 1973.

Hargreaves, J. K. The Upper Atmosphere and Solar-Terrestrial Relations. Van Nostrand Reinhold, New York, 1979.

Harper, R. M. Tidal winds in the 100 to 200 km region at Arecibo. J. Geophys. Res., 82, 3243 - 3250, 1977.

Harper, R. M. A semidiurnal tide in the meridional wind at F region heights at low latitude. J. Geophys. Res., 84, 411 - 415, 1979.

Harper, R. M. Some results on mean tidal structure and day-to-day variablity over Arecibo. J. Atmos. Terres. Phys., 43, 255-262, 1981.

Hays, P. B. and R. G. Roble. Direct observations of thermospheric winds during geomagnetic storms. J. Geophys. Res., 76, 5316 - 5321, 1971.

Hays, P. B., R. A. Jones, and M. H. Rees. Auroral heating and the composition of the neutral atmosphere. *Planet. Space Sci.*, 21, 559 - 573, 1973.

- Hays, P. B., D. W. Rusch, R. G. Roble, and J. C. G. Walker. The O I (6300 A) Airglow. Rev. Geophys. Space Phys., 16, 225 231, 1978.
- Hays, P. B., J. W. Meriwether, and R. G. Roble. Nighttime thermsopheric winds at high latitudes. J. Geophys. Res., 84, 1905 1913, 1979.
- Hays, P. B., T. L. Killeen, and B. C. Kennedy. The Fabry-Perot inteferometer on Dynamics Explorer. Space Science Inst., 5, 395 416, 1981.
- Hays, P. B., T. L. Killeen, N. W. Spencer, L. E. Wharton, R. G. Roble, B. A. Emery, T. J. Fuller-Rowell, D. Rees, L. A. Frank, and J. D. Craven. Observations of the Dynamics of the Polar Thermosphere. J. Geophys. Res., 89, 5597 5612, 1984.

- Hedin, A. E. A revised thermospheric model bsed on mass spectrometer and incoherenct scatter data: MSIS-83. *J. Geophys. Res.*, 88, 10170 10188, 1983.
- Hedin, A. E. and H. G. Mayr. Solar EUV induced variations in the thermosphere. J. Geophys. Res., 92, 869 875, 1987.
- Hedin, A. E., C. A. Reber, G. P. Newton, N. W. Spencer, H. C. Brinton, H. G. Mayr, and W. E. Potter. A global thermospheric model based on mass spectrometer and incoherent scatter data, MSIS, 2, Composition. J. Geophys. Res., 81, 2148 2156, 1977b.
- Hedin, A. E., J. E. Salah, J. V. Evans, C. A. Reber, G. P. Newton, N. W. Spencer, D. C. Kayser, D. Alcayde, P. Bauer, L. Cogger, and J. P. McClure. A global thermospheric model based on mass spectrometer and incoherent scatter data MSIS, 1, N₂ density and temperature. J. Geophys. Res., 82, 2139 2147, 1977a.
- Hedin, A. E., H. G. Mayr, C. A. Reber, N. W. Spencer, and G. R. Carignan. Empirical model of global thermospheric temperature and composition based on data from the OGO-6 quadropole mass spectrometer. J. Geophys. Res., 79, 215 225, 1974.
- Heelis, R. A. The effects of interplanetary magnetic field orientation on dayside high-latitude ionospheric convection. J. Geophys. Res., 89, 2873 2880, 1984.
- Heelis, R. A., J. K Lowell, and R. W. Spiro. A model of the high-latitude ionopheric convection pattern. J. Geophys. Res., 87, 6339 6345, 1982.
- Heelis, R. A. The polar ionosphere. Rev. Geophys. Space Phys., 20, 567 576, 1982.
- Heelis, R. A., W. B. Hanson, C. R. Lippoincott, D. R. Zuccaro, L. H. Harmon, B. J. Holt, J. E. Doherty, and R. A. Power. The ion drift meter for Dynamics Explorer-B. Space Science Inst., 5, 511 521, 1981.
- Heelis, R. A., W. B. Hanson, and J. L. Burch. Ion convection velocity reversals in the dayside cleft. J. Geophys. Res., 81, 3803 3809, 1976.
- Heppner, J. P. Polar cap electric field distributions related to interplanetary magnetic field directions. J. Geophys. Res., 77, 4877, 1972.
- Heppner, J. P. Empirical models of high-latitude electric fields. J. Geophys. Res., 82, 1115-1125, 1977.

Heppner, J. P. Polar cap electric field distributions related to the interplanetary magnetic field direction. J. Geophys. Res., 87, 6339 - 6345, 1982.

Heppner, J. P. and M. L. Miller. Thermospheric winds at high latitudes from chemical release observations. J. Geophys. Res., 87, 1633 - 1647, 1982.

Heppner, J. P. and N. C. Maynard. Empirical high latitude electric field models. J. Geophys. Res., 92, 4467 - 4490, 1987.

Hernandez, G. Fabry-Perot Interferometers. Cambridge University Press, New York, 1986.

Hernandez, G. Mid-latitude thermsopheric neutral kinetic temperatures, 1, solar, geomagnetic, and long-term effects. J. Geophys. Res., 87, 1623 - 1632, 1982.

restablished before the tableton about the sales of

12.22.64.64THK-54.645454

Hernandez, G. Determination of quenching of $O(^{1}D)$ by molecular nitrogen using the ionospheric modification program experiment. J. Geophys. Res., 77, 3625, 1972.

Hernandez, G. and R. G. Roble. Direct measurements of nighttime thermospheric winds and temperatures, 1, seasonal variations during geomagnetic quiet periods. J. Geophys. Res., 81, 2065 - 2074, 1976a.

Hernandez, G. and R. G. Roble. Direct measurements of nighttime thermospheric winds and temperatures, 2, geomagnetic storms. J. Geophys. Res., 81, 5173 - 5181, 1976b.

Hernandez, G. and R. G. Roble. Direct measurements of nighttime thermospheric winds and temperatures, 3, monthly variations during solar minimum. *J. Geophys. Res.*, 82, 5505 - 5511, 1977.

Hernandez, G. and R. G. Roble. Observations of large-scale thermospheric waves during geomagnetic storms. J. Geophys. Res., 83, 5531 - 5538, 1978.

Hernandez, G. and R. G. Roble. On divergences of thermospheric meridional winds at midlatitudes. Geophys. Res. Lett., 6, 294 - 296, 1979.

Hernandez, G. and R. G. Roble. The geomagnetic quiet nighttime thermospheric wind pattern over Fritz Peak Observatory during solar cycle minimum and maximum. J. Geophys. Res., 89, 327 - 337, 1984a.

Hernandez, G. and R. G. Roble. Nighttime variation of thermospheric winds and temperatures over Fritz Peak Observatory during the geomagnetic storm of March 2, 1983. J. Geophys. Res., 89, 9049 - 9056, 1984b.

Hernandez, G., R. G. Roble, and J. H. Allen. Midlatitude thermospheric winds and temperatures and their relation to the auroral electrojet activity index. *Geophys. Res. Lett.*, 7, 677 - 680, 1980.

Hernandez, G., R. G. Roble, E. C. Ridley, and J. H. Allen. Thermospheric response observed over Fritz Peak, Colorado, during two large geomagnetic storms near solar cycle maximum. *J. Geophys. Res.*, 87, 9181 - 9192, 1982.

- Hill, T. W. Magnetic merging in a collisionless plasma. J. Geophys. Res., 80, 4689 4699, 1975.
- Hill, T. W. Solar-wind magnetosphere coupling, in Solar-Terrestrial Physics, edited by R. L. Carovillano and J. M. Forbes, 261 302, D. Reidel, Hingham, MA. 1983.
- Hines, C. O., I. Paghis, T. R. Hartz, and J. A. Fejer. *Physics of the Earth's Upper Atmosphere*. Prentice Hall, Englewood Cliffs, N.J., 1965.
- Hinteregger, H. E. Representation of solar EUV fluxes for aeronomical applications. Adv. Space Res., 1, 39 52, 1981.
- Hinteregger, H. E., K. Fukui, and B. R. Gilson. Observational, Reference, and model data on solar EUV, from measurements on AE-E. Geophys. Res. Lett., 8, 1147 1150, 1981.
- Holton, J. R. An Introduction to Dynamic Meteorology. Academic Press, New York, 1979.
- Jacchia, L. G. Influence of solar activity on the earth's upper atmosphere. *Planet. Space Sci.*, 12, 355 378, 1964.
- Jacchia, L. G. Static diffusion models of the upper atmosphere with empirical temperature profiles. Smithson. Contrib. Astrophys., 8, 215, 1965.
- Jacchia, L. G. Thermospheric temperature, density, and composition. Smithson. Astrophys. Observ. Spec. Rep. 316, Cambridge, Mass., 1971.
- Jacchia, L. G. Thermospheric temperature, density, and composition: new models. Smithson. Astrophys. Observ. Spec. Rep. 170, Cambridge, Mass., 1977.
- Johnson, F. S. The gross character of the geomagnetic field in the solar wind. J. Geophys. Res., 65, 3049 3051, 1960.
- Jokipii, J. R. Propagation of cosmic rays in the solar wind. Rev. Geophys. Space Phys., 9, 27-87, 1972.
- Jorgensen, T. S., E. Friis-Christensen, V. B. Wickwar, J. D. Kelly, C. R. Clauer, and P. M. Banks. On the reversal from "sunward" to "antisunward" plasma convection in the dayside high latitude ionosphere. *Geophys. Res. Lett.*, 11, 887 890, 1984.
- Kamide, Y. and J. A. Slavin. Solar wind magnetosphere coupling: introduction. Solar Wind Magnetosphere Coupling. Edited by Y. Kamide and J. A. Slavin. D. Reidel Publishing, Boston, ix xii, 1986.
- Kelley, M. C., J. F. Vickrey, C. W. Carlson, and R. Torbert. On the origin and spatial extent of high latitude F region irregularities. J. Geophys. Res., 87, 4469, 1982.
- Kelly, J. D., J. F. Vickrey. F-region ionospheric structure associated with antisunward flow near the dayside polar cap. *Geophys. Res. Lett.*, 11, 907 910, 1984.
- Killeen, T. L. Energetics and dynamics of the Earth's thermosphere. Rev. Geophys. Space Phys., 25, 433 454, 1987.

- Killeen, T. L. and R. G. Roble. An analysis of the high-latitude thermospheric wind pattern calculated by a thermospheric general circulation model 2. Neutral parcel transport. J. Geophys. Res., 91, 11291 11307, 1986.
- Killeen, T. L. and R. G. Roble. Neutral parcel transport in the high latitude F-region; in *The Polar Cusp. J. A. Holtet and A. Egeland (eds.)*, D. Reidel Publishing, 261 278, 1985.
- Killeen, T. L. and R. G. Roble. An analysis of the high-latitude thermospheric wind pattern calculated by a thermospheric general circulation model, 1. Momentum forcing. J. Geophys. Res., 89, 7509 7522, 1984.
- Killeen, T. L., R. G. Roble, R. W. Smith, N. W. Spencer, J. W. Meriwether, Jr., D. Rees, G. Hernandez, P. B. Hays, L. L. Cogger, D. P. Sipler, M. A. Biondi, and C. A. Tepley Mean neutral circulation in the winter polar F region. *J. Geophys. Res.*, 91, 1633 1649, 1986.
- Killeen, T. L., R. A. Heelis, P. B. Hays, N. W. Spencer, and W. B. Hanson. Neutral motioons in the polar thermosphere for northward interplanetary magnetic field. *Geophys. Res. Lett.*, 12, 159-162, 1985.
- Killeen, T. L., P. B. Hays, G. R. Carignan, R. A. Heelis, W. B. Hanson, N. W. Spencer, and L. H. Brace. Ion-neutral coupling in the high-latitude F-region: Evaluation of ion heating terms from Dynamics Explorer 2. *J. Geophys. Res.*, 89, 7495 7508, 1984b.
- Killeen, T. L. and R. W. Smith, P. B. Hays, N. W. Spencer, L. E. Wharton, and F. G. McCormac. Neutral winds in the high latitude winter F-region: coordinated observations from ground and space. Geophys. Res. Lett., 11, 311 314, 1984a.
- Killeen, T. L., P. B. Hays, N. W. Spencer, and L. E. Wharton. Neutral winds in the polar thermosphere as measured from Dynamics Explorer. *Geophys. Res. Lett.*, 9, 957 960, 1982.
- Kohl, H. and J. W. King. Atmospheric winds between 100 and 700 km and their effects on the ionosphere. J. Atmos. Terr. Phys., 29, 1045 1062, 1967.
- Krehbiel, J. P., L. H. Brace, R. F. Theis, W. H. Pinkus, and R. B. Kaplan. The Dynamics Explorer Langmuir probe instrument. Space Science Inst., 5, 493 501, 1981.
- Langel, R. A. A comparison of electric and magnetic field data from the OGO 6 spacecraft. J. Geophys. Res., 80, 4661 4673, 1975.
- Lean, J. Solar ultraviolet variations: a review, J. Geophys. Res., 92, 839 868, 1987.
- Lyons, L. R. A simple model for polar cap convection patterns and generation of theta auroras. J. Geophys. Res., 90, 1561 1567, 1985a.
- Lyons, L. R., T. L. Killeen, and R. L. Walterscheid. The neutral wind "flywheel" as a source of quiet-time, polar-cap currents. *Geophys. Res. Lett.*, 12, 101 104, 1985.
- Lyons, L. R. and D. J. Williams. Quantitative Aspects of Magnetospheric Physics. D. Reidel, Boston, 1984.

- Maezawa, K. Magnetospheric convection induced by the positive and negative Z components of the interplanetary magnetic field: quantitative analysis using polar cap magnetic records. J. Geophys. Res., 81, 2289 2303, 1976.
- Massey, H. S. W. The thermal balance in the thermosphere at middle latitudes. Applied Atomic Collision Physics Volume 1, edited by H. S. W. Massey and D. R. Bates. Academic Press, New York, 78, 1982.
- Mayr, H. G. and I. Harris. Some characteristics of electric field momentum coupling with the neutral atmosphere. J. Geophys. Res., 83, 3327 3336, 1978.
- Mayr, H. G., I. Harris, and N. W. Spencer. Some properties of upper atmospheric dynamics. Rev. Geophys. Space Phys., 16, 539 565, 1978.
- McCormac, F. G. An Optical Investigation of Ions and Neutral Motions in the Polar Thermosphere. Ph.D Thesis, Ulster Polytechnic, Northern Ireland, 1984.
- McCormac, F. G. and R. W. Smith. The influence of the interplanetary magnetic field Y component. Geophys. Res. Lett., 11, 935, 1984.
- McCormac, F. G., T. L. Killeen, E. Gombosi, P. B. Hays, and N. W. Spencer. Configuration of the high-latitude thermosphere neutral circulation for IMF By negative and positive. *Geophys. Res. Lett.*, 12, 155 158, 1985.
- McCormac, F. G., T. L. Killeen, J. P. Thayer, G. Hernandez, C. R. Tschan, and J.-J. Ponthieu. Circulation of the polar thermosphere during geomagnetically quiet and active times as observed by DE-2. Submitted to J. Geophys. Res., 1987.
- Menke, W. Geophysical Data Analysis: Discrete Inverse Theory. Academic Press, London, 1984.
- Meriwether, J. W., P. Shih, T. L. Killeen, V. B. Wickwar, and R. G. Roble. Nighttime thermospheric winds over Sondre Stromfjord, Greenland. *Geophys. Res. Lett.*, 11, 931, 1984.
- Mintzer, D. Generalized orthogonal polynomial solutions of the Boltzmann equation. *Phys. Fluids*, 8, 1076 1090, 1965.
- Mizera, P. F. and D. S. Evans. Simultaneous measurements of polar cap electron distributions in opposite hemispheres. J. Geophys. Res., 91, 9007 9011, 1986.
- Moses, J. J., G. L. Siscoe, N. U. Crooker, and D. J. Gorney. IMF B_y and day-night conductivity effects in the expanding polar cap convection model. *J. Geophys. Res.*, 92, 1193-1198, 1987.
- Nagy, A. F., R. J. Cicerone, P. B. Hays, K. D. McWatters, J. W. Meriwether, A. E. Belon, and C. L. Rino. Simultaneous measurement of ion and neutral motions by radar and optical techniques. *Radio Science*, 9, 315 321, 1974.
- Nagy, A. F. and P. M. Banks. Photoelectron fluxes in the ionosphere. J. Geophys. Res., 75, 6260 6270, 1970.

- Nagy, A. F. and P. M. Banks. Photoelectron fluxes in the ionosphere. J. Geophys. Res., 75, 6260 6270, 1970.
- National Research Council. An Implementation Plan for Priorities in Solar-System Space Physics. Washington, D.C., National Academy Press, 1985.
- Noyes, R. W. The Sun, Our Star. Harvard University Press, Cambridge, Mass., 1982.
- Ossakow, S. L., W. Burke, H. C. Carlson, P. Gary, R. Heelis, M. Keskinen, N. Maynard, C. Meng, E. P. Szuszcewicz, J. Vickrey. High-latitude ionospheric structure. Solar Terrestrial Physics: Present and Future, edited by D. M. Butler and K. Papadopoulos, Chapter 12. NASA Reference Publication 1120, 1984.
- Pelz, D. T., C. A. Reber, A. E. Hedin, and G. R. Carignan. A neutral-atmosphere composition experiment for the Atmosphere Explorer-C, -D, and -E. Radio Science, 8, 277 285, 1973.
- Ponthieu, J.-J., T. L. Killeen, K.-M. Lee, and G. R. Carignan. Ionospheric thermospheric momentum coupling at solar maximum and solar minimum from DE-2 and AE-C data. Submitted to *Physica Scripta*, 1987.
- Potemra, T. A., L. J. Zanetti, P. F. Bythrow, A. T. Y. Liu, and T. Iijima. By-dependent convection patterns during northward interplanetary field. *J. Geophys. Res.*, 89, 9753-9760, 1984.
- Primdahl, F. and F. Spangslev. Cusp region and auroral zone field aligned currents. Ann Geophys, 37, 529 538, 1981.
- Primdahl, F. and F. Spangslev. Does IMF By induce the cusp field-aligned currents? *Planet. Space Sci*, 31, 363 367, 1983.
- Quegan, S., G. J. Bailey, R. J. Moffett, R. A. Heelis, T. J. Fuller-Rowell, D. Rees, and R. W. Spiro. A theoretical study of the distribution of ionization in the high-latitude ionosphere and the plasmasphere: first results on the mid-latitude trough and the lightion trough. J. Atmos. Terres. Phys., 44, 619 640, 1982.
- Rees, D., T. J. Fuller-Rowell, R. Gordon, T. L. Killeen, P. B. Hays, L. Wharton, and N. W. Spencer. A comparison of wind observations of the upper thermospherefrom the Dynamics Explorer satellite with the predictions of a global time-dependent model. *Planet. Space Sci.*, 31, 1299 1314, 1983.
- Rees, M. H., B. A. Emery, R. G. Roble, and K. Stamnes. Neutral and ion gas heating by auroral electron precipitation. J. Geophys. Res., 88, 6289 6300, 1983.
- Rees, M. H. and J. C. G. Walker. Ion and electron heating by auroral electric fields. Ann. Geophys., 24, 1-7, 1968.
- Reiff, P. H., R. W. Spiro, and T. W. Hill. Dependence of polar cap potential drop on interplanetary parameters. J. Geophys. Res., 86, 7639 7648, 1981.
- Reiff, P. H. and J. L. Burch. IMF B_y -dependent plasma flow and Birkeland currents in the dayside magnetosphere 2. a global model for northward and southward IMF. J. Geophys. Res., 90, 1595 1609, 1985.

Reiff, P. H., R. W. Spiro, R. A. Wolf, Y. Kamide, and J. H. King. Comparison of polar cap potential drops estimated from solar wind and ground magnetometer data: CDAW 6. *J. Geophys. Res.*, 90, 1318 - 1324, 1985.

Reiff, P. H. and J. G. Luhmann. Solar wind control of the polar-cap voltage. Solar Wind - Magnetosphere Coupling. Edited by Y. Kamide and J. A. Slavin. D. Reidel Publishing, Boston, 453 - 476, 1986.

Richmond, A. D., M. Blanc, B. A. Emery, R. H. Wand, B. G. Fejer, R. F. Woodman, S. Ganguly, P. Amayenc, R. A. Behnke, C. Calderon, and J. V. Evans. An empirical model of quiet-day ionospheric electric fields at middle and low latitudes. *J. Geophys. Res.*, 85, 4658 - 4664, 1980.

Rishbeth, H. Ion drag effects in the thermosphere. J. Atm. Terr. Phys., 41, 285-294, 1979.

Rishbeth, H. Drifts and winds in the polar F-region. J. Atm. Terr. Phys., 39, 111 - 116, 1977.

Rishbeth, H. F-region storms and thermospheric circulation. J. Atm. Terr. Phys., 37, 1055-1064, 1975.

Rishbeth, H. Ionospheric dynamics 1945-1970. J. Atm. Terr. Phys., 36, 2309 - 2319, 1974.

Rishbeth, H. Thermospheric winds and the F-region: a review. J. Atm. Terr. Phys., 34, 1-47, 1972.

Rishbeth, H. and O. K. Garriott. Introduction to Ionospheric Physics. Academic Press, New York, 1969.

Roble, R. G. Chemistry in the thermosphere and ionosphere. Chem. Eng. News, 64, 23 - 28, 1986.

Roble, R. G. The Thermosphere, Chapter 3 of *The Upper Atmosphere and Magnetosphere*. National Academy of Sciences, Washington, D. C., 1977.

Roble, R. G. and E. C. Ridley. An auroral model for the NCAR thermospheric global circulation model (TGCM). Submitted to Ann. Geophys., 1987.

Roble, R. G. and B. A. Emery. On the global mean temperature of the thermosphere. *Planet. Space Sci.*, 31, 597 - 614, 1983.

Roble, R. G., J. M. Forbes, and F. A. Marcos. Thermospheric dynamics during the March 22, 1979 magnetic storm (CDAW-6): (1.) model simulation. Submitted to J. Geophys. Res., 1987a.

Roble, R. G., E. C. Ridley, and R. E. Dickinson. On the global mean structure of the thermsophere. Submitted to J. Geophys. Res., 1987b.

Roble, R. G., B. A. Emery, R. E. Dickinson, E. C. Ridley, T. L. Killeen, P.B. Hays, G. R. Carignan, and N. W. Spencer. Thermospheric circulation, temperature, and compositional structure of the southern hemisphere polar cap during October - November 1981. J. Geophys. Res., 89, 9057 - 9068, 1984.

- Roble, R. G., R. E. Dickinson, E. C. Ridley, B. A. Emery, P. B. Hays, T. L. Killeen, and N. W. Spencer. The high latitude circulation and temperature structure of the thermosphere near solstice. *Planet. Space Sci.*, 31, 1479-1499, 1983.
- Roble, R. G., R. E. Dickinson, and E. C. Ridley. Global circulation and temperature structure of the thermosphere with high-latitude plasma convection. *J. Geophys. Res.*, 87, 1599-1614, 1982.
- Roble, R. G., R. E. Dickinson, and E. C. Ridley. Seasonal and solar cycle variations of the zonal mean circulation in the thermosphere. J. Geophys. Res., 82, 5493 5504, 1977.
- Romick, G. J., T. L. Killeen, D. G. Torr, B. A. Tinsley, and R. A. Behnke. CEDAR: An aeronomy initiative. EOS Trans. AGU, 68, 19 21, 1987.
- Roper, R. G. and J. E. Salah. Preliminary results from the URSI/IAGI cooperative tidal observations program (CTOP). J. Atmos. Terres. Phys., 40, 879 885, 1978.
- Rostoker, G. Geomagnetic indices. Rev. Geophys. Space Phys., 10, 935 950, 1972.
- Rostoker, G. Polar magnetic substorms. Rev. Geophys. Space Phys., 10, 157 211, 1972.
- Russell, C. T. ISEE-3 Solar wind and interplanetary magnetic field plots generated by the UCLA magnetometer group from the ISEE data pool tapes. *IGPP publication number* 2293, 1982.
- Russell, C. T. Geophysical coordinate transformations. Cosmic Electrodynamics, 2, 184-196, 1971.
- Russell, C. T. Critical Problems of Magnetospheric Physics. National Academy of Sciences, Washington, D. C., 1972.
- Salah, J. E., G. Hernandez, R. G. Roble, and B. A. Emery. Comparison of thermospheric winds from incoherent scatter radar and optical emission doppler shift measurments. Submitted to *Ann. Geophys.*, 1987.
- Salah, J. E., R. H. Wand, and R. Bernard. Comparison of simultaneous tidal observations by incoherent scatter radars. Ann. Geophys., 33, 95 102, 1977.
- Schatten, K. H. Large-scale properties of the interplanetary magnetic field. Rev. Geophys. Space Phys., 9, 773, 1971.
- Schunk, R. W., P. M. Banks, and W. J. Raitt. Effects of electric fields and other processes upon the nighttime high-latitude F layer. J. Geophys. Res., 81, 3271, 1976.
- Schunk, R. W. Mathematical structure of transport equations for multispecies flows. Rev. Geophys. Space Phys., 15, 429 445, 1977.
- Schunk, R. W. and A. F. Nagy. Electron temperature in the F region of the ionosphere: theory and observations. Rev. Geophy. Space Physics, 16, 355 399, 1978.
- Schunk, R. W. and A. F. Nagy. Ionospheres of the terrestrial planets. Rev. Geophy. Space Physics, 18, 813 852, 1980.

- Schunk, R. W. and W. J. Raitt. Atomic nitrogen and oxygen ions in the daytime high-latitude F region, J. Geophys. Res., 85, 1255, 1980.
- Schunk, R. W. and J. J. Sojka. Ion temperature variations in the daytime high-latitude F region. J. Geophys. Res., 87, 5169, 1982.
- Schunk, R. W., A. R. Baraket, H. Carlson, J. B. Evans, J. Foster, R. Greenwald, M. C. Kelley, T. Potemra, M. H. Rees, A. D. Richmond, and R. G. Roble. Assessment of plasma transport and convection at high latitudes. *Solar Terrestrial Physics: Present and Future*, edited by D. M. Butler and K. Papadopoulos, Chapter 11. NASA Reference Publication 1120, 1984.

PRESERVE (NAVARA) PERSONAN MEGICANI (NAVARA)

TO TO SELECT SECTION OF THE PROPERTY OF THE PERSON OF THE

- Sica, R. J. Auroral Zone Thermospheric Dynamics Using Fabry-Perot Interferometric Measurements of the OI 15867K Emission. Ph.D Thesis, University of Alaska, 1984.
- Sica, R. J., M. H. Rees, G. J. Romick, G. Hernandez, and R. G. Roble. Auroral zone thermospheric dynamics 1. averages. J. Geophys. Res., 91, 3231 3244, 1986a.
- Sica, R. J., G. Hernandez, G. J. Romick, M. H. Rees, and R. G. Roble. Auroral zone thermospheric dynamics 2. individual nights. J. Geophys. Res., 91, 13593 13611, 1986b.
- Slavin, J. A., G. Jungman, and E. J. Smith. The interplanetary magnetic field during solar cycle 21: ISEE-3/ICE observations. Geophys. Res. Lett., 13, 513 516, 1986.
- Smith, P. H., C. H. Freeman, and R. A. Hoffman. Dynamics Explorer science data processing system. Space Sci. Inst., 5, 561-573, 1981.
- Smith, R. W., D. Rees, F. G. McCormac, and P. Charleton. Two station observations of thermospheric winds in the auroral zone and the polar cap. J. Atm. Terr. Phys., 48, 97-105, 1986.
- Sojka, J. J., W. J. Raitt, and R. W. Schunk. Effects of displaced geomagnetic and geographic poles for high latitude plasma convection and ionospheric depletions. J. Geophys. Res., 84, 5943 5951, 1979.
- Sojka, J. J., W. J. Raitt, and R. W. Schunk. A theoretical study of the high-latitude winter F-region as solar minimum for low geomagnetic activity. *J. Geophys. Res.*, 86, 609-621, 1981a.
- Sojka, J. J., W. J. Raitt, and R. W. Schunk. Plasma density features associated with strong convection in the high-latitude F-region. J. Geophys. Res., 86, 6908 6916, 1981b.
- Sojka, J. J., R. W. Schunk, and W. J. Raitt. Seasonal variations of the high latitude F-region for strong convection. J. Geophys. Res., 87, 187 198, 1982.
- Sojka, J. J. and R. W. Schunk. A theoretical study of the global F-region for June solstice, solar maximum, and low magnetic activity. J. Geophys. Res., 90, 5285 5298, 1985.
- Sojka, J. J., C. E. Rasmussen, and R. W. Schunk. An interplanetary magnetic field dependent model of the ionospheric convection pattern. J. Geophys. Res., 91, 11281 11290, 1986.

- Sojka, J. J. and R. W. Schunk. A theoretical study of the production and decay of localized electron density enhancements in the polar ionosphere. J. Geophys. Res., 91, 3245-3253, 1986a.
- Sojka, J. J. and R. W. Schunk. Problems deducing ionsopheric plasma convection patterns. J. Geophys. Res., 91, 259 269, 1986b.
- Sonnerup, B. U. O. Reconnection of magnetic fields, 1. introduction. Solar Terrestrial Physics: Present and Future, edited by D. M. Butler and K. Papadopoulos, Chapter 1. NASA Reference Publication 1120, 1984.
- Sonnerup, B. U. O. Magnetic field reconnection at the magnetopause: an overview. *Magnetic Reconnection in Space and Laboratory Plasmas*, edited by E. W. Hones, Jr. AGU monograph 30, American Geophysical Union, Wash., D. C., 92 103, 1984.
- Spencer, N. W., L. E. Wharton, G. C. Carignan, and J. C. Maurer. Thermosphere zonal winds, vertical motions and temperatures from Dynamics Explorer. *Geophys. Res. Lett.*, 9, 953-956, 1982.
- Spencer, N. W., L. E. Wharton, H. B. Niemann, A. E. Hedin, G. R. Carignan, and J. C. Maurer. The Dynamics Explorer Wind and Temperature Spectrometer. Space Science Instrumentation, 5, 417 428, 1981.
- Spencer, N. W., H. B. Niemann and G. R. Carignan. The neutral-atmosphere temperature instrument. Radio Science, 8, 287 296, 1973.
- Spiro, R. W., M. Harel, R. A. Wolf, and P. H. Reiff. Quantitative simulation of a magnetospheric substorm, 3, Plasmaspheric electric fields and evolution of the plasmapause. J. Geophys. Res., 86, 2261 2272, 1981.
- St.Maurice, J.-P. and R. W. Schunk. Ion-neutral momentum coupling near discrete high latitude ionospheric features. J. Geophys. Res., 86, 11299 11321, 1981.
- St. Maurice, J.-P. and W. B. Hanson. A statistical study of F region ion temperatures at high latitudes based on Atmosphere Explorer C data. J. Geophys. Res., 89, 987 996, 1984.
- Stern, D. P. Large-scale electric fields in the earth's magnetosphere. Rev. Geophys. Space Phys., 15, 156-194, 1977.
- Stolarski, R. S. Energetics of the midlatitude thermosphere. J. Atmos. Terres. Phys., 38, 863-868, 1976.
- Stolarski, R. S.; P. B. Hays, and R. G. Roble. Atmospheric heating by solar EUV radiation. J. Geophys. Res., 82, 2266 2276, 1975.
- Straus, J. M., S. P. Creekmore, R. M. Harris, B. K. Ching, and Y. T. Chiu. A global model of thermospheric dynamics-II. Wind, density, and temperature fields generated by EUV heating. J. Atmos. Terres. Phys., 37, 1245 1254, 1975.
- Straus, J. M., S. P. Creekmore, R. M. Harris, and B. K. Ching. Effects of heating at high latitudes on global thermospheric dynamics. J. Atmos. Terres. Phys., 37, 1545 1554, 1975.

- Szuszcewicz, E. P. Summary of ionsopheric physics: high-latitude ionospheric plasma dynamics; phenomenology, irregularity distributions, transport, and magnetospheric coupling. Solar Terrestrial Physics: Present and Future. Edited by D. M. Butler and K. Papadopoulos, Appendix C. NASA Reference Publication 1120, 1984.
- Thayer, J. P., T. L. Killeen, F. G. McCormac, C. R. Tschan, and J.-J. Ponthieu. IMF By-dependent neutral wind signatures for northern and southern hemispheres from Dynamics Explorer-2 data. Submitted to Ann. Geophys., 1987.
- Thuillier, G., J. L. Falin, and C. Wachtel. Experimental global model of the exospheric temperature based on measurements from the Fabry-Perot interferometer on board the OGO-6 satellite discussion of the data and properties of the model. *J. Atm. Terres. Phys.*, 39, 399 414, 1977.
- Tolansky, S. An Introduction to Interferometry. Longmans, Green and Co., London, 1966.
- Torr, M. R., D. G. Torr, and H. E. Hinteregger. Solar flux variability in the Schumann-Runge continuum as a function of solar cycle 21. J. Geophys. Res., 85, 6063-6068, 1980c.
- Torr, M. R., P. G. Richards, and D. G. Torr. A new determination of the ultraviolet heating efficiency of the thermosphere. J. Geophys. Res., 85, 6819 6826, 1980b.
- Torr, M. R., D. G. Torr, and P. G. Richards. The solar ultraviolet heating efficiency of the midlatitude thermosphere. *Geophys. Res. Lett.*, 7, 373 376, 1980a.
- Torr, M. R., D. G. Torr, R. A. Ong, and H. E. Hinteregger. Ionization frequencies for major thermospheric constituents as a function of solar cycle 21. *Geophys. Res. Lett.*, 6, 771 774, 1979.
- Torr, D. G. and M. R. Torr. Review of rate coefficients of ionic reactions determined from measurements made by the Atmosphere Explorer satellites. Rev. Geophys. Space Phys., 16, 327 340, 1978.
- Tschan, C. R., T. L. Killeen, G. R. Carignan, R. G. Roble, B. A. Emery, R. A. Heelis, W. B. Hanson, and N. W. Spencer. How close are we to being able to forecast the motions of the thermsophere? *EOS Trans. AGU*, 67, 1138, 1986.
- Tschan, C. R., T. L. Killeen, and N. W. Spencer. Conjugate measurements of neutral winds in the northern and southern polar F-regions. EOS Trans. AGU, 66, 322, 1985.
- Vallance-Jones, A. Aurora. D. Reidel Publishing, Boston, 1974.

SESSI PERSONAL PROPERTY CONTROL PROPERTY SUSPENSION REPORTED RESERVES ARRESTED INVOLVED MESSAGE AINTER

- Van Allen, J. A., J. F. Fennell, and N. F. Ness. Asymmetric access of energetic solar protons to the Earth's north and south polar caps. J. Geophys. Res., 76, 4262, 1971.
- Vasyliunas, V. M. Theoretical models of magnetic field line merging, 1. Rev. Geophys. Space Phys., 13, 303 336, 1975.
- Vasyliunas, V. M. Steady state aspects of magnetic field line merging. *Magnetic Reconnection in Space and Laboratory Plasmas*, edited by E. W. Hones, Jr. AGU monograph 30, American Geophysical Union, Wash., D. C., 25 31, 1984.

Vernazza, J. E., E. H. Avrett, and R. Loeser. Structure of the solar chromosphere, II, the underlying photosphere and temperature minimum region. *Astrophys. J. Suppl. Ser.*, 30, 1-60, 1976.

Vernazza, J. E., E. H. Avrett, and R. Loeser. Structure of the solar chromosphere, III, models of the EUV brightness components of the quiet sun. *Astrophys. J. Suppl. Ser.*, 45, 635-725, 1981.

Vickrey, J. F., R. C. Livingston, N. B. Walker, T. A. Potemra, R. A. Heelis, M. C. Kelley, and F. J. Rich. On the current-voltage relationship of the magnetospheric generator at the intermediate spatial scales. *Geophys. Res. Lett.*, 13, 495 - 498, 1986.

WALLES CHOOSE CONTRACTOR CONTRACTOR

socretector (progetime postessos (modificies prostessos horonos)

Vincenti, W. G. and C. H. Kruger, Jr. Introduction to Physical Gas Dynamics. Robert E. Krieger Publishing. Malabar, Florida, 1982.

Volland, H. Magnetospheric electric fields and currents and their influence on large scale thermospheric circulation and composition. J. Atm. Terr. Phys., 41, 853 - 866, 1979.

Volland, H. A model of the magnetospheric electric convection field. J. Geophys. Res, 83, 2695-2699, 1978.

Wand, R. H. Lower thermospheric structure from Millstone Hill incoherent scatter radar measurements, 2, semidiurnal temperature component. J. Geophys. Res., 88, 7211 - 7224, 1983.

Wayne, R. P. Chemistry of Atmospheres. Clarendon Press, Oxford, U. K., 1985.

Weber, E. J., J. Buchau, J. G. Moore, J. R. Sharber, R. C. Livingston, J. D. Winningham, and B. W. Reinisch. F layer ionization patches in the polar cap. J. Geophys. Res., 89, 1683-1694, 1984.

Wilcox, J. M. Inferring the interplanetary field by observing the polar geomagnetic field. Rev. Geophys. Space Phys., 10, 1003 - 1014, 1972.

Wilcox, J. M. and N. F. Ness. Quasi-stationary corotating structure in the interplanetary medium. J. Geophys. Res., 70, 5793 - 5805, 1965.

Willmore, A. P. Exploration of the ionosphere from satellites. J. Atm. Terr. Phys., 36, 2255-2286, 1974.

Winningham, J. D., J. L. Burch, N. Eaker, V. A. Blevis, and R. A. Hoffman. The low altitude plasma instrument (LAPI). Space Sci. Inst., 5, 465 - 475, 1981.

EMED

MARCH, 1988

DTIC